INVESTIGATIONS OF STRUCTURE – PROPERTY RELATIONSHIPS IN SEMICRYSTALLINE THERMOPLASTIC POLYMERS: BLOWN POLYETHYLENE FILMS AND POLYACRYLONITRILE COPOLYMERS

by

DAVID L. GODSHALL

Dissertation submitted to the faculty of the
Virginia Polytechnic Institute and State University
in partial fulfillment of the requirements for the degree of

DOCTOR OF PHILOSOPHY

in

Chemical Engineering

APPROVED:

_____
G.L. Wilkes, Chairman

_____	_____
D.G. Baird	J.E. McGrath
_____	_____
R.F. Saraf	A.R. Shultz

October, 2002
Blacksburg, VA

Keywords: polyethylene, film, blown, polyacrylonitrile

Investigations of Structure – Property Relationships in Semicrystalline Thermoplastic Polymers: Blown Polyethylene Films and Polyacrylonitrile Copolymers

by

David L. Godshall

Chairman: G.L. Wilkes
Department of Chemical Engineering

ABSTRACT

Blown films of high molecular weight high density polyethylene (HMW-HDPE) were produced from two resins of differing molecular weight (MW) and molecular weight distribution (MWD) using a high stalk bubble configuration. The processing conditions were varied such that three film gauges, each fabricated at three frost line heights (FLH), were produced. Crystalline orientation and tear resistance properties of the films were measured. Under appropriate conditions, the formation of two populations of lamellar stacks with their surface normals orthogonal to one another were observed. Increasing the FLH increased the amount of transverse direction (TD) stacked lamellae. This finding was related to bubble shape and relaxation behavior. Balanced in plane crystalline orientation was noted to give the best dart impact performance. Interestingly, for the lower M_w resin in the study, this could be achieved by down gauging.

In a second project, structure-property-processing relationships were investigated in a series of high density polyethylene (HDPE) blown films. The use of metallocene and chromium oxide based resins allowed the effects of MW and MWD on orientation behavior to be studied. All films possessed Keller-Machin low stress morphologies oriented along the film MD. Under identical processing conditions, the narrower MWD resins produced films with greater orientation than the broader MWD resins of equivalent weight average MW. Greater processing stresses and shorter quench times were noted to produce higher levels of orientation. Moisture vapor transmission rate (MVTR) performance of these films was also measured. Orientation effects were seen to influence MVTR as permeation behavior did not scale directly with the crystalline content in the films.

Additional studies investigated the relationship between comonomer content and the thermal and structural properties of novel poly(acrylonitrile-co-methyl acrylate) materials. Five polymers were studied with methyl acrylate (MA) content varying between 0 and 15 mol%. The MA decreased both the glass transition and melting temperatures. Melting point depression was sufficient in the two highest MA content copolymers to allow for complete melting prior to the onset of thermal degradation using modest heating rates (20 °C/min). Insight into the heterogeneous structure of poly(acrylonitrile) homopolymer was gained through both conventional and modulated differential scanning calorimetry.

Acknowledgements

I would like to thank all of those people along the way who have shown remarkable patience with me over the past six years as I have worked, or at times more seemingly have stumbled, my way towards the completion of this dissertation. At the very top of the patience list is my advisor, Dr. Wilkes. The technical and professional guidance provided by Dr. Wilkes comes in such a reliable, accurate, and timely manner than it is difficult not to take these things for granted under his tutelage. Furthermore, his willingness to work with my personality, and indeed all of the personalities in our lab, as unique individuals, rather than as graduate student # X, has allowed me to develop the confidence in myself which I am convinced will carry me through the rough spots I will inevitably encounter in my professional future.

In addition, I would like to express my thanks to Dr. Baird, Dr. McGrath, Dr. Saraf, and Dr. Shultz for participating on the PhD committee, and taking the time to review this document. Particular thanks go to Dr. Baird and Dr. McGrath for including me in the carbon fiber project and paying my bills, while the majority of my energies were focused on other projects.

Chapter 3 would not have been possible without the generous support of Dr. Rajendra Krishnaswamy and Dr. Ashish Sukhadia of Chevron Phillips Chemical Company. I am grateful for the opportunity to join a project already in progress and become the lead author for the work. In addition I wish to thank them for the insights into both technical and practical matters regarding blown film which they have provided.

And then, of course, there are my coworkers in the lab. Actually three generations of them. In my final two years here I probably could not have asked for more forgiving labmates, as I occasionally transformed from a mild mannered graduate student to a cranky, old, cantankerous one. I've enjoyed the company of Jignesh, Pankaj, and Seugmen more than I ever thought I would. In the middle years there were Ashish, Brain, Matt J., and Varun, each with a vibrant personality that made each day in lab colorful to say the least. And last, but certainly not least there is the original group, those who were here in the early years, and in some cases have made the entire journey with me. More than anyone else, Chris was responsible for providing my early education in the lab. He also is a great friend, I look forward to getting back in touch after I crossover to the real world. What to say about Kurt? Upon meeting Kurt, I never would have guessed he would become one of the closest friends I've made during my time at Tech. How can I forget my first day in lab when he asked me if I was still in junior high. Thanks for the welcome

buddy. In time, however, I've come to rely on Kurt on technical matters and to value the advice and support he has given me as I work to complete this degree. Along with Chris and Kurt, a few people outside of the lab deserve special mention for helping me retain my tenuous grip on sanity. Jen M. and Jody top this list. Without their friendship I would undoubtedly have questioned why I was here. Others include Sandra, Amy, Emmett, Jen B., Tanya, and Kerri Ann. Thanks guys. While I have focused on graduate students, one lowly undergrad certainly deserves mention. I'm not sure where exactly Terri fits into this mix, but above all others, if ever I thought of giving up on the degree, or really on anything, she is the one I know I can count on to set met straight and believe in my potential. On to the final person on the friends/coworkers list. It could of course only Mr. O'Sickey. Technically, Dr. O'Sickey these days. For every time it seemed Matt was responsible for getting me into trouble, there are probably at least ten times he helped me stay out of it. Having become quite efficient at digging my own holes and becoming discouraged while here, Matt more than anyone else was responsible for getting me back into gear and in touch with reality during lean times, often on a weekly basis. On technical matters I know that I can count on him to remember what I have forgotten. On personal matters I've witnessed him guide others, as well as myself, in the right direction.

Finally, I wish to thank my family. They too have been patient in waiting for me to finish this task. With typical Godshall understatement, they have been behind me, unwavering in their support, without hype, drama, or question. I thank them for being patient as I so very slowly develop into the complete person I am destined to become.

Table of Contents

List of Tables

List of Figures

Chapter 1 – Introduction

This dissertation, as the title implies, documents work from three separate projects. Although two of the projects involve the production of blown high density polyethylene films, the focus of each is quite different. Therefore, chapters are presented as wholly independent from one another. The material is presented in the following order.

Chapter two contains background information and a review of the literature pertinent to the area of blown polyethylene films. Topics include the development of structure in the blown film process, a brief review of some of the analytical methods utilized in the dissertation, and a discussion of the factors pertinent to the permeation of small molecules through semicrystalline polymers. The material presented is relevant to

the work presented in the third and fourth chapters, as these represent the major projects of the dissertation.

Chapter three presents the first blown film project. This research into the processing-structure-property relationships of high density polyethylene films produced using a high stalk, or delayed blow out, blown film process, was conducted in collaboration with Chevron-Phillips. Unique morphologies consisting of bimodal orthogonal stacks of lamellae are observed, and the factors influencing their formation are discussed. Characterization of the tear and puncture resistances of these films is also examined in the context of film morphology.

Chapter four considers the role that crystalline orientation has in influencing the rate of water permeation through blown high density polyethylene films. This study was conducted in conjunction with Chevron, prior to the merger with Phillips. It contains the characterization results from a large number of films, fabricated under various processing conditions and using several resins. These results are then correlated with the measured moisture vapor transmission rate for each film in an attempt to quantify the importance of crystalline orientation to barrier performance.

Chapter five contains the final research topic included in the dissertation. This work undertakes a study of the thermal and structural properties of a series of novel poly(acrylonitrile-co-methyl acrylate) materials. The work presented represents a small portion of a much larger project. Funded by the Department of Energy, this multidisciplinary project involving groups at both Virginia Tech and Clemson University, has as its objective the development of new poly(acrylonitrile) based polymers which may be melt spun into precursors suitable for conversion into carbon fibers. The first portion of the material presented focuses on the effects of comonomer content on the thermal transitions and crystalline content of these materials. Additional experiments that address the nature of the glass transition of poly(acrylonitrile) homopolymer are also presented.

The final chapter contains a review of the major conclusions from each of the research topics. In addition, recommendations for future work are presented.

Chapter 2. Background and Literature Review

2-1. Introduction

This background section will begin with a very brief description of the film blowing process to introduce key processing variables and to give the reader a general understanding of the nature of the procedure. Next follows an introduction to the various types of polyethylene which are used commercially in the film blowing process. The differences among specific resins will be addressed to give an indication of how polymer topology can influence processing, final film texture, and hence film properties.

2-2. Blown Film Process

The single bubble blown film process is represented schematically in Fig.2.1. The process begins with the extrusion melting (A) of the polymer resin. This molten polymer is fed to an annular die (B) and forced out vertically forming a tube of polymer

melt referred to as the stalk (C). The melt is then drawn upward while its outer surface is being cooled by the air ring (D). Additionally, air is also being forced into the stalk from within the annular space. The pressure exerted by this air, in the enclosed space of the bubble sealed at bottom by the die, and at the top by the nip rolls, (E), causes the stalk to expand. The dual stretching nature (axial and radial) of the process at this step leads to a biaxial orientation of the polymer chains. The relative amounts of stretching which occur in the axial and radial directions will greatly influence the film's final properties. A short distance from the exit of the annular die the polymer crystallizes. This point can be observed by an increase in turbidity and is commonly referred to as the frost line. Above the frost line the solidified polymer film is pulled up to the nip rolls (E), collapsed, and wound onto a roll (F). Additional post treatment steps (e.g. relaxing, cutting, printing) may take place, though this study will not deal with any post treatment aspects. The production of multilayer films via coextrusion in the blown film process utilizes multiple extruders and specialized dies. Multilayer systems will not be addressed in this discussion, nor will the double bubble process commonly used to produce polypropylene films[1].

While at first glance this process may appear to be quite sensitive to slight perturbations in the system, it is currently the most common process for producing large quantities of polymeric films at a low cost. As with any process it has its advantages and disadvantages. Relative to a cast film process, the blown film process has the following difficulties. Uniformity in film thickness can be problematic (variations in thickness of ± 10% versus ± 5% for a cast system[10]). The source of thickness variation can be traced back to difficulties in exactly matching the cooling conditions around the entire circumference of the bubble, uneven tensions on the bubble, and variation in processing stress in the melt as material is fed to the circular annulus. Cast films can often be produced at greater rates than blown films[11]. To the credit of the blown film process it is generally recognized that the capital outlay for the blown film process is lower and less scrap material is produced. Furthermore, it is quite simple to adjust the film width on a blown film line by adjusting the blow up ratio, throughput and haul off speeds. The width of a cast film is essentially set by the die span[11]. Lastly, the tubular shape

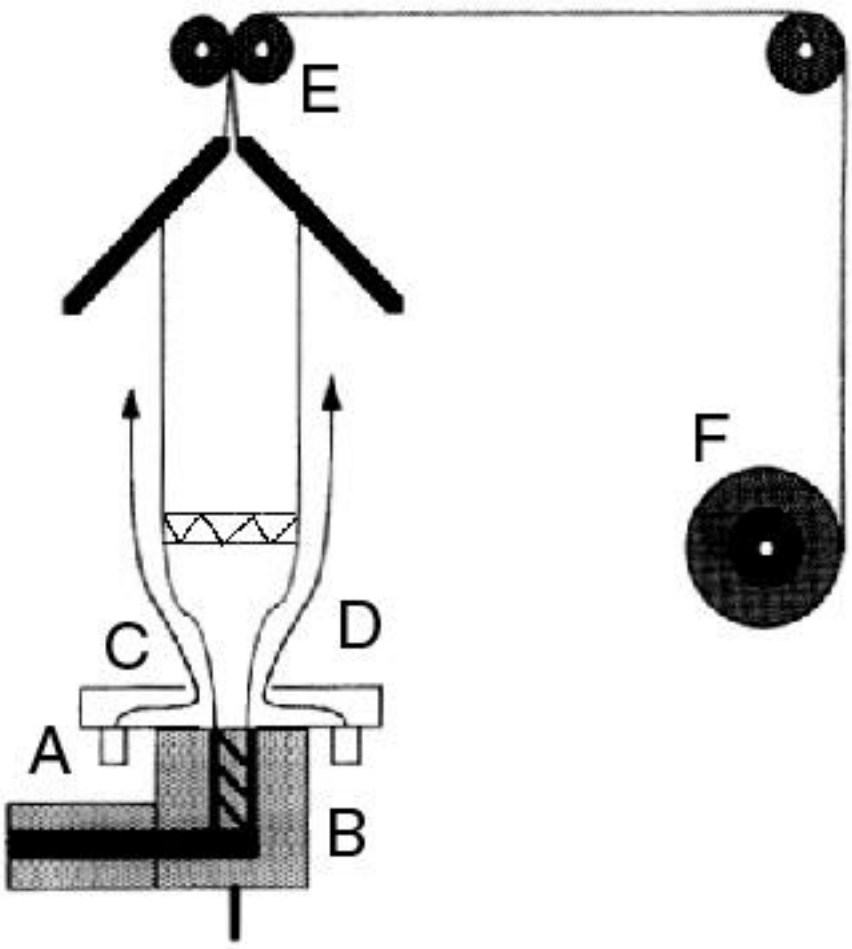

Figure 2.1. Schematic of blown film process

produced by the blown film process requires that only one end be sealed to form bags in contrast to multiple edges for a cast film process.

2-3. Use of High Density Polyethylene

High density polyethylene is used primarily in packaging applications for which barrier properties are a key attribute[12]. HDPE has excellent chemical resistance due to its high crystalline content, thus it is used in bottles for home cleaning agents, detergents, and bleach. Its excellent moisture barrier properties also make it an ideal candidate for food applications where the product is sensitive to water, such as cereal bags. In comparison to low density polyethylene, HDPE often has greater strength and toughness. In fact these two mechanical properties when combined in a thin (~ 0.5 mil) film make it an ideal material for grocery and shopping bags based on both weight and price savings. Finally, it is a combination of all of the above properties which plays a key role in making HDPE the resin of choice for milk, juice, and water containers.

The market for HDPE is continually growing as it replaces traditional paper and cardboard packaging. For the past several years domestic HDPE growth has outpaced the gross national product by a factor of 1.7, with the 13.86 million lbs. of U.S. production making up a large portion of the 21.27 million lbs. of plastics that were used in packaging for the year 1999[13].

2-4. Classes of Polyethylene

A better understanding of how HDPE can form products which are well suited for the packaging industry can be gained by examining its molecular structure. Specifically its topology will be compared to the two other commodity polyethylenes, low density polyethylene, LDPE, and linear low density polyethylene, LLDPE. Topology will play a key role in both the processing differences among these materials and their final morphological textures. Figure 2.2 contains schematics depicting the structures of each of the three major classes of polyethylene. High density polyethylene can be considered the simplest and the most ordered of the three. It consists of long, linear chains of

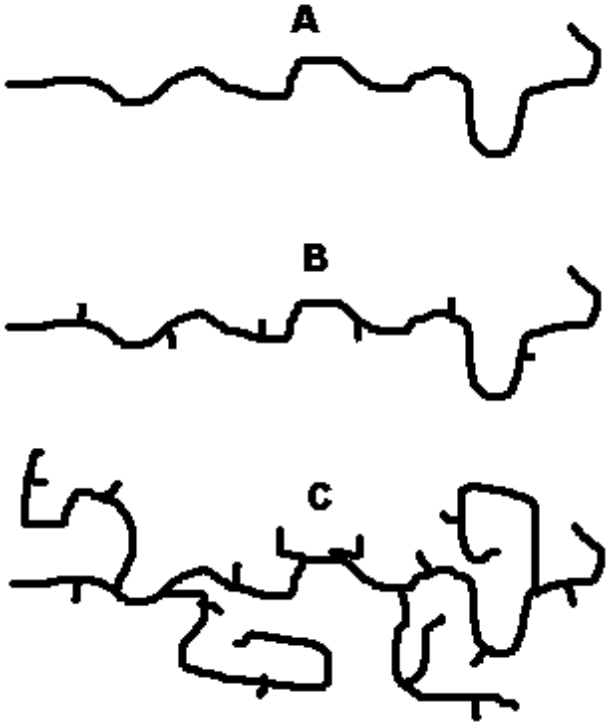

Figure 2.2. Idealized schematic of various types of polyethylenes. A) high density polyethylene, B) linear low density polyethylene, C) low density polyethylene.

polymerized ethylene. The lack of chiral centers and the linearity of the chain leads to a material which when below the melting point can easily and rapidly form a highly crystalline structure. A polyethylene is considered to qualify as an HDPE resin if its density is greater than 0.94 g/cm^3. It is important to note that while all of the chains have the same linear structure, many different chain lengths can be present. This variation in chain lengths, and thus molecular weight, can be quantified to a first approximation by the use of the polydispersity index (PDI). The PDI of a resin is found by dividing the weight average molecular weight, Mw, by the number average molecular weight, Mn. The PDI of a HDPE resin will be influenced by reactor conditions and catalyst type used for synthesis. Values of PDI ranging from 2 to 20 are typically achieved. The breadth of the molecular weight distribution can have a profound impact on the processability and properties as will be discussed later.

Linear low density polyethylene consists of a long chain backbone with short chain branches. The addition of these branches to the chain is accomplished by reacting a small amount of α-olefin comonomer with the ethylene during polymerization. The length of these "short" branches is typically two to eight carbon atoms. The nature of the short branches is such that they lead to a reduction in melt viscosity, when compared to an equivalent molecular weight HDPE chain, as they are too short to entangle. Clearly, a LLDPE chain will be shorter than its weight equivalent HDPE chain, resulting in fewer entanglements and hence a lower viscosity. A decrease in the crystallinity level of LLDPE relative to HDPE is also noted as the short chain branch points act as defects which cannot be easily accommodated by the crystalline lattice. As with HDPE a variety of chain lengths is produced. The distribution of chain lengths and branching per chain will be influenced by reactor conditions and catalyst type. Early LLDPE technology led to a preferential addition of the comonomer to the shorter chains.

Finally, low density polyethylene is composed of a highly random arrangement of both long and short chain branches along the backbone. In fact some of the long chain branches on a LDPE molecule may have short and long chain branches of their own. The greater amount of short chain branching in low density polyethylene tends to make this polymer have a lower crystalline content than HDPE. The branches in LDPE, both long and short, are a result of the less controlled nature of the high pressure and temperature

(~20,000 psi, 200 °C) free radical polymerization used to make this type of polyethylene. Because of the random nature of LDPE synthesis the resins show little variation in crystalline content The viscosity can of course be controlled through variation of the average molecular weight.

Broad generalizations about molecular architecture are sufficient to account for the gross differences observed among the various types of polyethylene. However, to better understand how small variations in branching type and content can lead to differences within a polyethylene class, specifically HDPE, it will be necessary to examine more in depth the effects these factors have on the polymer's ability to crystallize, the morphological structures it forms, and how the melt rheology is affected. The relevance of these questions has been renewed with the emergence of a relatively new class of polyethylene catalysts, the metallocenes. These catalysts allow the specific features of chain architecture in HDPEs to be controlled to a level that was not possible with the traditional Zeigler-Natta or chromium based systems.

2-5. Polyethylene Catalysis

The practical polymerization of high density polyethylene began with the nearly simultaneous discoveries of three different research groups. Karl Ziegler's discovery of a catalyst which was capable of polymerizing ethylene at moderate temperatures and pressures far below those used in LDPE production occurred in 1953[14]. Concurrently, Giulio Natta succeeded in polymerizing isotactic polypropylene from propylene[15]. The category of catalysts which bear these researchers' names, Ziegler-Natta catalysts, were innovative because they allowed for stereo specific polymerization. Or, in the case of ethylene, it became possible to generate high molecular weights of nearly linear chains. This is in contrast to the aforementioned high pressure ethylene polymerization scheme which is used to produce low density polyethylene, developed earlier by ICI. As discussed, the high pressure, LDPE process is characterized by a high degree of random branching.

Ziegler-Natta catalysts can be broadly defined as, "a mixture of a metal alkyl of base metal alkyls of group I to III and a transition metal salt of metals of groups IV to VIII."[16].

Not all of the possible combinations are active. In fact, an individual catalyst combination is usually very selective to the monomer type involved. A typical combination of compounds for ethylene polymerization includes $TiCl_3$ with $Al(C_2H_5)_3$.

The third concurrent group to make the synthesis of high molecular weight linear polyethylene feasible was developed by Phillips[17]. The Phillips catalyst has found wider use in the industrial production of HDPE than the Ziegler-Natta catalyst based process. The incorporation of comonomers such as 1-butene or 1-hexene into the reactor allows the Phillips catalyst system to polymerize linear low density polyethylene commercially as well. The Phillips system is often referred to as a chromium based system, or as a metal alkyl-free (MAF) catalyst when compared to the Ziegler-Natta type systems. The Phillips catalyst involves the use of chromium trioxide supported on silica and is capable of producing highly linear chains. A number of the resins used in this study were manufactured using chromium catalysts. The basic mechanism whereby monomer units are added to a growing chain is shown in Fig.2.3. While this diagram is very simplistic, it does represent a key point. In contrast to what will be seen below with the metallocene catalyzed systems, there are no ligands present on the catalyst to guide the coordination of the incoming monomer in a stereo specific fashion. Thus, these catalysts are not able to polymerize highly stereo-regular chains, e.g. isotactic polypropylene. Obviously this is not a concern for HDPE production, but it does limit the broadness of their applicability. A portion of the catalyst does remain with the polymer after synthesis. While residual catalyst can lead to reduced oxidative stability, this problem can be alleviated with the use of a suitable stabilizer package to prevent subsequent chain extension and crosslinking during melt processing.[18] An additional point of extreme interest to this research is the breadth of the molecular weight distribution which the chromium process leads to. Polydispersity indices ranging from 15-20 are common for the Phillips catalyst[19]. In contrast, Ziegler-Natta catalysts generally produce resins with PDI values between 4 and 8. The breadth and shape of the molecular weight distribution will have an impact on both processing and crystallization behavior.

The newest catalyst systems for high density polyethylene, the metallocenes, are noted for their ability to produce resins with a “narrow” molecular weight distribution. Polydispersity values can be as low as two, though PDI values of 4-5 will be used in this

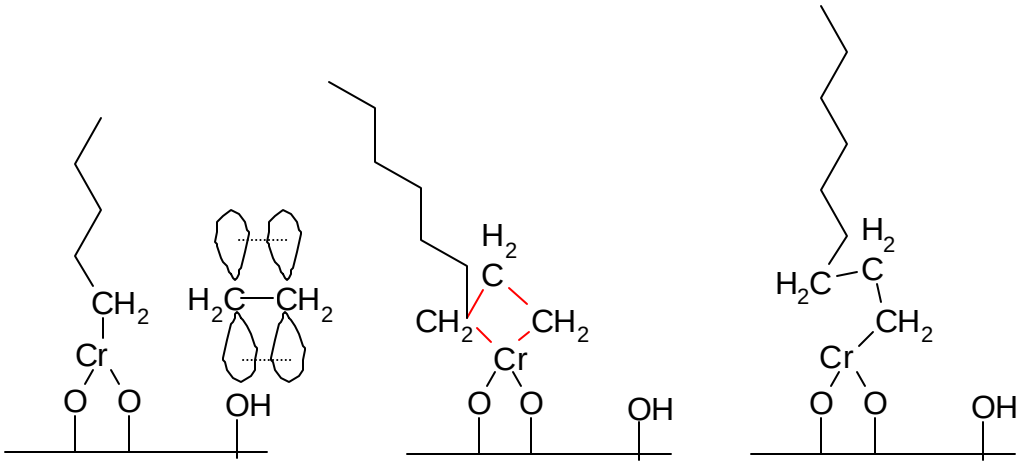

Figure 2.3. General insertion scheme for ethylene with Phillips type chromium oxide catalyst. Note that if the incoming monomer was of lower symmetry (e.g. possessed three hydrogens and a methyl group as in propylene) the catalyst provides no restrictions on the incoming orientation of the insertion. For this reason highly stereospecific polymerization would not be achieved with this catalyst. Figure adapted from Epacher[18].

study. The PDI value of two represents the most probable molecular weight distribution. For a heterogeneously catalyzed system this value implies that each reactive site has the same level of activity and that the monomer concentration is homogeneous throughout the reactor.[36] For this reason metallocenes are often referred to as single site catalysts. A typical metallocene catalyst consists of a positively charged group IV metal anion (e.g. Ti or Zr) bonded to two ligands and sandwiched between two negatively charged cyclopentadienyl anions to form a complex with no net charge. The choice of ligands (often halide atoms such as Cl), as well as the attachment of various groups to the cyclopentadienyl rings, allows for variation in activity towards a specific monomer and stereochemistry. The use of two cyclopentadienyl rings is not a prerequisite for a metallocene catalyst to be functional, in some cases one will suffice to provide the necessary coordination geometry. An example of a metallocene is given in Fig.2.4. This particular catalyst can be used for the stereo specific polymerization of isotactic polypropylene. However, research has found that a cocatalyst is needed to achieve reasonable activity levels in metallocene systems. One such cocatalyst is methylalumoxane, MAO. The mechanism of polymerization is believed to follow a reaction scheme very similar to that of a Ziegler-Natta system. A commonly proposed polymerization mechanism for a metallocene system is shown in Fig.2.5. Reaction of the metallocene with the MAO removes the chlorine atoms, while forming a positively charged complex with a methyl group, extracted from the MAO. The monomer then approaches the catalyst in an orientation which may be governed by steric hindrances between itself and the ligands on the metallocene. Next, a complex is formed by sharing the pi electrons of the double bond on the monomer resulting in its insertion. Lastly, the bond with the methyl group, which was initially attached to the metallocene, is broken to become a chain end, being replaced by one end of the monomer. Additional insertions allow the chain to grow. The use of MAO with zirconium based metallocenes, zirconecenes, allows up to $1x10^8$ grams of ethylene to be polymerized per gram of zirconium[20]. At such low levels of residual catalyst a separate step for its removal is unnecessary. It should be reiterated that while the basics of metallocene technology are understood, all of the details of reaction mechanisms have not been firmly established at

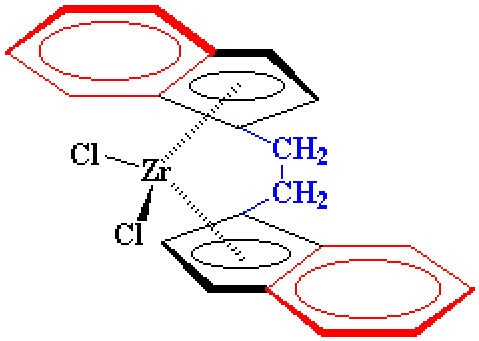

Figure 2.4. Example of pertinent metallocene structure[21].

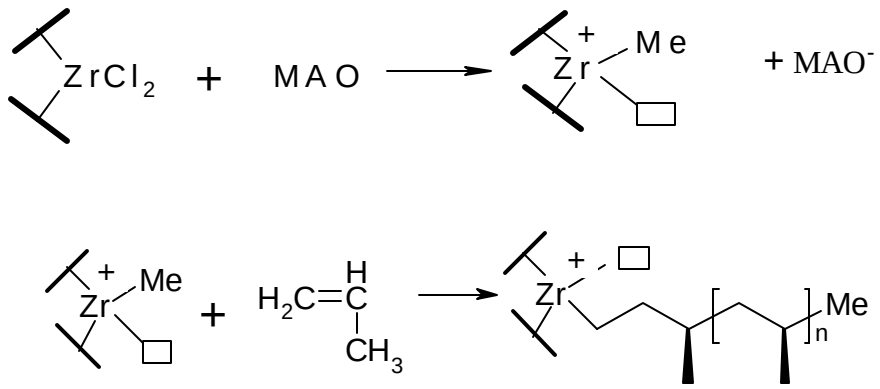

Figure 2.5. General reaction scheme for metallocene catalyzed polymerization of isotactic polypropylene[20].

the present, as is the case for the other catalyst systems[22]. The incorporation of comonomers allows the production of linear low density polyethylenes as noted above for chromium catalysts. Current LLDPE production using metallocenes is already greater than 10 million lbs. per annum[13]. Within the category of linear high density polyethylenes substantial variation in molecular weight and molecular weight distribution can be achieved by controlling reaction conditions such as temperature and monomer concentration. It is hoped that in this particular study the differences in chain architecture and molecular weight distribution achieved with Phillips and metallocene catalysts will allow for a detailed study of their effects on the blown film process as it relates to structure, moisture vapor transmission performance, and mechanical properties.

2-6. Deformation of Polymer Coils During Processing

The structures induced in the final blown film depend greatly on the state of ordering present in the melt just prior to crystallization. Thus it is of great interest to this research to understand how variations in resin properties lead to different states of orientation during processing. What follows is a brief introduction to the theory of chain deformation in macromolecular melts and solutions.

The earliest studies in the area of flow induced deformations of macromolecules were carried out in dilute solution. These early studies give a clear picture of the fundamental mechanism by which random coils deform in an extensional flow field. DeGennes was the first to predict the somewhat unintuitive concept of an abrupt coil-stretch transition[23]. These predictions have been verified subsequently by experimentation and are schematically represented in Fig.2.6 for a linear chain. One of the key parameters in these studies is that of the Deborah number, De, defined in the following equation.

$$De = \frac{t_p}{t_d} \qquad \text{Eq.2.1}$$

τ_p = characteristic relaxation time of the polymer
τ_d = characteristic time scale of the deformation

A)

B)

C)

Figure 2.6. Configurational states for the coil-stretch transition. A) unperturbed random coil, B) random coil under strain below the critical value, C) extended chain conformation at strain rates greater than the critical value. Direction of flow is horizontal.

The dimensionless Deborah number is a ratio that compares the rate at which the polymer is being deformed to the rate at which it can relax or recover during or after a deformation event. For small De the polymer is able to rapidly relieve the stress placed upon it. For this research, the principal stress is represented by the extensional and shearing effects of the flow which the polymer melt experiences after it exits the die. Under low De conditions very little deformation of the random coil will take place. However, at De >1, sufficient stress can develop such that the polymer can become highly extended. This extension can be frozen into the film's structure if crystallization or vitrification occurs prior to chain relaxation and disorientation. As stated above, this behavior has been studied and verified through experimentation. A few key results from these studies should be noted.

Using a specially designed flow apparatus to produce elongational flows, Keller, Odell and coworkers have published a number of studies relating dilute, semi-dilute, and concentrated (homogeneous melt) phase measurements. The results of these studies using flow birefringence verified, as mentioned above, that there is indeed a well defined coil-stretch transformation which occurs at a critical strain rate in dilute solution.[24] Below the critical strain rate only small deformations of the coil take place. At the critical strain rate the polymer chains become nearly fully extended. Interestingly, above the critical strain rate the extension of an individual extended chain saturates. That is, once extension is achieved at the critical strain rate, beyond that point no further extension occurs. This critical strain rate was found to be inversely proportional to the molecular weight to the 1.5 power, regardless of the solvent quality used[25]. The molecular weight dependence of the critical shear rate has important ramifications for the melt processing of polydisperse materials. At ever increasing deformation rates the number of polymer chains with a fully extended conformation increases at the expense of those in the coil conformation. Thus the amount of oriented material for a given resin will depend largely on the width and shape of the molecular weight distribution, not just its average. This is an important consideration when contrasting resins made from different catalytic processes. In fact this phenomenon has been used as a method to determine the molecular weight distribution of polymers[26].

Research which has been conducted more recently by Chu et al. to probe the relaxation dynamics of long chain molecules using isolated DNA molecules suggests that the molecular weight dependence of the critical strain rate for extension is 1.65[27,28]. Of additional interest from this group are results found on single DNA molecules in shearing flow[29]. A shearing flow can be considered to consist of the superposition of two components, a purely extensional component and a purely rotational component. The effect of the rotational component will be to cause an individual polymer chain to tumble in the solution. The processes of elongation and rotation are depicted in Fig.2.7. It can be seen in this figure that the rotational flow component can cause a deformed polymer coil to either continue to extend or revert back to its coiled dimensions. The influence of the two flow components causes the polymer coils to constantly coil and uncoil during shearing flow. A time averaged value for the coil dimensions as obtained by the researchers suggests that for a flexible chain in dilute solution that the maximum fractional extension that can be obtained for conditions of simple shear (rotational and extensional components equal in magnitude) is approximately 0.4[29]. It should be emphasized that by averaging over a finite time window the average chain will appear to have the average extension. However, in reality very few of the chains at any given time may take on the average dimensions. Many will be more fully elongated while others will be more completely coiled as the chains are constantly fluctuating back and forth. The applicability of the coil-stretch transition to the melt state has been studied and has been presented in a general review with a favorable correlation between the two systems[30]. However one major difference is observed. A unique feature of macromolecular systems when considering their extraordinary lengths is their ability to entangle. While entanglements between polymer chains will not be present in dilute solution, they will most certainly be present in a concentrated situation such as melt processing. Experiments have shown that it is possible at ever increasing concentrations and extension rates for a polymer solution to reach a second critical shear rate associated with the network nature of the entangled fluid. Additional experiments by Chu on DNA molecules in solutions above the critical concentration for coil overlap, C*, have verified the veracity of the reptation mode of polymer relaxation whereby polymer chains can

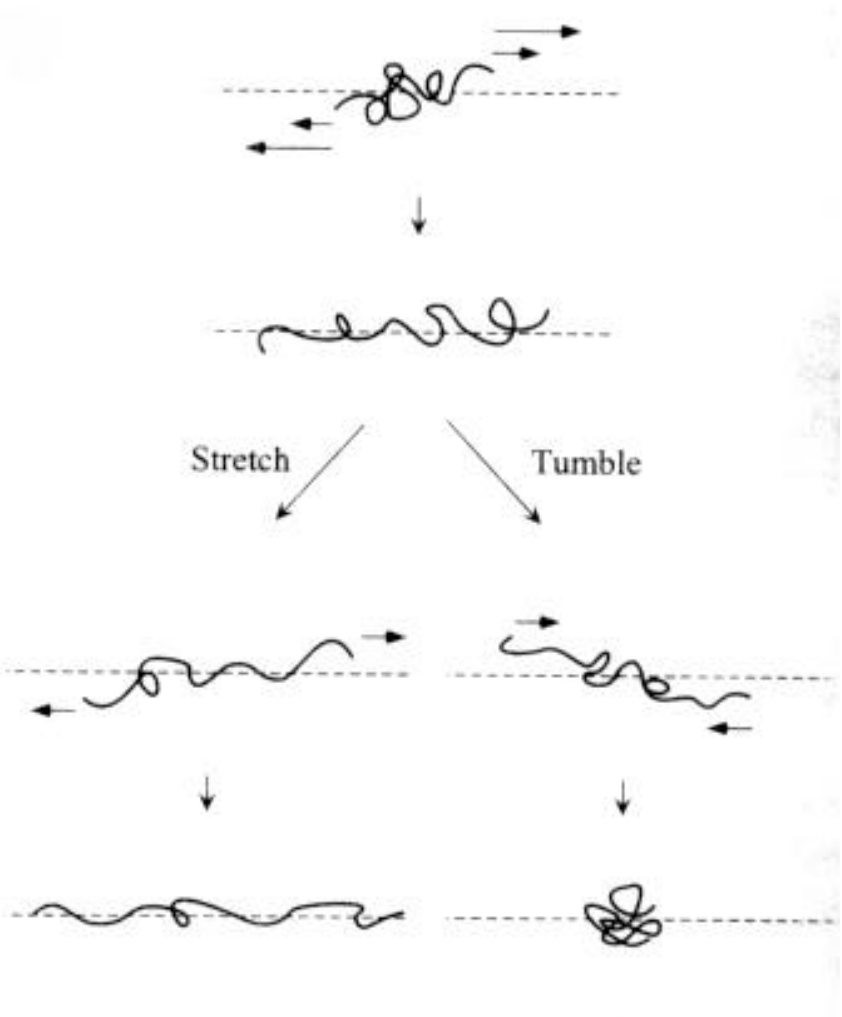

Figure 2.7. Possible modes of coil deformation for polymer coils in dilute solution. Left side of figure, rotational component of flow leading to additional stretching of the coil. Right side of figure, rotational component of flow leading to recoiling of chain. Figure adapted from Chu.[29]

only relax by diffusing through a hypothetical one dimensional tube whose dimensions are set by the length of the chain and the concentration of entangling neighbors[27].

It will also be of importance to briefly address a few qualifications to the aforementioned phenomena. It should be appreciated that a particular molecular chain must not only be deformed at a sufficient rate to promote extension, but also the required strain or distance for the unraveling to be affected must be given. The strain imposed on polymer chains in flow will be dependant on the particular geometry of the process. In an application such as blown film the elongational component of the flow as the molten film is pulled upwards from the die and drawn down should be adequate to allow substantial chain extension. An additional question arises as to the proper time scale to assign to both the process and the polymer chains. Experiments have found that the time scale associated with unraveling is much shorter than the time scale for retraction[31,32]. From a practical standpoint this hysterisis behavior means that a particular process can be thought of as having two relevant time ratios. The first ratio will involve the time scale of deformation in relation to the critical strain rate for the coil-stretch transformation. The second ratio will be related to the processing time after the deformation but prior to crystallization, relative to the retraction time of the extended macromolecule. Both factors will have an impact on the final structure which is obtained upon solidification.

2-7. Quiescent Crystallization of Polymers

While even a cursory examination of the film blowing process would lead one to the conclusion that crystallization of the polymer will not likely be under quiescent conditions, a discussion of the latter phenomenon will be fruitful. As stated in the previous section, polymer chains in the melt undergoing stress can be thought of as having one of two extreme possible conformations, coiled or completed extended. It then follows that if a substantial amount of the material is still in the random coil configuration at the time of cooling, structures related to quiescent crystallization may likely be observed. It is for this reason that a discussion of quiescent crystallization is necessary.

Of all the semicrystalline polymers, polyethylene, specifically linear high density polyethylene, is among the most readily crystallizable. Possessing no chiral centers, the polyethylene chain is highly symmetric making crystallization highly favorable from a thermodynamic perspective. Having a relatively flexible backbone allows the polyethylene chain ample rotational freedom to configure itself into the preferred trans planar conformation for crystallization. Thus it can be reasoned qualitatively why high density polyethylene can rapidly crystallize to such high extents in contrast to many other polymers. The exact morphological features of this crystallization will vary depending on the given crystallization conditions.

Polyethylene primarily crystallizes to form an orthorhombic unit cell as shown in Fig.2.8. By convention the c-axis of the unit cell is defined to be parallel to the chain axis. It is has also been found that for polyethylene crystallization, addition of unit cells occurs most rapidly along the b crystallographic axis[33]. These two key points will allow for a greater understanding of the structure present in the melt which leads to the end morphology. The state of the melt prior to crystallization can be hypothesized by examining the orientation of the three crystallographic axis in solidified samples using these facts.

While two other unit cells have been noted for polyethylene, they are not as common as the orthorhombic structure. A monoclinic based unit cell has been observed in samples which have been plastically deformed while a hexagonal packed structure can be formed under conditions of high temperature and pressure[34]. Adding the contributions along edges and corners for the orthorhombic unit cell in Fig.2.8 shows that each unit cell requires the contribution of two repeat units.

At a scale length larger than the unit cell, ~200 Å, a second type of crystalline order can be noted in polyethylene and in many other semi-crystalline polymers. The use of electron microscopy allows for a real space visualization of the structures present at this scale length. Under conditions of quiescent crystallization, crystalline domains in the shape of lamellae are typically observed. The sizes of these lamellae can be as large as 10 μm in length and width and approximately 0.01 μm in thickness when grown from solution. However, when one considers that for a polymer such as polyethylene that x-ray data show that the c-axis of the unit cell is generally oriented perpendicular to the

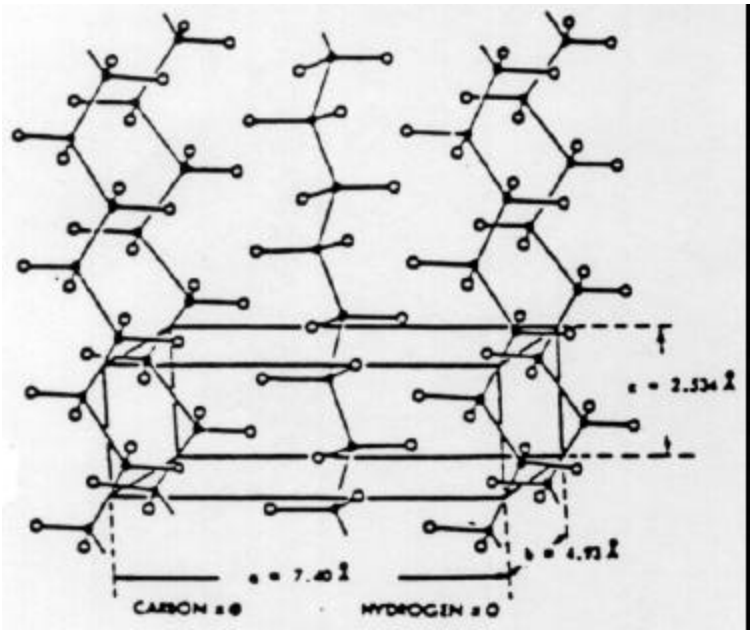

Figure 2.8. Unit cell of polyethylene. Orthorhombic lattice dimensions at room temperature are: a) 7.40Å b) 4.92 Å c) 2.534 Å. Figure adapted from Bunn.[35]

surface of the lamellae a problem arises. Extended chain lengths for a high molecular weight polyethylene are on the order of 0.1 μm, an order of magnitude greater than the thickness of the lamellae[36]. This apparent discrepancy can be accounted for by the concept of chain folding. A single polymer chain can participate in a given lamella by folding back onto itself. This structure is shown schematically in Fig.2.9, demonstrating both the concepts of adjacent re-entry and random re-entry. The exact manner in which the chain folds back upon itself is still unresolved. It should be reemphasized that these lamellar structures are typical of quiescent crystallization. Additionally, note that because of the chain folded nature every lamella carries with it a portion of amorphous material at its surface. This phenomenon is one factor that limits bulk crystallization of polymers to less than 100% crystallization. Chain folded lamellae represent a non-equilibrium crystalline structure, as folds and crystal faces have a higher energy than the bulk crystal. The true thermodynamically stable state would be that of the extended chain crystal. Such full extension of the polymer coils has not been shown to occur under typical quiescent or industrial crystallization conditions. Further morphological textures typical of these systems can be noted on even larger scale lengths.

Typically polymers form crystalline super structures know as spherulites under quiescent conditions. A sketch of a spherulite is provided in Fig.2.10. Spherulites consists of a combination of both crystalline and amorphous material. Ribbons of lamellae originate at the center of the spherulite and grow in a radial direction. Many polymers, including polyethylene, may display a twisting of the lamellae as they radiate out from the center of the spherulite. This phenomenon leads to the appearance of bands, alternating bright and dark regions, when these spherulites are observed in an optical microscope using crossed polarizers. For polyethylene the radial direction corresponds to the b crystallographic axis. The exact size of a spherulite will depend on the conditions under which it was formed, though in general its size is of the order of a few microns in diameter. The final size of the growing spherulite will be determined by the nucleation density during crystallization. A volume occupied by a few nucleating sites will allow for the growth of subsequent spherulites to a large size before impingement occurs. When two adjacent growing spherulites come into contact with each other, growth at the

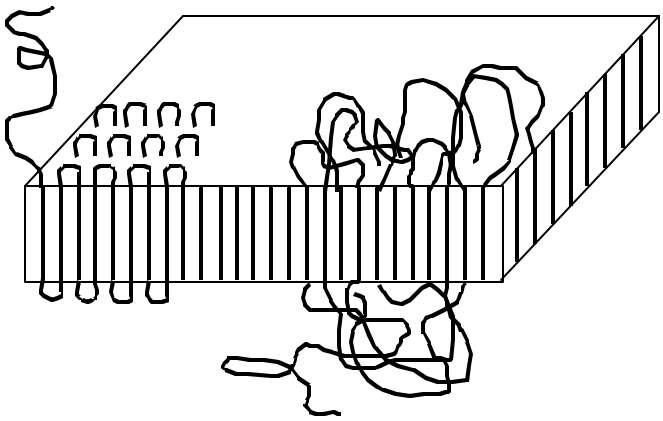

Figure 2.9. Basic structure of crystalline lamellae. Left side of lamellae showing adjacent re-entry model. Right side of lamellae showing switchboard or random re-entry[36].

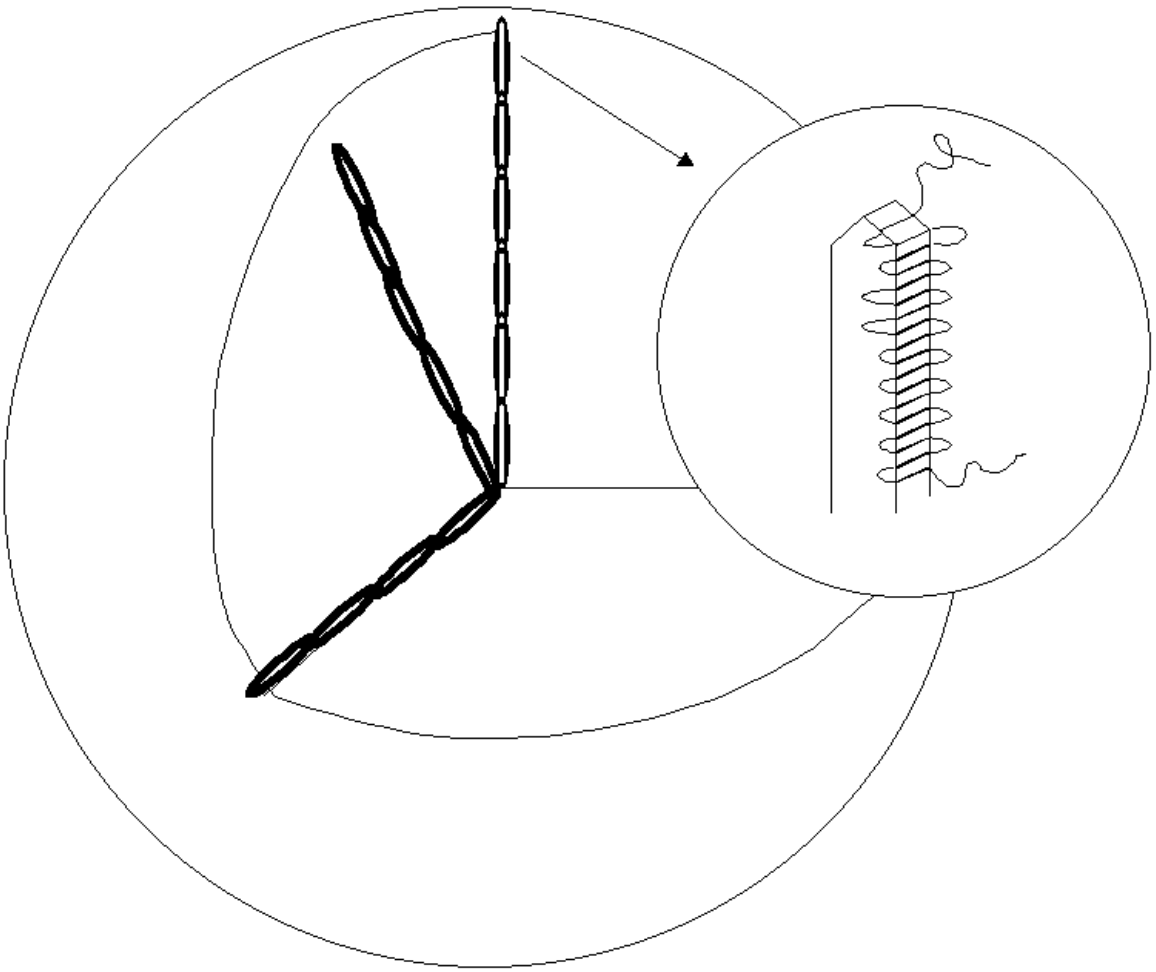

Figure 2.10. Diagram of spherulitic structure. Note twisting lamellae originating from the center of the spherulite with growth occurring along the b crystallographic axis of the unit cell in the radial direction. Figure adapted from Barham[37]

common interface for the two will be halted. Likewise, if many nucleating sites are present per unit of volume, numerous small spherulites will be formed as they rapidly bump into one another, limiting each other's overall size. This phenomenon is depicted in Fig.2.11.

A structural "subset" of the spherulite is that of the sheaf structure. The sheaf structure is simply the beginnings of a spherulite which has had its growth halted very early by impingement with neighboring sheaves. Essentially the sheaf like structure is an extreme case of high nucleation density. The exact nucleation density required to form sheaf structures will depend on the amount of branching/splaying and curvature of the lamellae as they grow. The sheaf structure and its associated nucleation and growth steps are depicted in Fig.2.12. If the growth of the sheaf were not interrupted it would continue to increase its radial dimensions until the characteristic spherical structure was formed. Sheaves give rise to a roughly four leaf clover H_v light scattering pattern, a technique which makes their detection relatively straightforward[38]. The exact shape of the clover pattern will depend on the aspect ratio, the width to height of the sheaf as depicted in Fig.2.12. The nucleation sites for sheaf structures often are the result of extended chain crystals, or fibril nuclei, which will be discussed in the following section on non-quiescent crystallization.

2-8. Non-Quiescent Crystallization

Of particular importance to this study will be the manner in which polyethylene crystallizes under conditions of a directed stress, or non-quiescent conditions. Crystallization in a blown film process will occur at the same time as a biaxial stress is being applied to the system. The early model systems for crystallization under conditions of flow have been conducted in dilute solution while stirring. An example of the structures obtained under these conditions for polyethylene is shown in Fig.2.13, as taken from Keller et al.[39]. This particular type of morphology has been termed shish-kabob. Of particular interest is the shish portion of the structure. This long, fibrillar strand consists of partially extended chain crystals. In contrast to the chain folded lamellar crystal which

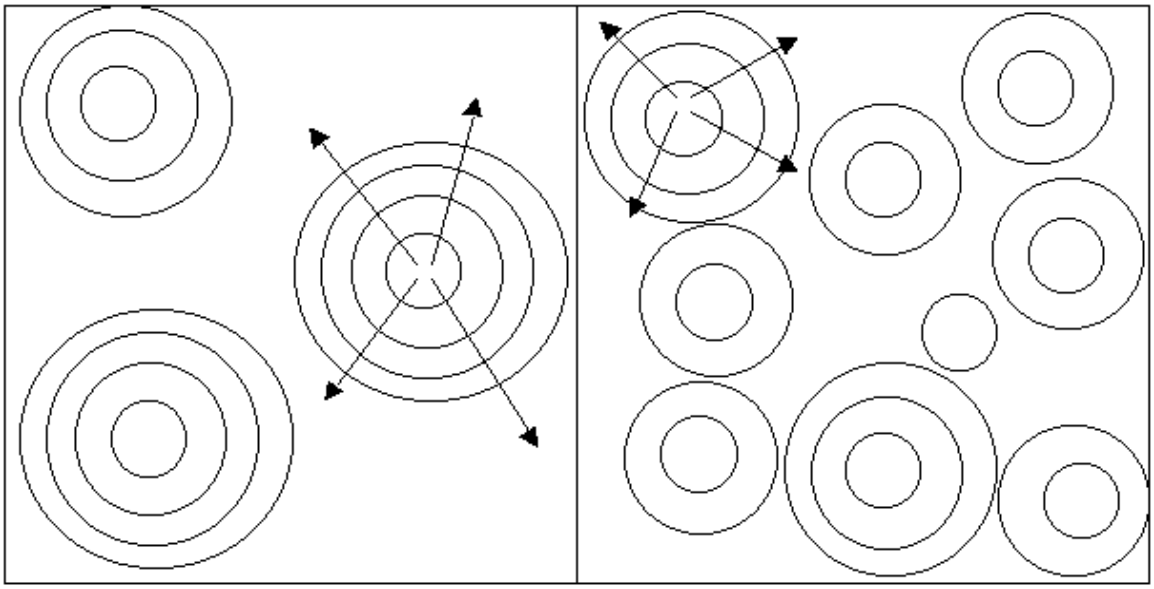

Figure 2.11. Schematic of the effect of nucleation density on spherulitic size.

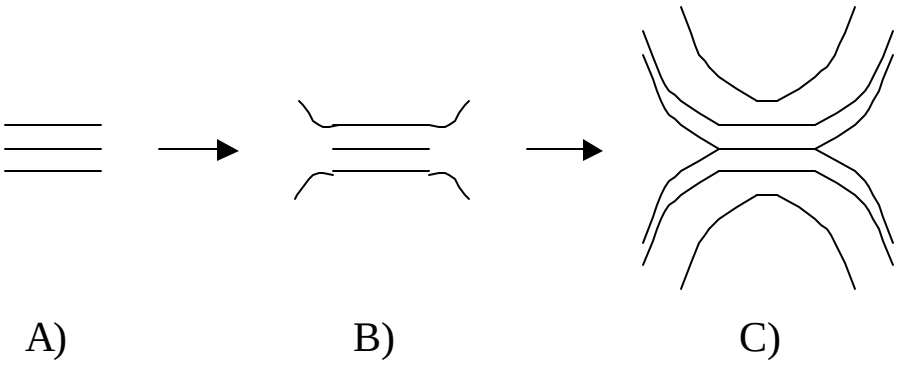

Figure 2.12. Schematic of sheaf growth process. A) nucleation of initial crystalline lamellae B) growth of crystalline lamellae from nucleation site with characteristic curving of lamellae C) continued lamellar growth with splaying. Figure adapted from Basset.[40]

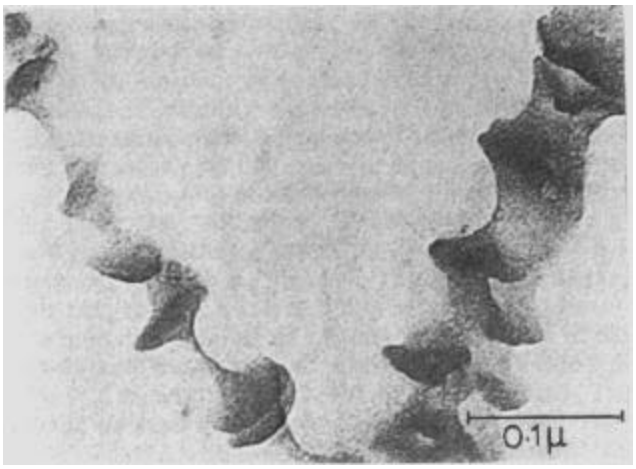

Figure 2.13. Shish-Kebob morphology. Polyethylene in dilute xylene solution crystallized under agitation. Note shish's of extended chain crystals and kebobs of chain folded lamellae.[39]

is typically associated with quiescent crystallization, here a crystalline structure can be seen that appears to have been initiated by a parallel arrangement of uncoiled chains without folding. The existence of these fibril nuclei has been substantiated experimentally using techniques such as microscopy, x-ray analysis and differential scanning calorimetry. In light of the previous discussion concerning the coil-stretch transition of macromolecules in extensional flows, it is not altogether surprising that such crystal morphologies exist. A flow situation which fully extends a number of chains in a parallel direction under the proper conditions of cooling can well be visualized to form such entities. Secondly, as discussed earlier, not all of the polymer coils subjected to a given directional stress undergo the transition from coil to extended chain based on differences in molecular weight. Lower molecular weight chains can stay coiled with little deformation. The coiled nature of these chains closely mimics the conformation of chains which are crystallized from a quiescent melt. Hence it not surprising that in a stirred solution one can also observe regions of chain folded lamellae, the kabobs. These observations present a coherent structural picture to describe the state of the polymeric chains during flow prior to crystallization and their subsequent ordering upon crystallization. One can then imagine the amount of shish content relative to the amount of kabob content will be a function of three variables, the stress applied during flow, the amount of time given to the system to relax prior to crystallization, and the relaxation characteristics of the polymer based on its molecular weight distribution and chain flexibility. Higher stresses coupled with rapid quench times should yield a final structure with a large content of fibril nuclei. Often times one can infer the presence of these fibril nuclei in the melt because of their ability to promote oriented nucleation, when direct observation by microscopy fails.

A key feature of the shish-kebob morphology is that the folded chain lamellae are nucleated from partially extended chain crystals. Thermodynamic arguments dictate that the extended chain crystals will have a higher melting point, and thus a higher crystallization temperature, based on their higher molecular weight and lower entropy when extended in the melt state. Thus these extended chain fibrils are formed first. The subsequent growth of the chain folded lamellae can be noted from micrographs such as the image given in Fig.2.13, which shows these features spaced along the lengths of the

fibril nuclei. Folded chain lamellae are not observed floating "unattached" in the solution. Also, it should be noted that the lamellae are oriented such that they grow perpendicular to the direction of the flow and the fibril nuclei. This behavior should be expected as the c-axis of a polyethylene crystal is parallel to the chain backbone. It was shown earlier how the nature of chain folded lamellae is such that the chain axis is perpendicular to the lamellar face. Thus chains which are in a coiled conformation can nucleate off of the oriented crystal faces formed by the fibril nuclei and then proceed to crystallize in their own preferred chain folded manner.

Work by Keller et al. in the area of blown and cast polyethylene film characterization has contributed greatly to the current understanding of fibril nuclei and their importance in the obtained morphological texture of the entire sample[30,39,41]. This research provides a model which describes the basic features of a high molecular weight polymer when it is crystallized under conditions during or subsequent to deformation. At the heart of this model are the fibril nuclei. It is the density of fibril nuclei which largely determines the overall texture of the material. A schematic of the model is shown in Fig.2.14. To understand the Keller-Machin model one must again return to the concept of the coil-stretch transition. Extrusion and drawing of a polymeric film in the melt state, such as that encountered in blown film processing, will lead to a preferred orientation of the chains with respect to the direction of flow. As earlier discussions have noted, the stresses imposed on the coiled polymer chains can cause them to unravel and extend. Just as in the stirred solution experiments, if these extended chains crystallize, they can serve as nucleating sites for the remainder of the polymer melt. And, just as was the case for the solution experiments, these nucleating sites, the fibril nuclei, will impart their own preferential orientation to the subsequently chain folded lamellae. The number of fibril nuclei present in the melt at the time of crystallization will depend on the relaxation behavior of the chains. The relaxation behavior will of course be governed by the molecular weight and its distribution, the temperature, and the amount of time which passes between the end of the deformation and crystallization. If only a few extended chains are present to serve as nucleating sites, all will be aligned in a parallel manner though the distance between these potential fibril nuclei will be quite large. When coiled molecules crystallize as lamellae, the lamellae will grow outwards from

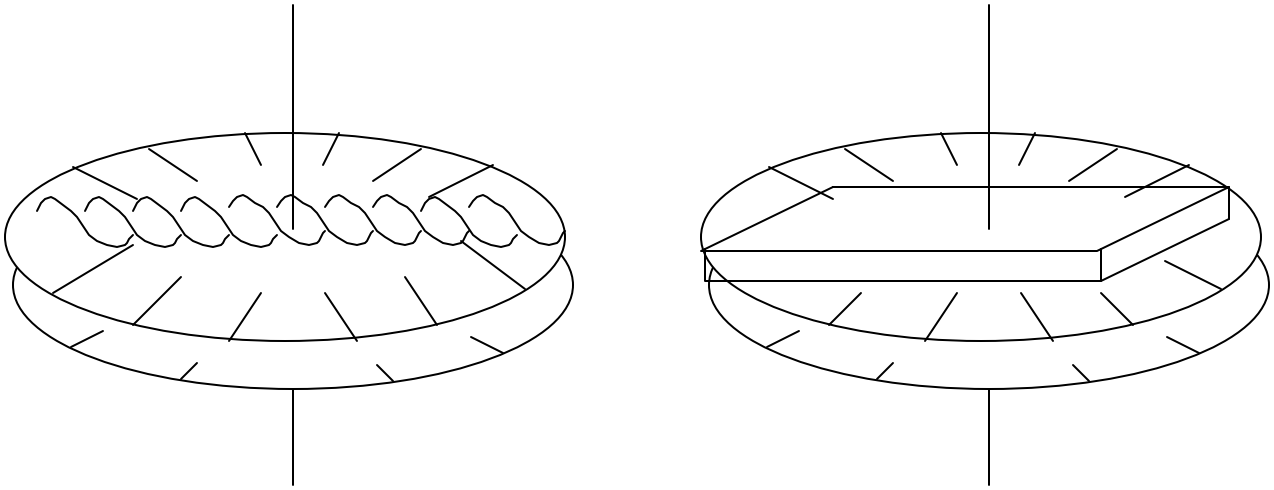

Figure 2.14. Row structure morphologies as described by Keller and Machin. Left diagram represents crystallization occurring under a low stress condition, showing twisting ribbons of lamellae emanating from the fibril nucleus. Right diagram represents high stress crystallization with flat lamellae[30].

these sites and typically will twist, splay, and branch as is commonly observed in spherulitic systems. The growth of these lamellae will not be stopped until they are interrupted by the lamellae growing from adjacent fibril nuclei. However, if the density of fibril nuclei in the melt is substantial at the time of bulk crystallization there will be a limited distance which each lamella can grow before it is interrupted by its neighbors. Hence a morphology with twisting lamellae oriented perpendicular to the stress direction can be associated with a low stress condition because only a limited number of fibril nuclei will have been generated, the Keller-Machin I row structure. In contrast, under conditions of high stress, many fibril nuclei will be generated in the melt leading to planer lamellae, the Keller-Machin II row structure.

If the number of fibril nuclei is quite small, the Keller-Machin model can be seen to influence structure on an even larger level. Given enough relatively undeformed material between fibril nuclei, the amount of lamellar twisting and branching which occurs as the lamellae grow outwards from the nuclei can build spherulitic like structures, sheaves. Sheaves are composed of bundles of lamellae growing from a common nucleation point just as in a spherulite. However, because of the presence of the fibril nuclei they differ from spherulites in two ways. The first difference is that because their growth is triggered by oriented, directionally dependent nuclei, the fibril nuclei, the majority of the sheaves will be aligned in the same direction, initiated perpendicular to the direction of flow. Secondly, due to the presence of adjacent fibril nuclei and hence other growing sheaves, their growth to full spherulitic stature is limited by impingement with their neighbors. While this behavior is analogous to what occurs in spherulitic systems, it is important to note that here the growth is halted much earlier in the process leading to structures which resemble the initial stages of spherulitic growth but do not reach sufficient maturation to be considered spherically symmetric structures.

2-9. Orientation Determination

It should be appreciated at this point that both resin and processing variables will have an impact on the final morphology which is obtained during the film blowing

process. The question then arises as how to quantify these differences. The overall orientation of the chains in the final film will give clues to the both the film morphology and the conditions under which it was formed. Quantifiable orientation values may also be of use for correlation with end use properties such as modulus, toughness, or of particular interest to this study, moisture vapor transmission rate. The quantification of orientation can be divided into three general categories, each relating to the specific nature of the material being observed. A technique such as birefringence will give a measure of the overall anisotropy of the system for both the crystalline and amorphous phases of the material. In contrast, the techniques of wide angle and small angle x-ray diffraction will only yield information about the orientation of the crystalline regions of the polymer. Finally, a method such as infrared dichroism allows independent monitoring of both the crystalline and amorphous phases, thus allowing orientation information particular to the amorphous phase to be determined. Using a battery of techniques allows one to gather information about the entire sample while providing internal checks on the analysis.

Before embarking on detailed discussions of any individual technique it is necessary to clarify the common language which is used to quantify the results of these procedures. A system which is uniaxialy symmetric (fiber symmetry) can adequately be described through the use of the Hermans orientation function. The relation is as follows:

$$f^{H} = \frac{1}{2}(3 < \cos^{2} q > -1) \qquad \text{Eq.2.2}$$

f^{H} : value of orientation function, $f^{H} = 1$ corresponds to perfect orientation, $f^{H} = 0$ corresponds to completely random state, $f^{H} = -1/2$ corresponds to perpendicular orientation.
θ : angle of object with respect to the reference axis
<> : denotes average quantity

This simple function allows quantitative values to be assigned to the results of a rheo-optical experiment. It can be seen from Eq.2.2 that the Hermans orientation function is derived from the second moment of the average angle of all the measured elements or structures with respect to a single reference axis. The Hermans orientation function is a simple method by which to tabulate uniaxial orientation data. This function is limited in

that it does not describe the orientation of a particular feature with respect to multiple axes. In the case of film blowing, a biaxial deformation takes place. Stretching along the machine direction, MD, occurs due to film windup. Stretching along the radial direction, commonly referred to as the transverse direction, TD, occurs due to the expansion of the bubble. In order to fully describe the orientation of chains in this system a more complicated orientation function formulation is needed.

The biaxial orientation functions as developed by White and Spruiell[42] are suitable for this purpose. The White-Spruiell biaxial orientation functions as written below are based on the assumption the property of interest (e.g. polarizabilty) is coaxial with the oriented segment of interest, the polymer chain. Averaging over all of the measured segments in the sample leads to the following expressions for a single phase system of a unidirectional component:

$$f_{MD}^{B} = 2\overline{\cos^2 f_{1,MD}} + \overline{\cos^2 f_{1,TD}} - 1 \qquad \text{Eq.2.3}$$

$$f_{TD}^{B} = 2\overline{\cos^2 f_{1,TD}} + \overline{\cos^2 f_{1,MD}} - 1 \qquad \text{Eq.2.4}$$

f_i^B : Biaxial orientation function with respect to reference axis, i

ϕ : Angle of segment with respect denoted reference axis, over bar denotes a quantity averaged over all measured segments

These two equations are useful for describing the orientation state of a wholly amorphous system. The added complexity afforded by these equations is still not sufficient to fully describe the orientation of a system as complex as that of a crystalline material in which the orientable component itself can be considered to have three intrinsic directions, each associated with a particular crystallographic axis. To fully describe a crystalline system of orthorhombic symmetry with respect to each of the crystallographic axis and the reference axis the following sets of equations may be used:

$$f^{B}_{MD,a} = 2\overline{\cos^2 f_{a,MD}} + \overline{\cos^2 f_{a,TD}} - 1 \qquad \text{Eq.2.5}$$

$$f^{B}_{TD,a} = 2\overline{\cos^2 f_{a,TD}} + \overline{\cos^2 f_{a,MD}} - 1 \qquad \text{Eq.2.6}$$

$$f^{B}_{MD,b} = 2\overline{\cos^2 f_{b,MD}} + \overline{\cos^2 f_{b,TD}} - 1 \qquad \text{Eq.2.7}$$

$$f^{B}_{TD,b} = 2\overline{\cos^2 f_{b,TD}} + \overline{\cos^2 f_{b,MD}} - 1 \qquad \text{Eq.2.8}$$

$$f^{B}_{MD,c} = 2\overline{\cos^2 f_{c,MD}} + \overline{\cos^2 f_{c,TD}} - 1 \qquad \text{Eq.2.9}$$

$$f^{B}_{TD,c} = 2\overline{\cos^2 f_{c,TD}} + \overline{\cos^2 f_{c,MD}} - 1 \qquad \text{Eq.2.10}$$

The nomenclature for Eq.2.5-10 is identical to those above with the addition of a subscript which denotes a particular crystallographic axis. There is no a priori reason why the orientation of the amorphous and crystalline phases of a oriented semi-crystalline material should be identical, in fact they rarely are. Thus, for a biaxially blown film of polyethylene Eq.2.3 and Eq.2.4 may be used to describe the orientation state of the amorphous phase while Eq2.5-10 may be used for the crystalline phase. The values of the White-Spruiell biaxial orientation functions may range from –1 to 1. A pictorial representation of the significance of particular values is given in Fig.2.15.

It is of importance to note that this system of classification still has inherent weaknesses. Because the system is based only on the second moment of the distribution of orientation states it cannot differentiate between certain orientation states as shown in Fig.2.15, parts d) and e). Higher moments of the orientation distribution would be required to parameterize these arrangements in unique ways. The amount of experimental information required to fully define the biaxial orientation function also proves to be a hindrance to the wide spread use of this approach. Only a few methods

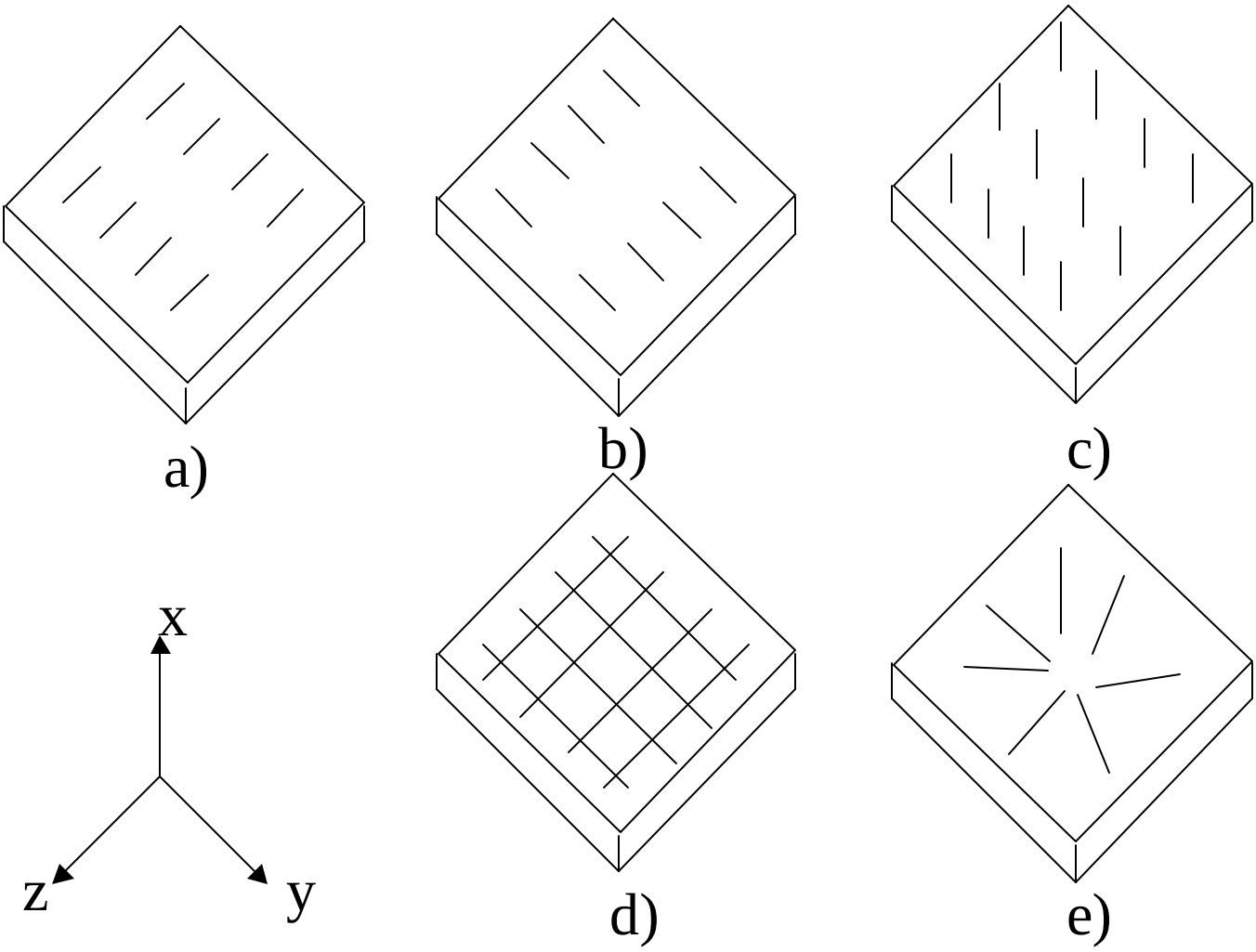

Figure 2.15. Values and schematics for various orientations using the White –Spruiell biaxial orientation functions. a) uniaxial planar – machine direction, $f_z^B = 1$, $f_y^B = 0$ b) uniaxial planar – transverse direction, $f_z^B = 0$, $f_y^B = 1$ c) uniaxial planar – normal direction, $f_z^B = -1$, $f_y^B = -1$ d) ,e) equal planar , $f_z^B = \frac{1}{2}$, $f_y^B = \frac{1}{2}$.[42]

such as IR dichroism and X-ray pole figure analysis allow one to potentially quantify the orientation state of each crystal axis. Often times another complimentary method such as birefringence must be utilized to determine the amorphous orientation. For experimental reasons the uniaxial Hermans orientation functions are often used in biaxial cases because of their relative simplicity. Specific experimental methods for the determination of the orientation state of a material will be the next subject of discussion.

2-10. Wide Angle X-Ray Scattering (WAXS)

Among the most useful techniques for studying the state of crystalline orientation in polymeric materials is wide angle X-ray scattering (WAXS). WAXS has an advantage over other types of characterization methods in that it can provide the complete orientation distribution, not just the second moment of the distribution as determined by many other techniques, through the use of pole figures. Pole figure analysis involves plotting the scattering intensity from the normal to a particular lattice plane with respect to each of three laboratory chosen reference axes (e.g. MD, TD, ND). To fully characterize a biaxial system of orthorhombic symmetry, at least two pole figures, representing two lattice planes, must be determined. The disadvantage of pole figure analysis is the cost and time investment to obtain the data. A simpler method, though less complete, to obtain orientation information for the crystalline phase can be obtained using a flat plate camera technique with a Warhaus camera type arrangement, shown schematically in Fig.2.16. Information regarding the spacing of known lattice planes can be obtained from this experiment by measuring the angle at which the x-ray beam is scattered with respect to the original beam direction. This scattering angle is commonly designated with the Greek symbol θ. Of greater interest for orientation measurements is the angular dependence of the scattered intensity in the azimuthal direction denoted by the Greek symbol ψ. The uniformity of the intensity of the concentric bands, or lack thereof, formed by the scattering pattern allows for the measurement of ψ. Figure 2.17 shows the angles of interest for this type of analysis along with pertinent reflections for polyethylene. It should be noted that a two dimensional scattering profile such as this cannot convey any information about orientation relative to the normal direction, ND. To

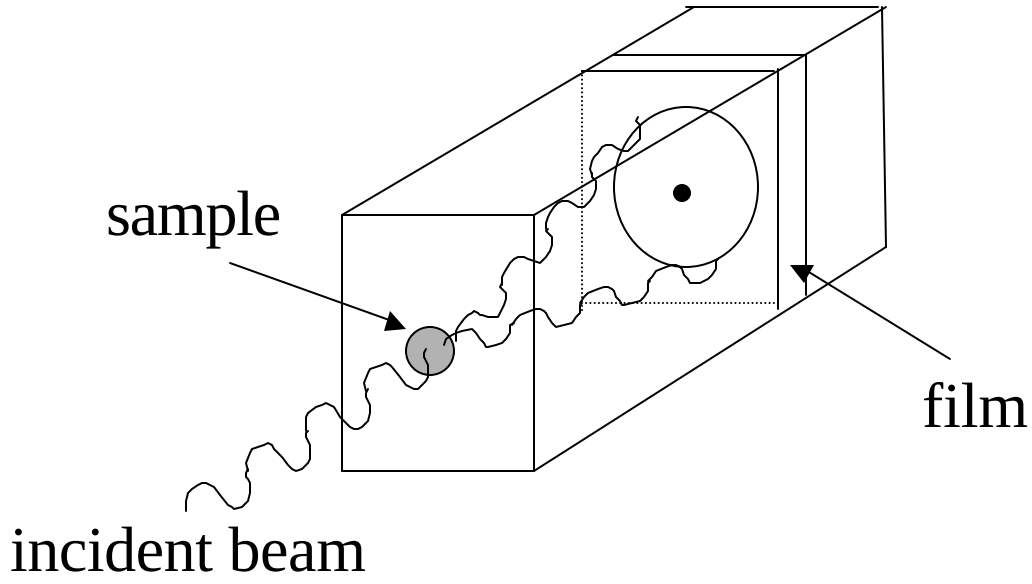

Figure 2.16. Diagram of wide angle x-ray scattering (WAXS) experiment.

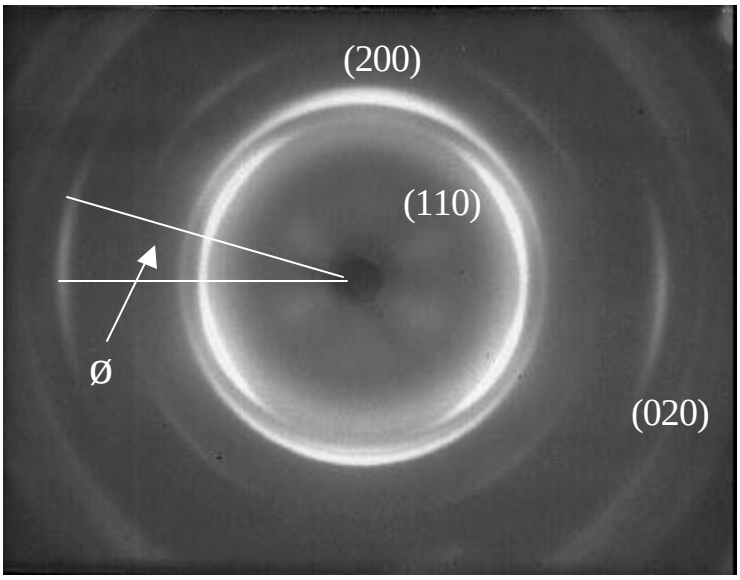

Figure 2.17. Example WAXS pattern of a blown polyethylene film. MD vertical, TD horizontal, ND parallel to beam. Note azimuthal dependence of 020 (b-axis) reflection denoting preferred orientation towards the TD direction.

obtain such data, a scattering profile would have to be obtained with the beam parallel to either the MD or the TD rather than the ND. In fact for situations with biaxial orientation, the use of only one scattering pattern can be very misleading. A material with planar orientation would show no orientation dependence if a scattering profile was taken with the beam normal to the planar surface as shown in Fig.2.18[43].

Of particular importance to this project, as mentioned earlier, are the morphological studies of Keller in which the row nucleated model of polyethylene structure was developed. Each of the two primary morphologies, high and low stress processing conditions, have distinctive flat plate x-ray patterns as viewed down the normal axis for a uniaxial system. These patterns are shown in Fig.2.19. While the systems of particular interest to this study are formed in a biaxial deformation process, often times these blown films display an orientation state which more closely resembles uniaxiality than equal planar. Thus, WAXS should be a simple method to determine relative orientation values and an indicator of the relative conditions of stress which were placed on the melt prior to and during crystallization.

2-11. Birefringence.

Above it was stated that the technique of WAXS was not useful for the direct study of amorphous orientation. Birefringence is a rheo-optical technique that is dependant on both the crystalline and amorphous phases. Unfortunately the orientation of each phase cannot be separated from the other. As a result birefringence experiments must be coupled with a crystalline phase sensitive method, such as WAXS, to allow independent determination of the amorphous phase orientation. Birefringence is defined as the difference in refractive index along two perpendicular axes as measured with linearly polarized light. Orientation birefringence arises from the anisotropy of bond polarizabilites. The interaction of an electromagnetic wave, light, with the electrons in a chemical bond is dependent on their relative orientation. A light wave impinging on a bond (carbon-carbon bond for polyethylene) parallel to the bond's axis will be retarded while a light wave passing perpendicular to the bond will interact to a lesser degree. Thus, if a polymer chain such as linear polyethylene, where the most electron dense

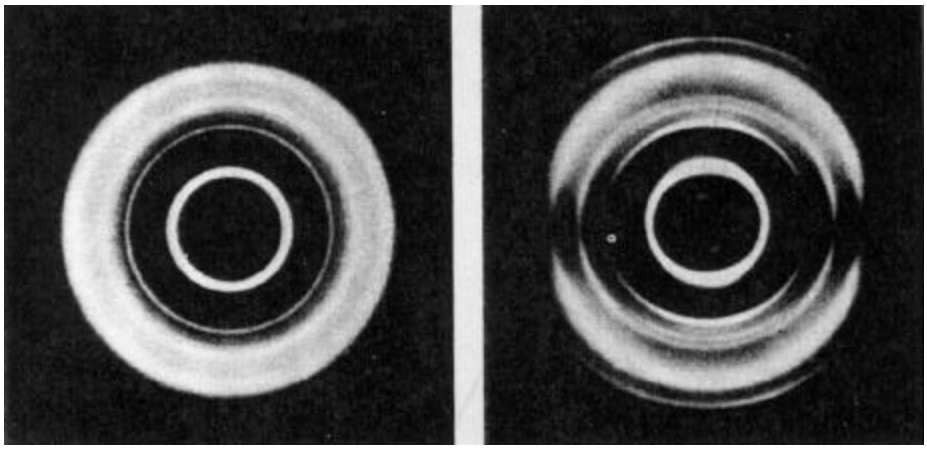

Figure 2.18. WAXS patterns of a material displaying planer orientation. Left pattern, beam parallel to film normal. Right pattern, beam parallel to film plane[43].

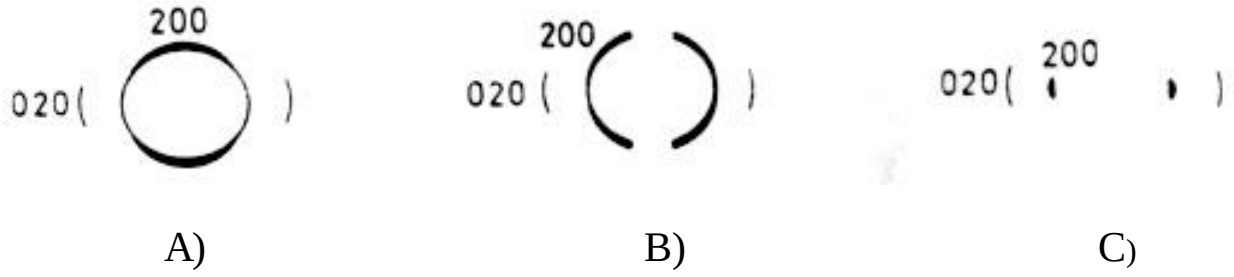

A) B) C)

Figure 2.19. Representative WAXS patterns for polyethylene, deformation direction vertical. A) Crystallization under conditions of low stress – b axis perpendicular to deformation direction, twisting lamellae leading to slightly preferential a axis orientation along MD. C) Crystallization under conditions of high stress – b axis perpendicular to deformation direction, planar lamellae with no a axis MD scattering. B) Orientation state intermediate to states A and B[30].

bonds are along the chain axis, is oriented preferentially in one direction, a birefringent effect should be noted. As the name implies no orientational birefringence will be produced if the anisotropic bonds are not preferentially oriented. In this case the polarization anisotropy averaged over all segments will be zero. It is of importance to note that birefringence may arise from effects other than orientation. Stress birefringence can be induced when a glassy material is subjected to a stress which, while not deforming the bulk dimensions of the sample, is sufficient to alter the local directionalities of bond polarizabilites. Form birefringence occurs in systems with regularly spaced anisotropic domains dispersed in a medium of dissimilar refractive index. For this effect to occur the spacing between domains must be substantially smaller than the wavelength of the probing light.

Like many rheo-optical methods, birefringence yields only the second moment of the distribution average. And, as stated above, it arises from anisotropy in both the amorphous and crystalline phases. Mathematically the contribution of both phases and the two non-orientation related sources of birefringence can be represented as follows

$$\Delta_T = \sum_i f_i \Delta_i^0 f_i + \Delta_d + \Delta_{form} \qquad \text{Eq.2.11}$$

Δ_T: Total measured birefringence
ϕ_i: Volume fraction of phase i
Δ_i: Intrinsic birefringence of phase i
f_i: Orientation of phase i
Δ_d: Stress birefringence
Δ_{form}: Form birefringence

Using the above relation with a measured value of the total birefringence, a measured value of the orientation state of the crystalline phase from an alternate method such as WAXS, and a measured value of the crystalline content, while assuming no contributions to the birefringence from form or stress effects, allows one to determine the orientation state of the amorphous phase for a semicrystalline polymer. It would be necessary to have values for the intrinsic birefringence of each phase on hand also. Experimentally

there are two principal methods for determining birefringence. The first method involves the use of an optical compensator to determine the retardation of light through a sample. The retardation is directly proportional to the birefringence of the material normal to the incident beam. This method requires a sample with sufficient clarity for a light source to pass completely through and will yield data indicative of the entire bulk birefringence of the sample. A drawback of this particular method is that to obtain birefringence information relative to the normal direction of a film requires that the sample be tilted in the beam at several angles to estimate the results that would be obtained if the beam could be passed parallel through the plane of the film. The second method commonly used to measure the birefringence of film samples is to measure the refractive index of the sample in three orthogonal directions and then calculate the birefringence through the differences of refractive index for the desired directions. Usually these directions are chosen to correspond with the MD, TD, and ND directions of the film. Thus, if all three refractive indices can be determined, three birefringence values can be calculated, though only two will be independent. While an Abbe refractomer can be used to obtain refractive index values, a more convenient method involves the use of a prism-coupler device. A schematic of the geometry and experimental setup for this method is shown in Fig.2.20. The device operates by varying the angle of incidence of the laser to the prism / film system. At certain angles, propagation modes based on the relative refractive indices of the prism and the film will result in the system acting as a planar dielectric light guide[44]. Under these conditions, light will propagate along the length of the film rather than be reflected at the prism interface. The angles at which this phenomenon occur can be observed by noting a drop in intensity as measured by the photodetector. If the film is sufficiently thick it may be possible to observe multiple coupling modes allowing for the independent measurement of refractive index and thickness. Refractive index values with respect to defined processing directions (MD, TD, and ND) can be determined through the appropriate alignment of the film and the polarization direction of the laser. Thus, with values of the refractive index defined for each of three orthogonal directions, biaxial orientation data can be determined. Once again it should be noted that the values obtained will depend on both the amorphous and crystalline orientation states.

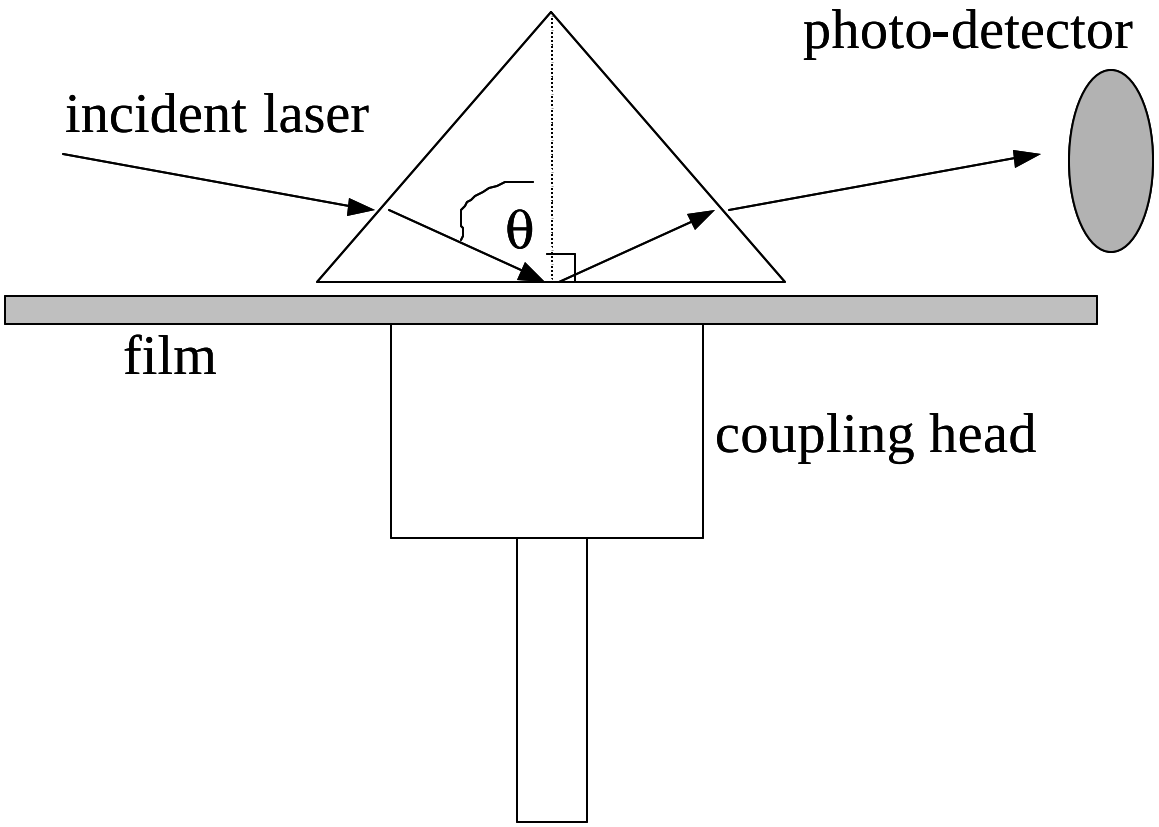

Figure 2.20. Schematic of prism coupler method for determining refractive index in three orthogonal directions[45].

2-12. Infrared Dichroism

A combination of the WAXS pole figure and birefringence techniques allows one to determine separate orientation functions for the amorphous and crystalline phases. The technique of infrared (IR) dichroism in many instances allows the independent determination of both the amorphous and crystalline phases with one experiment. IR spectroscopy measures absorbances specific to a given chemical bond. The correlation of absorbances with specific vibrations of a given bond allows one to trace behavior at known locations along the polymer chain. If a given vibration can be assigned to either the amorphous or crystalline phase, it gives the experimentalist a tool to probe that phase independent of the rest of the sample. Several crystalline and amorphous specific bands for polyethylene have been identified in the literature[46,47,48]. The degree to which a chemical bond will absorb the incident IR energy of the appropriate wavelength will depend on the relative orientation of the incoming wave and the dipole moment of the bond. Parallel alignment will result in maximum absorption, while perpendicular alignment will result in no absorption. Polarization of the incoming IR beam to produce measurements in two orthogonal directions allows one to determine the dichroic ratio, defined below, a measure of the orientation of the chemical bond.

$$D = A_{ll} / A_{\perp} \qquad \text{Eq.2.12}$$

D: dichroic ratio
A_{ll}: Absorbance with reference axis parallel to polarizer
$A_{\perp}$: Absorbance with reference axis perpendicular to polarizer

Application of the dichroic ratio to the determination of the Hermans uniaxial orientation function then follows to produce the final result shown below.

$$f_i = \left(\frac{D_0 + 2}{D_0 + 1} \right) \left(\frac{D - 1}{D + 2} \right) \qquad \text{Eq.2.13}$$

f_i: orientation value of chromophore I
D_0: defined as $2\cot^2\alpha$
D: dichroic ratio
α: angle between chromophore and chain backbone

The fact that this method provides a measure of the second moment of the orientation distribution makes its use applicable to the Hermans orientation function, but limits the applicability of this method to biaxial systems. Recently, work by two separate authors has led to a method which allows for the calculation of the White-Spruiell biaxial orientation functions using IR dichroism for the crystalline phase of polyethylene[49,50]. This method requires that assumptions regarding the orientation of the material be made in addition to the standard collection of dichroism data. Essentially, measurements are made for the absorptions at 719 cm^{-1} and 730 cm^{-1} which are related to the "b" and "a" crystallographic axis of polyethylene, respectively. By assuming that the amount of "b" axis orientation in the machine direction is very small and constraining the system to the known orthogonal symmetry of the polyethylene crystal, the biaxial orientation functions can be determined. In theory these assumptions should be valid for polyethylene samples which adhere to the Keller-Machin type I and II morphologies. However, it should be noted that this particular method will only provide the second moment of the orientation distribution and is specific to the crystalline phase.

2-13. Crystallinity Determination

Perhaps the factor which most contributes to the excellent barrier properties of high density polyethylene is its high crystalline content. There are several methods for the determination of the crystalline content of polymeric materials, each often yielding slightly different results. Only three particular techniques will be discussed: density gradient column, differential scanning calorimetry (DSC), and refractometry.

Perhaps the simplest and most accurate method to determine the crystalline fraction of a polymeric sample may be obtained using a density gradient column. Because the method relies on buoyancy, or the displacement of a given volume of fluid, it yields a volume average crystalline content. This method, as with most others, is based upon the assumption of a two phase system. The assumption reduces a semicrystalline material, such as polyethylene, into two clearly divided phases, amorphous and crystalline. The density of each of these phases is of a single value at any given temperature and pressure, with no gradient in density as one moves across the boundary from one phase to the other. With the limitations of this assumption aside, if a suitable non-interacting liquid can be found for use in the column, density values accurate to the fourth decimal place are possible (g/cm^3). Though this high resolution will permit small differences between samples to be separated, the crystallinity data will only be as accurate as the constants for the densities of the wholly amorphous and crystalline phases used in the analysis. The density of the orthorhombic crystalline phase of polyethylene (under conditions of standard temperature and pressure) has been determined using x-ray analysis as 1.00 g/cm^3 [51]. The value of a 100% wholly amorphous polyethylene has been substantially more difficult to quantify. Because polyethylene crystallizes so rapidly, it has not been possible to produce a completely amorphous specimen. The accepted value of 0.855 g/cm^3 for the amorphous phase has been obtained by extrapolating density data from the melt to room temperature[51]. As an aside, density values are frequently reported for specific polyethylene resins. It should be realized that these values represent the density of the entire pellet, amorphous and crystalline fractions. Higher values of this density correlate well with the linearity of the chain for a given set of quiescent crystallization conditions. Numerous branches, which cannot fit into the crystalline lattice, tend to lower the density value as the crystalline content of the resin is lowered by these imperfections.

The second method for the determination of crystalline content to be discussed is differential scanning calorimetry (DSC). DSC is one of the most widely employed methods because of its ease of operation, short test time, and wide availability of instrumentation. By comparing the heat required to raise an empty sample pan at a specified heating rate (often 10 – 30°C/min) to an identical sample pan with the material

to be tested, an analysis of the pertinent thermal transitions can be made. Of particular interest here will of course be the 1st order thermodynamic transition of melting. Figure 2.21 shows a typical DSC scan for the melting of an HDPE film. The crystalline content is obtained by integrating the area beneath the melting curve with respect to temperature while also accounting for the variables of heating rate and sample weight. In turn, this number can then be converted to a percent crystalline content for the sample by using the accepted value for the heat of fusion, ΔH_f. For a theoretical 100% crystalline polyethylene sample this value is 290 J/cm^3.[52] In most instances the baseline is determined by extrapolating the linear portion of the melt trace to the point of intersection with the data curve below the melting peak. Experimental errors can arise from several sources. It is well known that the crystalline content and perfection can be increased with appropriate annealing conditions. As a sample is heated from room temperature to the melting point in a DSC experiment it is possible that a small amount of annealing will occur. This effect can be minimized by increasing the heating rate, thereby reducing the amount of time spent under annealing conditions prior to melting. However, it is likely that for a material with substantial molecular mobility, such as polyethylene, this effect cannot be totally eliminated. Polyethylene is known to have a relaxation mechanism, referred to as α_c, associated with the crystalline phase that occurs well below the melt temperature. The α_c relaxation may potentially facilitate lamellar thickening. Thus it is possible for substantial molecular rearrangement to occur during the heating of the sample which is masked by the early stages of melting thereby changing the original structure and hence crystallinity of the sample. As with the density gradient column method, the DSC method relies on the assumption of a two phase system to translate measurements into crystallinity values. The area under the melting endotherm is considered to be comprised of the melting of crystalline regions superimposed on the inherent change in heat capacity as a function of temperature of the amorphous phase. Proper alignment of the baseline will cause the amorphous phase contribution to be subtracted out of the calculation. However, if a third phase is present which could be considered to have a heat capacity different from that of the amorphous phase, its contribution to the total heat signal will not be accounted for properly. Such a third phase may exist as constrained amorphous material between individual lamellae. Of final note,

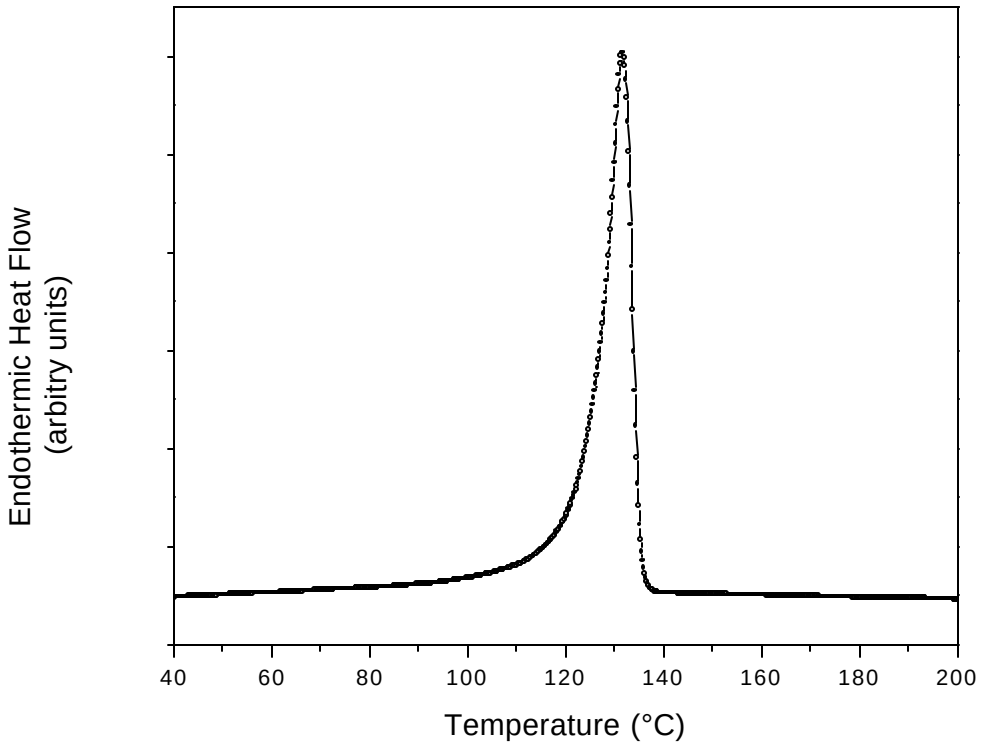

Figure 2.21. Typical DSC melting endotherm for HDPE. Heating rate 30°C/min.

residual stresses present in a sample may produce an appreciable heat signal. The quenching of an oriented melt will freeze some stresses into a polymeric system. The release of these stresses at the appropriate relaxation temperature will lead to an endothermic event which may confound the results of the test. This phenomenon is readily observable in fibers which have been heat set[53].

The final method for discussion to determine the crystalline content of a polymer was partially discussed in the above section on orientation determination. The prism-coupler method may also be used to determine the crystalline fraction. This method is based on the fact that the amorphous and crystalline phases have different refractive indices. If an average refractive index value can be determined for the entire sample it should be possible to determine the necessary fractions of each component which are necessary to give rise this measured value. The calculation of a sample average refractive index is quite straightforward with the prism-coupler apparatus. Three orthogonal measurements of the refractive index provide the required data which is then averaged to obtain the appropriate system average refractive index. Tabulated values for the refractive index as a function of crystalline content for polyolefins have been established in the literature[54]. Mathematically this method is analogous to the density gradient method in which an experimentally determined density is broken down into fractions of two known components. Again, as with the previous methods, the assumption of a two phase model is inherent. Also like the density gradient method, this technique provides a volume average crystalline content. This technique is superior to DSC in that there is no opportunity for the sample's morphology to change during the experiment. The refractive index method is non-destructive. The greatest downfall to this method is that penetration depth of the beam into the sample is limited. The data obtained represents a thin portion of the sample close to the surface. Unlike the density gradient and DSC methods which are averages of the entire sample, the refractive index method may be in error if a substantial gradient in crystalline content exists between the core and the surface of the sample.

2-14. Barrier Properties of Polymers

High density polyethylene finds widespread use in the packaging industry due to its relatively low cost and excellent barrier properties. In particular the ability of HDPE to retard the passage of water vapor is exploited. The excellent moisture barrier properties possessed by HDPE are a function of both the inherent chemical structures of the polymer and the morphological textures into which it packs. What follows is a brief review of the pertinent equations and relations regarding the permeation of small molecules through polymeric materials with additional information on specific studies relating to polyethylene and diffusion. The traditional approach to permeation will be presented. Newer work in the field utilizing activated site models or transition site models to describe the permeation behavior of small molecules through polymers will not be discussed. The goal of this project is not to develop or refine permeation models, but to simply determine the effects which morphology have on the barrier performance of the films.

In its most simple form the process of diffusion can be thought of as occurring in four distinct steps[55]. A penetrant molecule must first be adsorbed to the surface, followed by dissolution into the polymer matrix. Thirdly, the penetrant must diffuse through polymer via the driving force of a concentration gradient. Upon reaching the other surface of the polymer the penetrant must lastly desorb from the matrix. This description leads to the mathematical expression for the permeation of a diffusant as being dependant on both the properties of solubility and diffusion. The exact relation is presented below.

$$P = DS \qquad \text{Eq.2.14}$$

P: permeability
D: diffusivity
S: solubility

This definition of the permeability shows that it is a function of both a thermodynamic parameter, solubility, and a kinetic parameter, diffusivity. It becomes readily evident from this definition why HDPE is an excellent barrier to moisture. The hydrocarbon

nature of HDPE precludes there being any appreciable solubility of water, thus hindering permeation. Secondly, the highly linear and symmetric nature of the HDPE chains results in a substantial crystalline content thus producing a tightly packed structure which leaves little space for permeation. In fact, when modeling the permeation behavior of molecular species through polymeric systems it has been well established that the crystalline domains can be considered impermeable to permeation relative to the amorphous fraction. Experimental evidence from numerous semicrystalline polymers validates this assumption.[56,57] A general trend towards decreasing permeability results as the crystalline content increases Additional factors such as the size and shape of the permeant, temperature, presence of fillers or additives etc. will also be of importance in determining the permeation characteristics of a given polymer used for a particular application. However, the discussion here will be limited to the effects of polyethylene morphology on the permeation of water and a few other select compounds which have been used in key transport studies.

The majority of detailed studies which focus on the transmission of water through polyethylene films concentrate on two factors: firstly, how does the content and distribution of crystalline lamellae influence the path of a diffusant molecule and secondly, how does the nature of the constraints placed on the amorphous phase affect the diffusion process. For polyethylene in particular these two concepts are of vital importance. To re-emphasize the contrast in behavior between the crystalline and amorphous phases it should be noted that the crystalline phase represents a tightly packed structure which will be impassable while the amorphous phase represents a material which is disordered and well above its glass transition temperature resulting in what should be substantial local mobility of the chains. The amorphous phase can be considered to be in a rubbery or liquid-like state. However, as was briefly touched upon in the crystallinity determination section, much of this argument is based upon the fictitious concept of a two phase system. The two phase model ignores any role played by the crystalline phase in restricting or modifying the mobility of the amorphous phase, which may be of significance in the relatively high crystalline content realm of linear high density polyethylenes. This concept has been discussed in considerable depth by Peterlin[58], while the general behavior of diffusion in polyolefins has been reviewed by

Schlotter, and Furlan[59] (with an emphasis on antioxidant diffusion). Much of the following discussion will rely heavily on the reviews of the collective literature conducted by these authors.

The most simplistic models to address the rate of permeation through a semicrystalline polymer should take into account the effect that the amount of crystalline content will have on the overall permeation process. This can be done most easily by inserting the assumption of zero permeant solubility and diffusion through crystalline domains into the basic diffusion equation.

$$D = D_0 x_{am} \qquad \text{Eq.2.15}$$

$$S = S_0 x_{am} \qquad \text{Eq.2.16}$$

$$P = D_0 S_0 x_{am}^2 \qquad \text{Eq.2.17}$$

In each of the three above equations the volume fraction of amorphous material is denoted by x_{am} while the subscripts on the diffusivity and the solubility terms define these properties as those of a wholly amorphous sample. As one would expect the volume of amorphous phase present has a substantial influence on permeability noted by its influence to the second power. This simple model emphasizes this key point well. However, it fails to account for the influence of the orientation and distribution of the crystalline phase within the sample. This approach does not take into account the full range of morphological influences on permeability for semicrystalline polymers.

Unfortunately, in many studies the morphology of the systems have been very poorly documented thus making the interpretation and comparison of results dubious. To emphasize the importance of the morphological texture on permeation properties the reader is referred to the crystalline – amorphous two phase model schematically represented in Fig.2.22. The effect of the impenetrable crystalline domains is to increase the path length which a diffusant molecule must traverse to pass from one side of the film to the other. This increase in path length is referred to as the tortuosity. One can easily envision how various arrangements of the crystalline lamellae will affect the tortuosity.

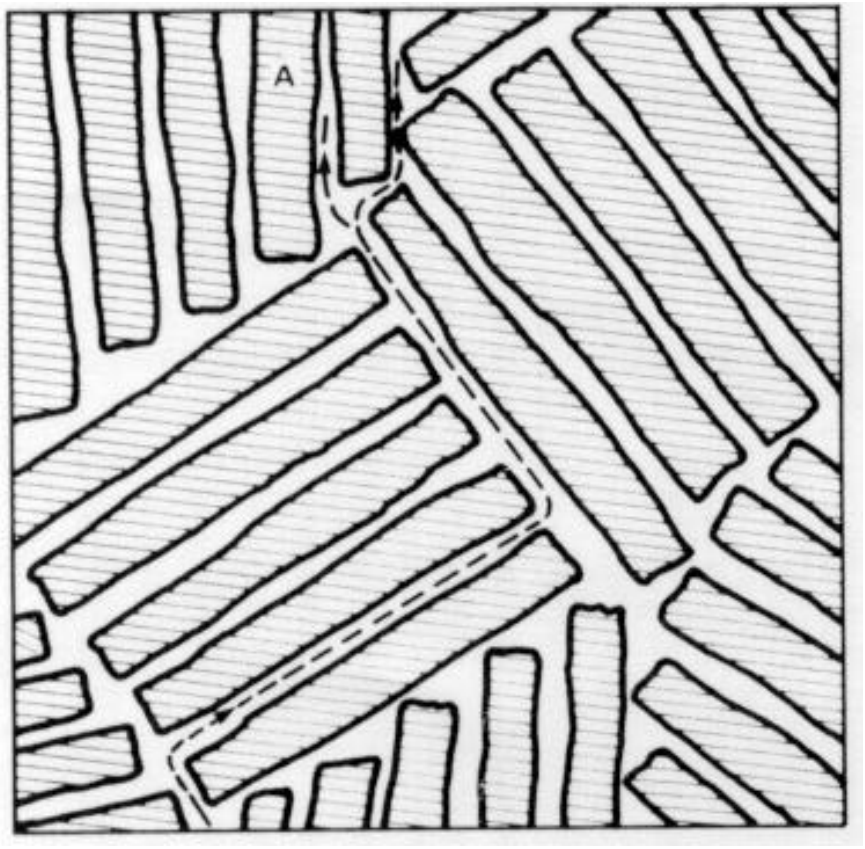

Figure 2.22. Schematic illustrating the concept of tortuosity whereby permeants must travel around crystalline lamellae[60].

In particular an arrangement of parallel, stacked lamellae with their normals perpendicular to the surface of the film would provide straight, uninterrupted pathways of amorphous material from one surface of the film to the other. A variant of this is shown in Fig.2.23 which represents what the authors call a transcrystalline model[60]. It is hypothesized that quenching occurs most rapidly at the surface leading to numerous nucleation sights at the surface of the film. These sites produce columnar lamellae growing perpendicular to the surface of the film. The bulk regions of the material are modeled as undergoing normal spherulitic crystallization. Whether or not such a morphological gradient exists in blown films is not clear. It should be noted that these researchers were investigating quiescently crystallized systems, the results of which may not be readily applicable to thin, non-quiescent systems. This particular morphological model does provide an excellent demonstration of how lamellar ordering can substantially influence permeation behavior. Factors to account for the tortuosity have been suggested in the literature. One such particular method is outlined in the equation below.

$$P = y\left(1-a\right)P_a \ / \ B \qquad \text{Eq.2.18}$$

P: Permeability of the entire sample (crystalline and amorphous phases)
ψ: Detour ratio (value of 0-1)
α: Volume fraction of crystallinity
P: Permeability of the amorphous phase
B: Blocking factor (values >1)

In this relation the permeation measured during an experiment is represented by P. The actual permeability of the amorphous phase, P_a, is thus greater than that which is experimentally observed. The detour ratio, ψ, accounts for the tortuous path which a diffusant molecule must take through the polymer while the blocking factor is related to the size of the diffusant and the spacing between lamellae. Its purpose is to account for regions between lamellae where the amorphous layer is too small to permit the passing of a sorbed molecule. In theory values for the detour ratio and the blocking factor could be calculated by geometric considerations. Due to the complex nature of twisted lamellae in

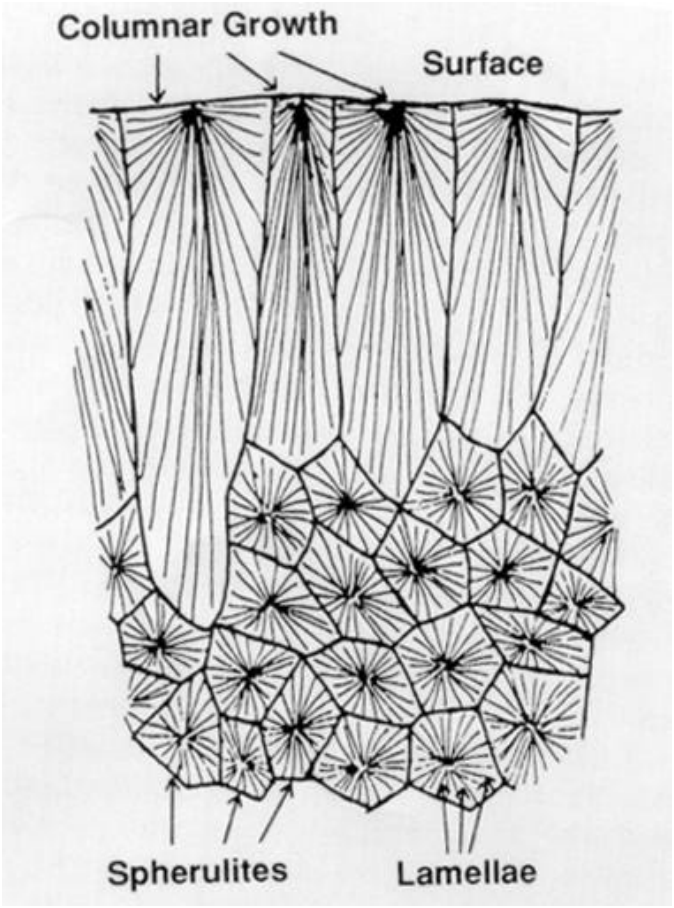

Figure 2.23. Transcrystalline morphological model. Rows of lamellae perpendicular to the surface providing straight paths of amorphous material through a portion of the sample[59].

a spherulitic structure with the complexities present in an oriented system, such a mathematical approach would be somewhat impractical. Additionally, separating the effects of both factors experimentally is not necessarily straightforward. Finally, this model disregards any impact on permeation that the variation in amorphous phase mobility brought about by the size and distribution of the crystalline domains may have. The constraints on the amorphous phase may have importance based on studies by Peterlin on both low density and high density polyethylenes using methylene chloride as the permeant[61,62]. These studies found that the equilibrium sorbed concentration of methylene chloride was greater for a drawn samples after annealing in comparison to identical drawn samples before annealing on a per unit amorphous phase content basis. The change in behavior was attributed to the different levels of amorphous phase free volume present in each sample type. The drawing step acted to densify the amorphous phase while annealing allowed the amorphous regions to relax to a less packed state. One can readily imagine that different processing histories may lead to variation in the level of amorphous phase mobility and free volume in the blown film process.

2-15. Polyethylene Blown Film Processing Studies

The effects of morphology on diffusion in blown polyethylene films have not been fully quantified in the literature. However, the range of morphologies obtained in the blown film process for polyethylene are well documented. In fact, the morphologies which are typically encountered were in large part discussed earlier. In most instances researchers have found that blown films of HDPE result in a morphological texture which is well described by the Keller-Machin model. This view seems to be shared by the majority of authors. What remains then is to fully connect the details of a blown film's morphology with permeation performance. In light of this fact a few select studies in a roughly chronological order will be touched upon to highlight their significance in relation to elucidating the structure of blown films and how these structures are related to resin and processing parameters. Passing remarks of how these structures influence mechanical properties will also be noted.

According to the previously discussed model of oriented crystallization from the melt, the final morphology obtained will be a strong function of the stress conditions of the melt at the time of solidification. During the blown film process there are three sources of processing stress that can be readily identified. First, orientation of the melt may occur as the polymer is extruded through the die gap, leading to a preferred machine direction orientation through shear. Secondly, there will be a circumferential stress imposed on the melt by the expansion of the bubble during blow up. Bubble expansion will tend to promote orientation in the transverse direction. Lastly, additional machine direction orientation can be induced by the nip rolls as it is typical to stretch the film axially during wind up to achieve the desired film gauge. This variable is referred to as draw down. The interplay of these stresses will be key in determining the subsequent morphology formed at the frost line.

In the early sixties Huck et.al. summarized the effect of processing conditions on the properties of blown polyethylene films for such industrially important characteristics as optical clarity and toughness[63]. The authors state that tougher films are produced by processes which have relatively balanced degrees of MD and TD drawing. A further result of this study found that the order in which the MD and TD stretching occurred had a substantial impact on the mechanical properties of the film. By varying extruder output and take up speeds it was possible to run the process with identical BUR's but with different bubble shapes. A schematic from their work of the drawing profile with respect to the die exit is shown in Fig.2.24. Films with enhanced impact properties were obtained when the TD stretching occurred just prior to the frost line. This effect is likely due to the relaxation behavior of polymer melts. Because the molten polymer has a fading memory, which decays exponentially, deformation events which occurred most recently will be of greatest importance. Thus, delaying the TD stretching until just before the frost line maximizes its impact on final properties. The authors noted additional effects on mechanical properties when the height and flow rate of the air ring was adjusted to obtain identical frost line heights. These phenomena emphasize that simple process variables such as MD stretch, TD stretch, or frost line height cannot fully account for the morphologies of blown films. Rather, the structure of a blown film will be a

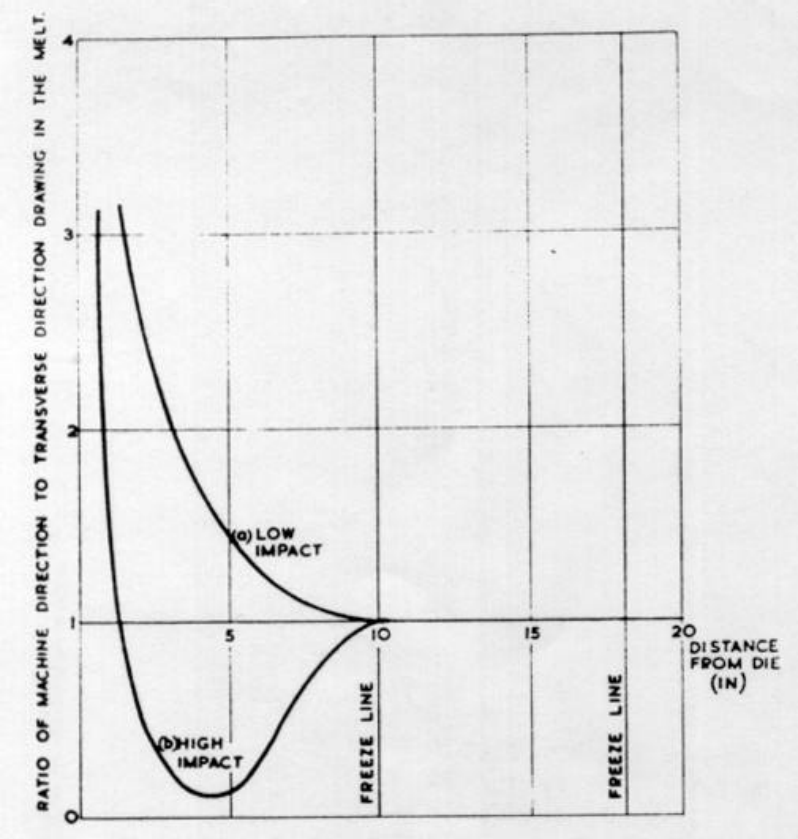

Figure 2.24. Bubble profile plot demonstrating distance from die where relative amounts of MD and TD stretching occur. "High" impact properties were obtained in the film with greater TD expansion.[63]

complex function of the entire deformation and cooling history which the melt experiences.

This point was furthered by Spruiell and White who attempted to correlate stresses at the frost line with crystalline and amorphous orientation[64]. Based on the premise that the stress on an amorphous melt will be linearly related to its birefringence, and hence its state of orientation, it was postulated that upon solidification these conditions should be "frozen" into the polymer. Results were quite successful for the amorphous polymer, atactic polystyrene used in an earlier study[65]. Experiments showed that the level of orientation that was achieved in the solidified polyethylene film was greater than that predicted by the stress optical coefficient. This behavior can be understood in terms of the Keller-Machin model. The presence of fibril nuclei, which act as oriented nucleating sites, promote crystallization in a preferred direction. As the lamellae grow, chains are removed from the melt into crystals with the proper alignment. Thus the overall orientation of the chains is modified during crystallization as the lamellae grow from these sites. This description of events was further supported by their results for films produced with varying BURs. Pole figure analysis and SAXS results suggested that the orientation state of the films could be well described by superimposed row structures as shown in Fig.2.25. This morphology is understood to develop from the presence of fibril nuclei in multiple directions due to the transverse stretching of the blown film process. It is important to note that the model of Keller-Machin was originally applied to uniaxial systems. The Spruiell-White study suggests that any extended chain can act as a nucleating site regardless of its orientation. Thus chains which become oriented in the TD just prior to crystallization due to bubble expansion lead to TD directed row structures while those chains which are extended in the MD direction due to nip roll draw down promote MD directed row structures. In light of the tortuosity concept and the impenetrability of lamellae to permeants one can hypothesize that the ideal arrangement of lamellae for barrier properties would be with lamellar normals parallel to the film surface. These results show that the attainment of such a morphology may not be possible. Attempts to produce a more balanced orientation through changes in the blow up ratio lead to varying amounts of "c" and "a" axis orientation with respect to the MD and TD directions. However because the crystal

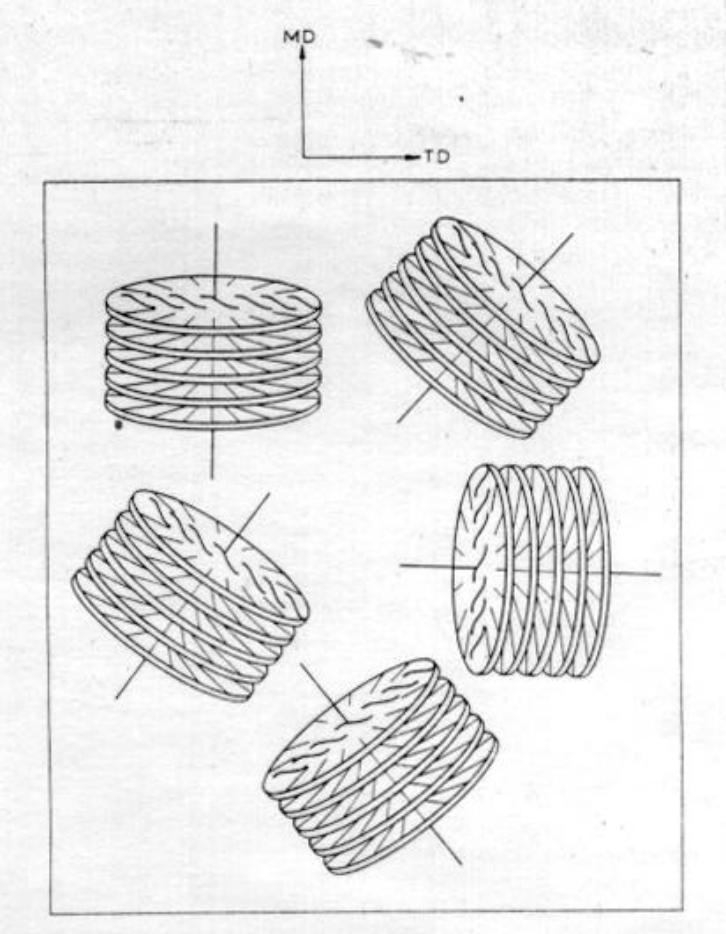

Figure 2.25. Proposed morphological model for film with equal biaxial orientation consisting of superimposed row structures[64].

growth axis of the polyethylene crystal is along the "b" axis, which orients itself perpendicular to the direction of applied stress, no amount of TD or MD stretching will discourage lamellar growth perpendicular to the film surface. Thus while the amount of "b" axis orientation relative to the MD and TD can be changed there will be an inherent amount of "b" axis orientation relative to the ND which will remain. Concurrent work by Maddams and Preedy have reinforced the applicability of the row nucleated model to blown films as their results clearly demonstrated that "a" axis orientation shifts towards the ND axis with increasing processing stress while the "b" axis remains parallel to the TD[66,67,68]. While many of the articles discussed to this point have included results with respect to amorphous orientation in blown films, a substantial amount of data was added to the literature regarding this topic by Patel, et.al.[69]. In their studies, by combining pole figure and birefringence analysis, it was calculated that in most instances the orientation of the amorphous phase is perpendicular to that of the crystalline phase in the plane of the film. This finding is certainly not intuitive and it is not the first time such behavior has been noted in the literature. Of additional significance from this work is the noted variation in birefringence as one examines different points around the bubble at the same distance from the die. The variations in birefringence found are a reminder of the difficulty in achieving a perfectly uniform film around the circumference, and may be a possible explanation for some of the scatter that is seen in blown film studies.

A more recent study on LDPE blown films by Prud'homme and Pazur sheds light on another controversial matter in the morphology of blown films[70]. The presence of a transcrystalline layer at the surface of blown films has been speculated by some investigators as arising from rapid quenching. It is reasoned that a high nucleation density at the surface will lead to columnar growth of lamellae normal to the film surface as was demonstrated in Fig.2.23. Evidence for transcrystalline structures are provided via pole figure analysis and two dimensional photographic SAXS patterns. The results suggested that the thickness of the transcrystalline region decreased as processing stress increased, whereby the morphology took on a more Keller-Machin like character. While the arguments are persuasive, no direct observation of the transcrystallization material by microscopy was attempted. Secondly, the nature of the melt stresses may not be similar

for the production of HDPE, which is the primary focus of this project, relative to the highly branched structure of LDPE

Two very recent studies have emphasized the importance of the interrelationship between resin properties, processing conditions and the obtained morphology. Prasad et. al.[71] have shown through TEM, SEM, and particularly two dimensional SAXS patterns that the degree of lamellar orientation present in the end film can be directly related to the elasticity of the melt at equivalent processing conditions. This study clearly shows the impact that the melt relaxation time has on lamellar orientation. An even more interesting study by Sue et al.[72] demonstrates how variation in the blow up ratio can produce morphologies with either MD dominant or TD dominant row nucleated structures. TEM and SAXS evidence suggests that two very distinct populations of row nucleated lamellae are present in both the MD and TD directions of the HDPE blown films. The production of such distinctly orthogonally directed row structures may have both mechanical properties and MVTR properties that are very interesting.

2-16. Blown Film MVTR Studies

Surprisingly, despite its commercial importance, there are relatively few studies which are directly focused on determining the relationship between resin and process variables in the blown film process to final MVTR properties. What few articles can be found are located in trade journals and thus usually contain fairly simplified arguments and broad generalizations of behavior, with little morphological or characterization data presented. In one such study[73] a correlation between film density and MVTR performance is noted as shown in Fig.2.26. This is of course expected as a greater crystalline fraction will reduce the amorphous content of the film, thus providing less volume for water vapor to pass. This study also noted that the MVTR was a function of film gauge. This effect is attributed to differences in orientation, though no data are presented. The authors did find a general trend in which the effects of varying process conditions were more pronounced for resins with broader molecular weight distributions. In a second article[74] from the same laboratory fewer data are presented but a new correlation is noted. The authors state that MVTR performance was enhanced by a more

balanced MD TD crystalline orientation, and that the Elmendorf tear test was an excellent indicator of this balance.

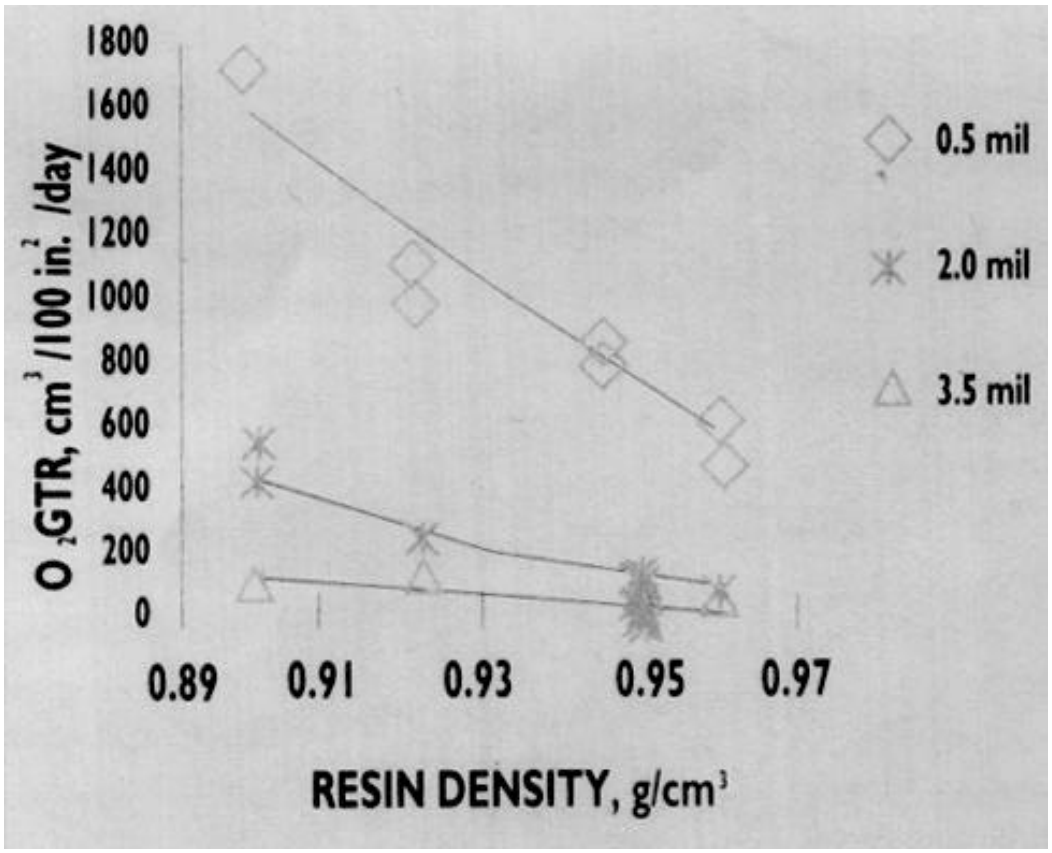

Figure 2.26. Relationship between film density and MVTR[73].

2.17 References

[1] Kanai, T., Campbell, G.A., Film Processing, Hanser Publishers, Munich, (1999).
[2] W. Michaeli, F. Ohlendorf, Hauk, J., *Journal of Polymer Engineering*, (2001), **21**, 167.
[3] Kuijk, E.W., Tas, P.P., Neuteboom, P., *Journal of Reinforced Plastics and Composites*, **18** (6), 508, (1999).
[4] Wongsomnuk, P., Banyam, J., Sirivat, A., *Journal of Macromolecular Science – Physics*, **B39** (5,6), 723, (2000).
[5] Campbell, G.A., Cao, B., *International Polymer Processing*, **4** (2), 114, (1989).
[6] Campbell, G.A. Ashok, BD, *International Polymer Processing*, **7** (3), 240, (1992).
[7] Campbell, G.A., Sweeney, P.A., Feeney, F.A., *International Polymer Processing*, **7** (3), 229, (1992).
[8] Campbell, G.A., Babel, A.K., *Tappi Journal*, **78** (5), 199, (1995).
[9] Campbell, G.A., Bullwinkel, M.D., Rasmussen, D.H., Krexa, J., Brancewitz, C.J., *International Polymer Processing*, **16** (1), 39, (2001).
[10] Tadmor, Z., Gogos, C., Principles of Polymer Processing, John Wiley and Sons, New York, (1979).
[11] Briston, J., Plastic Films, John Wiley and Sons, New York, (1989).
[12] Oswin, C.R., Plastic Films and Packaging. John Wiley and Sons, New York, (1975).
[13] www.americanplasticscouncil.org
[14] K. Ziegler, E. Holzkamp, H. Breil, H. Martin, *Angew. Chem.*, **57**, 541, (1955).
[15] Natta, G., *Angew. Chem.*, **68**, 393, (1956).
[16] Boor, J., Ziegler-Natta Catalysts and Polymerizations, Academic Press, New York, (1979).
[17] Hogan, J.P., Banks, R.L., Belg. Pat. 530617 (1955).
[18] Epacher, E., Krohnke, C., Pukanszky, B., *Polymer Engineering and Science*, **40** (6), 1458, (2000).
[19] Weckhuysen, B., Schoonheydt, R., *Catalysis Today*, **51**, 215, (1999).
[20] Kaminskky, W., *Catalysis Today*, **62**, 23, (2000).
[21] www.pssc.usm.edu/macrog/index.htm, University of Southern Mississippi, Department of Polymer Science.
[22] Bochmann, M., *Dalton Transactions*, 255, (1996).
[23] De Gennes, P.G., *Journal of Chemical Physics*, **60** (12), 5030, (1974).
[24] Pope, D.P., Keller, A., *Colloid and Polymer Science*, **256**, 751, (1978).
[25] Odell, J.A., Narh, K.A., Keller, A., *Journal of Polymer Science: Part B: Polymer Physics*, **30**, 334, (1992).
[26] Keller, A., Odell, J.A., *Colloid and Polymer Science*, **263**, 181, (1985).
[27] Chu, S., Perkins, T., Smith, D., *Science*, **264**, 819, (1994).
[28] Chu, S., Perkins, T., Quake, S., Smith, D., *Science*, **264**, 822, (1994).
[29] Chu, S., Smith, D, Babcock, P., *Science*, **283**, 1724, (1999).
[30] Keller, A. Kolnaar, W.H., *Progress in Colloid and Polymer Science*, **92**, 81, (1993).
[31] Farrel, C.J., Keller, A., Miles, M.J., Pope, D.P., *Polymer*, **21**, 1292, (1980).
[32] Miles, M.J., Keller, A., *Polymer*, **21**, 1295, (1980).
[33] Basset, D.C., Hodge, A.M., *Proc. R. Soc. Lond.*, **359**, 121, (1978).
[34] Wunderlich, B., Macromolecular Physics, Academic Press, New York, (1973).
[35] Bunn, C.W., Fibers From Synthetic Polymers, Hill, R editor, Elsevier Publishing, Amsterdam, 1953.
[36] Rosen, S. L., Fundamental Principles of Polymeric Materials, Wiley-Interscience, New York, (1993).
[37] Class notes – Polymer Morphology – Virginia Tech, unknown source.
[38] Stein, R.S., Picot, C., Motegi, M., Kawai, H., *Journal of Polymer Science A-2*, **8**, 2115, (1970).
[39] Keller, A., Machin, M.J., *Journal of Macromolecular Science: Part B Physics*, **B1** (1), 41, (1967).
[40] Basset, D.C., Principles of Polymer Morphology, Cambridge University Press, 1981.
[41] Keller, A., Sandeman, I., *Journal of Polymer Science*, **15**, 133, (1955).
[42] White, J.L., Spruiell, J.E., *Polymer Engineering and Science*, **21** (13), 859, (1981).
[43] Wilkes, G.L., Encyclopedia of Polymer Science and Engineering – Rheooptical Properties, **14**, 542, (1988).
[44] Ulirch, R., Torge, R., *Applied Optics*, **12** (12), 2901, (1973).
[45] Metricon model 2010 equipment manual, (1991).
[46] Keller, A., Sandeman, I., *Journal of Polymer Science*, 511, (1954).
[47] Aggarwal, S.L., Tilley, G.P., Sweeting, O.J., *Journal of Applied Polymer Science*, **1** (1), 91, (1959).

[48] Read, B.E., Stein, R.S., *Macromolecules*, **1**, 116, (1968).
[49] Kissin, Y.V., *Journal of Polymer Science, Part B: Polymer Physics*, **30**,1165, (1992).
[50] Krishnaswamy, R.K., *Journal of Polymer Science, Part B: Polymer Physics*, **38**, 182, (2000).
[51] Brandup, J., E.H. Immergut editors, Polymer Handbook, 2nd edition, Wiley-Interscience, New York, (1975).
[52] Hoffman, J.D., Miller, R.L., Marand, H., Roitman, D.B., *Macromolecules*, **25**, 2221, (1992).
[53] Bair, H. E., "Glass Transition Measurements by DSC", *Assignment of the Glass Transition, ASTM STP 1249*, R.J. Seyler, Ed., American Society for Testing and Materials, Philadelphia, pp. 50, (1994).
[54] Schael, W., *Journal of Polymer Science*, **12**, 903, (1968).
[55] Salame, M., Steingiser, S., *Polymer and Plastics Technology and Engineering*, **8** (2), 155, (1977).
[56] Tock, R.W., *Advances in Polymer Technology*, **3** (3), 223, (199?).
[57] Krevelen, D.W., Properties of Polymers – Their Estimation and Correlation With Chemical Structure 2nd ed., Elsevier, New York, (1976).
[58] Peterlin, A., *Journal of Macromolecular Science-Physics*, **B11** (1), 57, (1975).
[59] Schlotter, N.E., Furlan, P.Y. *Polymer*, **33** (16), 3323, (1992).
[60] Muccigrosso, J., Phillips, P.J., *IEEE Transactions Electircal Insulation*, **EI-13**, 172, (1978).
[61] Meinel, G., Peterlin, A., *Journal of Polymer Science, A-2*, **9**, 67, (1971).
[62] Araimo, L., De Candia, F., Vittoria, V., Peterlin, A., *Journal of Polymer Science, Polymer Physics*, **16**, 2087, (1978).
[63] Huck, N.D., Clegg, P.L., SPE Transactions, 121, July (1961).
[64] Choi, K., Spruiell, J.E., White, J.L., *Journal of Polymer Science: Polymer Physics*, **20**, 27, (1982).
[65] Choi, K., J.L White, J.E., Spruiell, *Journal of Applied Polymer Science*, **25**, 2777, (1980).
[66] Maddams, W.F., Preedy, J.E., *Journal of Applied Polymer Science*, **22**, 2721, (1978).
[67] Maddams, W.F., Preedy, J.E., *Journal of Applied Polymer Science*, **22**, 2738, (1978).
[68] Maddams, W.F., Preedy, J.E., *Journal of Applied Polymer Science*, **22**, 2751, (1978).
[69] Gilbert, M., Hemsley, D.A., Patel, S.R., *British Polymer Journal*, **19**, 9, (1987).
[70] Pazur, R.J., Prud'homme, R.E., *Macromolecules*, **29**, 119, (1996).
[71] Prasad, A., Shroff, R., Rane, S, Beaucage, G., *Polymer*, 42, 3103, (2001).
[72] Sue, H.J., Lu, J., Rieker, T.P., *Polymer*, 42, 4635, (2001).
[73] Krohn, A.V., Jordy, D.W., *TAPPI Journal*, **80** (3), 151, (1997).
[74] Krohn, J., Tate, R., Jordy, D., *Proceedings of the SPE 55th ANTEC*, 1654 (1997).

Chapter 3

Unique morphologies consisting of orthogonal stacks of lamellae in high density polyethylene films – Formation in the delayed blow out process and effect on tear properties.

3.1 Introduction

Blown films of high density polyethylene are used in numerous packaging applications because of their combination of chemical resistance, barrier properties, mechanical properties, and low cost. It is well known that the mechanical properties obtained in a given product are a strong function of both resin and process parameters. In particular, the resistance of a film to tear propagation is known to be highly dependent upon the balance of crystalline and amorphous orientation in the film plane. In general, a uniaxial orientation will enhance tear resistance in the transverse direction (TD), with a

concurrent decrease in tear resistance along the direction of orientation, the machine direction (MD). The majority of commercial film processes attempt to impart a biaxial orientation in order to produce a balanced mechanical response. However, the effects of biaxial orientation on end properties are still not completely understood. It is clear from a survey of the literature that the manner in which states of biaxial orientation are formed, and the resulting properties of these structures, requires further study.

This chapter will examine resin-processing-structure-property relationships in blown films made from two high molecular weight, high density polyethylene (HMW-HDPE) resins. Specifically, the interaction between a resin parameter, molecular weight distribution (MWD), with the "high stalk", or delayed blow out, blown film process will be examined. It has been found that unique morphologies consisting of orthogonal stacks of lamellae may be generated under appropriate conditions. A representative micrograph of this morphology is shown in Fig.3.1 (the details of the production of this film and others will be discussed later in the text). The possible benefits of such morphologies for influencing MD and TD tear resistance and dart impact properties will also be examined.

3.2 Background Information

Many decades of research have been conducted in the area of blown polyethylene films. As surveyed in the literature review, early work by numerous authors have led to a basic understanding of how structure develops during PE film blowing[1-9]. The consensus formed by this early body of work is that the blown film process, under conditions relevant to industrial film production (i.e. MD stresses greater than TD stresses), produces HDPE films with preferential orientation of the "b" crystal axis perpendicular to the MD, while the "a" and "c" crystal axis tend to orient between the MD and film normal (ND).

The morphological description of these data has typically been visualized in terms of the Keller-Machin (K-M) row nucleation model. Work by Keller and coworkers has been very successful in describing the mechanism of structure formation in semicrystalline polymers as it arises from oriented melts and solutions, in terms of row nucleated crystallization, an excellent review of which is found in the literature[10].

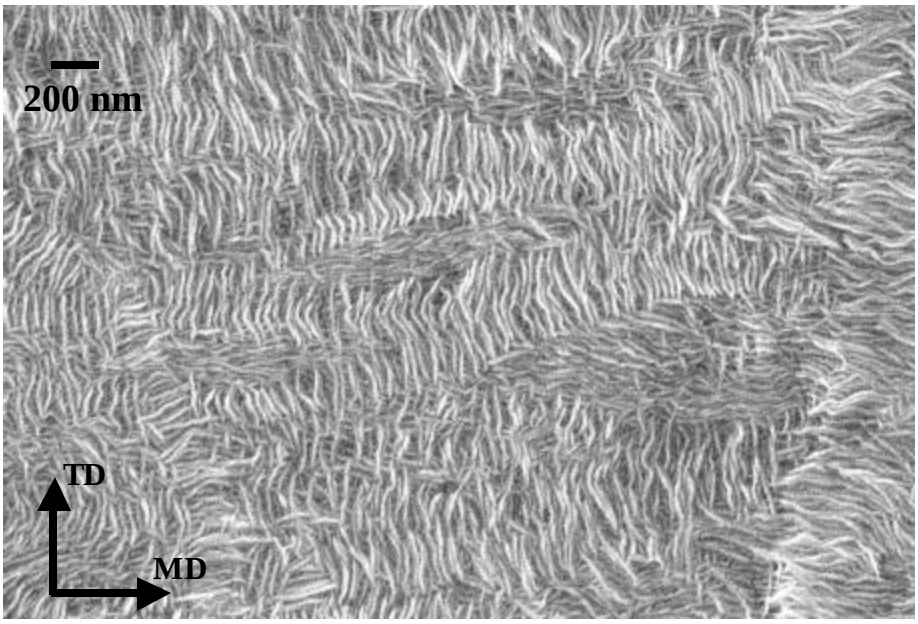

Figure 3.1. FESEM micrograph of film displaying orthogonal stacked lamella structures. Lamellae are seen to reside in stacks oriented primarily along the film MD and TD.

A more complete description of the model, than what follows, was presented in the literature review section. Therefore, a reader familiar with this material may wish to skim through the following description. The material has been restated here in order to retain the "modified manuscript" format of each of the chapters, thus allowing each to stand alone.

The K-M model postulates that the stresses imparted by the flow field upon a polymer coil can lead to a partial extension of the chain along the direction of flow. As the temperature is lowered, it becomes possible for a small amount of material to crystallize in this semi-extended and oriented state. This material is referred to as a fibril or fibril nucleus. Subsequent crystallization of the bulk, whether oriented or not, occurs in a chain folded manner, nucleated from the oriented fibrils. Noting that the crystal axis of most rapid growth in PE occurs along the "b" crystallographic axis (orthorhombic unit cell with the "c" axis coincident with the chain backbone), the net effect of the fibril nuclei is to promote a preferential orientation of the bulk crystalline material with its "b" axis perpendicular to the direction of flow. For the blown film process, this constitutes "b" axis orientation in the TD-ND plane. During bulk crystallization the "a" and "c" axis may align themselves between two possible orientation states. Under conditions of low stress the K-M model considers the lamellae to twist freely about the growth axis, the "b" axis, leading to "a" and "c" axis orientation which is oriented roughly evenly about the "b" axis. Conversely, under conditions of high stress, the "c" axis tends to remain parallel to the direction of imposed stress, leading to a preferential orientation of the "a" and "b" axis perpendicular to the principal stress direction. In the blown film process the high stress condition results in orientation of the "c" axis along the MD with the "a" and "b" axis lying in the TD-ND plane. Stress levels between the low and high regimes lead to orientation states between these two extremes.

The K-M model does not describe the direction or degree of amorphous phase orientation which may be imparted by the deformation process. While it may seem intuitively obvious that chains comprising the amorphous phase should be aligned along the flow direction, this may not be the case. Conflicting results for blown PE films[1,9,12,20] have been published. The state of preferred orientation of the amorphous phase has been found to be along the principle deformation axis in certain studies, while others have

determined it to be perpendicular to this direction. The latter result may be plausible as a significant amount of chain reorientation must accompany the crystallization process. The lack of agreement can be attributed to at least three sources. Identical processing conditions and resins are not typically found between studies, which may account for the variations in the amorphous orientation observed. In addition, the quantification of amorphous phase orientation in blown PE films requires the combination of data from two separate experiments, WAXS and birefringence, which introduces the potential for errors over that of a single experiment. Lastly, the magnitude of amorphous orientation tends to be small, making accurate quantification difficult.

The work of Maddams and Preedy[4-6] in particular demonstrated how the full range of orientation states from the low stress to the high stress conditions in the K-M model could be imparted to HDPE via the blown film process. Thus, it has been demonstrated that the stresses applied to the bubble during processing have a profound effect upon the final orientation state of the film. Furthermore, the means by which stress affects the final morphology of the film is through the orientation of chains in the melt. Indeed, a simple but elegant study by Choi et. al.[8] demonstrated the relationship between stress and orientation in the melt, during film blowing, using atactic polystyrene. Because atactic polystyrene does not crystallize upon solidification, there is no reorientation of the chains upon cooling beyond that which is expected from molecular relaxation. Thus, Choi et. al. were able to directly relate the processing stress, through the stress optical coefficient, to the birefringence of the final film, with the implicit assumption that the measured birefringence was due only to orientation effects. Hence, the orientation state of the final film could be predicted *a priori* based upon knowledge of the stresses imposed by the fabrication process.

As alluded to in the previous paragraph, while measurements of the stresses imposed upon the melt of a semicrystalline polymer may be capable of describing the orientation state of the chains through the stress optical coefficient, prior to crystallization, the subsequent reorganization of chain orientation during crystallization makes a direct connection between the melt stress level and the end orientation state impossible. Despite this complication, in a subsequent study, Choi et. al.[9] were able to demonstrate a consistent correlation between processing stress and film orientation by

interpreting their results in terms of the K-M model. When one considers the range of blow up ratios (BUR) used in their study, 1~10, this result becomes more remarkable for the following reason.

It must be stressed that the K-M model for oriented crystallization was developed to describe the behavior resulting from a uniaxial deformation. In contrast to this situation, the blown film process generally involves some level of biaxial deformation. The application of such large BUR values leads to a highly biaxial stretching of the melt. This is in contrast to many of the earlier studies, which were not conducted under conditions of such large TD deformation. The Choi study demonstrated that the crystalline orientation produced in these films could be described as a superposition of row nucleated structures as shown in Fig.3.2. Subsequent works by numerous researchers have confirmed the applicability of the K-M model to the blown film process for varying levels of biaxial stretching[11-16].

Thus, based upon the results of earlier work, two basic statements can be made regarding the relationship between processing variables and the orientation state of the final film for HDPE. Firstly, the state of crystalline orientation in the film is determined by the prior orientation of chains in the melt. Specifically, the orientation of a small population of fibril nuclei play a key role in determining the resultant crystalline orientation. Secondly, the orientation of the fibril nuclei are determined by the relative levels of MD and TD stresses imparted by the process. Therefore, by manipulating process variables the level of orientation in a given direction can be affected.

Implicit in the above statements is the assumption that a simple relationship exists between stress level and molecular orientation in the melt. This, however, is not necessarily the case for a process involving complex deformations. The state of melt orientation found at the frost line will not only be a function of the stresses present at the frost line, but will also be a function of the deformation history the melt has experienced as well as the relaxation characteristics of the melt. That is, orientation induced well below the frost line may persist due to the time dependent nature of molecular relaxation in long chain molecules. Thus, a process which accomplishes biaxial deformation via sequential deformation, extension along the MD followed by TD extension, may produce melt orientation states at the frost line which are dramatically different than those formed

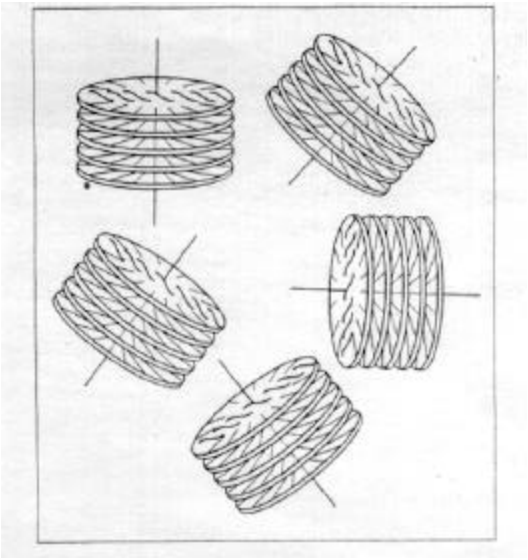

Figure 3.2. Superposition of row nucleated structures leading to a biaxial orientation. Adapted from Choi et. al.[9].

by a more simultaneous biaxial deformation. Both types of biaxial stretching are commonly utilized in the PE blown film industry. The latter refers to the "in pocket" configuration while the former refers to the high stalk configuration. A schematic of the high stalk process is provided in Fig.3.3. The vast majority of blown film studies make no explicit reference to the bubble shape employed (comparisons with the sequential biaxial stretching used in the tenter frame process[17] are not directly applicable here as the tenter method incorporates an additional solidification step, not present in the blown film process, between the MD and TD stretches).

Thus, the first aim of this chapter is to describe the effect of processing variables on film structure within the context of the bubble configuration employed, in this case, the high stalk process. By varying the ratio of MD to TD stress (through changes in draw down rate) and the time lag between MD and TD stretching (through variation in the frost line height) it should be possible, theoretically, to alter the number of, and orientation of, fibril nuclei present at the frost line. Because the fibril nuclei largely determine the end state of crystalline orientation, their presence may be inferred from measurements of the crystalline orientation in the final film.

The second goal of this chapter is to investigate how the molecular weight distribution of a resin interacts with a given set of processing conditions. As stated above, blown films typically display morphologies which can be described in terms of row nucleated structures. A direct implication of this observation is that two resins with, similar weight average molecular weights, may produce quite different structures if they contain differing levels of high molecular weight, slowly relaxing, material. These slowly relaxing chains may consist of a small fraction of very high molecular weight material (a high molecular weight tail) or a small fraction of long chain branched material. In either case, their presence will alter the density of extended chains in the melt and thus may have an impact on the final structure which belies their small numbers.

Finally, the majority of studies available relate processing parameters directly to end properties and contain little structural analysis beyond the measurement of birefringence or shrinkage. This chapter will attempt to characterize film performance, as determined by Elmendorf tear and dart impact tests, and relate the results to film structure.

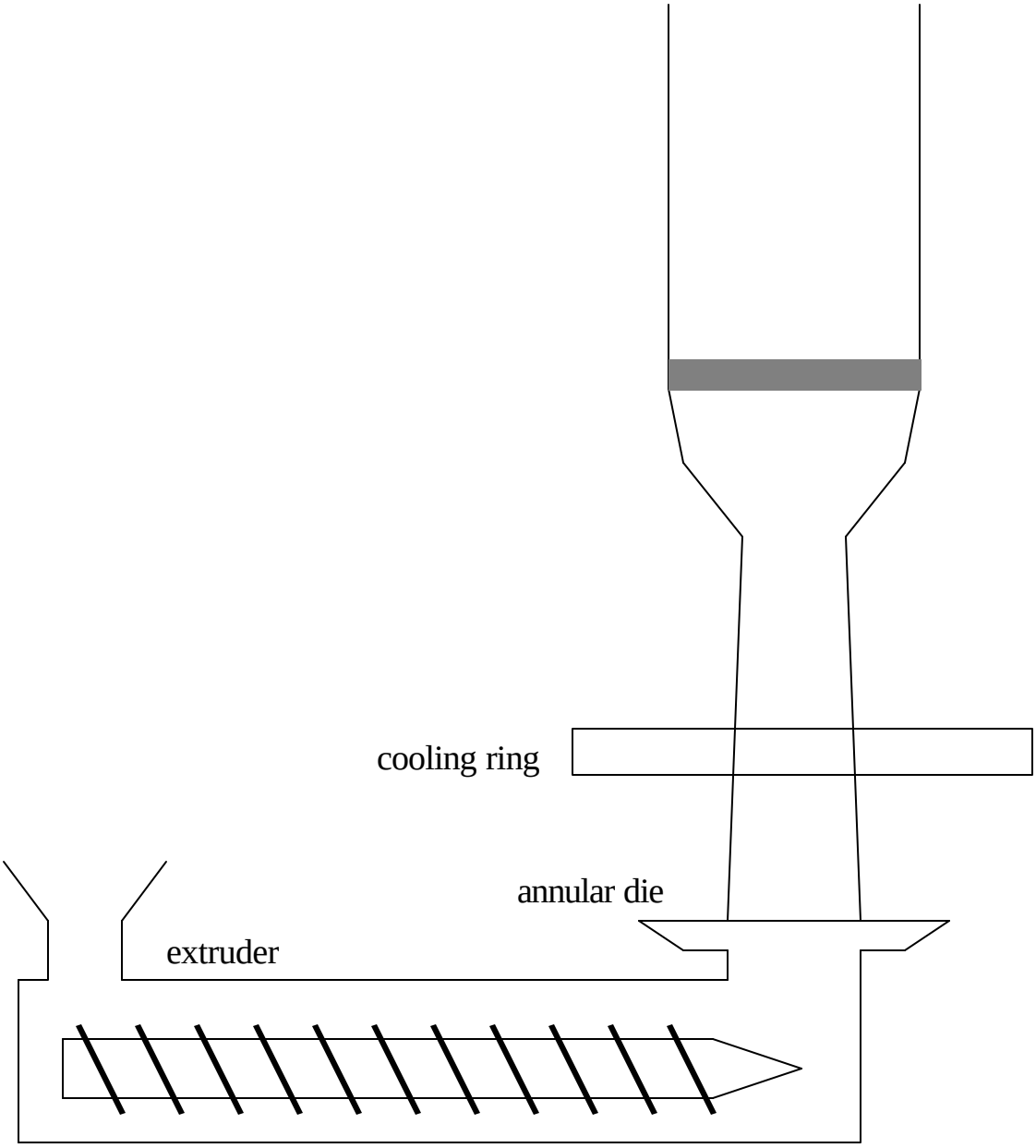

Figure 3.3. Schematic of the high stalk blown film process (also referred to as the delayed blow out or HDPE process). Pellets are melted and extruded upwards through an annular die. This ring of polymer melt is then stretched vertically (along the MD). Note that a slight contraction of the bubble diameter occurs prior to bubble expansion. After cooling/solidification, the bubble is subsequently collapsed and collected on a winding device (not shown).

Reviewing a portion of the literature which addresses the Elmendorf tear and dart impact resistance of blown PE films, it becomes apparent that there is general agreement that balanced in-plane orientation leads to balanced tear properties[2-4,7,18-23]. The microstructural details which determine tear resistance have not yet been fully elucidated, though a number of attempts have been made to understand the nature of yielding at the lamellar level[19-21,24-27]. The starting point for many of these interpretations is the analysis of a primarily MD oriented, row nucleated structure subjected to tensile deformation. The application of a tensile stress along the MD should lead to deformation of the amorphous material located between lamellar stacks, as this material is much more compliant than the crystalline lamellae. In contrast, applying a stress along the TD places the load primarily upon the long axis of the lamella. Thus, the MD tensile response tends to lead to a lower modulus and a larger yield strain than measurements made along the film TD.

Two recent studies have attempted to describe the microstructural deformations of row nucleated structures during the Elmendorf tear and dart impact tests[19,20]. Using the imbalance of tensile properties, noted above, arising from the anisotropic arrangement of amorphous and crystalline material found in row nucleated films as a basis, Krishnaswamy[20] concluded that MD Elmendorf tear is dominated by interlamellar yielding while TD Elmendorf tear is a result of plastic deformation and chain pull out from lamellae. In a different study of dart impact resistance, Sue[19] was not able to directly correlate the relative levels of MD versus TD oriented row structures with performance. Rather it was hypothesized that differences in tie chain connectivity between MD and TD lamellar stacks were responsible for controlling dart impact. These studies make it apparent that the lamellar orientation state, and the details of its formation, are key factors in determining tear performance.

To briefly summarize, this chapter will examine resin-processing-structure-property relationships in two high density polyethylene films of differing molecular weight distribution. Emphasis will be placed on interpretation of the results using the K-M model, in alignment with previous studies. However, the context will be with respect to bubble shape and relaxation behavior, relevant topics that have often been neglected.

The work presented is the result of a joint effort by the author's lab at Virginia Tech and Chevron-Phillips staff. Film fabrication and the measurement of tear properties were conducted by Chevron-Phillips staff, while the morphological characterization was conducted at Virginia Tech. The films were based on two resins produced using proprietary Chevron-Phillips catalyst technology. Thus, the nature of the catalyst systems employed cannot be divulged. Shear rheological data and moments of the MWD will be used to describe the differences between the resins.

3.3 Experimental Methods

Blown films of three gauges (12.5, 20, and 30 microns) were each produced at three different frost line heights (FLH) (23, 38, and 54 cm) using a high stalk process. A schematic of the process is provided in Fig.3.3. Individual film gauges were achieved by changing the draw down ratio, DDR, (11, 15, and 18) for a constant extruder output and die gap. In all cases the blow-up ratio was maintained at 4:1. A 38 mm diameter single screw Davis standard extruder (L/D=24; 2.2:1 compression ratio) fitted with a barrier screw and a Maddock mixing section at the end was used. A 5.1 cm Sano film die with a single lip air ring was used to quench the films. Extruder and die temperatures were set at 210°C with a 0.90 mm die gap. Extruder output was held constant at 13.2 kg/hr. It is noted, with gratitude, that the films were produced, and the GPC and rheology data collected by staff at Chevron-Phillips. In particular thanks go to Dr. Raj Krishnaswamy for his transfer of this information and material.

For each of the above conditions, two HDPE resins were utilized. The first designated HDPE-A and the second resin designated HDPE-B. Molecular weight data were obtained using a Waters 150 CV Plus Gel Permeation Chromatograph and trichlorobenzene as the solvent at a temperature of 140°C. The rheological measurements were made in dynamic oscillatory shear with a parallel plate geometry on a Rheometrics RMS-800 at 190°C. Wide angle x-ray scattering (WAXS) patterns were obtained using a flat plate Warhaus camera with CuKα irradiation produced at 40 kV and 20 mA using a Philips model 1720 tabletop x-ray generator. Additional WAXS pole figure data were collected on selected samples at AMIA labs of The Woodlands, Texas.

Small angle x-ray scattering (SAXS) patterns were obtained using the synchrotron source at Brookhaven. Special thanks are due to Dr. Srivatsan Srinivas for the needed data. Further SAXS data were collected at Virginia Tech using a compact Kratky camera fitted with a one dimensional, position sensitive detector, using a Philips 1729 table top x-ray generator. Field emission scanning electron micrographs (FESEM) were obtained using a Leo system 1550 at an operating voltage of 2 kV. Samples were prepared for viewing by sputtering with a five nanometer thick layer of platinum/palladium. A Metricon 2010 prism coupler was used to determine the refractive indices of the films in the three principle orthogonal directions: MD, TD, and ND. The average values from these measurements were used to determine the crystalline content by applying the Lorentz-Lorenz equation as discussed by others[28,29]. The variation in crystalline content between films was found to be small by this technique (overall contents 60-63 vol%), *hence all discussions will consider differences in crystalline content negligible.* Elmendorf tear tests were conducted in accordance with ASTM D-1922 using a TMI universal tear tester. Dart impact resistance tests followed the procedures outline in ASTM D 1709. The Elmendorf and dart impact tests were conducted by Chevron-Phillips staff.

The experimental design consisted of each resin being processed using three different frost line heights and three different gauges. However, due to a lack of bubble stability at the lowest FLH and highest DDR for HDPE-A, this film could not be produced. Thus, nine films of HDPE-B and eight films of HDPE-A were produced. Furthermore, approximately only two thirds of these films were produced in sufficient quantities to be available for analysis at Virginia Tech. Those films, which were analyzed structurally, are listed with their respective key processing parameters in Table 3.1. The following nomenclature will be used throughout the rest of the chapter when referring to a specific film; ##-##-X, where the first two digit number refers to the FLH, in cm, the second two digit number refers to the film gauge, in microns, and the final letter refers to the resin used, HDPE-A or B. Thus, a film produced using resin HDPE-B at a FLH of 23 cm to a thickness of 12.5 microns would be designated 23-12-B.

Table 3.1. Films available for morphological analysis – nomenclature, resin type, and key processing variables.

Designation	Resin	Frost Line Height (cm)	Gauge (μm)
38-12-A	HDPE-A	38	12.5
54-12-A	HDPE-A	54	12.5
23-20-A	HDPE-A	23	20
38-20-A	HDPE-A	38	20
54-20-A	HDPE-A	54	20
23-12-B	HDPE-B	23	12.5
38-12-B	HDPE-B	38	12.5
54-12-B	HDPE-B	54	12.5
23-20-B	HDPE-B	23	20
38-20-B	HDPE-B	38	20
54-20-B	HDPE-B	54	20

3.4 Resin Characterization

As briefly stated in the opening section of this chapter, one of the major variables of interest to this study was the influence of MWD on the ability of a given resin to form unique, orthogonal lamellar stacks. Two resins were studied, both belonging to the general class of HDPEs. Numerical results of the GPC analysis are summarized in Table 3.2. A cursory examination of the numbers shows that HDPE-A has larger values for the first three moments (M_n, M_w, and M_z) of the molecular weight distribution. These results clearly indicate that HDPE-A is of higher molecular weight than HDPE-B. Of additional importance are the polydispersity indices (PDI). Note that while HDPE-B has a slightly larger M_w/M_n ratio (22.0 vs. 19.5), HDPE-A clearly has a larger M_z/M_w ratio (11.2 vs. 6.3). It appears that HDPE-A contains a larger fraction of high molecular weight material (chains of molecular weight greater than M_w) than HDPE-B. Putting these two factors together, it is evident that HDPE-A has both a greater M_w, and a high molecular weight tail which is more substantial than that of HDPE-B. Thus, if no long chain branching (LCB) is present, it is expected that HDPE-A will be the more slowly relaxing resin, and hence be the resin most likely to form highly oriented structures under flow.

Quantification of the relaxation characteristics of the two resins was conducted using dynamic oscillatory parallel plate rheometry. As briefly addressed in the introductory material, it is expected that the degree of orientation obtained in a given film will be a strong function of the level of orientation present in the melt at the time of crystallization. This melt orientation level should be related to the imposed process stresses and the rate of molecular relaxation. A measure of this second factor can be obtained through rheological measurements. Complex viscosity frequency sweep data are presented in Fig.3.4 for each resin. Examining the shapes of the flow curves it becomes apparent that HDPE-A has both a broader MWD (evident by its less sharp transition into shear thinning behavior), and a greater M_w than HDPE-B. These observations can be quantified by fitting the data to a suitable viscosity function. The Carreau-Yasuda (C-Y) model was used in this instance. A full description of the model and its parameters was provided earlier in the literature review section.

Table 3.2. Molecular weight characteristics of resins. Note that HDPE-A has a greater M_w, M_z and M_z/M_w, suggesting that it contains a greater portion of high molecular weight material than HDPE-B.

Resin	M_n (kg/mol)	M_w (kg/mol)	M_z (kg/mol)	PDI (M_w/M_n)	PDI (M_z/M_w)
HDPE-A	19	368	4800	19.5	11.2
HDPE-B	14	307	2180	22.0	6.28

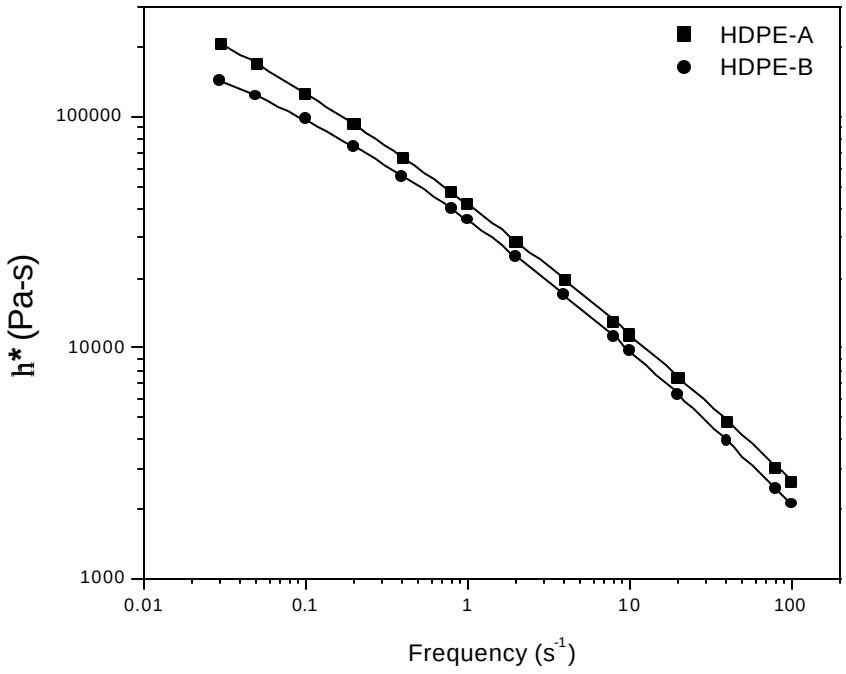

Figure 3.4. Complex viscosity versus frequency data obtained at 190C for each resin (data points). Solid lines represent data fit using the Carreau-Yasuda model. This region of flow behavior clearly shows that HDPE-A is of greater M_w and has a broader MWD than HDPE-B.

Briefly recapping, the C-Y model contains five adjustable parameters which are used to fit the data. In the fitting of PE data it is common practice to fix two of the variables (n, η_∞) leaving only three adjustable[30]. These three parameters are the zero shear viscosity, η_0, the average terminal relaxation time, τ, and the shear thinning transition breadth, a. Table 3.3 summarizes the obtained parameters for the two resins studied. The parameter of greatest interest here is τ, which provides a measure of the average terminal relaxation time associated with the melt. It can be seen that the model assigns HDPE-A a greater value of τ (19.6 seconds for HDPE-A versus 4.8 seconds for HDPE-B). Thus, the earlier statement, that HDPE-A is the slower relaxing material, appears to be justified by the complex viscosity results.

Two qualifications must accompany the above observation. These data are only representative of the relative viscoelastic respsonses of the resins at 190 °C and under dynamic shear deformation. It is recognized that a wide range of temperatures are experienced during the blowing process. Furthermore, the dominant mode of deformation in the melt will be that of extension. The sensitivity of viscosity to temperature should be similar for the two resins if they have nearly identical chain topology. Thus for equivalent MWD's, if the levels of LCB in the two resins are very similar, the viscoelastic trends obtained at 190 °C using shear should hold at other temperatures as well. To determine if the levels of LCB were indeed comprable additional analysis to quantify the LCB content in each resin was conducted using the method of Janzen[31]. This model, based primarily on ascribing deviations in zero shear viscosity from the theoretical value for a completely linear chain of given molecular weight, determined the levels of LCB to be 0.02 and 0.008 branch points per 10,000 carbons for HDPE-A and HDPE-B respectively. By this analysis both resins appear to be essentially linear. Considering the lack of LCB, if the two resins had identical MWD's it would be expected that the relative response in shear would hold in extension as well. However, the GPC data demonstrated that HDPE has a greater M_z. Thus, the slower relaxation rate of HDPE-A (or greater propensity to orient) revealed by the shear measurements may be even more pronounced in extension.

Table 3.3. Carreau-Yasuda model parameters for resins studied obtained using dynamic parallel plate shear rheometry. Note the substantially longer characteristic terminal relaxation time of HDPE-A relative to HDPE-B.

Resin	η_0^* (Pa-sec)	τ_0 (sec)	a
HDPE-A	3.4E+06	19.6	0.19
HDPE-B	4.9E+05	4.8	0.30

Based on the GPC and rheological results HDPE-A will be considered to be the more slowly relaxing resin due to its greater M_w and apparently larger high molecular weight tail for all further discussions.

3.5 Morphological Characterization

3.5.1 Flat Plate WAXS results

The state of amorphous and crystalline orientation is known to have a profound effect on the properties of polymeric materials, and can vary widely based upon the processing conditions used. The determination of crystalline orientation, independent of amorphous orientation, is possible using x-ray scattering. Birefringence, a method which depends on both the crystalline and amorphous phases, cannot independently separate the effects arising from each phase. The combination of birefringence and WAXS results have been employed to overcome this problem by several researchers, thought the results have not been conclusive[9,12]. For these reasons the focus of this study will be placed solely upon the deduction of crystalline orientation.

The first series of WAXS patterns for examination is presented in Fig.3.5. This series consists of the range of FLH's studied for HDPE-A at 20 μm thickness. (samples 23-20-A, 38-20-A, 54-20-A). To seasoned observers of PE WAXS patterns, these exposures may appear unusual. In this figure, as well as the next, Fig.3.6, the film was purposely moved closer to the sample than typical so as to fully capture the (020) reflection. Additionally, the film was exposed for a time period such that the (020) reflection was very clear, even though this resulted in an overexposure of the stronger (200) and (110) reflections. The (020) reflection was chosen as a key structural parameter because it is associated with the b-axis of the polyethylene unit cell. Recall from the literature review section that according to the Keller-Machin model, lamellar growth occurs primarily along the direction of the b-crystallographic axis, perpendicular to the direction of imposed stress. Thus, the orientation of the crystal b-axis should be an indirect indicator of the orientation state of any fibril nuclei present during crystallization. The WAXS pattern of the lowest FLH film shown in Fig.3.5, 23-20-A, displays what can be considered a pattern typical of a film uniaxially oriented along the MD.

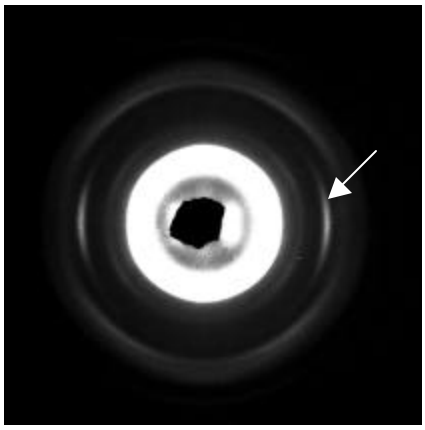

[23-20-A]

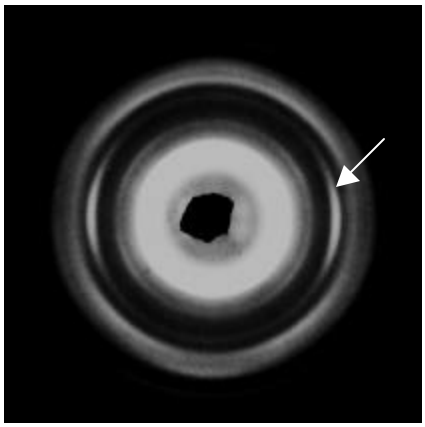

[38-20-A]

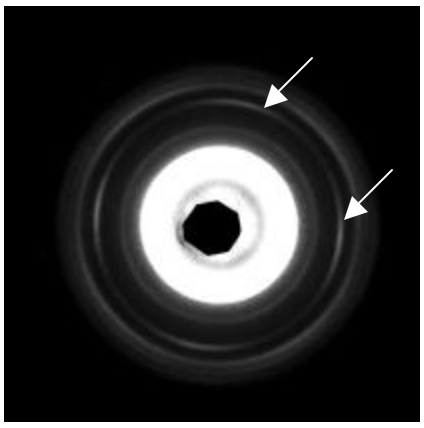

[54-20-A]

Figure 3.5. WAXS patterns for films of HDPE-A of 20 μm thickness. FLH's from top to bottom are 23, 38, and 54 cm respectively. MD is vertical, TD horizontal. Note that at the lowest FLH a two point (020) reflection is observed while at the highest FLH a four point pattern is noted. Arrows indicate (020) reflection.

The (020) reflection appears on the equator indicating its preferential orientation perpendicular to the MD. Also, note the lack of any intensity due to the (020) plane in the TD. This pattern will heretofore be referred to as a two point b-axis WAXS pattern. Moving to the next highest FLH, sample 38-20-A, it is observed that the (020) reflection has become somewhat broader (less variation in intensity along the azimuthal angle). Furthermore, a faint band of intensity due to the (020) plane can be noted along the MD. These results indicate that the level of "b" axis orientation has decreased as the FLH was increased. Such a result is entirely expected as increasing the FLH should provide additional time for molecular relaxation (loss of some orientation of the chains in the melt). Moving to the final pattern of Fig.3.5, 54-20-A, a quite striking change has occurred. Rather than simply observing a further decrease in "b" axis orientation, the (020) reflection now demonstrates distinct maxima along both the MD and TD. This pattern will hereafter be referred to as a four point b-axis WAXS pattern. This four point b-axis WAXS pattern strongly suggests the presence of a bimodal population of orthogonaly oriented crystals, possibly similar in structures to those observed directly via microscopy in Fig.3.1. An in-depth discussion of the factors which lead to the formation of this orientation at the highest FLH studied will be undertaken after the morphological characterization section.

The next set of WAXS patterns presented in Fig.3.6. is of HDPE-B films (23-20-B, 38-20-B, 54-20-B) processed under identical conditions as those discussed in Fig.3.5. As with the previous set, at the lowest FLH a uniaxial orientation about the MD is present. Increasing the FLH is seen to cause a decrease in the level of orientation as noted by the (020) reflection. At the highest FLH, 54-20-B, it is difficult to ascertain if a four point b-axis WAXS pattern is present. It is clear, however, that the (020) intensity occurs around the entire azimuth with intensity maxima along the equator. These results suggest that HDPE-A may more readily form sharply bimodal orientation states than HDPE-B under these same processing conditions. This further implies that the presence of high molecular weight material may be necessary for the formation of the distinctly bimodal HDPE-A orientation.

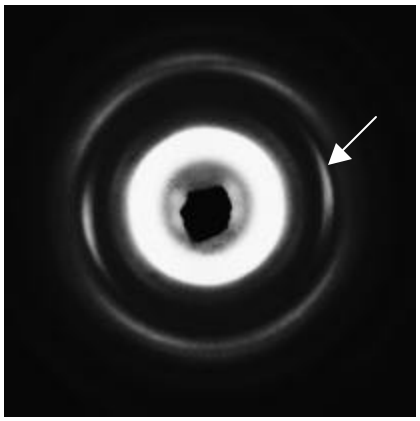

[23-20-B]

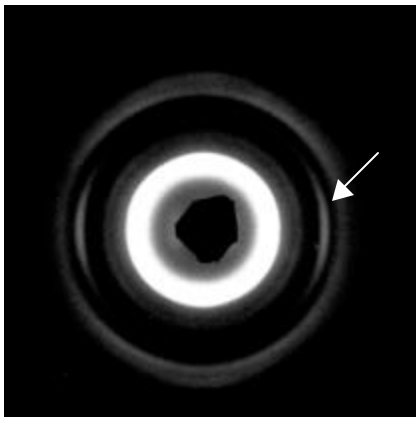

[38-20-B]

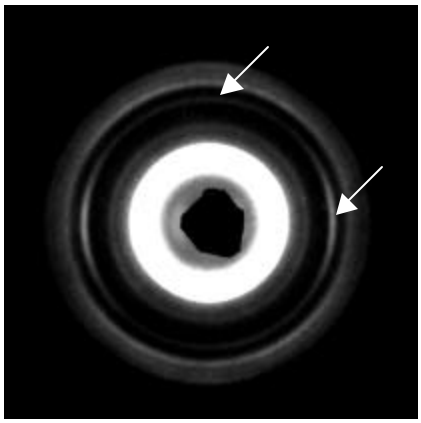

[54-20-B]

Figure 3.6. WAXS patterns for films of HDPE-B of 20 μm thickness. FLH's from top to bottom are 23, 38, and 54 cm respectively. MD is vertical, TD horizontal. Orientation of (020) plane can be seen to decrease with increasing FLH. Arrows indicate (020) reflection.

If the melt relaxation times are related to the formation of the bimodal orthogonal crystalline orientation, theoretically it should be possible to compensate for HDPE-B's lack of high molecular weight material by increasing the process stresses (decreasing processing time). By altering the process such that less time is given for relaxation it may be possible to make the shorter chains of HDPE-B behave similarly to the longer chains present in HDPE-A. Stated in an alternate manner, using the Deborah number concept (see literature review for details), it may be possible to achieve the same time scaling present for HDPE-A processed to a film thickness of 20μm in HDPE-B by offsetting its shorter relaxation time with an equally shorter processing time. By holding the extruder output constant while increasing the haul off rate, a thinner film with a shorter processing time will be produced. Such conditions were employed to produce the 12.5μm thick films of HDPE-B presented in Fig.3.7. As in both previous examples, at the lowest FLH a two point WAXS pattern of the (020) reflection is noted, indicative of a uniaxial orientation along MD. Increasing the FLH to the intermediate value, 38-12-B, results in a decrease in the degree of b-axis orientation relative to the MD. Finally, at the highest FLH, 54-12-B, the four point b-axis WAXS pattern has returned. Thus, it can be seen that the ability to form an orthogonal, bimodal orientation state is not a characteristic which can be attributed solely to HDPE-A. However, the conditions necessary for the formation of such structures can be seen to depend greatly on the relaxation characteristics of the resin as is expected. Further support for this statement can be found in the WAXS patterns for HDPE-A processed to a thickness of 12.5 μm as shown in Fig.3.8. As with the previous HDPE-A sample, the 38 cm FLH sample does not show a four point WAXS pattern while the 54 cm FLH samples does. It is also of interest to note that at the medium FLH, the thinner gauge sample, 38-12-A, shows greater (020) orientation relative to the MD than the thicker sample, 38-20-A, as expected, because of the increase in MD draw down used to achieve the given thickness levels.

The WAXS results clearly indicate that both resins, under the appropriate conditions, may produce films with biaxial orientation. Furthermore, the orientation state appears to be bimodal in nature. Two distinct modes (maxima) occur in the (020) reflection, one along the MD, the other along the TD.

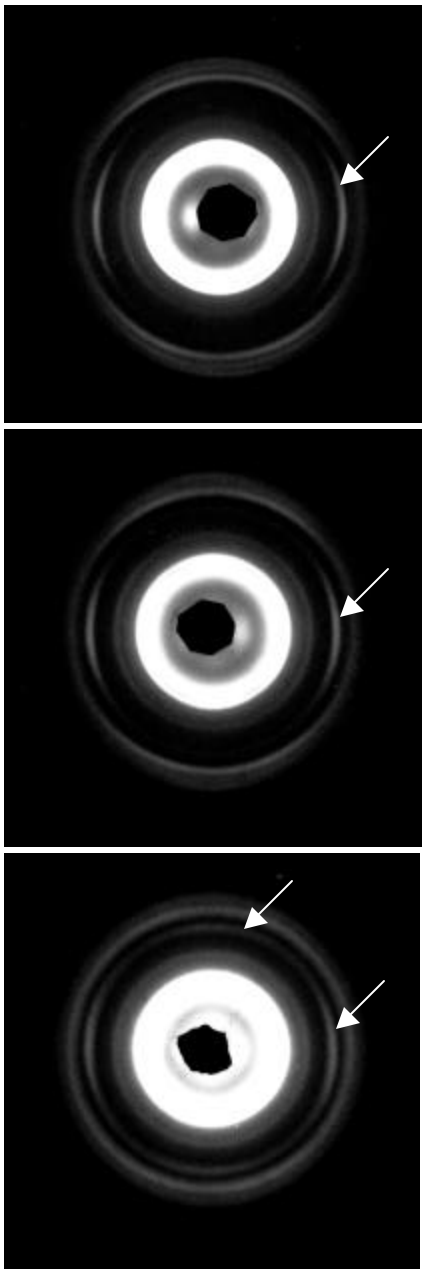

Figure 3.7. WAXS patterns for films of HDPE-B of 12.5 μm thickness. FLH's from top to bottom are 23, 38, and 54 cm respectively. MD is vertical, TD horizontal. Note that at the lowest FLH a two point (020) reflection is observed while at the highest FLH a four point pattern is noted. Arrows indicate (020) reflection.

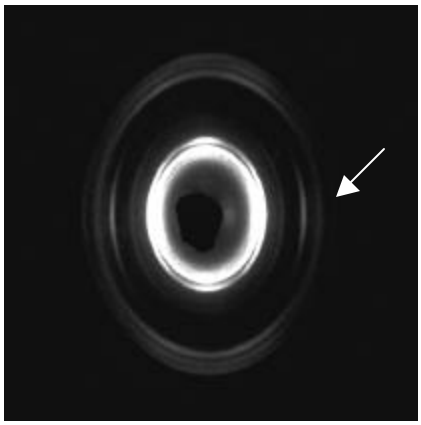

[38-12-A]

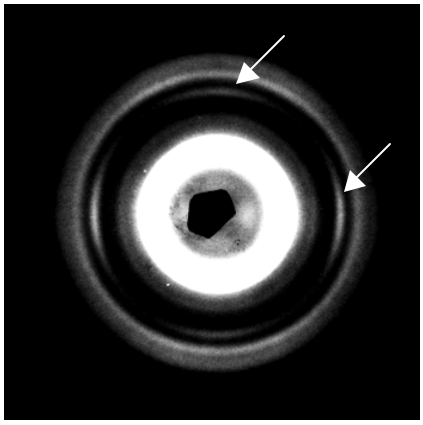

[54-12-A]

Figure 3.8. WAXS patterns for films of HDPE-A of 12.5 μm thickness. FLH's are 38 cm (upper) and 54 cm (lower). Note two point pattern at lower FLH but four point pattern at the higher for the (020) plane. Arrows indicate (020) reflection.

Comparing the azimuthal dependence of the (020) reflections demonstrates that the distribution of orientation states of the "b" axis appears to be more narrowly defined in the HDPE-A films relative to the HDPE-B films.

Of additional mention, close examination of the WAXS patterns reveals an additional difference between the resins. The width of the observed reflections, the line breadth, of the patterns is smaller in the HDPE-A films than those of the HDPE-B films. While it is difficult to assign a single factor for differences in line breadth in polymeric materials, this observation suggests that the crystallites formed in HDPE-A may be larger and/or posses greater long range order.

3.5.2 Two dimensional SAXS results

WAXS results cannot describe the structures within which these bimodal crystalline populations exist. To determine if the noted orientation is due to the formation of orthogonally aligned stacks of lamellae, a technique which probes structure at a larger length scale must be used. A direct method to detect the presence of such structures can be obtained from SAXS. Whereas WAXS yields information regarding the orientation of the crystalline unit cell, SAXS provides information from scattering structures with dimensions of the order of lamellar thickness. By obtaining the SAXS data in two dimensions, it is possible to deduce the state of lamellar orientation. SAXS measurements corresponding to the films analyzed in Fig.3.5, are presented in Fig.3.9. As with the WAXS patterns, the presence of orthogonally stacked lamellae should be indicated by a four point SAXS scattering pattern. However, in SAXS the direction of scattering will be rotated 90° relative to the WAXS patterns. That is, whereas the b-axis, (020), reflection for material stacked along the MD is found at the equatorial regions of the scattering pattern, MD stacks of lamellae will lead to scattering along the meridian of the SAXS pattern. Thus, it is clear from the sample at the lowest FLH (23-20-A) in Fig.3.9 that a uniaxial orientation of lamellar stacks along the MD is present. This is in harmony with the earlier WAXS results.

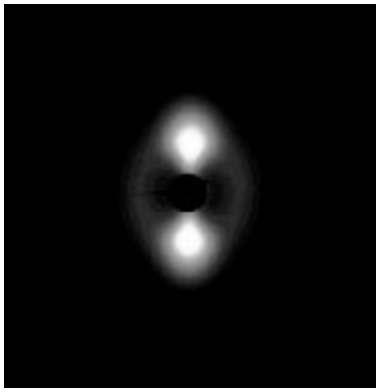

[23-20-A]

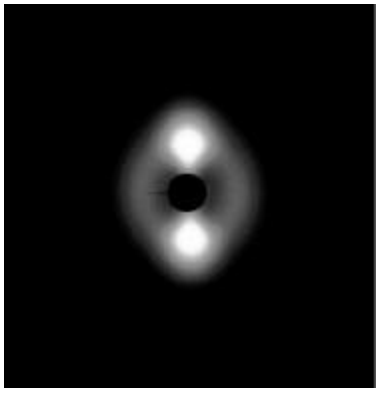

[38-20-A]

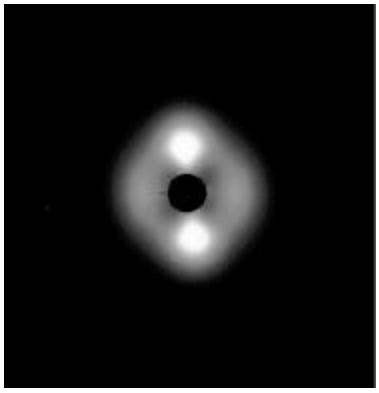

[54-20-A]

Figure 3.9. SAXS patterns for films of HDPE-A of 20 μm thickness. FLH's from top to bottom are 23, 38, and 54 cm respectively. MD is vertical, TD horizontal.

As with the previous WAXS results it can be seen that increasing the FLH leads to an apparent decrease in the orientation of the lamellae. Additionally, at the highest FLH (54-20-A) a four point SAXS pattern is noted. This pattern clearly shows the presence of lamellar units stacked along *both* the MD and TD. Based on the relative intensities at the equator and meridian, it is clear however, there is a greater portion of material stacked along the MD. The equivalent films for HDPE-B are presented in Fig.3.10. The lowest FLH, 23-20-B, displays a uniaxial ordering of the lamellae along the MD. Similar to the behavior of HDPE-A, the intensity along the equatorial region of the scattering pattern can be seen to increase with increasing FLH. However, it is clear from the patterns in Fig.3.10. that the equatorial scattering produced by HDPE-B under these conditions is not as sharp as that of the equivalent HDPE-A film. The lack of a clearly definable maximum in intensity along the equator may be indicative of TD stacked lamellae which do not have the same long range order (i.e. shorter stacks) as found in the HDPE-A films. The comparative diffuseness may also be the result of a different orientation state in the HDPE-B films relative to HDPE-A. It is possible that the film 54-20-B posses a more homogeneous planar orientation within the film plane, characterized by a small preference for orientation of the lamellar stacks along the MD and TD (planar-balanced). In contrast, the orientation state of 54-20-A may also be described as planar, but consisting of two very distinct populations of lamellar stacks, one along the MD and another along the TD (planar-bimodal). A schematic comparing these orientation states is given in Fig.3.11.

Based on the previous WAXS results, which considered the effect of processing to a thinner gauge on orientation, it is expected that the SAXS patterns for the 12.5 μm films should be sharper than those of the 20 μm films just discussed. Indeed, this is the case for the HDPE-B films as shown in Fig.3.12. In accordance with the WAXS results, the SAXS equatorial scattering intensity is observed to increase with increasing FLH. The scattered intensity along the equator in the highest FLH film, 54-12-B, is quite substantial, suggesting this film has a large fraction of material stacked along the TD.

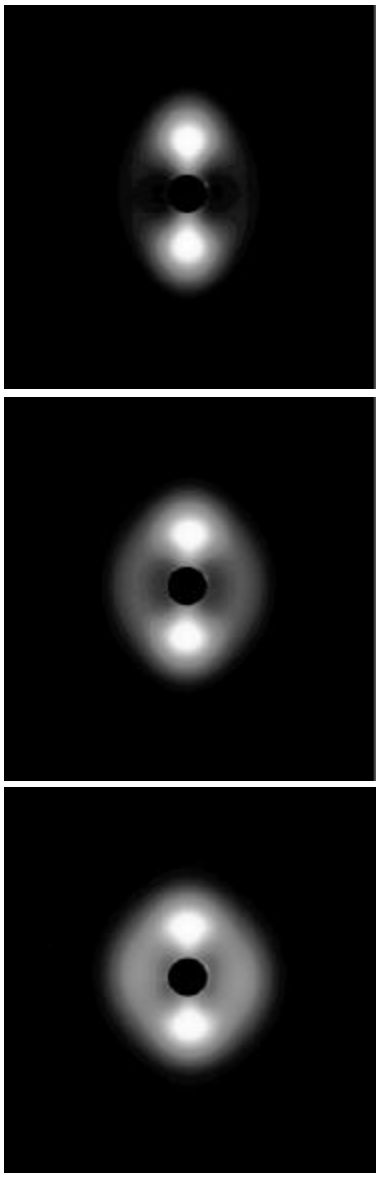

Figure 3.10. SAXS patterns for films of HDPE-B of 20 μm thickness. FLH's from top to bottom are 23, 38, and 54 cm respectively. MD is vertical, TD horizontal

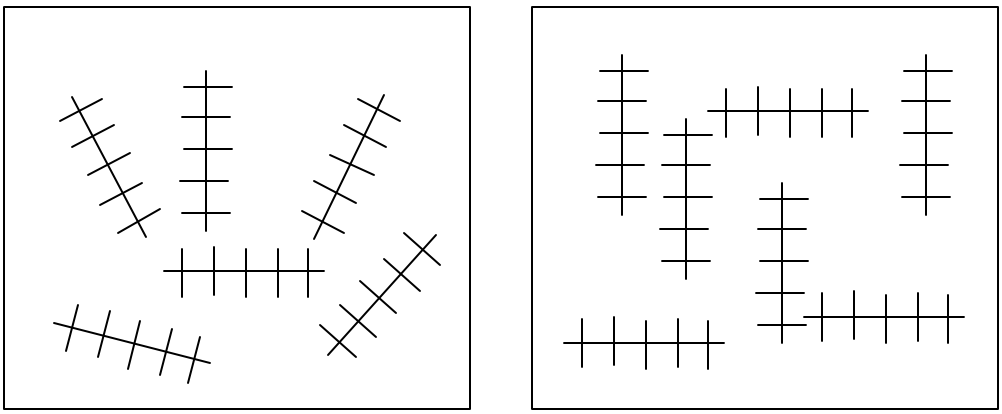

Figure 3.11. Comparison of planar-balanced (left) and planar-bimodal (right) orientation states.

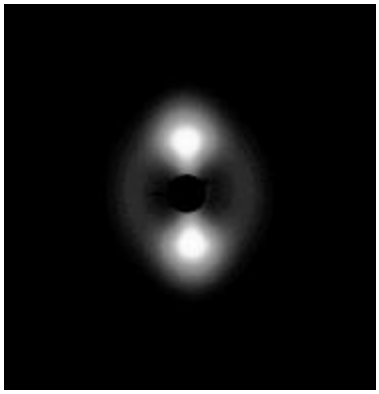

[23-12-B]

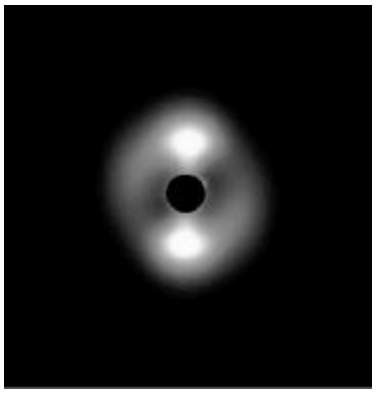

[38-12-B]

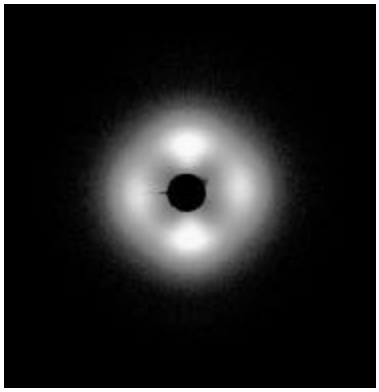

[54-12-B]

Figure 3.12. SAXS patterns for films of HDPE-B of 12.5 μm thickness. FLH's from top to bottom are 23, 38, and 54 cm respectively. MD is vertical, TD horizontal. The lack of symmetry of intensity in the 38 cm FLH sample is believed to be due to an error in the background scattering procedure.

Close examination of the pattern for film 54-12-B shows that while the equatorial scattering is very intense, the scattering maxima are not as sharply defined as those found in the HDPE-A film, 54-20-A, of Fig.3.9. This may be indicative of the balanced versus bimodal orientation argument given in the previous paragraph. Thus, the SAXS pattern for film 54-12-A should show the sharpest four point pattern of all the samples. Unfortunately, only a limited number of samples could be submitted for analysis using the synchrotron source, thus the 2D SAXS profile for film 54-12-A is unavailable. However, 1D SAXS data are available and will be used to make the necessary analysis to determine if indeed film 54-12-A shows the strongest bimodal orientation behavior.

3.5.3 One dimensional SAXS results

It is possible to obtain data which approximates those of the 2D detector using a 1D detector. Measurements are made with the 1D instrument at a series of discrete angles between the detector and an arbitrarily chosen reference axis for the film. In this case the reference axis chosen is the film MD. Scattering patterns were obtained with the film MD at 0°, 30°, 45°, 60°, and 90° with respect to the detector wire. Thus a measure of the scattered intensity as a function of both the radial and azimuthal angles was obtained. It should be noted that the data presented in the 2D patterns and that of the 1D systems will not be rigorously identical due to the differences in instrument geometry employed by the two instruments (pin hole vs. slit columnation respectively). The slit columnation employed in the 1D experiments will cause the intensity maximum to be broadened (smeared) relative to the 2D results and shifted to smaller scattering vectors.

The data of a primarily MD oriented film (23-12-B), a balanced film (54-12-B), and the film for which 2D SAXS data is unavailable, HDPE-A film (54-12-A), are given in Fig.3.13. Film 23-12-B clearly displays a sharp scattering peak parallel to the MD with decreasing intensity as the film is rotated towards the TD. These results are supported by its 2D SAXS pattern found in Fig.3.12. In contrast, film 54-12-B produces scattering which is less variable with respect to the azimuthal scattering angle. No peaks in the intensity data are noted.

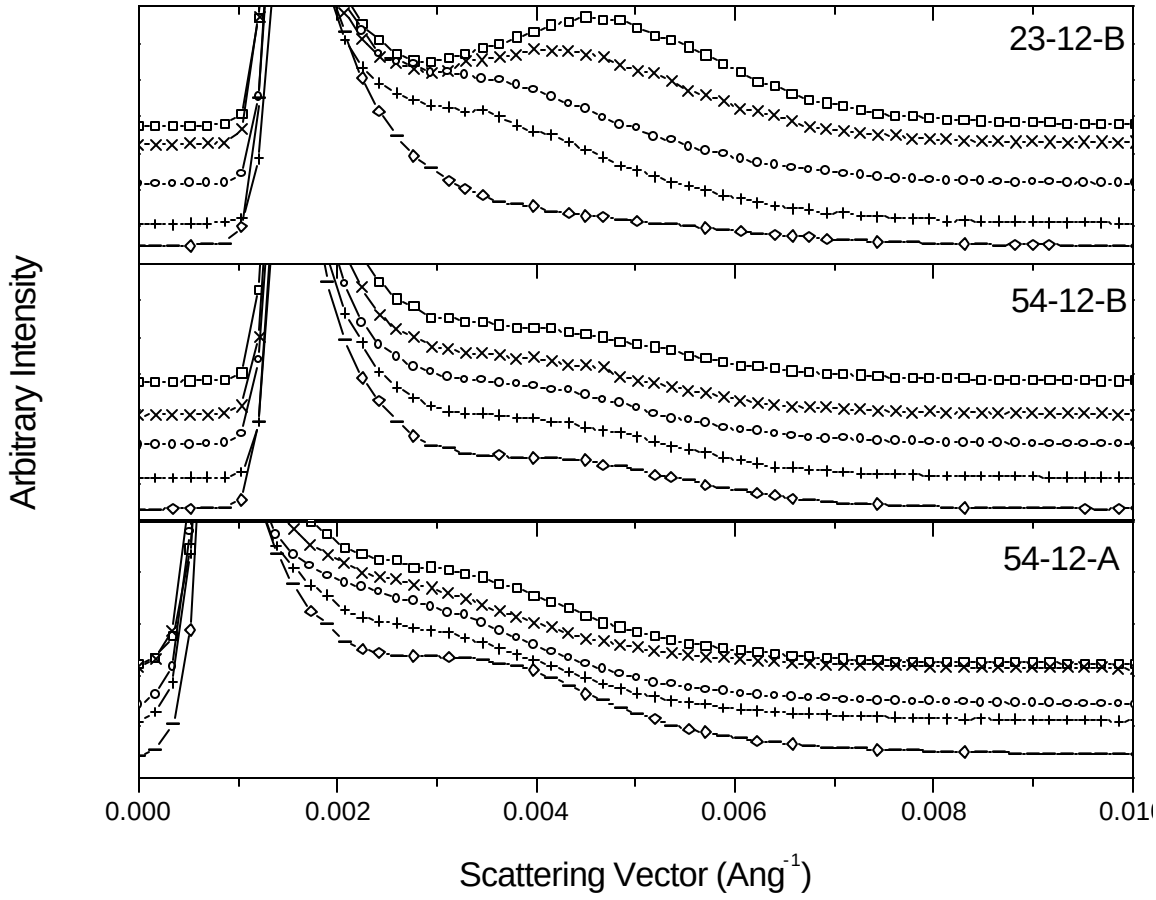

Figure 3.13. 1D SAXS patterns of selected films. Symbols represent angle between detector and film MD of ( ) 0º, (x), 30º, ( ) 45º, (+) 60º, ( ) 90º, thus 0º represents a scan along the meridian while 90º represents a scan along the equator. Note progression from top to bottom of a primarily MD stacked structures (23-12-B) to an apparent balance of MD and TD structures (54-12-B) to a slight preference for TD scattering structures (54-12-A)

Recall that film 54-12-B showed fairly uniform scattering around the azimuth in Fig.3.12. These results, as well as those for other films not shown, suggest that insight into the 2D SAXS pattern can be obtained using these 1D scan profiles. Examination of the scattering profile for film 54-12-A in Fig.3.13 suggests that it contains a majority component of TD stacked material as the scan taken along the equator (90° from the MD) shows the most pronounced peak. This result is in accordance with the behavior which was predicted based on the trends present in the 2D SAXS data. Thus, to briefly summarize, SAXS (as well as WAXS) demonstrates that increasing the FLH and/or decreasing the film gauge (assuming constant extruder output) leads to a greater proportion of lamella stacked along the TD. Furthermore, it has been observed that the tendency to form the TD stacks is greater for the higher molecular weight, slower relaxing resin (processing conditions equal). In addition, it appears that there are subtle differences in the distribution of oriented material within the film plane. The slower relaxing resin, HDPE-A, appears to form a sharply defined bimodal population of lamellar stacks. In contrast, the biaxial orientation present in the films of HDPE-B, while also bimodal in nature, is less strongly so.

3.5.4 WAXS Pole Figure results

A complete picture of the distribution of crystalline orientation within a sample can, in principle, be obtained through pole figure analysis. Because this technique was not readily available within the author's lab, and outside analysis is fairly expensive, only a limited number of films were analyzed with this technique. To facilitate the understanding of the pole figure data, a brief summary of the types of patterns obtained from uniaxial studies of polyethylene will be presented. As outlined in the literature review section, the K-M model of crystallization from the oriented melt, for PE, can be roughly divided into three categories; low stress, medium stress, and high stress. A schematic of the structures formed by the low and high stress conditions are provided in Fig.3.14. Note that the primary difference between the two conditions is the amount of lamellar twisting which occurs as the lamellae grow outwards from the nucleating fibrils.

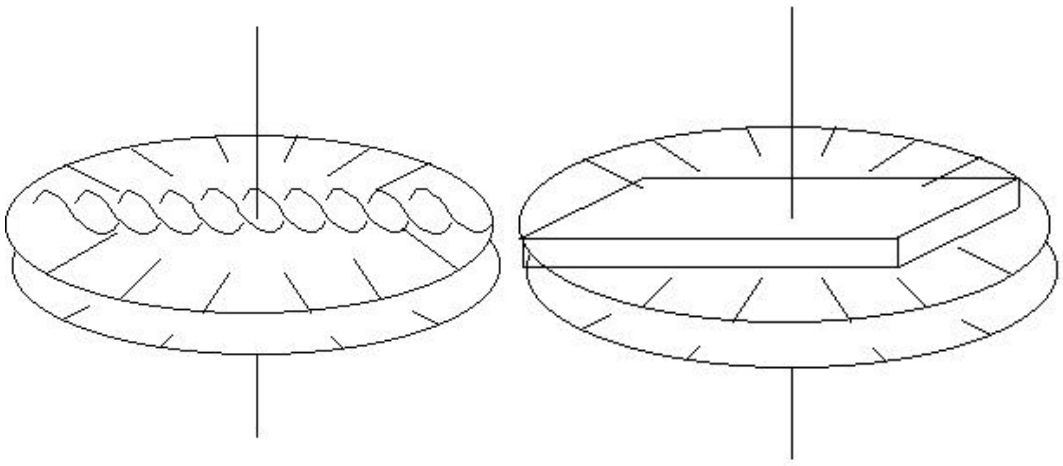

Figure 3.14. Schematic of K-M low (left) and high (right) stress morphologies, uniaxial orientation, stretch direction vertical. Representations do not account for possible differences in lamellar curvature.

It is also anticipated that substantial differences in lamellar curvature will also exist between these two extremes. This behavior is not represented in the K-M model, shown in the schematic of Fig.3.14. As an individual lamella grows out from the fibril, there is a tendency for its growth direction to deviate. Rather than remain perfectly perpendicular to the fibril, the lamella may curve. This curvature will result in a lowering of the degree of "b" axis, as well as "a" and "c" axis, orientation relative to the fibril. As the stress level increases, and the distance between fibrils decreases, lamellar curvature should become less pronounced. The medium stress condition will produce a level of twisting and curvature intermediate to the two extremes depicted.

The presence of lamellar twisting should be evident in x-ray diffraction patterns. A low stress, highly twisted system, will lead to "a" axis and "c" axis crystal orientation concentrated in the MD-ND plane. Conversely, a high stress condition should lead to a preferential orientation of the "a" axis along the ND and the "c" axis along the MD. As mentioned above, the situation is somewhat complicated by the tendency for lamellae to curve as they grow. It is expected that the amount of lamellar curvature should be least in those films crystallized under the highest stress conditions. A schematic of hypothetical (200) pole figures ("a" axis) for the low and high stress conditions are given in Fig.3.15, for a uniaxial system. Recall from the literature review section that the in a pole figure meridonal points represent MD scattering, the equatorial points represent TD scattering, and that the center of the figure is indicative of ND scattering. Note that in the low stress case that the (200) plane tends to show a preference for orientation along the MD while the high stress condition leads to a preferential orientation of the (200) plane along the TD and ND. Thus, based on the position of the (200) scattering maximum, it may be possible to deduce the relative levels of stress, or orientation, present in the films at the time of crystallization. This interpretation is dependent upon the formation of row nucleated structures. Based on the SAXS results, this assumption appears justified. Additional support will be provided by direct observation using FESEM in a subsequent section. Furthermore, because information regarding the "b" axis is also available and the unit cell of polyethylene possesses orthorhombic symmetry it should be possible to infer the state of c-axis orientation.

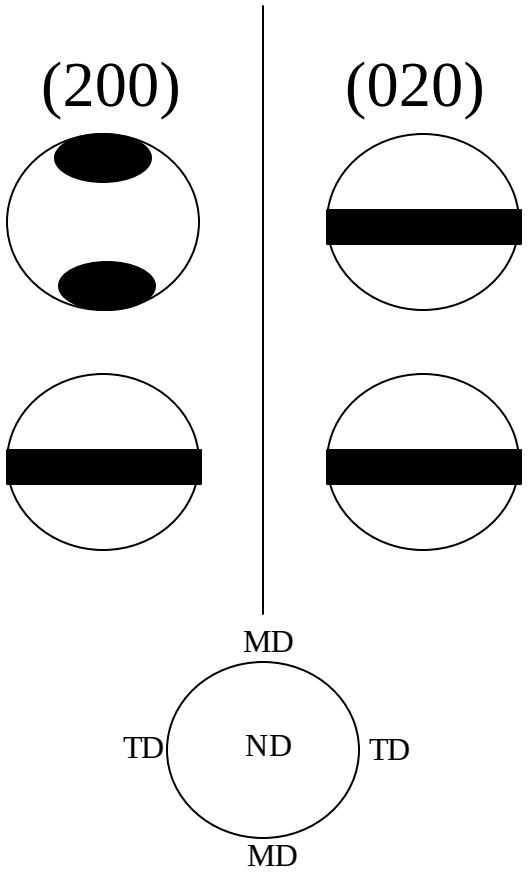

Figure 3.15. Schematic of pole figure data produced by K-M low (left) and high (right) stress conditions.

The first set of (200) and (020) pole figures presented correspond to films 23-20-A and 54-20-A, and are displayed in Fig.3.16. As expected, at the lower FLH, 23cm, a pattern typical of a uniaxial, medium stress system is obtained. The "b" axis can be observed to orient preferentially along the TD while the "a" axis is positioned between the MD and ND. Earlier results demonstrated that increasing the FLH led to the formation of a second population of lamellar stacks oriented along the TD. Evidence of this phenomena can be seen in the (200) pattern. A region of substantial scattered intensity between the TD and ND appears, in addition to the scattering found between the MD and ND. Unfortunately, in this sample, and most of the pole figure data to follow, it is difficult to infer any major information from the (020) data.

If the (020) pole figure results are to match the "four point" flat plate WAXS patterns presented earlier, two sets of distinct maxima should be present, one along MD and the other along TD, for sample 54-20-A. It should be noted that a flat plate photograph corresponds only to a small region of the data presented in the corresponding pole figure. It is thus possible that the flat plate data does not provide a full representation of the state of orientation because it samples a limited ensemble of reflecting planes. However, combining the (200) and (020) axis data provided by the pole figures to calculate the "c" axis biaxial orientation functions leads to physically impossible values for the "c" axis in two of the six samples. These results are presented in Fig.3.17 (recall that the utility of using the biaxial orientation triangle in representing orientation data was presented in the literature review). It is clearly observed that two samples lie outside of the orientation triangle, a clear indicator of suspect data. Because the (020) plane scatters relatively weakly (relative to the (200) plane) it is likely that insufficient scattered intensity was collected above the background to yield quantitatively accurate data for the (020) plane. It is for these reasons that the author will rely more heavily on the flat plate data, and only utilize the pole figure data from the (200) planes.

Returning to Fig.3.16, it can be inferred from the (200) data that increasing the FLH has led to the formation of crystalline material stacked along both the MD and TD. The corresponding films produced using the more rapidly relaxing resin, HDPE-B, are presented in Fig.3.18.

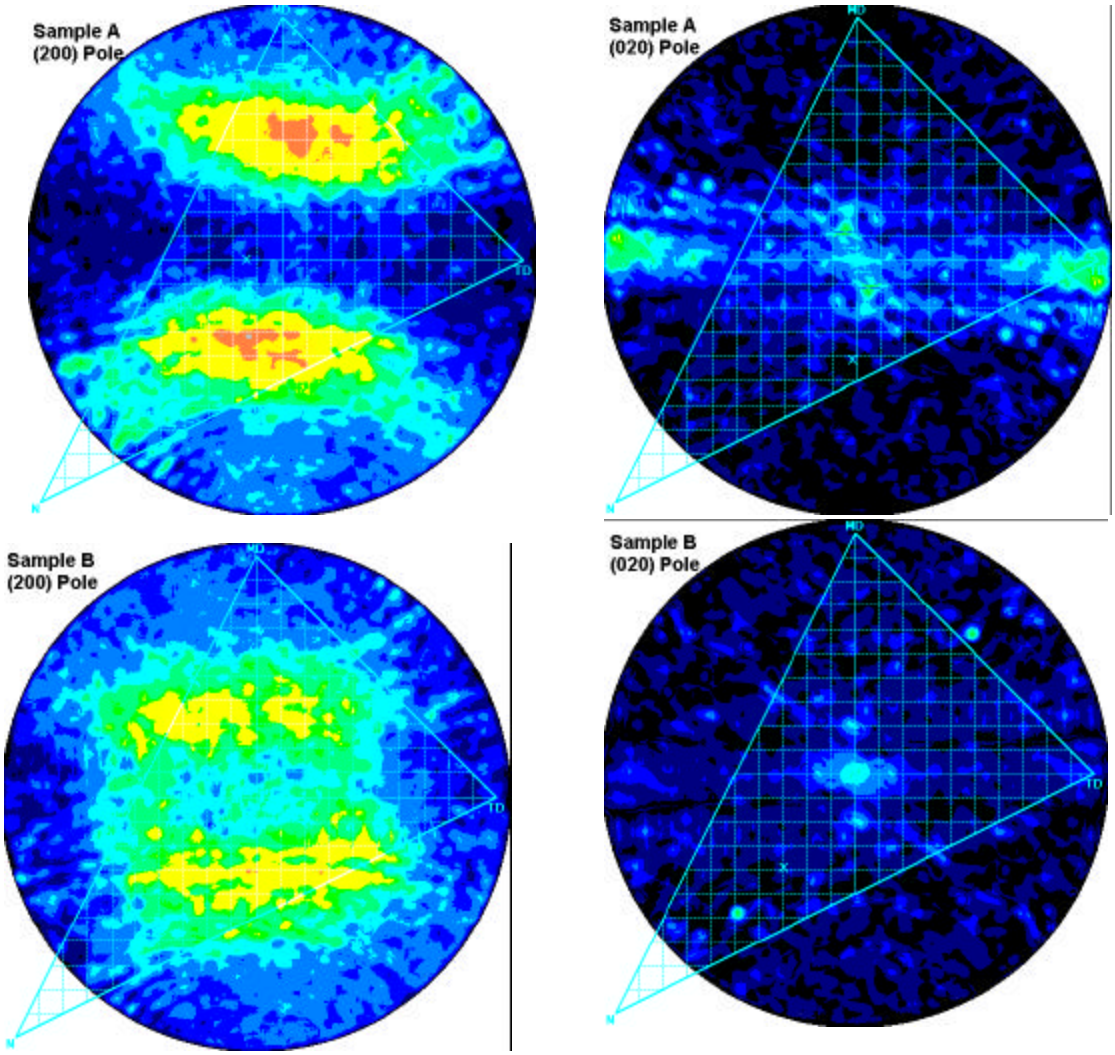

Figure 3.16. (200) left, and (020) right, pole figures for films 23-20-A, upper, and 54-20-A, lower.

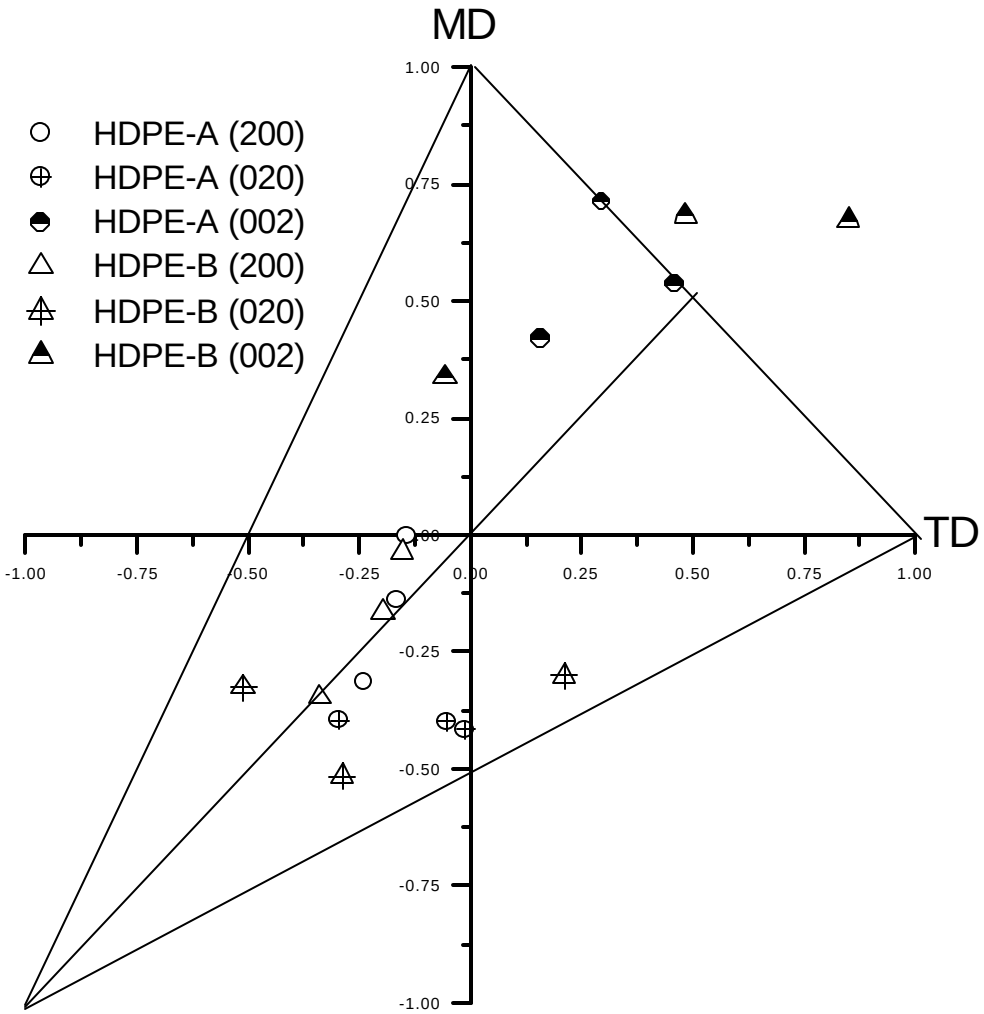

Figure 3.17. White-Spruiell biaxial orientation for selected films as derived from pole figure data. Note that in two instances c-axis data falls outside of the orientation triangle suggesting errors in the original data. See text for discussion.

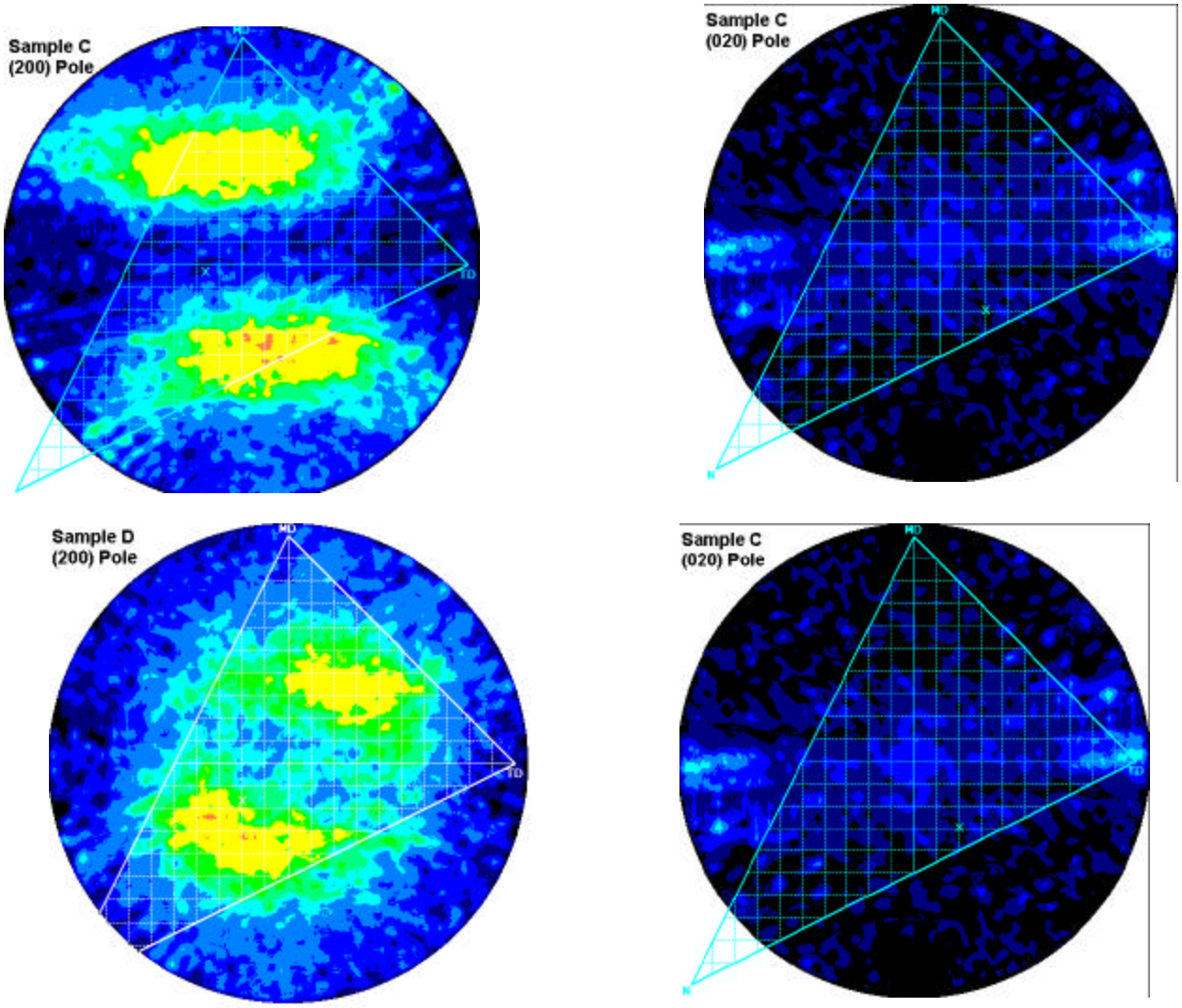

Figure 3.18. (200) left, and (020) right, pole figures for films 23-20-B, upper, and 54-20-B, lower. The (200) pole figure for film 54-20-B appears to be skewed due to misalignment during testing, pattern should be rotated roughly 30º counter clockwise to obtain correct orientation of scattering pattern relative to MD and TD.

The results are similar (note that the (200) pole figure for film 54-20-B appears to be skewed, likely due to misalignment during testing by AMIA labs personnel – the pattern should be rotated ~30° counter clockwise to obtain the correct orientation relative to MD and TD). A uniaxial orientation along MD is noted at the lowest FLH from both the (200) and (020) planes. At the FLH of 54 cm the (200) data shows the emergence of material which is oriented along the TD, as anticipated. Comparing the (200) data for the 54 cm FLH's in Fig.3.16 and Fig.3.18 it can be seen that the amount of TD stacked material appears to be greater for HDPE-A relative to HDPE-B. This result is in agreement with SAXS and flat plate WAXS results.

The final set of pole figure data, Fig.3.19, compares the two resins processed at the greatest FLH to the thinnest gauge: 54-12-A and 54-12-B. Recall that these conditions produced films which displayed the greatest amount of TD stacked material for each resin. Of immediate note is the dramatic level of ND "a" axis orientation. Orientation of the (200) plane along the ND corresponds to a high stress crystallization level according to the K-M model. Thus, it appears that processing to a thinner gauge (12.5 μm relative to 20 μm in the previous two figures) leads to higher stresses. This is entirely expected as the thinner gauge was achieved by increasing the draw down rate while keeping extruder output constant. The greater degree of symmetry of scattered intensity about the ND for HDPE-B relative to HDPE-A suggests, in accordance with the SAXS and flat plate WAXS results, that a more balanced in-plane orientation is achieved with HDPE-B.

In summary, the pole figure data of the (200) plane corresponds well with previous WAXS and SAXS results, *increasing the FLH leads to the development of a second population of material oriented along the TD.* The sharpness of the bimodality appears to be greater for the more slowly relaxing resin, HDPE-A. Additionally, down gauging by increasing the draw down rate for a fixed extruder output is seen to increase the level of stress present at the time of crystallization. The (020) pole figure data are supportive of earlier results in select instances. It is believed that this inconsistency is a result of the poor quality of the (020) pole figure data (due to insufficient collection time) in certain samples, and thus does not conflict with the structural interpretation put forward.

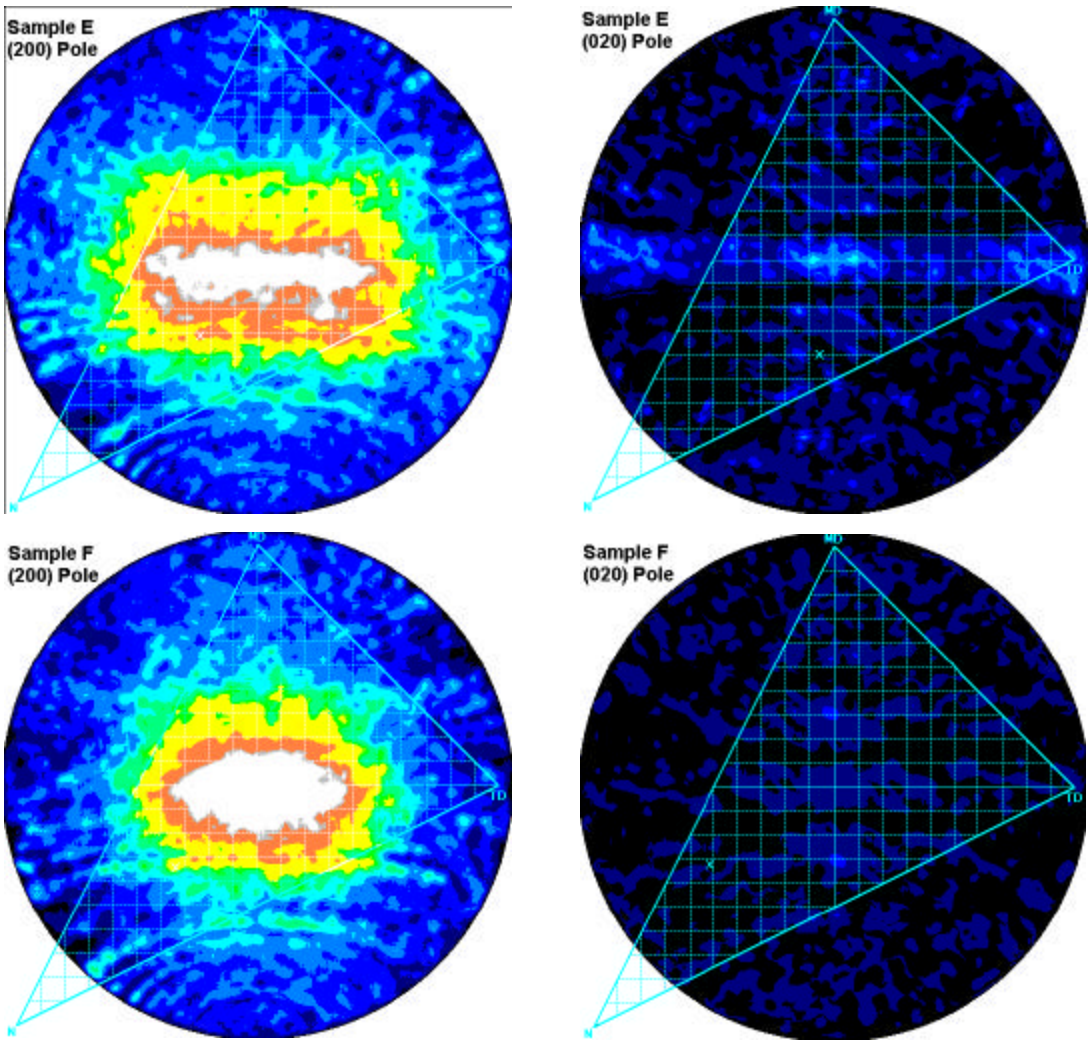

Figure 3.19. (200) left, and (020) right, pole figures for films 54-12-A, upper, and 54-12-B, lower.

3.5.5 FESEM results

A direct observation of the films' morphology can be obtained using FESEM. However, possibly as a surprise to the reader, this technique was not used as a primary source of information for two reasons. FESEM only provides a picture of the surface morphology. No information about the structures present within the film bulk can be deduced. The use of x-ray scattering experiments, which sample the entire film, were favored for this reason. Secondly, early results showed that on the level of microscopic observation (a viewing window on the order of 20x20 μm) considerable heterogeneity existed. Thus, obtaining images that were demonstrative of the sample as whole required a large number of images to be acquired and substantial subjective interpretation as to which were representative. For these reasons, while the FESEM images provide validation of the scattering results, they were relegated to a supportive role.

The micrographs for 20 μm films of HDPE-A are presented in Fig.3.20. The trend is clear, as the FLH is increased, a greater portion of the stacked material is oriented along the TD. It was not possible to draw a quantitative conclusion regarding the extent of intermeshing between the orthogonal stacks. That is, a consistent observation of the degree to which orthogonal lamellae overlapped or intersected could not be obtained. In some of the micrographs to follow, the lamellar stacks appear to form distinct domains of MD or TD stacked material with very little "mixing" in contrast to those of Fig.3.20. The corresponding HDPE-B films are shown in Fig.3.21. For this series of micrographs it again demonstrates that the amount of TD stacked material increases as the FLH is increased. The down gauged (12.5 μm thick films) of HDPE-B are shown in Fig.3.22. Again, the trend is consistent, increasing FLH leads to a greater amount of TD stacked material. Based on the qualitative nature of the micrographs no attempt to compare the relative amounts of TD stacked material for the different thicknesses was attempted. The final pair of films in the series correspond to 12.5 μm thick films of HDPE-A which are presented in Fig.3.23. Recall that at the lowest FLH condition, a stable bubble could not be formed, thus no data is available. As with the other films, increasing the FLH leads to a greater fraction of material oriented along the TD.

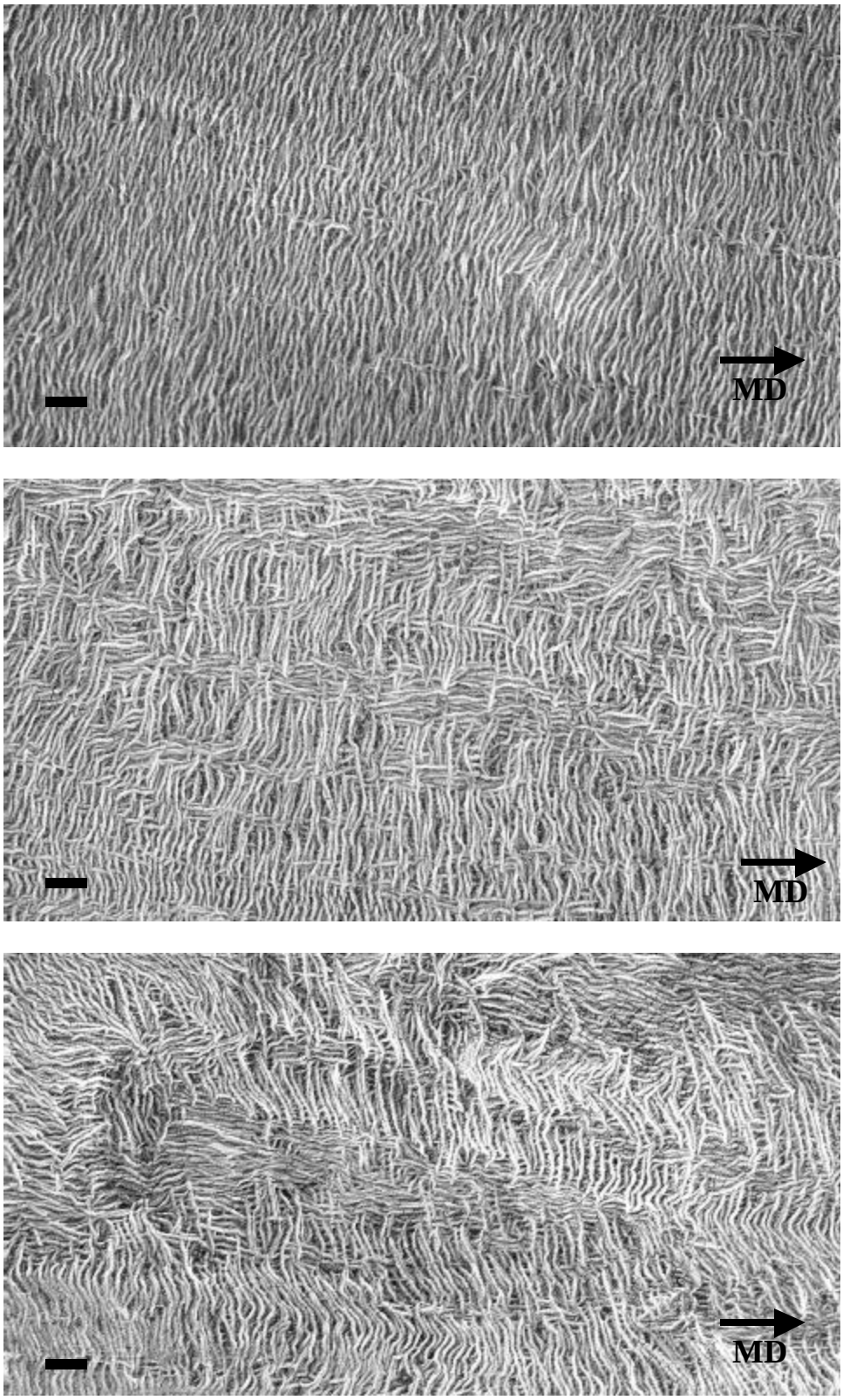

Figure 3.20. FESEM micrographs for films 23-20-A, 38-20-A, and 54-20-A from top to bottom respectively. MD horizontal, TD vertical. Scale bar length 200 nm.

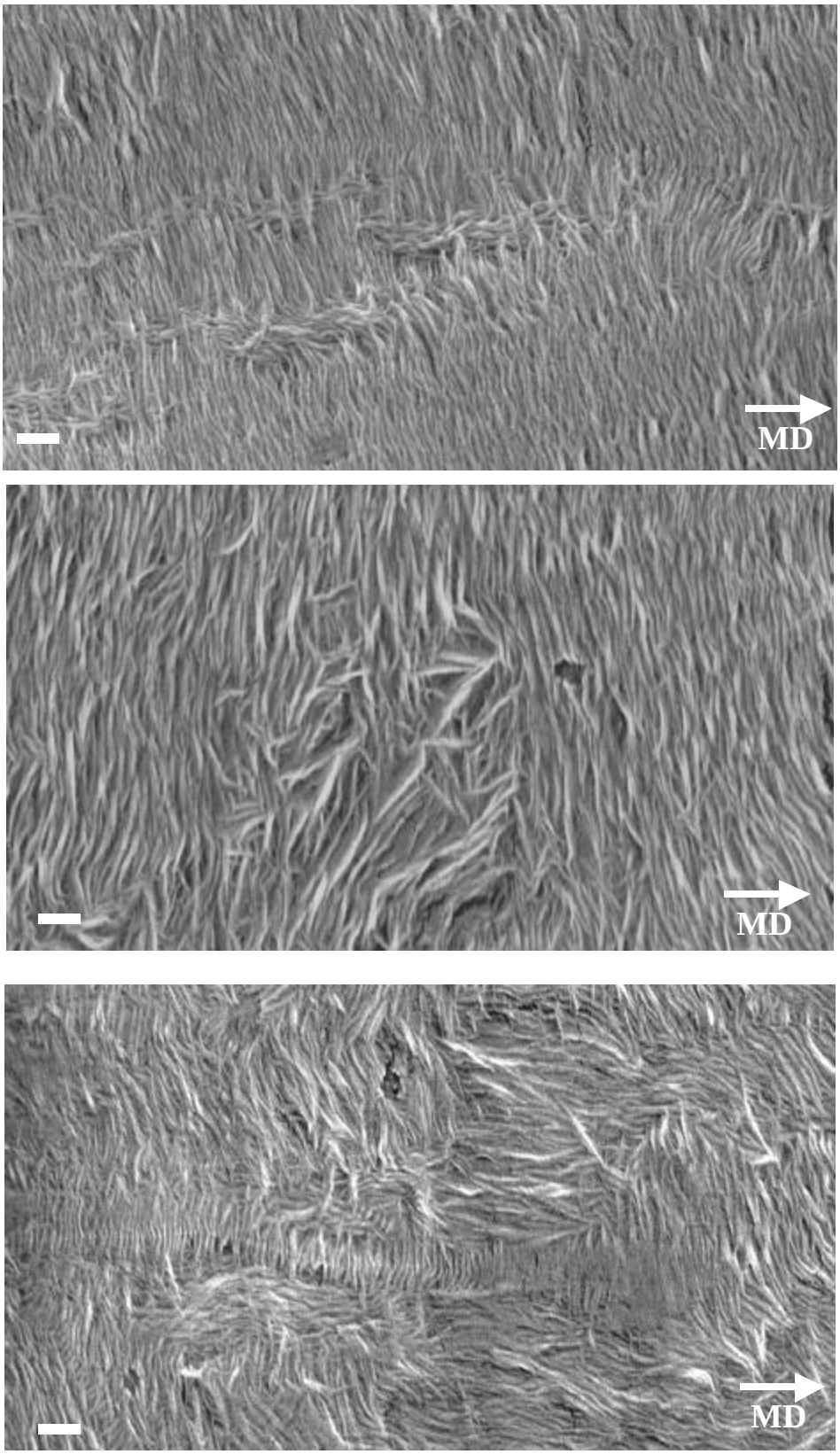

Figure 3.21. FESEM micrographs for films 23-20-B, 38-20-B, and 54-20-B from top to bottom respectively. MD horizontal, TD vertical. Scale bars 200 nm

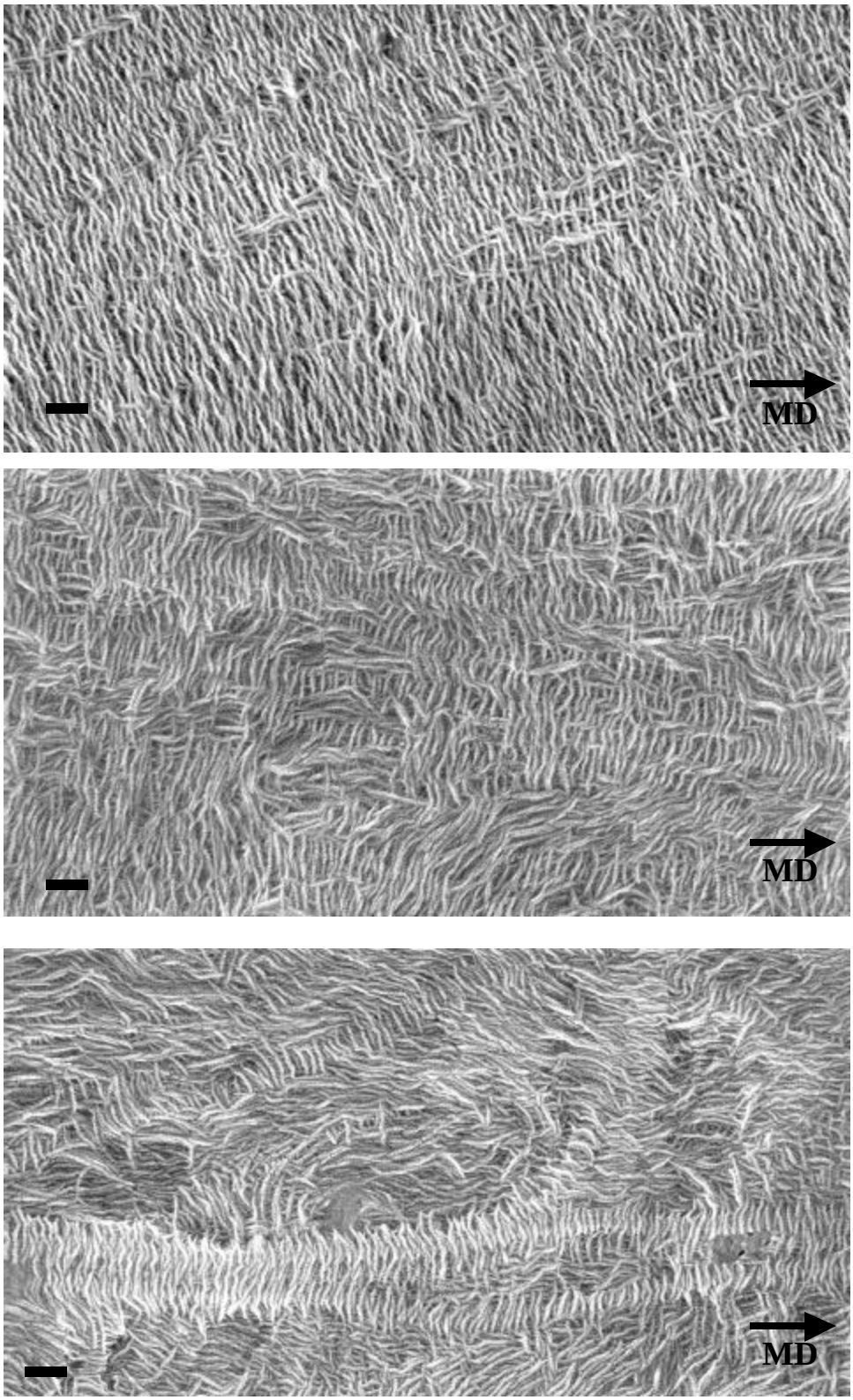

Figure 3.22. FESEM micrographs for films 23-12-B, 38-12-B, and 54-12-B from top to bottom respectively. MD horizontal, TD vertical. Scale bars 200 nm.

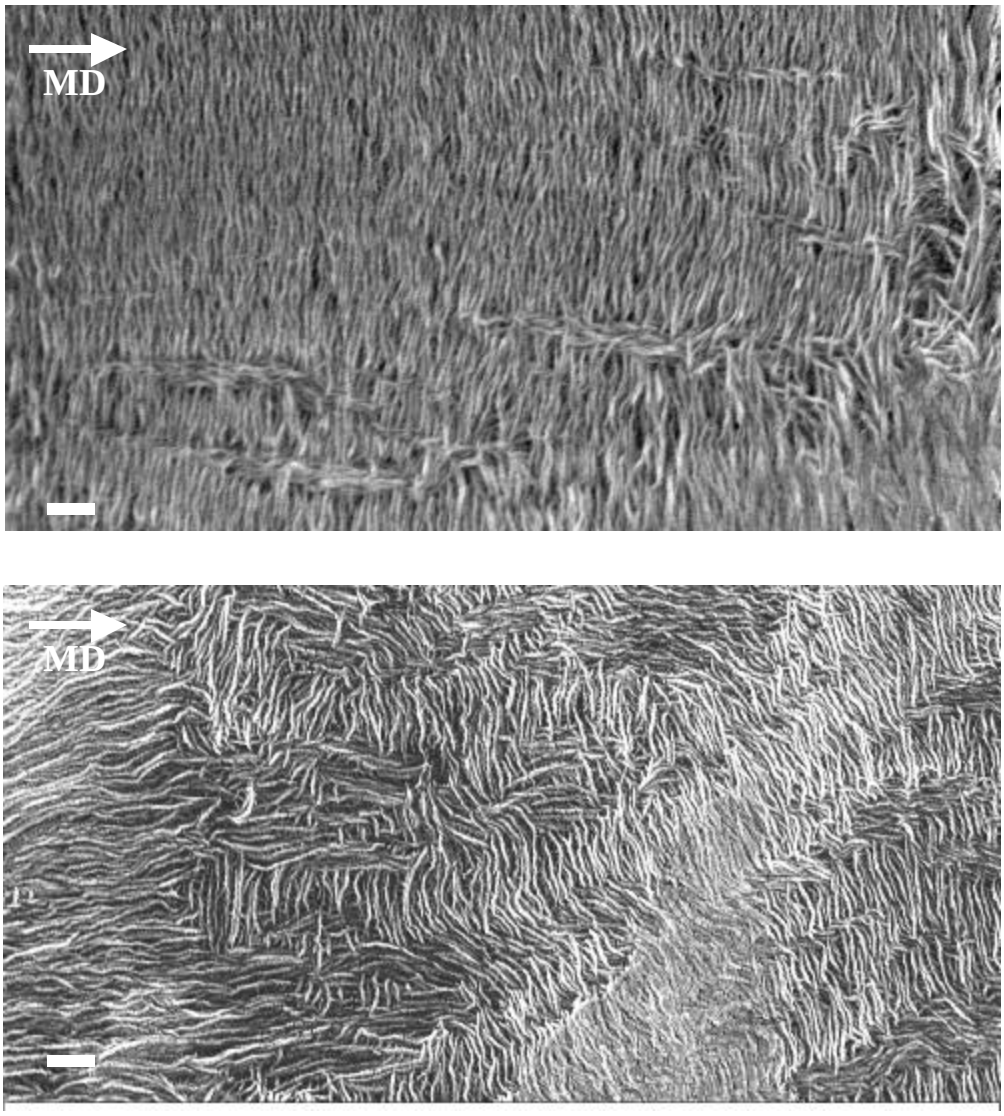

Figure 3.23. FESEM micrographs for films 38-12-A, and 54-12-A from top to bottom respectively. MD horizontal, TD vertical. Scale bars 200nm

Two examples of the large scale heterogeneity encountered when observing the surface of these films are provided in Fig.3.24. The upper micrograph contains what were considered to be two confounding factors. First, note that depending on which region of the micrograph is examined, two completely different interpretations of the state of orientation could be made. The edges contain MD stacked material while the center of the micrograph contains TD stacked material. This "regionally different" behavior was observed in most films. The upper micrograph of Fig.3.24 also shows differences in what can be termed the density of stacking. Comparing the left and right edges of the micrograph it appears that the lamellar size and spacing is greater on the right. This observation is likely due to the differences in the lamellae's angle of intersection with the surface. Such an effect makes the left side of the micrograph appear to be at a lower magnification than the right. The lower micrograph of Fig.3.24 contains a variation on the "regionally different" theme. Here large scale structures composed of lamellae of the same orientation can be seen. Again, as with the above micrograph, the area of observation strongly influences the apparent orientation state of the surface.

3.5.6 Refractive Index

The use of birefringence to determine system orientation is a technique which is commonly employed in the film industry. Birefringence can be obtained by determining the difference in refractive index in two orthoganol directions. Typically the MD and TD are chosen. Additional information can be obtained by measuring the refractive index in a third, orthogonal direction. The reader is referred to the literature review section for a more complete discussion of birefringence. Because the technique is sensitive to both the amorphous and crystalline phases, it provides information which x-ray scattering cannot. Applying both techniques to the same sample often allows one to differentiate between amorphous and crystalline orientation. That however will not be the goal here. Rather, the goal will be to gain insight into the effect of processing conditions on the average, total (amorphous and crystalline) chain orientation. Recall that the WAXD data was efficient at quantifying the state of "a" and "b" axis orientation of the crystalline phase. Information regarding the "c" axis (chain axis) must be inferred from the WAXD results.

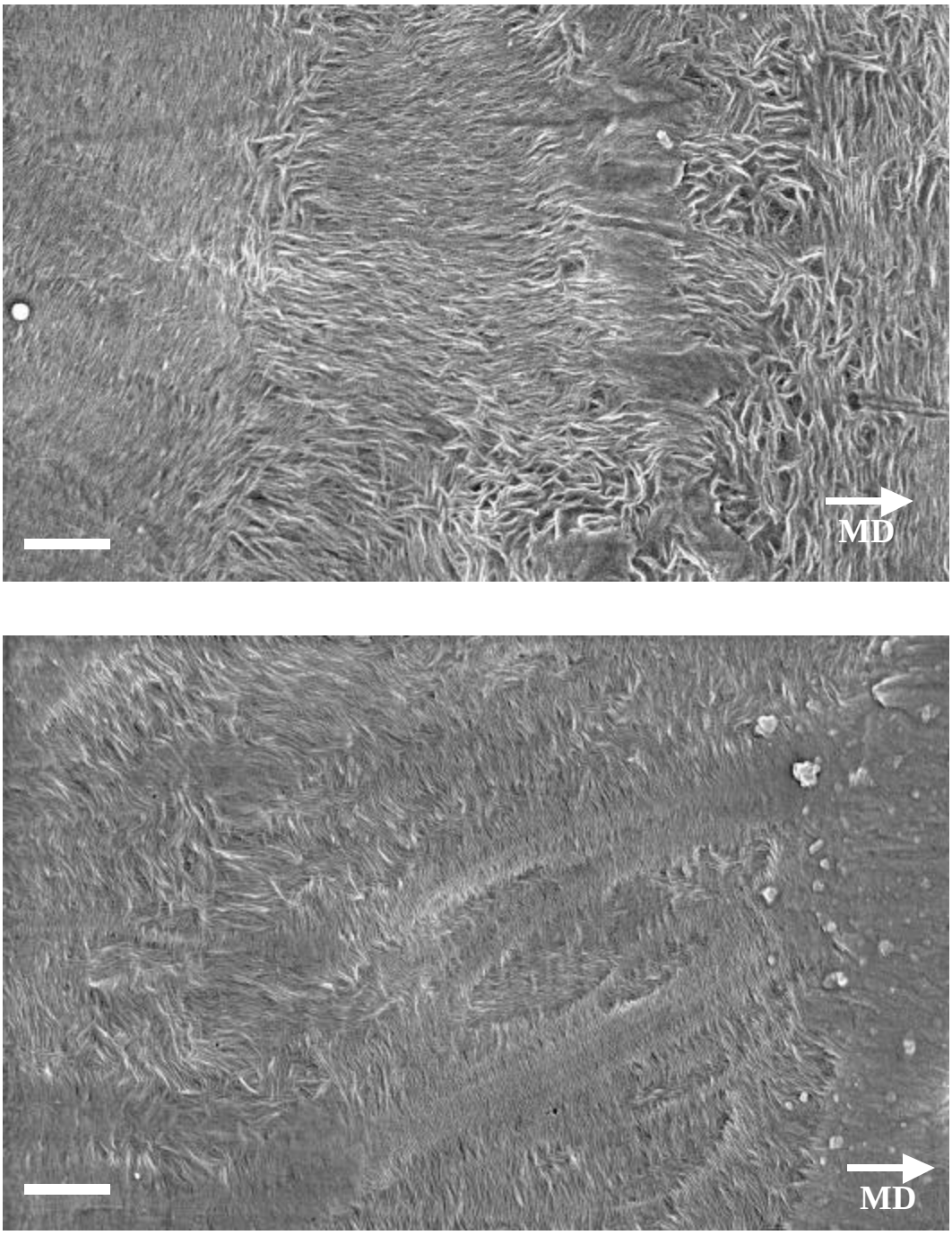

Figure 3.24. Micrographs displaying surface heterogeneity. Upper image 38-12-A, displaying domains of MD and TD stacked lamellae. Also note differences in MD "stacking density" on left side of image relative to right, due to differences in lamellar tilt with respect to the film surface. Lower image 54-20-B, showing large scale structures dominated by one direction of lamellar orientation. MD horizontal, TD vertical. Scale bars 1 μm.

Because the refractive index of PE is greatest along the backbone, determination of its angular dependence should be a direct indicator of chain orientation. Thus, quantification of the orientation dependence of refractive index should provide information which could not be provided directly by the x-ray data. However, the data provided by the analysis of refractive index is limited in that it can only provide a second moment average of the orientation states present. This is in contrast to the WAXD data which yields the entire distribution of orientation states. Therefore, measurements of refractive index cannot differentiate between balanced planar and bimodal planar orientation states.

A comparison of the average refractive index within the film plane with the refractive index normal to the film will be referred to as planarity. The planarity should be a measure of the extent to which the chain backbone is oriented within the film plane. Planarity results are given in Fig.3.25. It should be noted that because the refractive indices were obtained using a prism coupler, the results are representative of the surface of the film. It is quite obvious from the plot that the thinnest films are those which can be considered to be the most planar. This is entirely expected as thinner film gauges were achieved by increasing the DDR for a constant extruder output. This result is also in agreement with the pole figure data. Recall that the pole figures indicated that at the thinnest gauge, 12.5 μm, the "a" axis was strongly aligned along the film normal. The geometry of the unit cell dictates that the "c" axis must be preferentially oriented within the film plane under these circumstances. No justification can be given for the apparently anomalous data point in Fig.3.25 representing sample 23-30-A.

As stated previously, while the determination of in-plane birefringence cannot distinguish different orientation distributions within the film plane, it does provide a measure of the overall balance of chain orientation. Thus, the birefringence of those films which displayed uniaxial orientation (lowest FLH's) should be quite different from those which contain substantial amounts of TD stacked material. This is indeed the case as shown in Fig.3.26. Those films produced at the highest FLH, 54 cm, have the lowest in-plane birefringence values. This result is in total agreement with WAXS and SAXS results. Raising the FLH allows for the formation of TD stacked material.

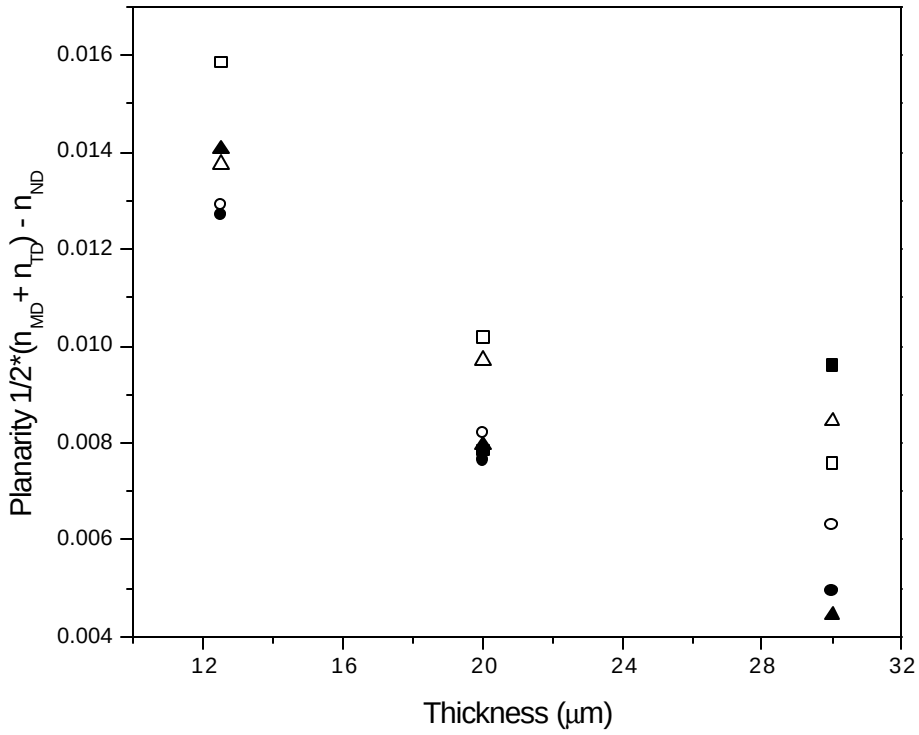

Figure 3.25. Planarity of films calculated using refractive indices. HDPE-A:( ) – FLH = 23 cm, ( ) – FLH = 38 cm, ( ) – FLH = 54 cm. HDPE-B: ( ) – FLH = 23 cm, ( ) – FLH = 38 cm, (△) – FLH = 54 cm. As the refractive index of the PE chain parallel to the backbone is greater than perpendicular, the refractive index should give an indication of chain orientation. The planarity term provides a measure of the degree to which the chain axis lies within the film plane. As expected, thinner films (greater DDR) lead to a more planar orientation state (i.e. less random) of the chain axis.

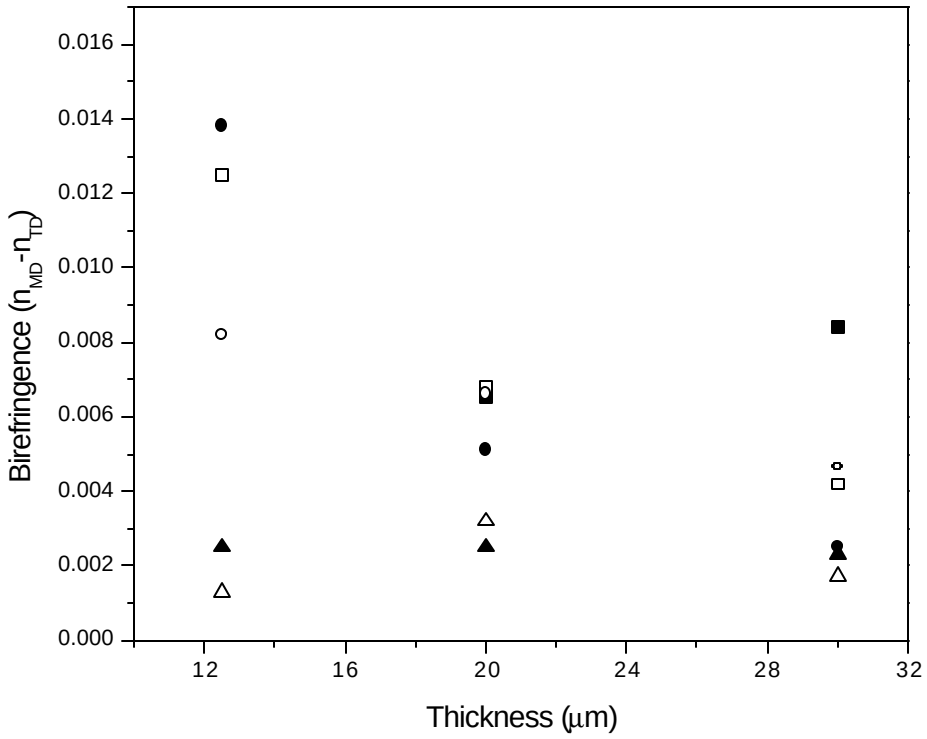

Figure 3.26. In plane birefringence of films. HDPE-A:( ) – FLH = 23 cm, ( ) – FLH = 38 cm, ( ) – FLH = 54 cm. HDPE-B: ( ) – FLH = 23 cm, ( ) – FLH = 38 cm, (△) – FLH = 54 cm. In plane orientation balance is greatest for highest FLH films. Also note the importance of FLH to achieving balance increases with decreasing thickness (greater DDR).

The TD stacks increase the balance of in-plane orientation over the uniaxial states produced at the lower FLH's. It is quite interesting to note that the birefringence values at the 54 cm FLH are nearly independent of the film thickness (DDR). Furthermore, the birefringence is much more sensitive to changes in FLH as the film gauge is decreased. Again, the 23-20-A sample appears to be an anomaly.

Considering the measurement of refractive index to be an indicator of chain orientation provides two straightforward conclusions regarding the effects of the studied process variables on orientation (i.e. constant BUR). The degree to which chains are aligned within the film plane can be controlled by the DDR. Increasing the DDR (thinner film gauges) causes the chains to preferentially align within the film plane. This is in agreement with the pole figure data. The orientation of those chains found within the film plane appears to be determined by the FLH. This too is in agreement with the x-ray data which showed that the film texture progressed from uniaxial to biaxial with increasing FLH. Thus, it appears that variations in DDR and FLH provide means of affecting the orientation of the film in two distinctly different manners. The DDR can be used to influence the orientation of the chains relative to the film normal, while changes in FLH can be used to tailor the orientation of the chains within the film plane (MD vs. TD).

3.6 Mechanical Properties

3.6.1 Elmendorf Tear

The Elmendorf tear test (ASTM D-1922) is commonly used in industry to quantify the resistance of a film to tear propagation along the MD and as well as the TD. While the test is quite simple, interpretation of the results is not always straightforward. The data are a measure of the load required to propagate a tear *initially* started along either the MD or TD. As stated in the opening section, tear properties should be related to the orientation state of the film. It has been demonstrated by the structural analysis so far presented that there are substantial differences in the orientation states amog the films studied, thus a wide variation in mechanical response is anticipated. The goal of this

portion of the discussion is to correlate the observed morphological textures with the tear properties of the films. Results of the Elmendorf tear tests conducted along the MD for the entire set of films are presented in Fig.3.27. The data clearly demonstrate that the resistance to tear along the MD improves as the film gauge is increased. This result is somewhat misleading in that the tear values have not been normalized based on film thickness. Thus, one would expect the value of the tear resistance to increase with film thickness, orientation effects aside, simply because a greater amount of material is being tested. The data are presented in this manner to emphasize the role played by altering the FLH in influencing the mechanical properties of the films. For each of the gauges studied it can be observed that increasing the FLH leads to an enhancement of tear resistance along the MD. Recall that increasing the FLH caused the orientation states of the film to change from a primarily uniaxial state along the MD to a more balanced state with a substantial amount of material oriented along the TD. Thus, it is clear that decreasing the amount of MD orientation leads to an improvement in tear properties along the MD. Data for the same films conducted along the TD are presented in Fig.3.28. As with the MD results, the tear resistance is also seen to increase with increasing film gauge largely because the data are not normalized on film thickness. Further observation reveals that the FLH effect has been reversed for the TD tear test, increasing FLH leads to a decrease in tear resistance along the TD. Again, this result is expected. While a strongly MD oriented film will have poor tear properties along that same direction, the orientation serves to enhance tear properties in the TD as it more difficult for the tear to propagate perpendicular to the chain axis than parallel. Because increasing the FLH produces a loss of preferred MD orientation, the tear resistance along the TD is observed to decrease as expected. To determine how well the tear properties are balanced within each film, the Elmendorf tear data are re-plotted in Fig.3.29 as the ratio of TD/MD tear. As anticipated, those films processed at the highest FLH show the most balance. Additionally, the HDPE-B films consistently show better balance than the HDPE-A films under identical processing conditions. Taking the ratio of the TD to MD tear resistances acts to normalize out the effect of film thickness.

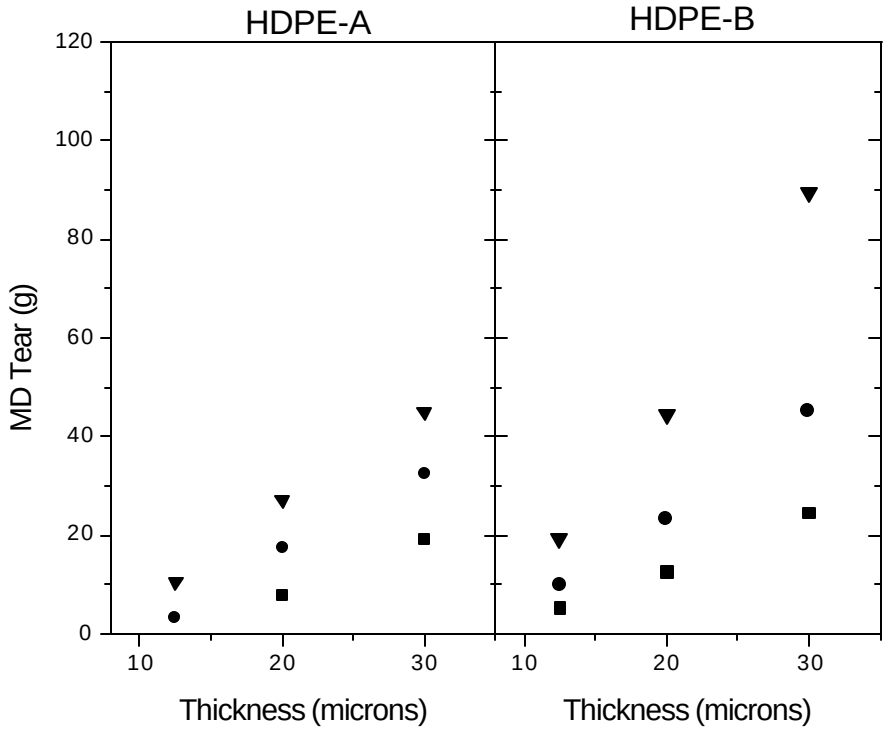

Figure 3.27. Elmendorf tear results. Test conducted along film MD. ( ) – FLH = 23 cm, ( ) – FLH = 38 cm, ( ) – FLH = 54 cm

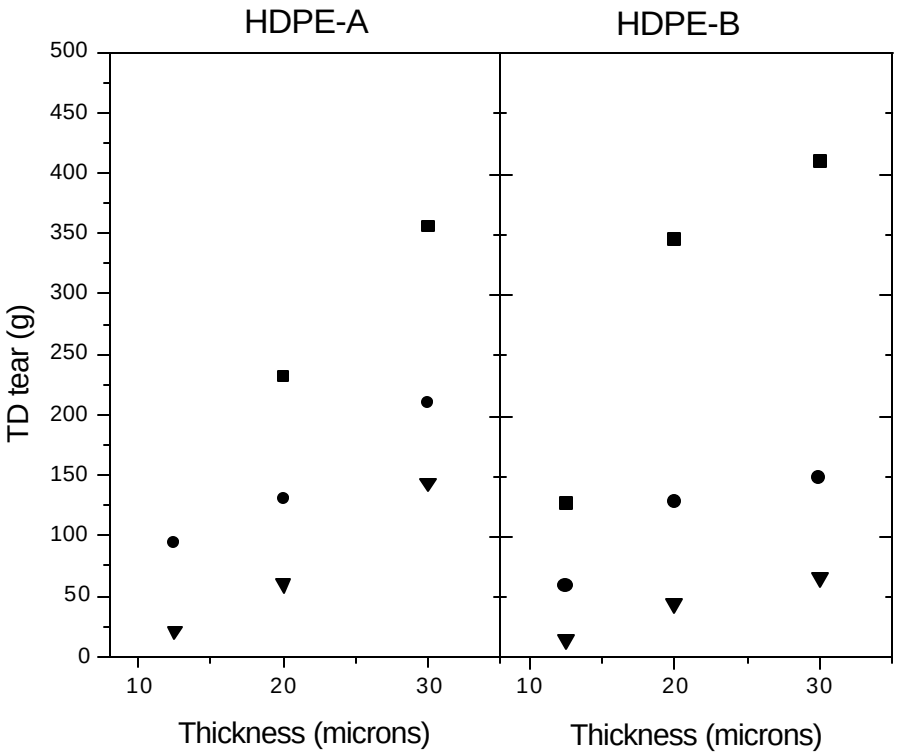

Figure 3.28. Elmendorf tear results. Test conducted along film TD. ( ) – FLH = 23 cm, ( ) – FLH = 38 cm, ( ) – FLH = 54 cm

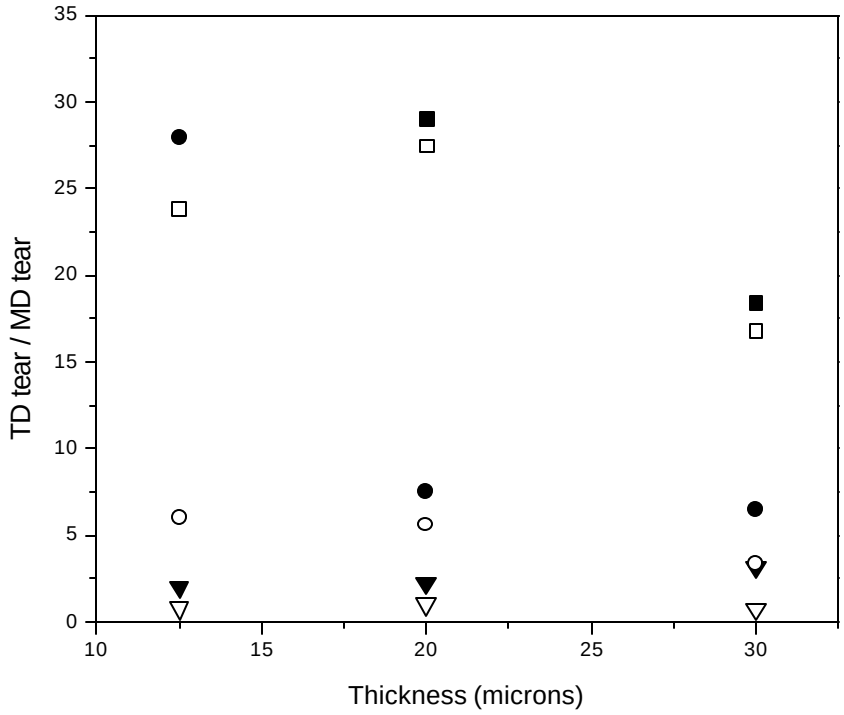

Figure 3.29. Balance of tear properties. HDPE-A:( ) – FLH = 23 cm, ( ) – FLH = 38 cm, ( ) – FLH = 54 cm. HDPE-B: ( ) – FLH = 23 cm, ( ) – FLH = 38 cm, (∇) – FLH = 54 cm.

Thus, any trend with respect to thickness will be an indicator of orientation induced effects as a result of changing the draw down rate. Interestingly, the influence of draw down rate on tear balance appears to be non-existent.

3.6.2 Dart Impact

A second test commonly used to quantify the resistance of a film to tear is the dart impact test, ASTM D1709. This test differs from the Elmendorf test in that the dart imposes a simultaneous deformation along both the MD and TD. The deformation rate of the dart test is also greater than that of the Elmendorf tear test. Dart impact results are an indicator of a film's ability to resist puncture. Because the test involves rapid deformation along both the MD and TD simultaneously, any imbalance or weakness in a given direction will be revealed by an asymmetric puncture. Furthermore, the puncture resistance will only be as strong as the weakest link in the film. Thus, the dart impact test is generally a sensitive indicator of imbalanced properties within the film plane. The dart impact results are given in Fig.3.30. As with the Elmendorf tear results, the data have not been normalized with respect to film thickness. The results obtained for HDPE-A are straightforward. Increasing the FLH leads to a more balanced orientation state, thus the dart impact is seen to increase with FLH. The dart impact is also seen to increase with film thickness, as expected, since a thicker film will require a greater force to achieve puncture, all other factors equal. The results for HDPE-B are perplexing. While the medium (38 cm) FLH films appear, on average, to give the best dart impact, the magnitude of the error bars are such that the data overlap with those of the highest (54 cm) FLH. Of greatest interest is the dart impact trend as a function of film gauge. The thinner films of HDPE-B appear to have better dart impact resistance despite the fact that the data have not been normalized for thickness. *These results suggest that the thinner gauge HDPE-B films have better orientation balance than the thick films, and thus produce better absolute dart impact resistance values, even though they are not as thick.* Comparing the SAXS (Fig.3.10 and Fig.3.12) and WAXS (Fig.3.6 and Fig.3.7) patterns of films 54-20-B and 54-12-B it can be seen that the thinner gauge films have greater orientation balance.

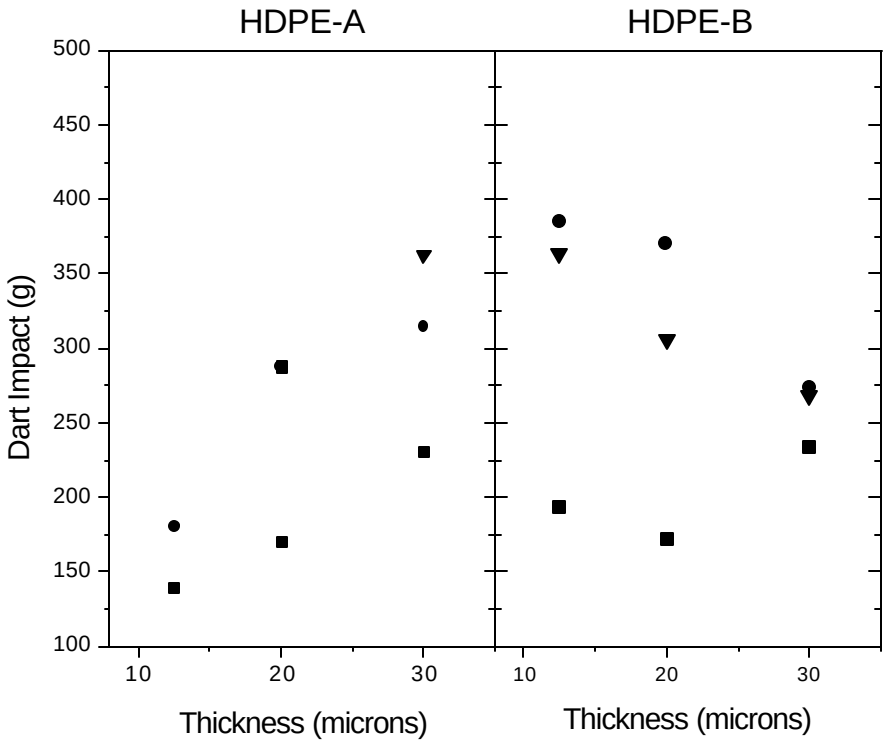

Figure 3.30. Dart impact properties. ( ) – FLH = 23 cm, ( ) – FLH = 38 cm, ( ) – FLH = 54 cm.

It is not completely understood at this time why the dart impact properties of the HDPE-B films show a clear dependence on film gauge while the TD-MD Elmendorf tear ratio does not. The differences in behavior between the two resins can be seen by plotting the normalized dart impact resistance as shown in Fig.3.31. Here the benefits of the thinnest gauge HDPE-B films are distinctly seen in relation to the others.

In an attempt to better understand the differences in mechanical response between the resin types, stress-strain data were obtained for the two thinnest gauge, highest FLH films, 54-12-A and 54-12-B. The tests were conducted parallel to the MD, parallel to the TD and at an angle of 45° to the MD. If the dart impact properties are a function of the balance of mechanical response in the film plane, based on Fig.3.30, film 54-12-A should show marked anisotropy while 54-12-B should appear more balanced. The results of the stress-strain tests are presented in Fig.3.32. Indeed, the HDPE-B film does show a more balanced response than the HDPE-A film. Also note that HDPE-B film has a greater tendency to yield in each measured direction, further suggesting that it may be more efficient at absorbing the energy of impact.

The relative levels of mechanical anisotropy between films 54-12-A and 54-12-B can be noted directly by examining the puncture shape, after failure, produced by the dart impact test. Photographs comparing these two films are shown in Fig.3.33. These pictures make it clear that the tearing experienced by film 54-12-B is isotropic while film 54-12-A is highly anisotropic. Recall that the WAXS and SAXS data suggested that the crystalline orientation of film 54-12-B was the most balanced, and possessed the second greatest dart impact resistance, of the films studied. It is also interesting to note that film 54-12-A displays preferential tearing along the TD, suggesting that it contains greater chain orientation along the TD relative to the MD. However, the Elmendorf tear results for this film suggested the orientation imbalance was skewed in favor of the MD. While both the dart impact and Elmendorf tear tests provide a measure of a film's ability to resist tearing, the different rates of testing involved with each test evidently result in different modes of failure which are controlled by film morphology.

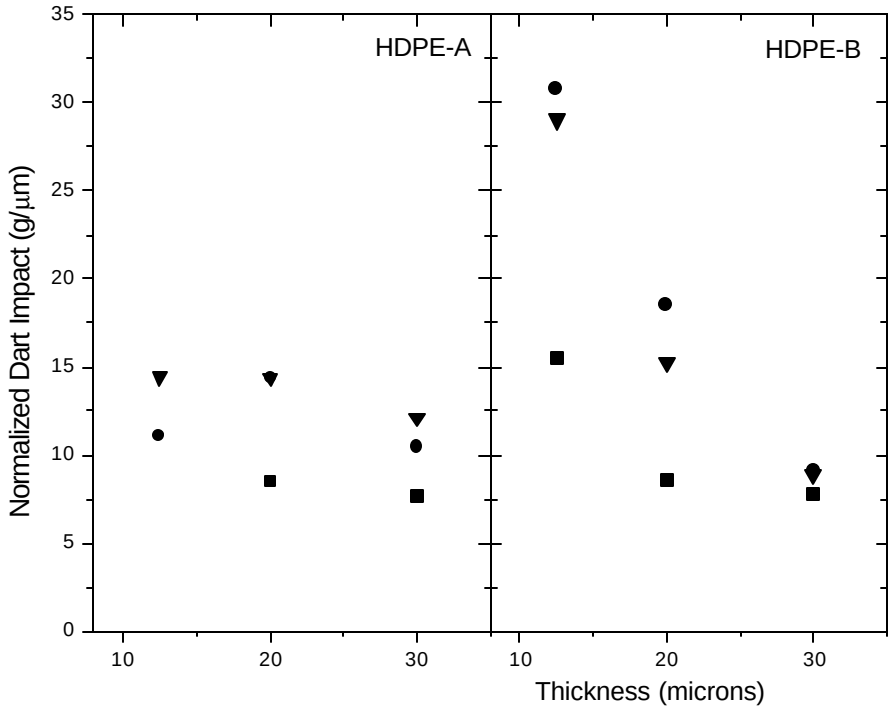

Figure 3.31. Normalized dart impact results. ( ) – FLH = 23 cm, ( ) – FLH = 38 cm, ( ) – FLH = 54 cm.

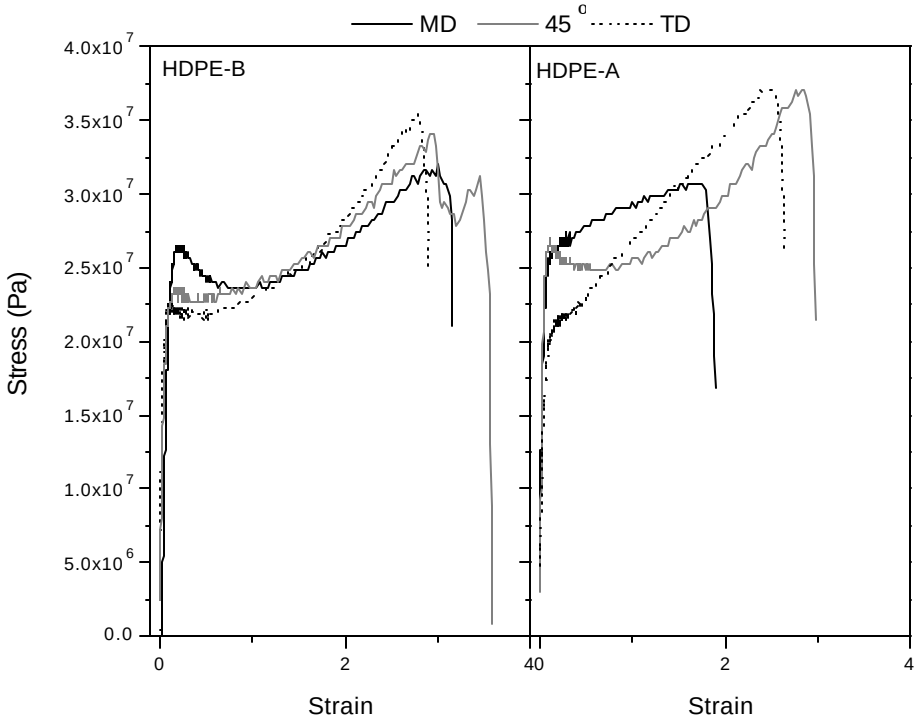

Figure 3.32. Stress-strain data for films 54-12-B (left) and 54-12-A (right) along various directions.

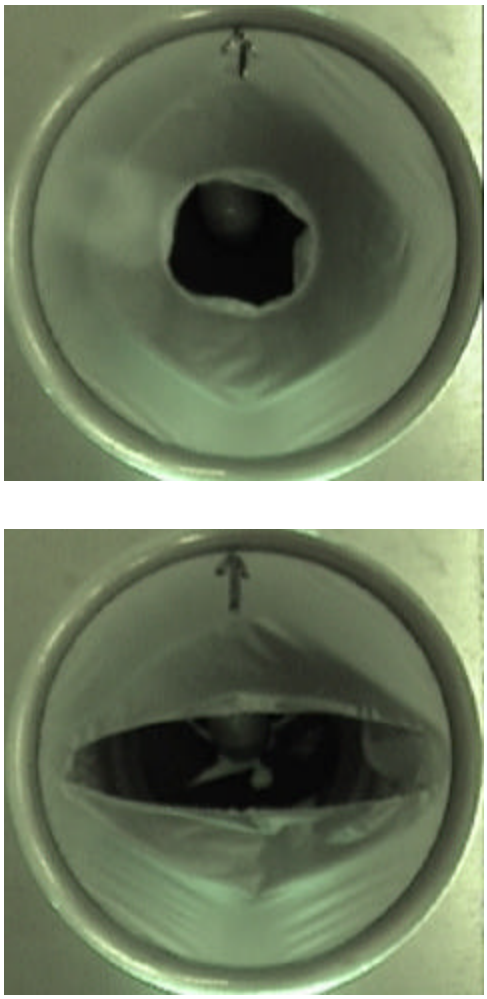

Figure 3.33. Photographs of films 54-12-B (upper) and 54-12-A (lower) after failure in dart impact test. Film MD vertical. Note that 54-12-B displays a nearly isotropic puncture, indicative of balanced in-plane mechanical properties, while tear propagation along TD in 54-12-A suggests chain orientation along TD which is greater than MD for this film.

3.7 Processing-Structure Relationships – Discussion

Thus far it can be appreciated that substantial differences exist in the manner in which each of the two resins interact with the process, under identical conditions. Varying levels of orientation have been observed which have a marked influence on mechanical properties. This section will attempt to make connections between the process conditions and end structure by noting how the two resins interact with the process. Recall from the resin characterization section that HDPE-A is of greater average molecular weight and possesses a larger high molecular weight tail than HDPE-B. These facts, combined with the determined absence of LCB content, suggest that HDPE-A will be the more slowly relaxing resin. It is thus expected that HDPE-A will be more prone to form more oriented structures when processed under identical conditions, relative to HDPE-B. Furthermore, extrapolating the rheological data to shear rates relevant to the processing conditions, HDPE-A is expected to have a greater viscosity, and thus generate greater stresses.

In this study there are three primary process variables which determine each films' structure; resin type, frost line height, and film gauge (draw down rate). Describing the effects due to differences in resin type is relatively straightforward. As stated above, due to its slow relaxing character, HDPE-A is more susceptible to orientation and orientation retention than HDPE-B. Deformation due to draw down (MD) or bubble expansion (TD) will have a more pronounced effect on films produced using HDPE-A. This logic is substantiated by HDPE-A's tendency to form a strongly uniaxial film at the lowest FLH and a distinct, planar bimodal orientation at the highest FLH. Varying amounts of orientation along the MD and TD are imparted to the melt by the draw down and bubble expansion deformations respectively, the results of which are captured in the final film structure of HDPE-A. Resin HDPE-B is also strongly influenced by the process stresses as evidenced by its strong uniaxial orientation at the lowest FLH. However, because HDPE-B undergoes more rapid relaxation, relative to HDPE-A, less orientation is frozen into the structure at the frost line. Thus, because HDPE-B disorients more rapidly from the imposed stresses than does HDPE-A, the state of planar orientation obtained is more balanced, or less bimodal. Evidence of this

behavior was well noted in the earlier WAXS and SAXS patterns presented. The relative balance in tear and stress-strain behavior of HDPE-B relative to HDPE-A at the highest FLH (those conditions under which the differences in relaxation behavior should be most pronounced) further bolster this argument.

The analysis of the effect of FLH on orientation is more complicated. Two effects may be leading to the increased amount of TD stacked material with increasing FLH. First, it is important to recognize the subtle changes which occur in bubble shape when the FLH is raised. A schematic is provided in Fig.3.34 to illustrate. Note that increasing the FLH leads to a decrease in the neck diameter prior to expansion[32]. Thus, the effective BUR increases with FLH. This may well be one reason why increasing the FLH is effective in increasing the amount of TD stacked material.

The second effect is related to melt relaxation times. A comparison of crystalline content as a function of processing conditions for the films studied is given in Fig.3.35. It can be seen that the overall crystalline content of all of the films studied are very similar. Therefore, the crystalline content of a film processed at the lowest FLH can be considered to be approximately equivalent to that of a film processed at the highest FLH. It then follows that the formation of TD stacked material, with increasing FLH, must occur at the expense of material stacked along the MD. This observation leads to the question: What is the orientation state of the material which becomes oriented along the TD just prior to bubble expansion? Was the material unoriented (relaxed) or was it oriented along the MD? If those chains which become oriented along the TD during bubble expansion were drawn from the pool of material oriented along the MD, then it would be expected that greater amounts of MD orientation in the neck should lead to greater levels of TD orientation as more material will be available for reorientation. However, the opposite effect is observed. As the FLH is increased, and hence MD orientation in the neck just prior to bubble expansion decreases, the amount of TD stacked material increases. The level of MD orientation must decrease with increasing FLH because increasing the FLH allows more time for relaxation along the MD. The FLH effect implies that the material which orients along the TD is drawn from the pool of material which is not substantially oriented just prior to inflation. Apparently chains which are oriented along the MD cannot readily become reoriented along the TD.

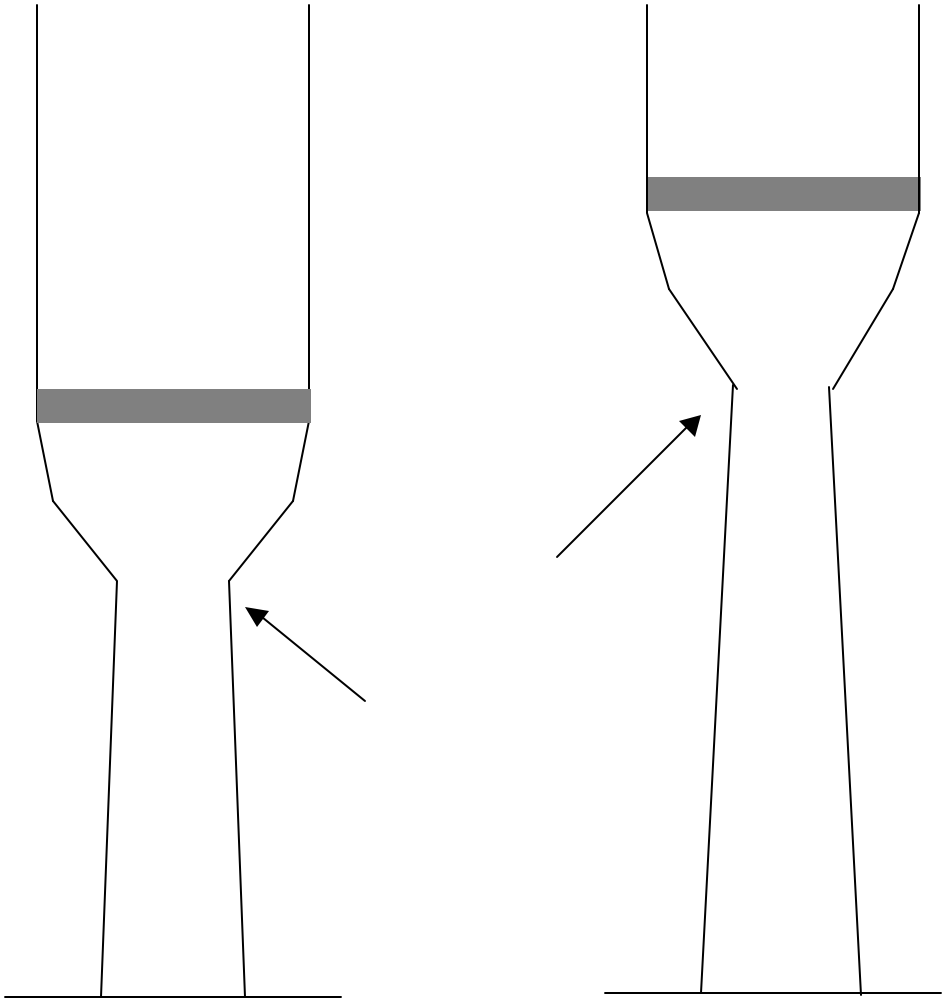

Figure 3.34. Effect of FLH on bubble shape. Arrows indicate regions of decreased stalk diameter (neck in), prior to bubble expansion, which result in greater effective BUR.

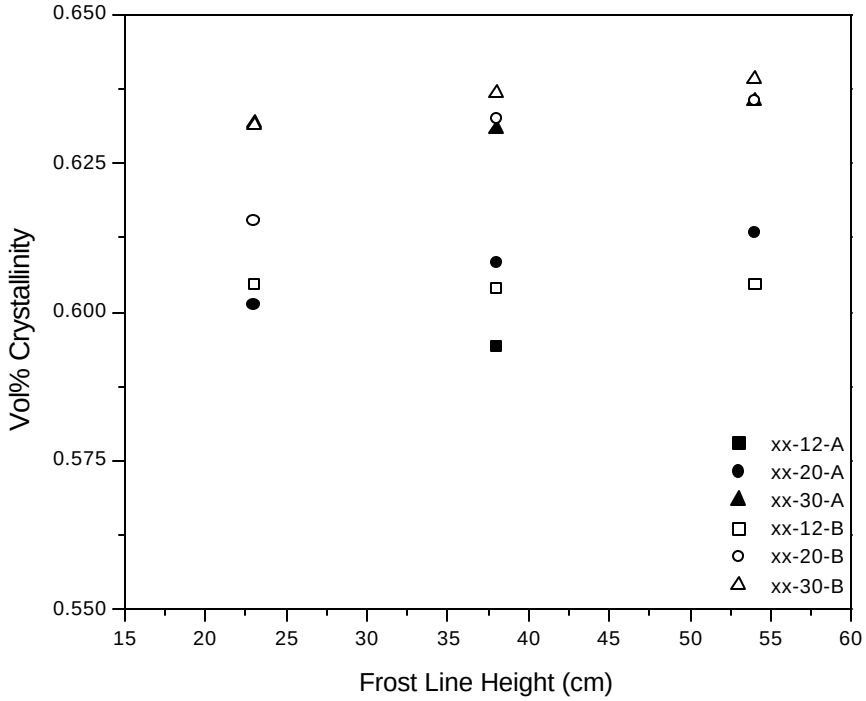

Figure 3.35. Crystalline content of films as determined using refractometry.

However, because a chain's propensity to become oriented, and stay oriented, is proportional to its length, it is reasonable to assume that those chains which do become oriented along the TD will be the longest chains in the system, which did not remain oriented along the MD at the inflation point. This fraction of chains represents material which is of sufficient length to become oriented initially, but short enough to substantially relax while traversing the neck region. By this reasoning, subtleties in the MWD should play a key role in determining the relative amounts of MD and TD stacked material formed for a given set of processing conditions. Note also that because the TD expansion occurs later in the process than the MD stretching, the bubble will be cooler, and hence more susceptible to becoming oriented. Thus, as the FLH is increased melt strain more readily results in TD orientation.

In this study the most difficult effect to address is that of film gauge. Thinner gauges were achieved by increasing the draw down rate. One can expect two primary effects due to increased draw down, greater process stresses (greater acceleration of the melt) and decreased time for relaxation, as the melt will move more rapidly from the die exit to the frost line. It is clear that greater stresses are imparted to the bubble by down gauging. The high stress crystallization conditions noted in the pole figure data provide definitive evidence for this. At first glance, this would imply that increasing the draw down rate should decrease the amount of TD stacked material, as a greater fraction of the chains will be become oriented along the MD. This however, ignores two key points. Most importantly, as the degree of stalk diameter reduction is related to the stress levels present in the bubble, increasing the DDR acts to increase the effective BUR, in the same manner that raising the FLH does, as discussed above. This greater effective BUR at higher processing stresses will favor the formation of additional TD stacked material. Furthermore, increasing the DDR leads to a greater film velocity. This increased velocity affords less time for relaxation in the neck, which affects MD orientation, and after bubble expansion, which affects TD orientation. Thus, increasing the DDR allows chains with rapid relaxation rates to be "captured" in an oriented state. The net effect of increasing the draw down rate is to make a greater fraction of the molecular weight distribution available for orientation. Again it seems likely that subtle differences in

molecular weight distribution will play a major role in determining the amount of material which becomes stacked along the MD and TD.

3.8 Conclusions

This work has focused on elucidating the relationships between processing conditions, morphology, and tear performance in blown films produced from two HDPE resins of differing average MW and MWD. The results have been presented in the context of bubble shape and molecular relaxation. It is quite apparent from the results that under the conditions studied, increasing the FLH leads to a greater proportion of TD stacked material. Those films produced at the lowest FLH produced a uniaxial texture while those at the highest FLH demonstrated a biaxial orientation. It was hypothesized that the longest chains lead to the formation of MD stacked material. In contrast, TD oriented chains were argued to be those which were long enough to initially become partially oriented along the MD, but were able to substantially relax while traversing the neck region, prior to the expansion point. Bubble inflation leads to TD orientation, which can become rapidly frozen into the film due to the proximity of the expansion point to the frost line. Essentially, the high stalk process can be conceptualized as consisting of two inter-related, but distinct processes. The first consists of MD stretching and relaxation in the neck region. The second is bubble expansion, resulting in TD expansion. The level of orientation induced in each step is a function of the resin's relaxation behavior, the time scale (strain rate and quench time) of the step, and the stresses generated. Conditions which lead to greater stress levels result in a larger effective BUR, thus favoring the formation of TD stacked material.

Rheological characterization, coupled with GPC results, demonstrated that HDPE-A undergoes molecular relaxation more slowly than HDPE-B and has a greater viscosity. These factors cause HDPE-A to be more susceptible to the orienting influence of the process. It is for this reason that HDPE-A was observed to form more "extreme" orientation states. This difference between the films resulted in structures which were

more balanced in the plane of the film for HDPE-B (planar-balanced) in contrast to HDPE-A (planar-bimodal) at the highest FLH.

Finally, the results of tensile stress-strain tests demonstrated that HDPE-B's mechanical properties were indeed more balanced in the film plane. This greater balance would appear to be beneficial for producing tear and puncture resistant films. It was interesting to note that, under the conditions studied, it was possible to produce greater balance in the plane of the film for HDPE-B by down gauging. The same was not true for HDPE-A. This final result serves to demonstrate the complex nature of the interaction between the molecular weight and its distribution of a resin with the process during blown film fabrication.

3.9 References

[1] Aggarwal, S.L., Tilley, G.P., Sweeting, O.J., *Journal of Applied Polymer Science*, **1** (1) 91 (1959).
[2] Lindenmeyer, P.H., Lustig, S., *Journal of Applied Polymer Science*, **9** 227 (1965).
[3] Desper, R.C., *Journal of Applied Polymer Science*, **13** 169 (1969).
[4] Maddams, W.F., Preedy, J.E., *Journal of Applied Polymer Science*, **22** 2721 (1978).
[5] Maddams, W.F., Preedy, J.E., *Journal of Applied Polymer Science*, **22** 2739 (1978).
[6] Maddams, W.F., Preedy, J.E., *Journal of Applied Polymer Science*, **22** 2751 (1978).
[7] Hofmann, D.Geiss, D., Janke, A., Michler, G.H., Fielder, P., Journal of Applied Polymer Science, 39 1595 (1990).
[8] Choi, K.J., White, J.L., Spruiell, J.E., *Journal of Applied Polymer Science*, **25** 2777 (1980).
[9] Choi, K.J., White, J.L., Spruiell, J.E., *Journal of Polymer Science; Polymer Physics*, **20** 27 (1982).
[10] Keller, A., Machin, M.J., *Journal of Macromolecular Science Physics*, **B1**, (1) 41 (1997).
[11] White, J.L., Cakmak, M., *Advances in Polymer Technology*, **8** (1) 27 (1988).
[12] Pazur, R.J., Prud'homme, R.E., Macromolecules, **29** 119 (1996).
[13] Butler, M.F., Donald, A.M., *Journal of Applied Polymer Science*, **67**, 321 (1998).
[14] Yu, T., Wilkes, G.L., *Polymer*, **37** (21) 4675 (1996).
[15] Yu, T., Wilkes, G.L., *Journal of Rheology*, **40** (6) 1079 (1996).
[16] Prasad, A., Shroff, R., Rane, S., Beaucage, G., *Polymer*, **42** 3103 (2001).
[17] Kanai, T., Campbell, G.A., Film Processing, Hanser Pub., Cincinnati, (1999).
[18] Harris, W.D., Van Kerckhoven, C.A.A., Cantu, L.K., *Journal of Plastic Film and Sheeting*, **6** 306 (1990).
[19] Lu, J., Sue, H.J., Rieker, T.P., *Polymer*, **42** 4635 (2001).
[20] Krishnaswamy, R.K., Sukhadia, A.M., *Polymer*, **41** 9205 (2000).
[21] Kim, Y.M., Kim, C.H., Park, J.K., Lee, C.W., Min, T.I., *Journal of Applied Polymer Science*, **63** 289 (1997).
[22] Patel, R.M., Butler, T.I., Walton, K.L., Knight, G.W., *Polymer Engineering and Science*, **34** (19) 1506 (1994).
[23] Huck, N.D., Clegg, P.L., S*PE Transactions*, 121 (1961).
[24] Murakami, S., Kohjiya, S., Shimamura, K., *Journal of Macromolecular Science, Physics*, **B39** 645 (2000).
[25] Sherman, E.S., *Polymer Engineering and Science*, **24** (11) 895 (1984).
[26] Butler, M., Donald, A.M., *Journal of Applied Polymer Science*, **67** 321 (1998).
[27] Lin, L., Argon, S., *Journal of Materials Science*, **29** 294 (1994).
[28] Pepper, R.E., Samuels, R.J., Encyclopedia of Polymer Science and Engineering, John Wiley and Sons, New York, **14** 261 (1988).
[29] Krishnaswamy, R., Janzen, J., *ANTEC 2001 - San Francisco*, SPE 297 (2001).
[30] Janzen, J., Rohlfing, D.C., Hicks, M.J., "Presenting Polyolefing Melt Viscoelsasticity data with Carreau-Yasuda Models: Some Industrial Experience, Journal , Vol (year)
[31] Janzen, J., Colby, *Journal of Molecular Structure*, **485-486** 569 (1999).
[32] Sukhadia, A., Private communication.

Chapter 4

Correlation of Moisture Vapor Transmission Performance with Structure-Property-Processing Relationships in Blown High Density Polyethylene Films

4.1 Introduction

Among the factors, along with low cost, which make high density polyethylene (HDPE) attractive for use in packaging applications, is its ability to act as a barrier to the passage of moisture. Considering the hydrocarbon character of the repeat unit and the symmetric nature of the chain, which makes the attainment of substantial crystallinity possible, it is readily evident why HDPE is an effective moisture barrier. Because the barrier performance, on a thickness basis, of all HDPE blown films are not the same, even for films produced from identical resins, it is apparent that variables other than

chemical structure play a role in determining the permeation characteristics of a given film. Assuming that HDPE films can be adequately represented by a two phase morphological model, consisting of separate amorphous and crystalline domains with well defined boundaries, the two most likely sources leading to the observed variation in barrier properties in HDPE films are: 1) differences in the relative volume fractions of crystalline and amorphous material, and 2) differences in the distribution and orientation of crystalline material within the film. Additional sources of variability do exist, such as the effect of amorphous phase orientation, but these will not be investigated here in detail. The morphology and crystalline content of a blown film are functions of the processing conditions and resin used to produce the film. More specifically, end film morphology is determined by the interaction between the resin and the process. Thus, with the goal of understanding how the moisture barrier performance of HDPE films can be maximized, this chapter will investigate how resin and process variables interact to yield variations in final film structure. These morphological states will then be related to a measure of moisture barrier performance, the moisture vapor transmission rate (MVTR). As a result, those resin and processing variables which are most advantageous to barrier performance will be identified.

The chapter will begin with a brief review of the factors which influence permeation in semicrystalline polymers as well as the morphological textures typically found in blown PE films. Next, the experimental details are presented followed by the resin characterization results. The crystalline content and orientation in the films is then addressed with respect to resin and processing variables. Because the MVTR data are discussed primarily in the context of the overall processing-structure trends, its presentation is delayed until the end of the chapter.

4.2 Background Information

4.2.1 Diffusion in Semicrystalline polymers

A brief review of the fundamental concepts relative to diffusion in semicrystalline polymers will be undertaken. This will give the reader an appreciation of the basic mechanism by which crystal orientation in the final film can affect barrier performance.

The discussion will only consider diffusion in one dimension, under steady state conditions, with no bulk flow of the permeating species. Furthermore, it will be assumed the diffusing molecules move through the matrix independently, that is each penetrant molecule is fully solubilized in the matrix. The diffusion of small molecules through a polymeric matrix can roughly be divided into three regimes.[1] When the rate of molecular relaxation is much more rapid than the rate of diffusion, the diffusion behaves in a manner typically referred to as Fickian. Under these conditions the penetrant molecules move in a random walk with the concentration gradient as the driving force for net motion. This type of diffusion is applicable to polymeric materials above Tg (i.e. rubbery materials). Because the Tg of PE is well below room temperature this mode of diffusion is applicable to this study. The other two regimes of diffusion behavior in polymeric materials will not be discussed here, as they relate to the situations where the rate of diffusion is much more rapid than molecular relaxation (glassy materials), or the rates of diffusion and molecular relaxation are of the same magnitude.

Under steady state conditions, the rate of permeation through a rubbery matrix is generally considered to be a function of two independent variables; the coefficient of permeant solubility in the matrix, S, and the coefficient of permeant diffusivity in the matrix, D. The simple relation is provided in the equation below.

$$P = SD \qquad \text{Eq.4.1}$$

The solubility can be thought of as proportional to the number of sites available for dissolution of the permeant, while the diffusivity is related to the resistance of movement from one site to the next. To accurately describe the permeation behavior of a permeant through a semicrystalline polymer above Tg, this equation must be modified to take into account the impermeability of the crystalline phase relative to the amorphous phase. The much lower levels of chain mobility in the crystalline phase, in comparison to the amorphous phase, has been used to account for the wide disparity in permeation rates between the two phases[2]. Because the density of the crystalline phase in most semicrystalline polymers is greater than that of the amorphous phase, the permeation rate is further hindered in the crystallites. This is the case for PE with amorphous[3] and

crystalline[4] phase densities of 0.855 g/cm^3 and 1.011 g/cm^3 respectively. Based on the assumption of an impermeable crystalline phase, it follows that the solubility and diffusivity coefficients of a permeant in the bulk film will be functions of the film's amorphous content, as shown below where x_{am} is defined as the amorphous phase volume fraction, and S_0 and D_0 are the intrinsic amorphous phase solubility and diffusivity coefficients of the permeant-polymer pair respectively.

$$S = S_0 x_{am} \qquad \text{Eq.4.2}$$

$$D = D_0 x_{am} \qquad \text{Eq.4.3}$$

$$P = S_0 D_0 x_{am}^2 \qquad \text{Eq.4.4}$$

Here, the intrinsic solubility and diffusivity of the permeant in the amorphous phase are considered to be independent of the overall crystalline content. This may not be rigorously correct as the crystalline phase may act to restrict the motion of amorphous chains. Recognizing this shortcoming, this simple "first approximation" relationship postulates that the rate of moisture permeation will scale with the square of the amorphous content. Thus, resin or process variables which have an impact on the crystalline content of the film should have a major influence on barrier performance.

Equation 4.4 implicitly assumes that the crystalline domains are isotropic in shape and distributed evenly throughout the film. This assumption is invalid for PE as it is known to crystallize in the form of thin, chain folded lamellar sheets. The shapes of the crystalline domains in PE are highly anisotropic. To account for this a slightly different relationship has been proposed[2].

$$P = \gamma P_a x_{am} / B \qquad \text{(Eq.4.5)}$$

The new terms are; P_a, the intrinsic permeability of the amorphous phase, ø, the "detour ratio", and B, the blocking factor, where ømay take on values between from 0-1 and B is greater than 1. In Eq.4.5 the influence of amorphous content is represented both explicitly, and implicitly through the detour ratio. At the heart of this equation is the

concept of the tortuous path. A permeant molecule passing from one side of a semicrystalline film to the other cannot do so via a direct path, perpendicular to the surfaces of the film. Because the crystalline lamellae are essentially impermeable to the diffusant, it must travel a distance greater than the thickness of the film as it makes it way around and in between the lamellae. The size and orientation of the lamellae will therefore play a key role in determining how large a distance this tortuous path represents. It can be easily envisioned that the permeation rates for two films of equal crystalline content, one with a random orientation of lamellae (spherulitic), and the other with lamellae neatly stacked with their surface normals perpendicular to the surface of the film will be quite different. The former will present a tortuous path to the permeant while the latter provides channels of continuous amorphous material spanning from one surface of the film to the other. The purpose of the detour ratio in Eq.4.5 is to account for this phenomenon. The blocking factor, B, is included to account for the presence of amorphous channels between crystalline material which are not large enough to accommodate the permeant molecule. Obviously then, the magnitude of the blocking factor will depend not only on the morphological details of the polymer, but also on the size of the diffusing species.

In theory, for simple geometries and distributions of crystalline material within an amorphous matrix, it should be possible to calculate the values of ø and B. Due to the complexities of the morphologies commonly encountered in non-quiescently crystallized (as well as in quiescent, sphereulitic materials) polymers, such an approach is not feasible. Nevertheless, Eq.4.5 does serve to illustrate, if not quantify, the basic phenomena which are important in determining the rate of permeation through a semicrystalline film.

4.2.2 Structure Formation

Many decades of research have been conducted in the area of blown polyethylene films. As surveyed in the literature review, early work by numerous authors has led to a basic understanding of how structure develops during PE film blowing[5-13]. The basic consensus formed by this early body of work is that the blown film process,

under conditions relevant to industrial film production (i.e. MD stresses greater than TD stresses), results in HDPE films with preferential orientation of the "b" crystal axis perpendicular to the MD, while the "a" and "c" crystal axes tend to orient between the MD and film normal (ND).

The morphological description of these films has typically been visualized in terms of the Keller-Machin (K-M) row nucleation model. Work by Keller has been very successful in describing the mechanism of structure formation in semicrystalline polymers, as it arises from oriented melts and solutions, in terms of row nucleated crystallization[14]. A more complete description of the model can be found in the literature review section, though a brief review is believed to be of benefit here. The K-M model postulates that the stresses imparted by the flow field upon a polymer coil can lead to a partial extension of the chain along the direction of flow. As the temperature is lowered, it becomes possible for a small amount of material to crystallize in this semi-extended and oriented state. This material is referred to as a fibril or fibril nucleus. Subsequent crystallization of the bulk occurs in a chain folded manner, nucleated from either the oriented fibrils, impurities, or spontaneously formed nuclei. The latter two modes of nucleation will, in theory, produce crystallites with random orientation. However, it is possible that stresses existing in the supercooled melt will lead to preferentially oriented crystallization despite the random orientation of nucleation sites. In contrast, crystallization nucleated from the oriented fibrils is well known to result in oriented crystallites via epitaxial growth. Noting that the crystal axis of most rapid growth in PE occurs along the "b" crystallographic axis (orthorhombic unit cell with the "c" axis coincident with the chain backbone), the net effect of the fibril nuclei is to promote a preferential orientation of the bulk crystalline material with its "b" axis perpendicular to the direction of flow. For the blown film process, this constitutes "b" axis orientation in the TD-ND plane. During bulk crystallization the "a" and "c" axes may align themselves between two possible orientation states. Under conditions of low stress the K-M model considers the lamellae to twist freely about the growth axis, the "b" axis, leading to "a" and "c" axis orientations distributed approximately evenly about the "b" axis. Furthermore, it is anticipated that the lamellae will not only twist as they grow out from the fibril nucleus, but they will also curve. As a result, the growth direction of the

lamellae will not remain perfectly perpendicular to the deformation direction. Oriented sheaf-like structures, which resemble the early growth stages of a sphereulite, represent a commonly observed consequence of this phenomenon.

Conversely, under conditions of high stress, the "c" axis tends to remain parallel to the direction of imposed stress, leading to a preferential orientation of the "a" and "b" axis perpendicular to the principal stress direction. In the blown film process the high stress condition results in orientation of the "c" axis along the MD with the "a" and "b" axes lying in the TD-ND plane. Stress levels between the low and high regimes lead to orientation states between these two extremes.

The K-M model of row oriented crystallization makes no prediction as to the state of amorphous orientation that is obtained. As outlined in the literature review, conflicting results have been obtained in the literature. Obviously, the state of chain packing in the amorphous phase will have an impact on the diffusion behavior. Because no general correlation has been found to directly link the states of amorphous and crystalline phase orientation, this study will initially consider the states to be formed and exist independently, though this likely is an oversimplification. Stated in an alternate manner, the presence of crystalline orientation will not lead the author to assume any specific state of amorphous phase orientation.

It can be appreciated from this brief review that it is possible to obtain a wide range of oriented lamellar morphologies using the blown film process. It will be the goal of this study to investigate how the various crystalline orientation states and structures affect the tortuous path through the film, thus influencing the permeation behavior.

A brief review of some literature results demonstrates that overall crystalline content and orientation have measurable effects on permeation behavior. While most studies have not focused on water as the permeant, the results are still generally applicable.

A representative study by Ng[15] examined the permeation behavior of toluene in unoriented and plastically deformed HDPE films. This study found, as did all of the subsequent studies cited herein, that the permeation rate decreased with increasing crystalline content. It was also demonstrated by Ng that the *amorphous phase* diffusion coefficient in isotropic films decreased as the crystalline content increased. This result

suggested, as expected, that a higher crystalline content can be associated with a more tortuous path, per unit amorphous phase. Furthermore, drawing in the solid state was observed to profoundly decrease the permeation rate and the equilibrium sorbed concentration. Ng concluded that the small increase in crystallinity upon drawing could not account for this dramatic change, thus orientation effects were important. This result demonstrates how orientation can actually decrease the rate of permeation. However, the results of this study, and indeed many of those found in the literature, on oriented samples, are for specimens which possessed an initial spherulitic morphology from which orientation was induced by cold drawing. This method of producing orientation results in morphologies which are very different from those produced via melt deformation (i.e. film blowing). Indeed, the authors describe the end morphology after drawing as fibrillar, rather than lamellar. *It is also anticipated that the state of amorphous orientation induced by cold drawing will be substantially greater than that induced by a melt process*. In fact, this is the conclusion reached by Ng et al. Cold drawing of the specimen simultaneously destroys the original lamellar morphology and increases the taughtness of the amorphous chains through which the permeant molecules travel. This is associated with an increase in density of the amorphous phase, and thus a decrease in free volume. The authors attribute the decrease in permeant sorption sites to this decrease in free volume. Similar results have been published by Peterlin for low density polyethylene and HDPE using methylene chloride[16]. These studies demonstrate tortuous path effects, and the influence of high levels of amorphous phase orientation on the permeation process.

Direct evidence that the rate of permeation is influenced by the state of lamellar orientation has been provided by Eby[17]. In this study sheets approximately 0.2 mm thick of PE were melt pressed utilizing three cooling procedures which can loosely be defined as quenched, intermediate, and slowly cooled. Microtomed sections of these films revealed, via optical microscopy, that a skin layer roughly 60 μm thick, distinct from the sphereulitic morphology of the core, was formed in the quenched films. This surface layer was reasoned to consist of lamellae which nucleated at the surface and grew perpendicular to the sheet normal, thereby creating amorphous channels with preferential orientation along the sheet normal. Such channels would be expected to enhance the rate

of permeation. WAXS measurements confirmed the orientation state of the surface layer. Upon removal of the surface layer by grinding, the permeation rate of ethane through the sheets, corrected for the change in thickness, was found to decrease. Thus, Eby concluded that the surface layer, composed of lamellae oriented such that their thickness direction is normal to the surface, was less effective at blocking the permeant molecules than the randomly oriented, sphereulitic material found in the core. Some caution should be observed in the interpretation of these findings as the grinding step may alter the original morphology of the sample, though the author reported no significant change in density or crystalline orientation of the bulk after grinding.

In depth studies in the literature which specifically address the permeation behavior of water through blown films of high density polyethylene are surprisingly rare, despite the commercial significance. Indeed, as discussed in the literature review chapter, these studies are primarily limited to trade journals[18-22]. Most studies focusing on the permeation behavior of HDPE in the technical literature do not deal with blown films[1,2,15-17,23-27]. However a few studies concerned with oxygen and/or water permeability through HDPE blown films in the technical literature can be found[28-30]. Two basic conclusions have been drawn from these limited studies. The first, films with greater crystalline content provide a better barrier to the passage of moisture. The second, those process and resin variables which are least likely to promote preferentially oriented crystallization along the MD produce better barrier HDPE films. Unfortunately, the processing, rheological, and morphological details of these studies tend to be lacking. Thus, to fill this void, it is the goal of this chapter to investigate, in detail, the structure-property-processing relationships of blown HDPE films in the context of moisture barrier performance.

Unfortunately, the ambitious goals of this chapter had to be scaled back due to the loss of the project sponsor, Chevron, midway through the research. A corporate merger between Chevron and Phillips led to the departure of nearly all of those associated with the project. The set of films examined represent the original design of experiment, suggested and produced by Chevron staff. The original research plan called for the production of additional films, after examination of the initial set, for further examination of a few key variables. Without access to Chevron's facilities, no such films could be

produce, thus greatly limiting the scope of the research. Despite this difficulty, a substantial body of data which forms the content of this chapter was collected from the initial set of films.

4.3 Experimental Methods

The films and MVTR analysis, as well as the resins and GPC analysis, were supplied by Chevron as part of a collaborative research effort. The processing conditions and resin associated with each film are summarized in Table 4.1. The blow up ratio (BUR) was held constant at a value of 2.9 for all films while extruder output, die gap, frost line height (FLH), and line speed were varied for selected samples. The reader is asked to note the conditions used to produce film s1: output = 100 lb/hr, die gap = 0.16 cm, frost line height = 15.25 cm, line speed = 90 ft/min. *This set of parameters will be referred to as the "base set" of processing conditions. In the text, any description of the conditions used to make a specific film will be referenced relative to this base set of conditions*. Thus, film s2: output = 100 lb/hr, die gap = 0.16 cm, frost line height = 15.25 cm, line speed = 45 ft/min, would be described as processed under conditions of decreased line speed. The combination of process variables utilized resulted in the production of three film gauges: 0.76 mil, 1.23 mil (base conditions), and 2.46 mil.

MVTR analysis was conducted by Chevron in accordance with ASTM D-160. Four measurements were made on each film studied. A summary of the GPC data obtained by Chevron staff for the twelve resins can be found in Table 4.2.

WAXS patterns of the films were obtained using a Philips 1720 tabletop generator (40 kV, 20 mA) to produce Ni filtered CuKα radiation of wavelength 1.54Å. A Warhaus camera under vacuum was used to obtain flat plate photographs of the scattered intensity for exposure times of 1 hour. Multiple layers of film were stacked such that the MD and TD directions remained parallel from one layer to the next, producing a sample approximately 1mm thick for examination. Additional WAXS pole figure data were collected on selected samples at AMIA Labs of The Woodlands, Texas.

Table 4.1. Summary of key parameters for each film studied. MI = melt index, BUR = blow up ratio, QT = quench time parameter, MD = machine direction extension parameter, MVTR = moisture vapor transmission rate in g-mil/100^2/day

Sample	catalyst	MI	Output	Die Gap	Frost Line	BUR	Line Speed	Gauge	QT	MD	Average MVTR
			(lb/hr)	(cm)	(cm)		(ft/min)	(mil)	(sec.)		
S1	CrO	1	100	0.16	15.25	2.9	90	1.23	1.58	14.17	0.27
S2	CrO	1	100	0.16	15.25	2.9	45	2.5	3.06	7.09	0.25
S3	M	0.9	100	0.16	15.25	2.9	90	1.23	1.58	14.17	0.26
S4	M	0.9	100	0.16	15.25	2.9	45	2.5	3.06	7.09	0.26
S5	M	0.85	100	0.16	15.25	2.9	90	1.23	1.58	14.17	0.27
S6	M	0.85	100	0.16	15.25	2.9	45	2.5	1.04	7.09	0.23
S7	M	1.5	100	0.16	15.25	2.9	90	1.23	1.58	14.17	0.26
S8	M	1.5	100	0.16	10	2.9	90	1.23	1.04	14.17	0.29
S9	M	1.5	100	0.1	15.25	2.9	90	1.23	1.55	8.86	0.26
S10	M	1.5	62	0.1	15.25	2.9	90	0.76	1.58	14.29	0.27
S11	M	1.5	100	0.16	15.25	2.9	45	2.46	3.06	7.09	0.24
S12	M	0.35	100	0.16	15.25	2.9	90	1.23	1.58	14.17	0.30
S13	M	0.35	100	0.16	10	2.9	90	1.23	1.04	14.17	0.32
S14	M	0.35	100	0.1	15.25	2.9	90	1.23	1.55	8.86	0.30
S16	M	0.35	100	0.16	15.25	2.9	45	2.46	3.06	7.09	0.29
S17	CrO	1	100	0.16	15.25	2.9	90	1.23	1.58	14.17	0.25
S18	CrO	1	100	0.16	10	2.9	90	1.23	1.04	14.17	0.28
S19	CrO	1	100	0.1	15.25	2.9	90	1.23	1.55	8.86	0.28
S20	CrO	1	62	0.1	15.25	2.9	90	0.76	1.58	14.29	0.27
S21	CrO	1	100	0.16	15.25	2.9	45	2.46	3.06	7.09	0.26
S22	CrO	1.7	100	0.16	15.25	2.9	90	1.23	1.58	14.17	0.25
S23	CrO	1.7	100	0.16	10	2.9	90	1.23	1.04	14.17	0.29
S24	CrO	1.7	100	0.1	15.25	2.9	90	1.23	1.55	8.86	0.27
S25	CrO	1.7	62	0.1	15.25	2.9	90	0.76	1.58	14.29	0.28
S26	CrO	1.7	100	0.16	15.25	2.9	45	2.46	3.06	7.09	0.22
S27	M	0.8	100	0.16	15.25	2.9	90	1.23	1.58	14.17	0.27
S28	M	0.8	100	0.16	15.25	2.9	45	2.46	3.06	7.09	0.26
S29	M	0.6	100	0.16	15.25	2.9	90	1.23	1.58	14.17	0.28
S30	M	0.6	100	0.16	15.25	2.9	45	2.46	3.06	7.09	0.26

Sample	catalyst	MI	Output	Die Gap	Frost Line	BUR	Line Speed	Gauge	QT	MD	Average MVTR
			(lb/hr)	(cm)	(cm)		(ft/min)	(mil)	(sec.)		
S33	M	2.01	100	0.16	15.25	2.9	90	1.23	1.58	14.17	0.28
S34	M	2.01	100	0.16	15.25	2.9	45	2.46	3.06	7.09	0.23
S35	M	0.93	100	0.16	15.25	2.9	90	1.23	1.58	14.17	0.27
S36	M	0.93	100	0.16	10	2.9	90	1.23	1.04	14.17	0.30
S37	M	0.93	100	0.1	15.25	2.9	90	1.23	1.55	8.86	0.30
S38	M	0.93	62	0.1	15.25	2.9	90	0.76	1.58	14.29	0.28
S39	M	0.93	100	0.16	15.25	2.9	45	2.46	3.06	7.09	0.24
S40	M	0.95	100	0.16	15.25	2.9	90	1.23	1.58	14.17	0.27
S41	M	0.95	100	0.16	10	2.9	90	1.23	1.04	14.17	0.27
S42	M	0.95	100	0.1	15.25	2.9	90	1.23	1.55	8.86	0.30
S43	M	0.95	62	0.1	15.25	2.9	90	0.76	1.58	14.29	0.27
S44	M	0.95	100	0.16	15.25	2.9	45	2.46	3.06	7.09	0.24
S45	M	0.55	100	0.16	15.25	2.9	90	1.23	1.58	14.17	0.27
S46	M	0.55	100	0.16	10	2.9	90	1.23	1.04	14.17	0.29
S47	M	0.55	100	0.1	15.25	2.9	90	1.23	1.55	8.86	0.30
S48	M	0.55	62	0.1	15.25	2.9	90	0.76	1.58	14.29	0.31
S49	M	0.55	100	0.16	15.25	2.9	45	2.46	3.06	7.09	0.27

One dimensional SAXS data was collected using a Braun position sensitive detector fitted to an evacuated Kratky compact camera with slit columnation. A Philips 1719 tabletop generator (40 kV, 20 mA) was used to produce Ni filtered CuKα radiation of wavelength 1.54 Å. Intensity data was corrected for parasitic scattering and normalized relative to a Lupolen standard.

Small angle light scattering (SALS) data was obtained by recording the scattering profiles obtained with a He-Ne laser (ë= 632.8 nm) on Polaroid film. Crossed polarization of the polarizer and analyzer were used in all cases, thus only H_v patterns were recorded. The sample to film distance was fixed at 10 cm, while the exposure time was varied, based upon film thickness, to yield appropriate levels of brightness and contrast. Each sample consisted of a single layer of film sandwiched between two glass slides. Furthermore, spurious scattering from the surfaces of the film was reduced by coating each side of the film with a non-interacting silicone based oil of refractive index, 1.530.

Field emission scanning electron microscopy (FESEM) was utilized to observe the surface structure of the films. A Leo system 1550 FESEM at an operating voltage of 2 kV was utilized. Samples were prepared for viewing by sputtering with a five nanometer thick layer of Platinum/Palladium.

Transmission electron microscopy (TEM) results were obtained using the following procedure. Small rectangular samples were carefully cut from the original films, such that the film MD and TD could be identified throughout the process, to serve as reference axes during observation. These samples were stained in chlorosulfonic acid for 6 hours at 60 °C, and subsequently rinsed in concentrated sulfuric acid three times followed by three additional rinsing steps in water. The staining procedure was required to obtain sufficient contrast between the amorphous and crystalline phases. The stained samples were then embedded in an epoxy matrix and cured at room temperature overnight. The embedded samples were ultramicrotomed with a diamond knife to produce cross sections approximately 80 nm in thickness. These thin sections were then soaked in a solution of uranyl acetate (0.7 wt%) for one hour to enhance stability in the

microscope. Viewing was performed on a Philips EM 420 TEM at an operating voltage of 100 kV.

Measurements of the films' refractive indices in three orthogonal directions (MD, TD, and ND) were obtained using a Metricon 2010 prism coupler. In addition to using the values to calculate birefringence data, the average values from these measurements were used to determine crystalline content by applying the Lorentz-Lorenz equation as discussed by others[31,32]. Individual values of the refractive index were found to be reproducible within approximately +/- 0.0003.

Complex viscosity data was obtained using a TA instruments AR 1000 rheometer. A parallel plate configuration with 1.5 mm gap, was used to collect data at a strain amplitude of 5% over a frequency range spanning from 0.314 –314 rad/sec at 160, 190, 210, and 220 °C. Samples were compression molded at 200 °C for 5 minutes into 1" diameter discs suitable for use in the rheometer. A fresh sample, along with a nitrogen purge, was utilized at each temperature.

The crystalline content of the films, as determined through the heat of melting, was measured using a Perkin-Elmer series 7 differential scanning calorimeter (DSC). A sample size of approximately 5 mg and heating rate of 30 C/min were employed with nitrogen purge. Instrument calibration was achieved using an indium standard.

The densities of the films studied were determined by Chevron staff using a density gradient column in accordance with ASTM D 1505-85.

Tensile stress-strain data was collected using an Instron, model 1120, with crosshead speed of 1"/min. Dog bone shaped samples (width and gauge length of 4.5 mm and 17 mm respectively) were punched from the films along the MD and TD respectively. A total of 10-12 measurements were made for each film along both directions.

4.4 Resin Characterization

Twelve HDPE resins of varying molecular weight (MW), molecular weight distribution (MWD), and catalyst type were studied. A summary of the GPC results can be found in Table 4.2. Both metallocene and chromium oxide (CrO) based catalyst

systems were utilized. It is of interest to note that the metallocene resins used in this study have MWDs, as evidenced by their polydispersity values (PI ~ 5.5), which are substantially broader than those typically associated with resins produced by these catalyst systems (PI ~ 2). The CrO based systems have even broader MWDs, as expected, with PI values larger than eight. While the GPC curves are not available for direct analysis, one can obtain an impression of the relative amounts of low and high molecular weight species by examining the various molecular weight averages. In Fig.4.1 the molecular weight associated with the peak of the GPC curve (M_p) along with the first four moments of the MWD are plotted for each resin. While all of the resins share approximately the same M_p, it is clear that the CrO resins are of broader MWD, as evidenced by their lower M_n values yet greater M_{z+1} values, relative to the metallocene based resins. Furthermore, the larger M_{z+1} values of the CrO resins implies that these materials have a greater amount of high molecular weight material, which may in turn strongly influence the processing characteristics of these resins.

To better understand the potential differences in processability among the resins, rheological measurements were made. Complex viscosity data as a function of frequency and temperature were obtained for each resin as outlined in the experimental section. For a review of the Carraeu-Yasuda (C-Y) model and the physical interpretation of the parameters, the reader is referred to the earlier literature review section. A summary of the parameters obtained from these measurements is given in Table 4.3. The results from two representative samples are presented in Fig.4.2. In this plot the deformation response of resins A and I, CrO and metallocene based materials respectively, are compared. These two resins were chosen because, based upon the GPC results, they have identical M_w values (113 kg/mol). This noted, it can be seen that their rheological behavior is different. The data indicates that the CrO resin has a greater rheological dispersity, thus it undergoes shear thinning over a broader range of shear rates. Also, if one extrapolates the data to zero shear rate, it becomes apparent that the CrO has a greater zero shear viscosity. Indeed, the parameters obtained from fitting the data to the C-Y model are η^*_0 = 73,700 and 24,900 Pa-sec, and a = 0.206 and 0.264 for the CrO and metallocene resins, respectively. Recall, that the magnitude of the parameter, a, is inversely related to the breadth of the shear thinning transition. Typically, the

Table 4.2. Summary of GPC results. Abbreviations are as follows: S – sample number, MI – melt index, M_n – number average molecular weight, M_w - weight average molecular weight, M_z – z average molecular weight, PI – polydispersity index (M_w/M_n), CrO – Chromium Oxide, M – metallocene.

Resin	Catalyst	S	MI	M_n (kg/mol)	M_w (kg/mol)	M_z (kg/mol)	M_{z+1} (kg/mol)	PI
A	CrO	1-2, 17-21	1	14	113	709	2,000	8.08
B	M	3-4	0.9	23	123	620	1,690	5.28
C	M	5-6	0.85	23	118	550	1,250	5.05
D	M	7-11	1.5	21	106	546	1,530	5.10
E	M	12-16	0.35	27	150	713	1,850	5.57
F	CrO	22-26	1.7	13	105	696	2,050	8.16
G	M	27-28	0.8	23	131	626	1,680	5.77
H	M	29-30	0.6	24	130	644	1,700	5.42
I	M	33-34	2.01	21	113	555	1,570	5.45
J	M	35-39	0.93	24	115	571	1,570	4.77
K	M	40-44	0.95	19	117	689	1,780	6.01
L	M	45-49	0.55	21	141	776	1,910	6.71

Table 4.3. Summary of rheological parameters. The complex zero shear viscosity (η_o^*), characteristic viscous relaxation time (τ), and rheological breadth parameter (a) were obtained by fitting complex viscosity vs. frequency data collected at 190 C to the Carreau-Yasuda model. Activation energy (E_a) determined from temperature dependance of η_o^*. Number of long chain branches per 10,000 carbons (LCB) obtained by Janzen-Colby analysis at 190 C. See text for details.

Resin	Catalyst	MI	M_w (kg/mol)	PI	η_o^* (Pa-s)	τ (s)	a	E_a (kJ/mol)	LCB
A	CrO	1	113	8.1	73,700	0.137	0.206	21	0.13
B	M	0.9	123	5.3	42,400	0.103	0.267	20	0.06
C	M	0.85	118	5.1	42,300	0.137	0.278	26	0.08
D	M	1.5	106	5.1	19,900	0.051	0.276	26	0.06
E	M	0.35	150	5.6	112,000	0.285	0.251	25	0.06
F	CrO	1.7	105	8.2	42,200	0.059	0.210	25	0.12
G	M	0.8	131	5.8	42,600	0.116	0.264	23	0.05
H	M	0.6	130	5.4	59,400	0.137	0.268	23	0.07
I	M	2.01	113	5.5	24,900	0.052	0.264	24	0.06
J	M	0.93	115	4.8	27,700	0.062	0.260	24	0.06
K	M	0.95	117	6.0	74,400	0.282	0.245	26	0.12
L	M	0.55	141	6.7	115,000	0.373	0.247	24	0.08

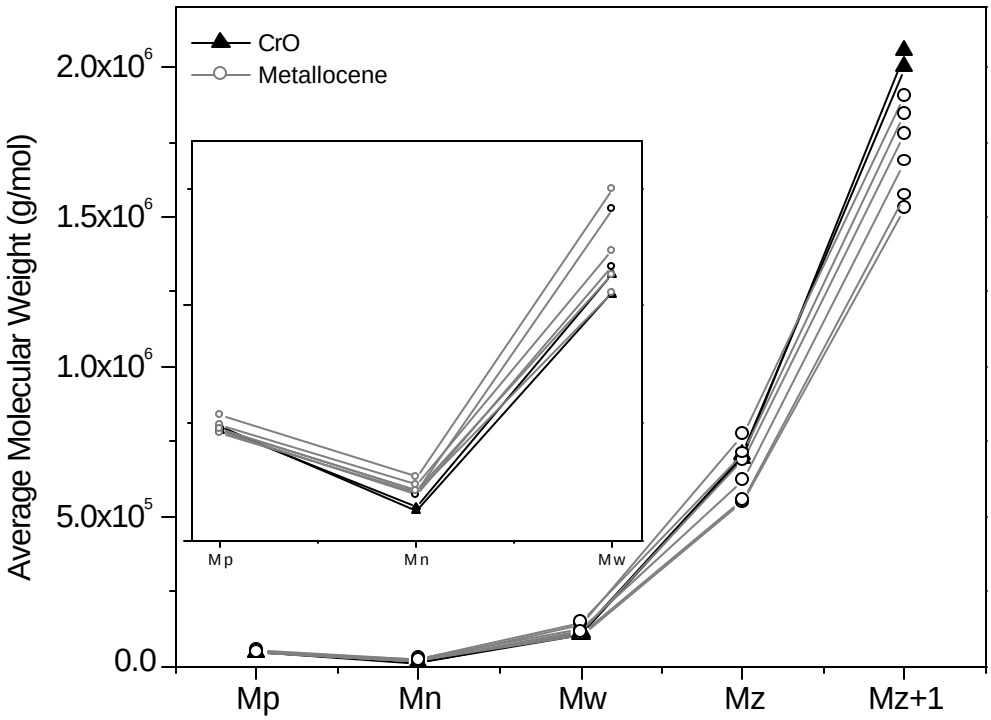

Figure 4.1. Peak molecular weight (M_p) and first four moments of the molecular weight distribution for each of the resins studied. Note that while all resins have approximately the same M_p, the CrO resins, because of their greater MWD breadth, have lower M_n values and greater M_{z+1} than the metallocene based resins. Inset plot contains magnified view of M_p through M_w data.

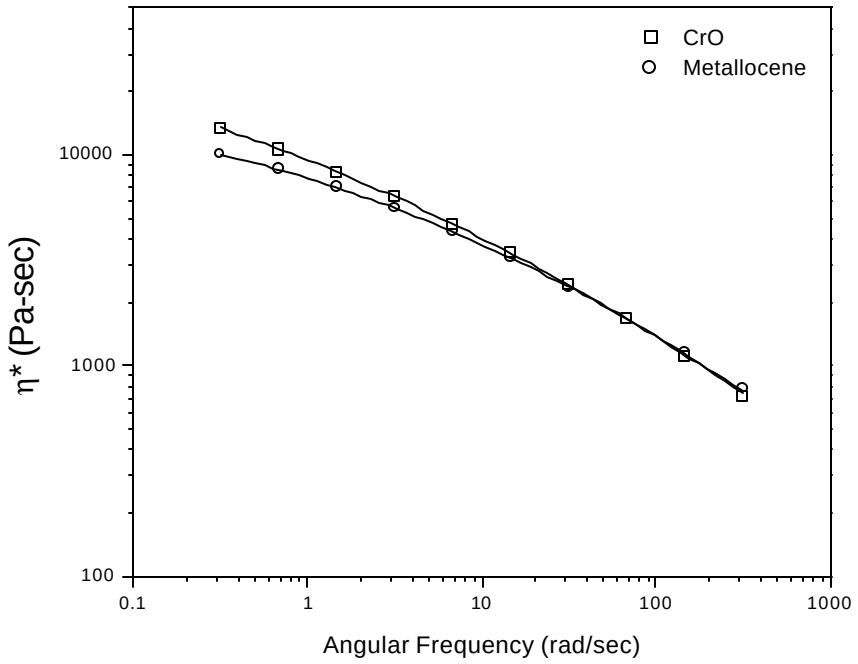

Figure 4.2. Oscillatory parallel plate rheometric results for two representative resins obtained at 190 C. The resins used are A (CrO) and I (Metallocene). Note that these resins have identical values of M_w, 113 kg/mol. Solid lines result from fitting data to C-Y model. The relative shapes of the viscosity curves indicate that a broader transition zone for and greater viscosity in the limit of zero shear rate for the CrO based resin.

dependence of the zero shear viscosity of polymer melts on molecular weight increases rapidly above the critical molecular weight for entanglement. While below this critical M_w a direct proportionality is noted, above this threshold, the zero shear viscosity scales with M_w to the 3.4 power ($\eta_0 \sim M_w^{3.4}$) for linear chains. The M_w associated with this change in behavior in PE is approximately 3,800 g/mol. Experimental work by Arnett et al.[33] has demonstrated that a completely linear, narrow MWD PE should obey the following relationship at 190 °C:

$$\eta_0 = 5.8 \times 10^{-14} M_w^{3.41} \qquad \text{Eq.4.6}$$

According to Raju[34], and quoting Larson[35], "polydispersity (without LCB) is thought to produce little or no deviation…" from the above relationship. Because the two resins from Fig.4.2 have identical M_w, but different η_0 values, it is possible that the two catalyst technologies used in this study may produce resins with different LCB levels. An indication of LCB content in each resin can be found in Fig.4.3. Here the zero shear viscosity results obtained at 190 °C are plotted along with Eq.4.6. All of the resins examined display positive deviations from the idealized, linear case. The effect is somewhat greater in the two CrO based materials. These positive deviations, while small, suggest that all of the resins may posses a finite fraction of LCB material. To quantify this behavior, two methods of analysis were applied to the rheological data.

It is known that the incorporation of LCB alters the temperature sensitivity of viscosity in polymer melts. The effect of LCB is to increase the temperature dependence of viscosity. An index of this sensitivity can be obtained by calculating the flow activation energy. This value can be obtained through time-temperature superposition of dynamic viscosity or loss modulus data, and noting the temperature dependence of the shift factor. Similar results can be obtained by fitting the variation in zero shear viscosity with temperature to a function of Arrhenius form. The latter method was applied in the calculation of flow activation energies here. A representative plot of the rheological data (resin C) used to produce these results is provided in Fig.4.4. Zero shear viscosities were determined at each temperature by fitting the data to the C-Y model.

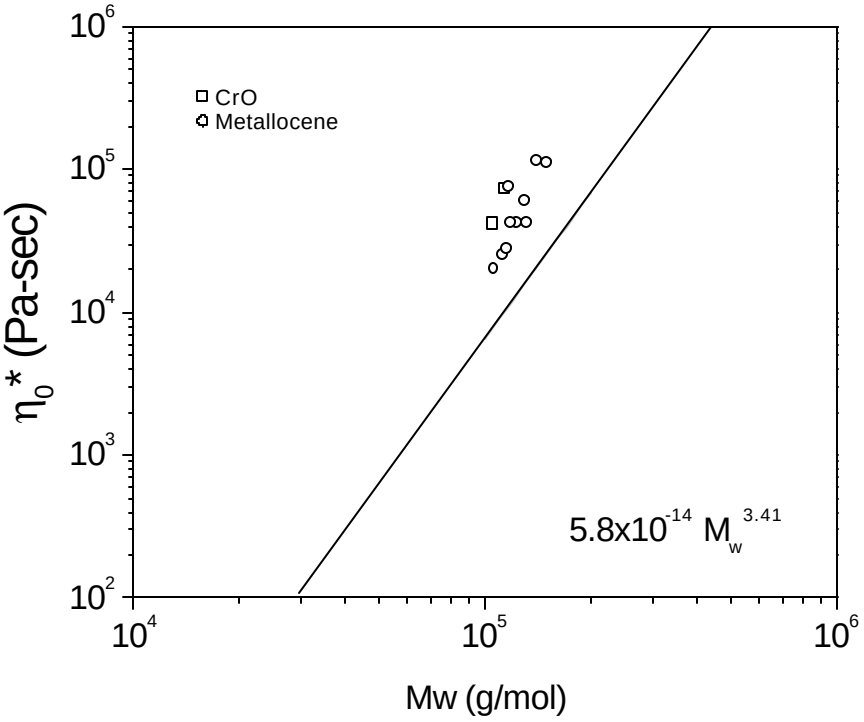

Figure 4.3. Comparison of measured zero shear viscosities at 190 C with theoretical values for completely linear PE chains by Arnett and Thomas[33].

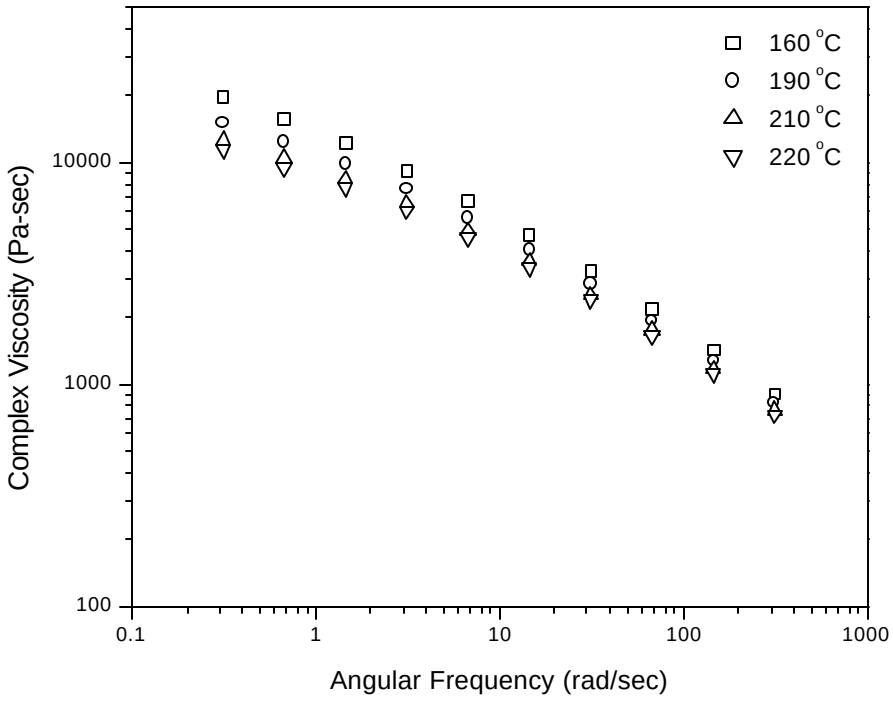

Figure 4.4. Complex viscosity data for resin C obtained at four temperatures, used in calculating flow activation energy.

To determine the flow activation energy, the natural logarithms of these values were plotted against the corresponding reciprocal temperature of measurement and the slope determined, as suggested by the following equation:

$$h_0^*(T) = Ae^{\Delta Ea/RT} \qquad \text{Eq.4.7}$$

where ΔE_a is the flow activation energy, R is the gas constant, and A is the pre-exponential factor. This plot is shown in Fig.4.5. While values of roughly 23 kJ/mol are normal for linear PE materials, highly branched, low density PE resins typically yield values on the order of 37 kJ/mol[36]. The value obtained for the data presented in the previous two figures, resin C, a metallocene resin, is 26 kJ/mol. The values for all of the materials studied can be found in Table 4.3. When one considers that the error associated with this measurement is about +/- 3 kJ/mol, it is evident that metallocene resin C does indeed fall into the linear category. Reviewing the results in Table 4.3 it is also apparent, due to the highly similar results obtained for each material, that this method of analysis is not sensitive enough to discern any possible differences in LCB among the resins. This result is in agreement with recent work by Bin Wadud et al.[37] which showed that very low levels of LCB could not be differentiated by flow activation energy analysis.

The second method employed to evaluate LCB content was that due to Janzen and Colby[38]. The reader is referred to the original source for a detailed description. This analysis allows the measured deviation in η_0, from the theoretical, completely linear value to be used in quantifying the number of LCBs present. The results of the analysis are summarized in Table 4.3, and plotted in Fig.4.6. It should be noted that despite the need for extrapolation to obtain η_0^* values, duplicate runs demonstrated that the results could be reproduced within better than 10%. Taking 10% as an upper error limit, at the highest MW studied (the effect of LCB on η_0 increases with MW), this translates into ~ 6% error in LCB content determination. Thus, the differences in LCB content displayed in Fig.4.6 are meaningful. The CrO resins contain approximately twice the number of LCBs per 10,000 carbons as the metallocene catalyzed resins with the exception of resin K. The apparent discrepancy for resin K is not understood at this time.

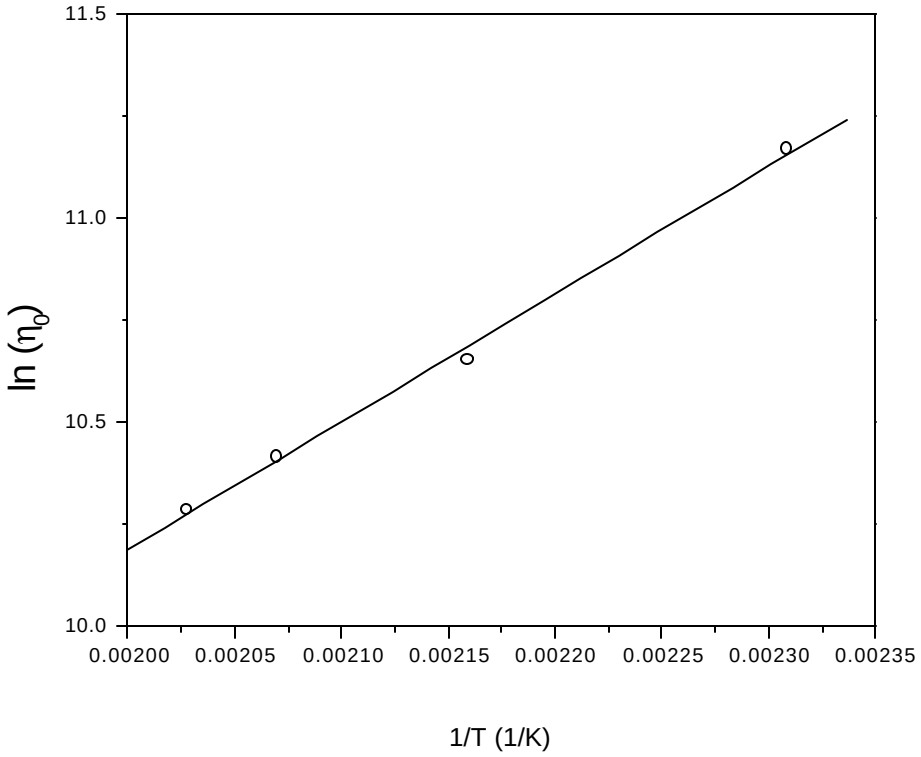

Figure 4.5. Arrhenius plot to determine the flow activation energy of resin C.

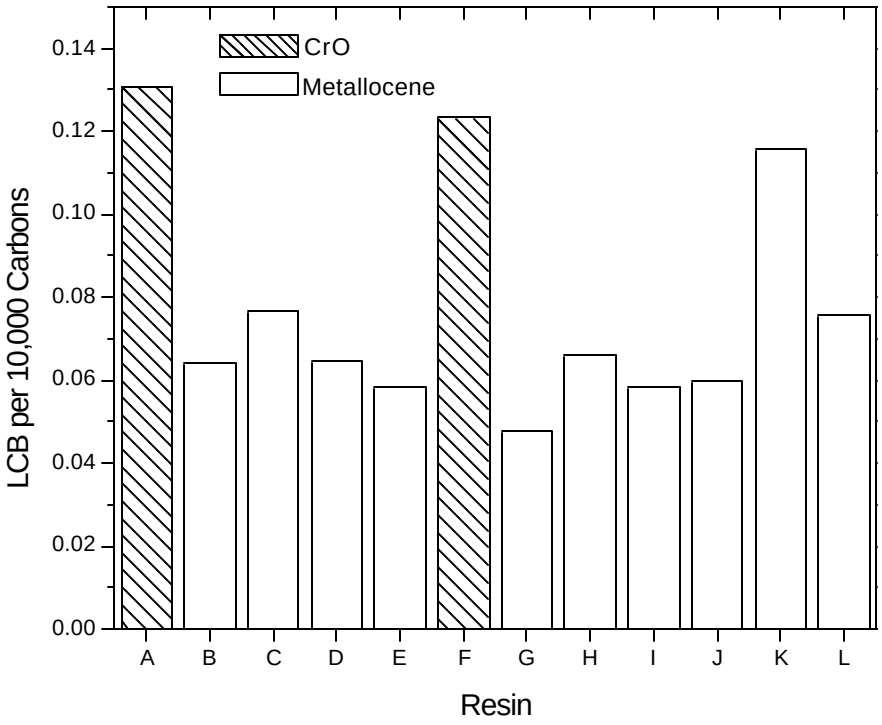

Figure 4.6. Results of LCB analysis due to Janzen and Colby[38].

It should be stated that although the focus here is on comparisons of LCB content between resins with respect to catalyst type, it cannot be known a priori from this data if the LCBs are due to the catalysts themselves. Degradation during pelletization can introduce LCBs to an initially completely linear material. The focus of this chapter is to understand how the interaction of process and resin variables establishes end product morphology and performance. Thus, while the data does not show that the CrO catalyst was responsible for introducing greater LCB than the metallocene systems, it can be stated that, with the exception of resin K, the CrO resins have about twice the LCB content of the metallocene materials examined.

The results of the resin characterization work can be summarized as follows. GPC results demonstrated that the CrO based resins are of greater polydispersity. A consequence of this broader MWD can be noted from the upper moments of the MWD which show that the CrO resins have a greater fraction of very high molecular weight species. The GPC results are suggestive of a more substantial high molecular weight tail in the CrO based materials.

The rheological data confirmed the greater polydispersity of the CrO based materials as they have a broader transition from Newtonian to shear thinning behavior. Furthermore, positive deviations in η_0^*, as a function of M_w, from that of the ideal linear PE chain indicated that all of the resins studied contain a small, but observable amount of LCB.

Additional analysis demonstrated that while the use of flow activation energy is not sensitive enough to differentiate the LCB contents of the materials used in this study, the method of Janzen was sufficient. The LCB content of the CrO resins, ~ 0.12 LCB per 10,000 carbons, is roughly double that of the metallocene resins studied.

4.5 Morphological Characterization

To better understand the structures and orientation states that affect barrier performance, a series of 46 films was examined. The resins and processing conditions used to produce these films are summarized in Table 4.1. Up to five different processing conditions were employed for each resin by altering the die gap, frost line height (FLH),

extruder output, and line speed (haul off speed). In Table 4.1, the first film listed for each resin was produced by what was referred to earlier as the base set of processing conditions. When describing the conditions used to produce a given film, the parameters will be indicated relative to this base condition. Thus, film s2 would be referred to as being processed with reduced line speed, as all of the other processing conditions used were identical to that of the base case. Not all conditions were studied for all resins.

Based upon the background discussion, it is expected that the overall crystalline content of the films will play a major role in determining barrier performance. Recall that the permeation rate is expected to scale with the square of the amorphous content, other effects, such as orientation, absent. Therefore, the morphological characterization will begin by quantifying the level of crystallinity found in each film. Three different methods were employed to determine the crystalline content of the films; density gradient column, refractive index, and DSC. The accuracy of each method will be contrasted with the others.

Subsequent sections will concern themselves with the quantification of orientation. Overall crystallinity and crystalline phase orientation will be examined. The techniques employed are WAXS, SAXS, FESEM, TEM, IR dichroism, SALS, and birefringence. At times the data will be correlated with resin and processing parameters when presenting the morphological data. However, connections between morphology and permeation performance will be delayed until the latter portion of the chapter.

4.5.1 Crystalline Content Determination

As stated above, three independent methods were used to determine crystallinity. The density gradient column technique, however, was not applied to films s33-s49. In all calculations a two phase model was assumed with amorphous phase[39] and crystalline phase[40] densities of 0.852 and 1.010 g/cm^3 respectively under ambient conditions. The heat of fusion of a wholly crystalline PE sample[41] was taken to be 293 J/g. The specific refraction, r, in the Lorentz-Lorenz equation, shown below, allows one to relate the average measured refractive index of a sample to its density.

$$\frac{n^2-1}{n^2+2}\frac{1}{\rho}=r \qquad \text{Eq.4.8}$$

The terms n and ρ represent the average refractive index and density of the sample. The application of refractometry for use in crystallinity determination has been reviewed in the literature[31,32]. Here, the specific refraction was taken as 0.3272 in accordance with Krishnaswamy's results[32].

Beginning with the refractometry data, which is presented in Fig.4.7, it can be seen that the crystalline contents of the samples studied only span a range between 59% and 65% on a volume average basis. Small, but quantifiable differences can be noted among the films. Thus, it is expected that differences in crystalline content will play a role in determining much of the noted variation in barrier performance observed in this study. Similar plots could be presented for the DSC and density gradient column results; however, this would be redundant. An interesting observation can be made by comparing the results from each method directly as shown in Fig.4.8. Because the density gradient column is known to be very sensitive, and is widely applied by the polyolefins industry, it was chosen as the basis on which to compare the methods. Figure clearly shows that an excellent correlation between the refractometry and density gradient column results was achieved, with crystallinity values agreeing within +/- 1vol%. The DSC results display much more scatter. While using a slightly different value for the heat of fusion would shift the values relative to the other results, *it would not change the variance in the data*. The greater spread in the DSC data likely arises from the two separate measurements, heat of melting and sample mass, needed in this method. In contrast, the others require essentially one (the average of three measurements on the same film is required to obtain refractometry results). The small samples required by the DSC, to produce sharp melting endotherms, limits the accuracy with which the sample mass can be determined. In this study sample masses on the order of 5mg were employed, with mass measurements accurate to 0.1mg. Adding this source of error to the inherent difficulty in accurately assigning the limits for peak integration, likely accounts for the greater scatter observed by DSC. A further source of inaccuracy may arise from structural changes which take place during the heating scan (e.g. melting-recrystallization, lamellar thickening).

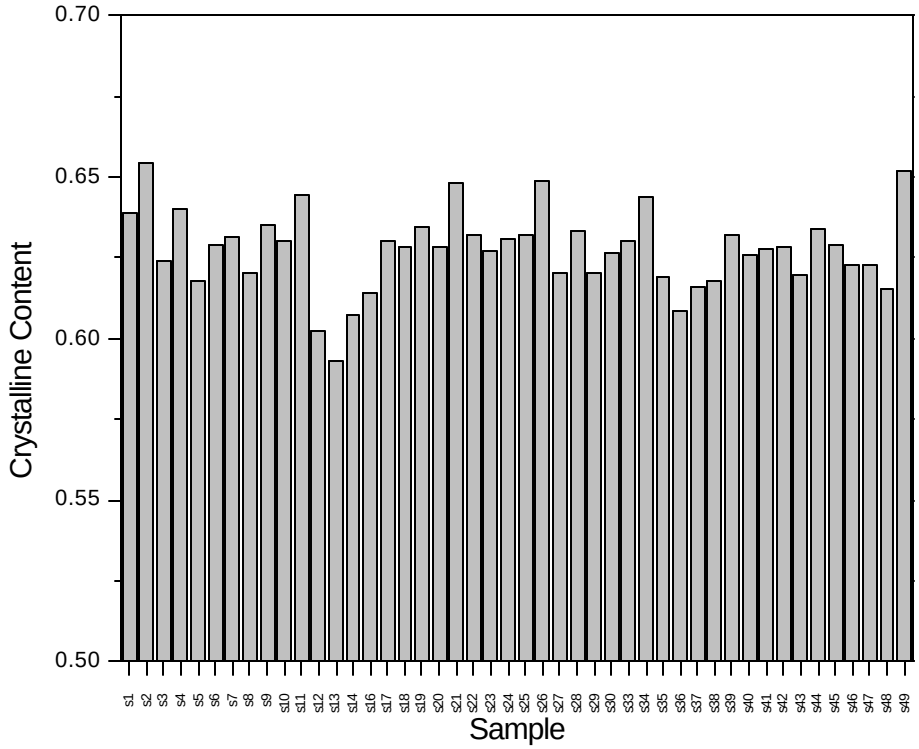

Figure 4.7. Crystalline content (volume basis) as determined by refractometry for all films.

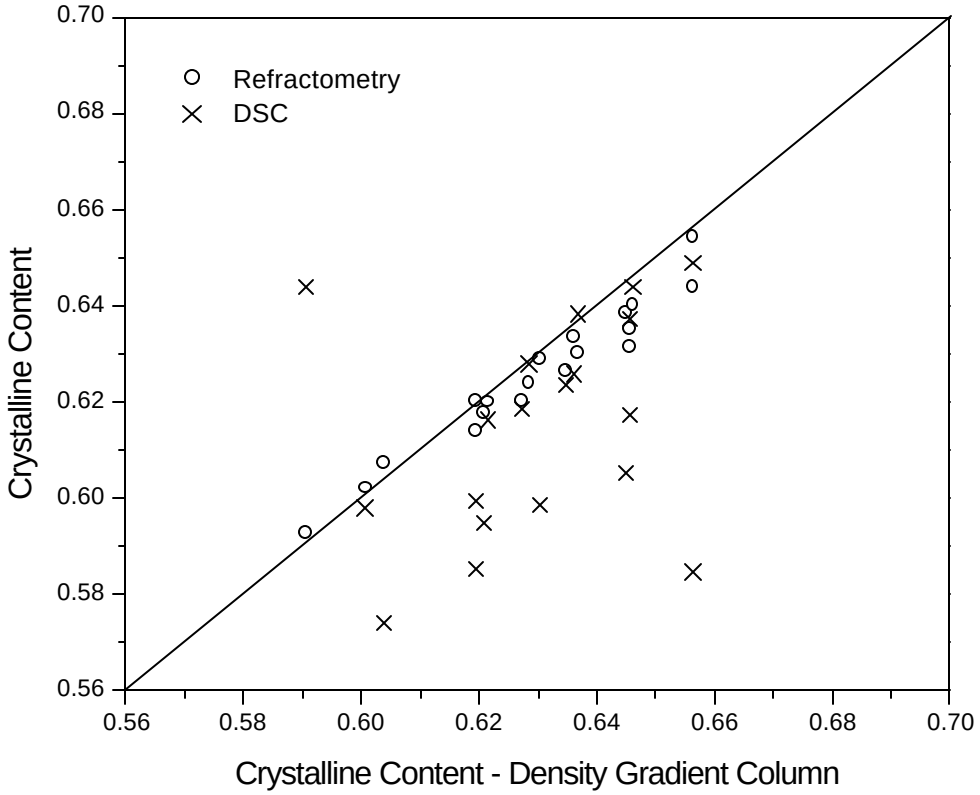

Figure 4.8. Comparison of three methods used to measure crystalline content (volume basis). The x-axis value corresponds to results obtained using a density gradient column. The y-axis values correspond to results obtained via refractometry and DSC. The diagonal line represents equivalent results between the methods. Data taken from samples s1-s30.

4.5.2 Wide Angle X-ray Scattering – Pole Figures

Two sources were identified in the review section as possible factors responsible for influencing permeation behavior. The first, crystalline content was discussed in the preceding section. The second source, state of orientation, will now be examined. The crystalline orientation of the films was investigated through x-ray scattering. While, flat plate photographic data was collected for all of the films, a select number were also submitted for pole figure analysis by an outside lab (AMIA Labs). Films s1-s6 were submitted for pole figure analysis as they represent the first set of films produced and examined in the study. Films s11, s12, and s18 were selected because they represent barrier performance extremes while at the same time sharing certain common resin or processing variables with films s1-s6. The (200) and (020) results for sample s4 are presented in Fig.4.9 as typical patterns for initial discussion. When analyzing the pole figures within this dissertation, recall the following: the intensity of scattering is proportional to brightness, scattering at the meridonal poles is indicative of MD orientation, scattering at the equatorial poles is indicative of TD orientation, and scattering at the center of the figure is indicative of ND orientation. The patterns of Fig.4.9 clearly indicate a preferential orientation of the crystalline a-axis along the film MD and preferential b-axis orientation along the TD. This texture is indicative of a nearly uniaxial, K-M low stress crystallized PE. It is important to note that although this film is the product of a biaxial melt deformation, it displays very little preferential TD orientation. In all cases the BUR was held constant at 2.9. Judging by this pole figure, and indeed the balance of the WAXS data yet to be discussed, it appears that over the range of conditions studied, this BUR was not sufficient to produce substantial TD oriented row structures. This point can be further addressed by plotting the pole figure results in the form of biaxial orientation functions.

A White-Spruiell orientation triangle, summarizing all of the pole figure results, can be found in Fig.4.10. Using this representation, positive values along the y-axis correspond to orientation parallel to the MD, while negative values indicate orientation perpendicular to the MD. In the same manner, the x-axis is indicative of TD orientation.

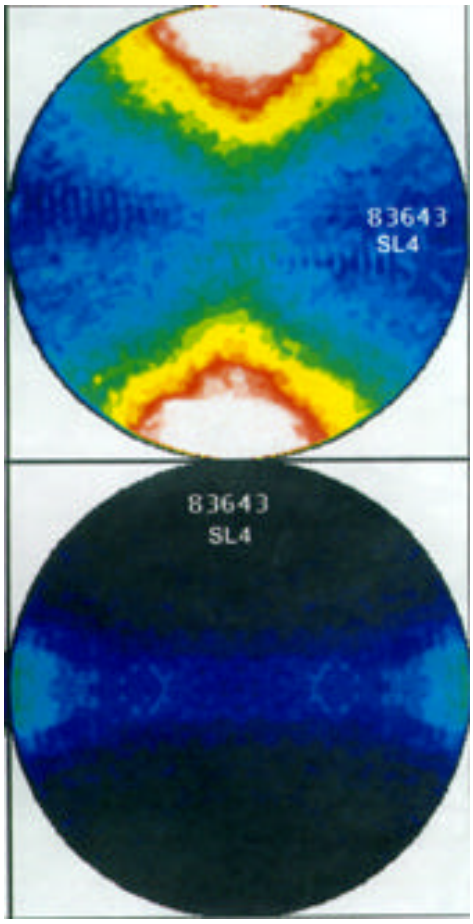

Figure 4.9. Upper - (200), lower – (020) pol figures for film s4. Intensity of scattering is proportional to brightness. Scattering at the meridonal poles is indicative of MD orientation, scattering at the equatorial poles is indicative of TD orientation, scattering at the center of the circle is indicative of ND orientation.

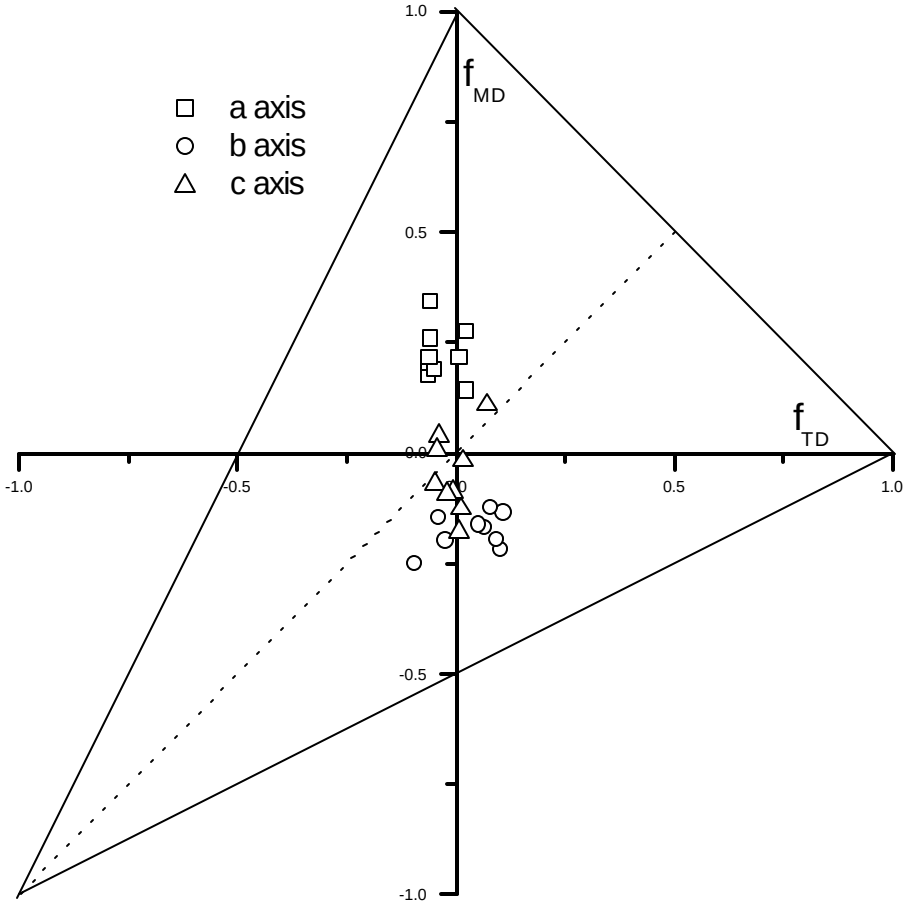

Figure 4.10. White-Spruiell orientation triangle derived from pole figure data.

This plot makes it clear that for the nine samples analyzed (s1-s6, s11, s12, and s18), a preferential orientation of the a-axis along the film MD exists. The c-axis is observed to have a low degree of orientation, and is noteworthy in its apparent randomness with respect to the film TD. Thus, the c-axis tends to remain in the MD-ND plane. Finally, the b-axis displays preferential orientation perpendicular to the film MD, being distributed along the TD-ND plane. All of these results are indicative of a moderately uniaxial, K-M low stress crystallized film. Thus, while quantifiable difference in the orientation states of the films exist, all the samples can be considered to consist of low stress, row nucleated morphologies. As with the crystallinity results, the variation among the samples is measurable, but small. Because the level of crystalline orientation obtained in blown films is substantially greater than that of the amorphous phase, these results further suggest that the level of amorphous orientation present in these films is very small. Shrinkage measurements will be used to confirm this hypothesis in the barrier properties section of the chapter.

The relative levels of orientation obtained when resin and processing variables are altered, will be addressed in the following series of pole figures, beginning with Fig.4.11. In this figure, a set of films (s1,s2,s18) produced from resin A under three different conditions is examined. Sample s1 represents the "base" operating conditions. Recall, that the entire set of conditions can be found in Table 4.1. Relative to the base processing conditions, film s2 resulted from decreasing the line speed (haul off rate), while in film s18 the FLH was reduced. Therefore, it is expected that sample s2 will be the least oriented, as it was given the greatest time for relaxation, while film s18 is expected to be the most oriented, as it was given the least amount of time for relaxation, prior to crystallization. Because the films are not of identical crystalline content, it is not possible to directly compare the intensity levels from one pole figure to the next. What can be noted, however, is the relative shapes and positions of the scattered intensity profiles. In Fig.4.11, it is observed from the (200) pole figure of sample s2 that the intensity maximum is less sharply focused at the MD (meridonal poles), relative to the other samples. Therefore, it appears that sample s2 is the least oriented of the specimens. This is in accordance with the expected behavior. No such simple observation can be made for the (020) data.

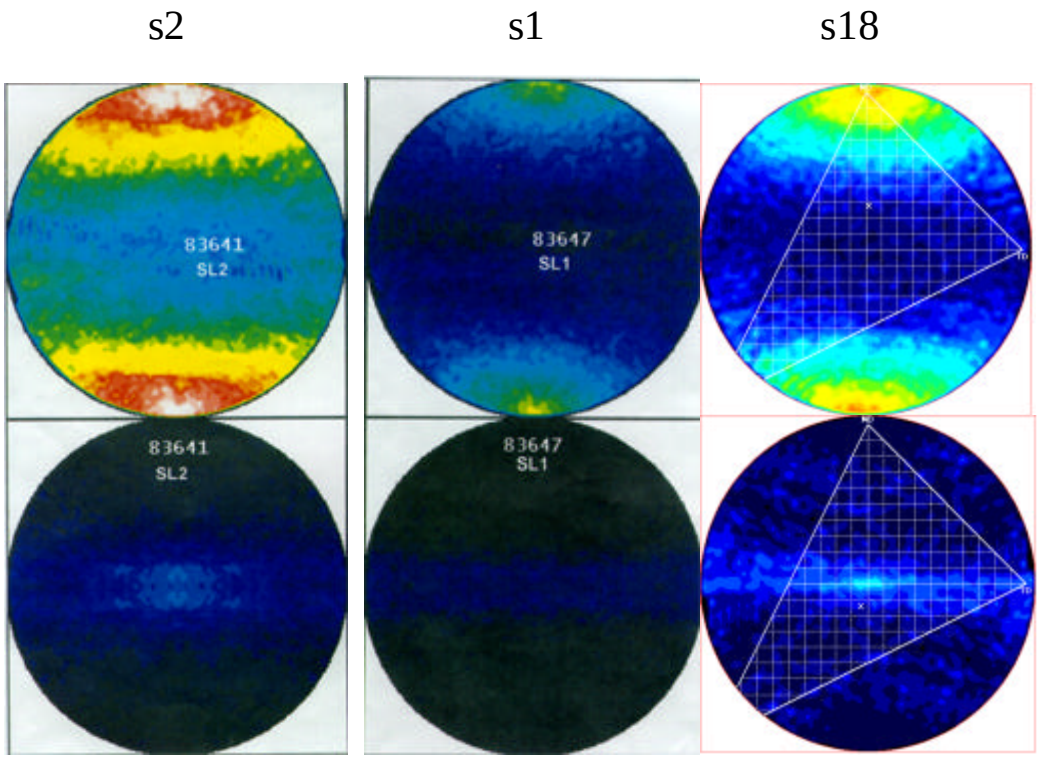

Figure 4.11. Upper – (200), lower – (020) pole figures for films s1, s2, and s18. Film set represents variation in processing conditions using resin A. Film s1 represents the "base" operating conditions. Film s2, decreased line speed. Film s18, decreased FLH. Based upon processing parameters, expect orientation to increase from left to right. See text for details. Pole figure for s18 contains a White-Spruiell orientation triangle imbedded in the background, which is not scattered intensity.

Data representing variation in M_w, for a constant set of processing conditions and catalyst type, are presented in Fig.4.12. The films, s4, s6, s12 were fabricated under the decreased line speed condition, and all are metallocene based. The M_w values of the films increase from left to right (s6 = 118 kg/mol, s4 = 123 kg/mol, s12 = 150 kg/mol), thus it is anticipated that the orientation level will also increase from left to right in the figure. While the differences in M_w between samples s4 and s6 may be too small to have any obvious effect on orientation, it is clear that sample s12 is substantially more oriented than the others, indicated by the narrower (200) intensity maximum along the MD.

A set of films allowing for a direct comparison among resins of identical M_w, but different catalyst technology, was not submitted for pole figure analysis. However, two films with similar M_w's, from the different catalysts, were submitted, and are compared in Fig.4.13. Sample s1 is CrO based (113 kg/mol) while sample s3 is metallocene based (123 kg/mol). Both films were produced using the base set of processing conditions. These two films provide interesting insight into the complexity of the problem. The pole figures indicate that film s3 is slightly more oriented along the MD than is sl1. This is to be expected, based on the relative M_w values. However, despite the lower M_w value, the resin used to produce sample s1 has a greater zero shear viscosity than the metallocene based resin (73,700 Pa-sec vs. 42,400 Pa-sec). The CrO resin also has a longer characteristic relaxation time (0.14 sec vs. 0.10 sec, +/- 0.01 sec). In the rheological characterization section this apparent discrepancy was ascribed to the slightly greater LCB content of the CrO based resins. Thus, while the C-Y parameters cited above suggest that sample s1 should produce the more highly oriented film, the M_w values suggest otherwise. No single value can be used to specify the entire relaxation spectrum, thus it is not surprising that such apparent contradictions arise from the application of only one parameter. *In this specific example, while the differences in the characteristic relaxation time are small, it appears that the M_w value is the better indicator.*

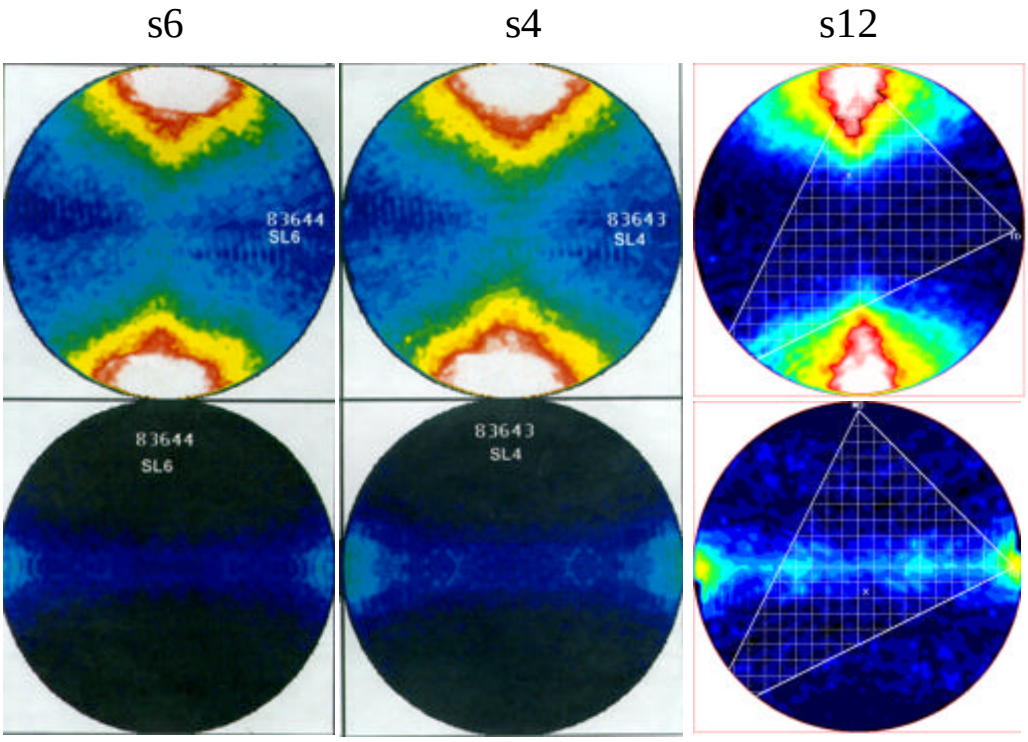

Figure 4.12. Upper – (200), lower – (020) pole figures for films s4, s6, and s12. Film set represents variation in resin molecular weight at constant catalyst type, metallocene, and constant processing conditions, decreased line speed set. Weight average molecular weight increases from left to right, thus expect orientation to increase form left to right. Pole figure for s12 contains a White-Spruiell orientation triangle imbedded in the background, which is not scattered intensity.

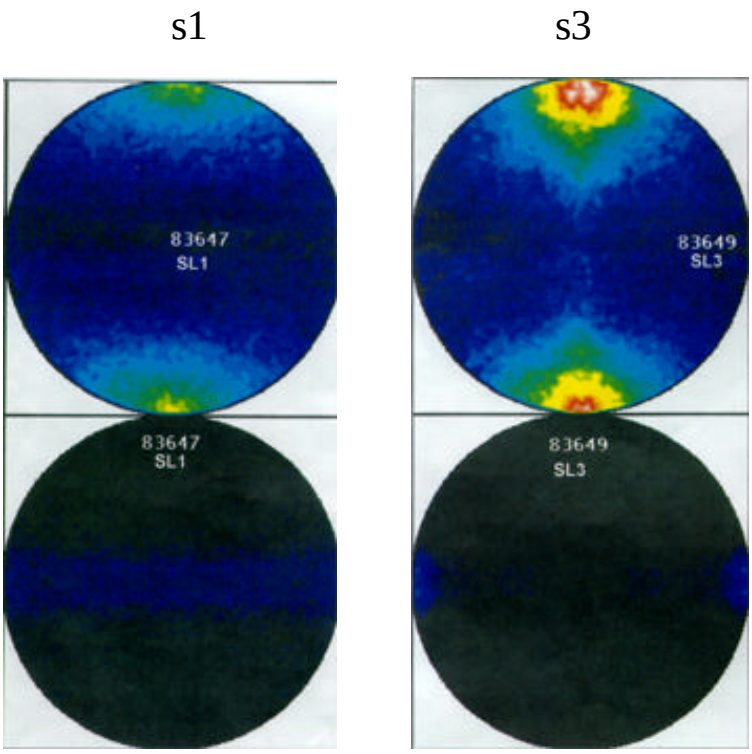

Figure 4.13. Upper – (200), lower – (020) pole figures for films s1 and s3. Film set represents variation in catalyst type, at constant processing condition, base set, Note that M_w values are 113 kg/mol and 123 kg/mol for the CrO based film, s1, and the metallocene based film, s3, respectively.

4.5.3 Wide Angle X-ray Scattering – Flat Plate Images

Flat plate WAXS patterns, while not containing as much information as the pole figure data, are a useful and simplified means for characterizing the state of crystalline orientation. This is especially true when a relatively simple state of orientation is present, such as the approximately uniaxial symmetry observed in these films, as demonstrated in the White-Spruiell orientation triangle of Fig.4.10. Unfortunately, because of the limited spread in orientation states encountered in these films, and the difficulty in quantifying the results with high precision, the assignment of orientation function values via this technique does not provide the necessary resolution to differentiate among the majority of the films. The two films which appear, visually, to represent the extremes of orientation found in this study are presented in Fig.4.14. In agreement with the pole figure results, these patterns show that the a-axis, (200) reflection, is preferentially oriented along the MD while the b-axis, (020) reflection, can be found along the film TD. These exposures are clearly indicative of K-M low stress crystallized films. Comparing the (200) and (020) reflections of the
two patterns, it is evident that sample s13 is more highly oriented than sample s11. This is expected as sample s13 was produced from a higher M_w resin and with less process time provided for relaxation. *The orientation levels of all other films examined in this study fall between these two extremes. This reinforces the earlier observation that differences in orientation among the films are real, though small in magnitude*.

4.5.4 Infrared Dichroism

A second method employed to quantify the state of crystalline orientation in this study was that of infrared dichroism. By measuring the absorbance of the 719cm^{-1} band with infrared radiation polarized parallel, and then perpendicular, to the film MD, it is possible to quantify its orientation. The 719cm^{-1} band in PE is known to arise from both crystalline and amorphous material, and is oriented parallel to the crystallographic b-axis.

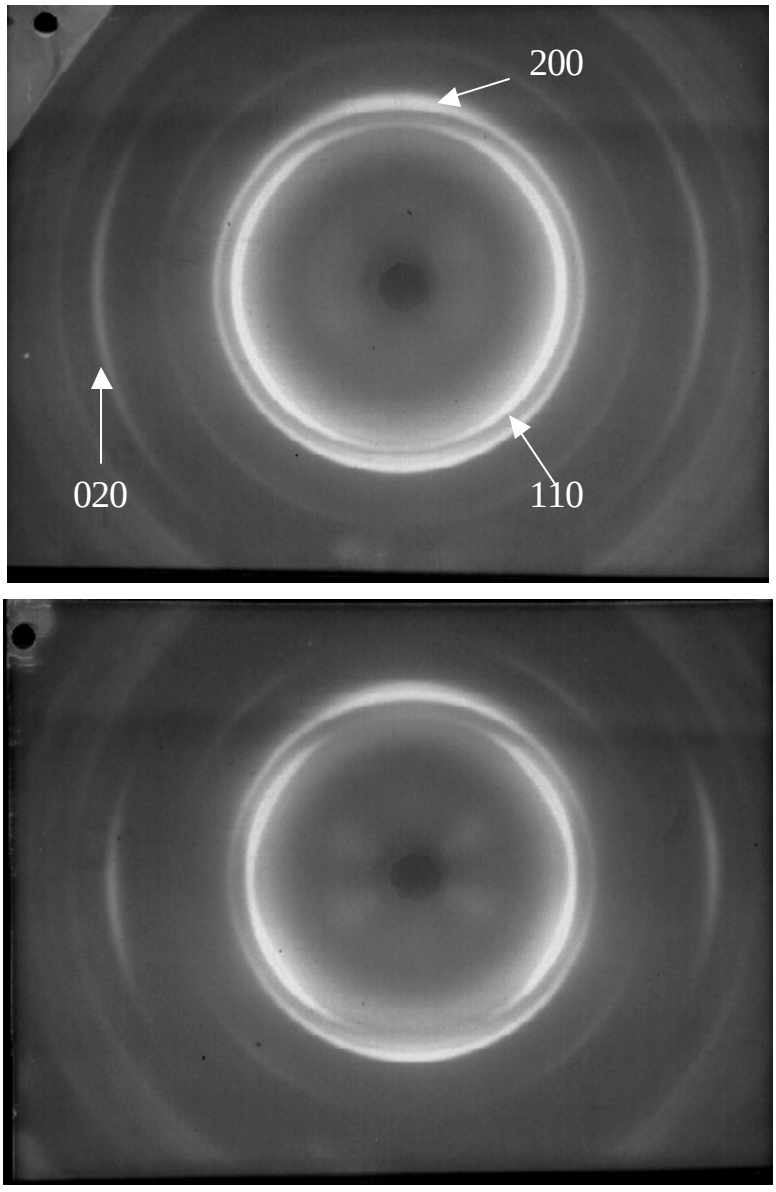

Figure 4.14. WAXS patterns of apparent crystalline orientation extremes of films studied. Upper pattern, s11 (metallocene, M_w=106 kg/mol, reduced line speed), lower pattern, s13 (metallocene, M_w=150 kg/mol, reduced FLH). MD vertical, TD horizontal – x-ray beam parallel to film ND. Key reflections are labeled in the upper pattern.

If one assumes that the level of amorphous phase orientation is small in comparison with that of the crystalline phase and fiber symmetry, the dichroic ratio obtained from the $719cm^{-1}$ band can be used to calculate the Hermans orientation function for the crystalline b-axis. The earlier WAXS results suggested that the films studied could be considered to have very little biaxial texture. Two example IR spectra, obtained with parallel and perpendicular polarization relative to the film MD are provided in Fig.4.15. The film examined in Fig.4.15 is sample s48. This sample was produced under conditions of reduced extruder output and die gap, resulting in a 0.76 mil thick film. Thus, film s48 belongs to the thinnest set of films examined in this study. Returning to Fig.4.15, inspection of the y-axis reveals that even at this thinnest gauge studied, the absorbance values measured by the instrument are quite large (~1.3). Values below one are typically considered ideal. Because of the logarithmic scaling of absorbance data, the plot exaggerates the observed differences in beam transmission when the absorbance is large. In practical terms, this means that the instrument is measuring a very small transmitted intensity (large absorbance) for the thinnest films studied. This situation will worsen as the film gauge is increased. Thus, while all of the films were characterized by this method, only the results from the thinnest films were of sufficient precision for comparative purposes. Figure 4.16 contains the orientation function results obtained from the IR dichroism measurements for the thinnest (0.76 mil) films (s10, s20, s25, s38, s43, s48) represented in the study. Here, the crystalline b-axis orientation is plotted as a function of resin M_w, a relation suggested by the pole figure results. Because the b-axis tends to align itself perpendicular to the MD as the orientation level is increased, larger negative values of f_b correspond to greater orientation. As anticipated, for identical processing conditions, the films produced with the higher M_w resins result in greater negative orientation.

A second trend, again suggested by the pole figure data, can be noted by comparing the relative orientation levels of those films which have approximately the same M_w, but different polydispersity values. The two lowest M_w films in Fig.4.16, samples s20 (CrO, M_w=105 kg/mol) and s10 (metallocene M_w=106 kg/mol) are of nearly identical weight average molecular weight. The dichroism results indicate that the narrower MWD resin resulted in greater negative orientation.

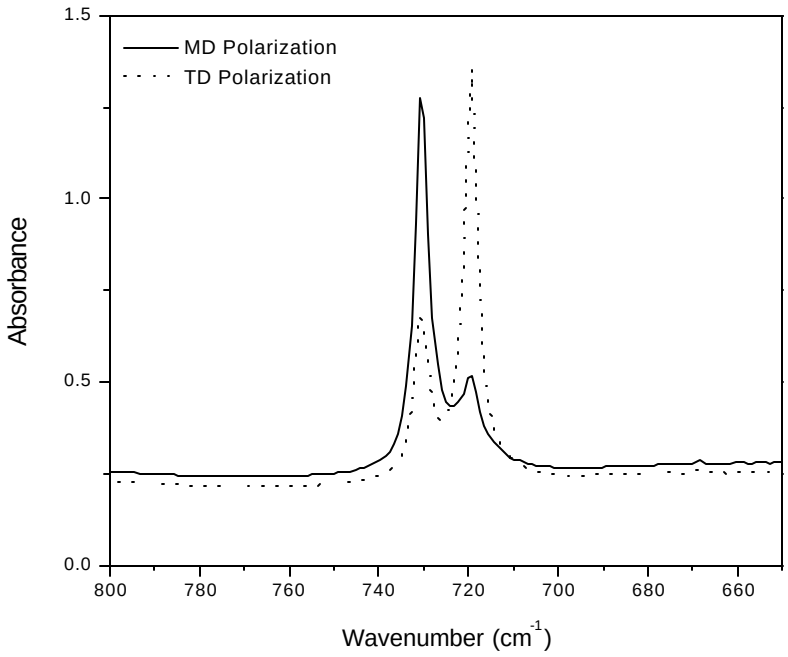

Figure 4.15. IR spectra of s48 with polarization parallel and perpendicular to the film MD. Absorbance band at 719 cm^{-1} is related b-axis crystalline orientation. When polarization is parallel to TD, 719 cm^{-1} absorption is maximized.

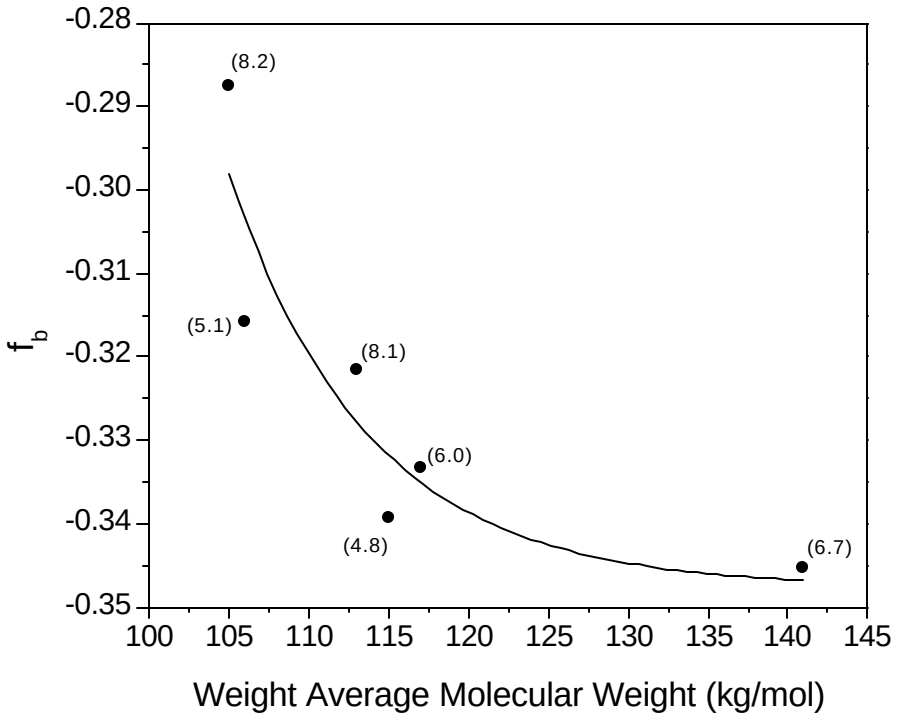

Figure 4.16. Hermans orientation function values obtained for the crystalline b-axis by IR dichroism. Films represented in plot are s10, s20, s25, s38, s43, s48 – the thinnest (0.76 mil) films represented in the study. Solid line provided as visual guide. Numbers in parentheses are polydispersity values for the resin used to make each film.

Indeed, it appears that differences in polydispersity may influence the level of orientation. Thus, the use of M_w alone does not completely explain the differences in orientation shown in Fig.4.16.

4.5.5 In-Plane Birefringence

Further quantification of the orientation state of the films was obtained through refractive index measurements. The same data which was used, with great accuracy, to determine the crystalline content of the films can also be used to calculate the in-plane birefringence, a measure of the optical anisotropy within the film. Being a positively birefringent material, the refractive index of PE is greatest parallel to the chain axis. Therefore, the direction of greatest refractive index should indicate the direction of preferential chain orientation. Like the dichroism data discussed previously, this method is not capable of describing the entire orientation distribution, rather it can only provide a second moment average. Thus, three orthogonal measurements of refractive index suffice to completely describe the birefringence of each film.

The in-plane birefringence results of the same films analyzed in Fig.4.16, are given in Fig.4.17. As it is expected that the higher M_w resins will orient to a greater extent, for identical processing conditions, it is anticipated that the birefringence should increase from left to right in Fig.4.17. This is the general result for all but the highest M_w film. Curiously, in contrast to the dichroism results, which showed that the highest M_w film contained the most highly oriented crystalline b-axis and thus implying substantial c-axis orientation, the birefringence data indicate that this film is the least oriented of the 0.76 mil films in the study. While this plot represents only six films out of the 46 films studied, this contradictory behavior was found to be quite characteristic of the birefringence results as a whole. The absence of consistent trends in the birefringence data is not fully understood at this time. It was noted in the literature review section that birefringence may arise from sources other than molecular orientation, the effect of form birefringence being of relevance to this study. Others in the literature[42] have noted this anomalous birefringent effect in polyolefin materials with lamellar morphologies.

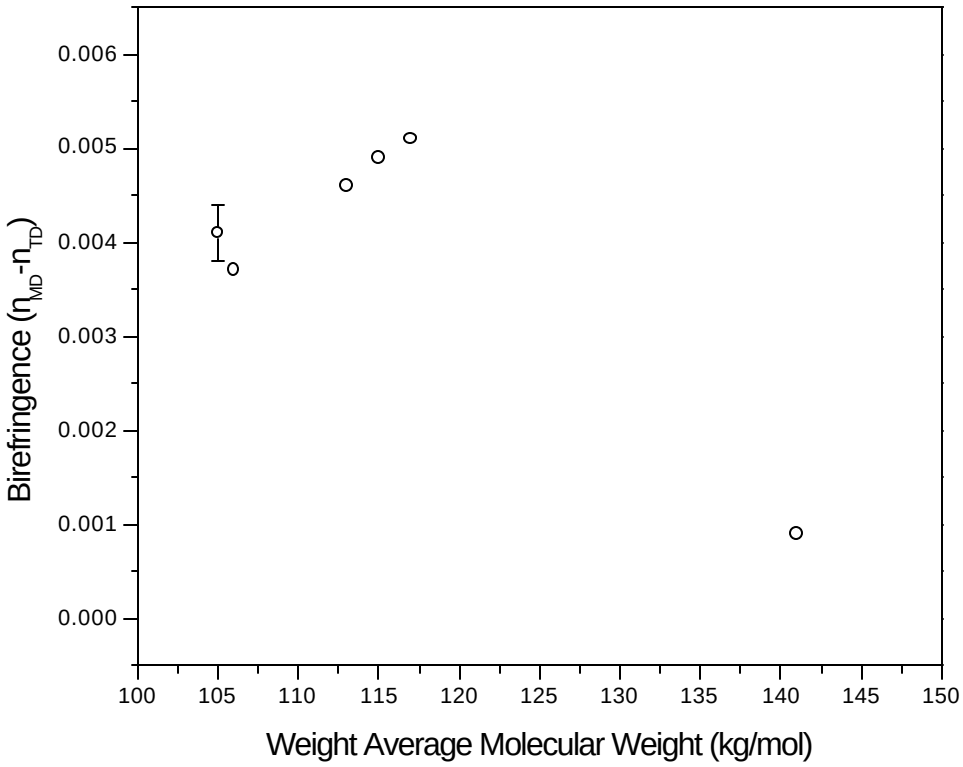

Figure 4.17. In plane birefringence of thinnest (0.76 mils) films in study. The films shown are s10, s20, s25, s38, s43, s48. Error bar represents accuracy with which birefringence values could be obtained, not error associated with measurement of multiple samples.

Form birefringence is due to fluctuations in refractive index of preferentially oriented, geometrically anisotropic domains spaced on the order of $\lambda_m/20$. The term λ_m represents the wavelength of the probing radiation in the film. It is not clear at this time whether the difficulty in interpreting the birefringence results arises from form birefringence. However, previous experience with highly stacked lamellar PE morphologies in the author's lab suggest that the effect is very small[43].

A clearer indication of the occasionally confounding nature of the birefringence results is presented next. In Fig.4.18 the in-plane birefringence of two sets of films are compared. These films represent two resins of nearly identical M_w but different polydispersity (s7-s11, metallocene M_w = 106 kg/mol, and s22-s26 CrO M_w = 105 kg/mol). In this bar chart, the five sets of processing conditions are represented along the x-axis, with the corresponding birefringence values for each pair of films. The processing conditions, from left to right, are in no particular order (i.e. relative processing stress or quench time are not in order from left to right). The first four processing conditions presented in Fig.4.18 yield a trend opposite that of the dichroism data. That is, the films with the broader MWD have greater anisotropy, on average. However, as with the previous birefringence plot, one data point is in stark disagreement with the general trend. The final processing condition presented in Fig.4.18 indicates that the metallocene resin is the most anisotropic film in the plot. It is possible that the observed discrepancies in the birefringence data could result from a transition from a uniaxial orientation to a more highly oriented, but biaxial state. This effect would tend to produce a balanced in-plane birefringence. However, the WAXS data do not seem to support this.

The error levels associated with these measurements suggest that the results obtained are real. It is important to remember that birefringence only provides an average measure of the in-plane chain axis anisotropy. This anisotropy found in the final film is not a simple function of the chain axis orientation in the melt, prior to solidification, because substantial chain rearrangment must occur during crystallization. Thus, the measured birefringence may not be an accurate indicator of prior melt orientation. Furthermore, because the c-axis crystalline orientation found in low stress K-M morphologies varies primarily along the MD-ND plane, not the MD-TD plane, birefringence may not be a sensitive indicator of differences in orientation in these films.

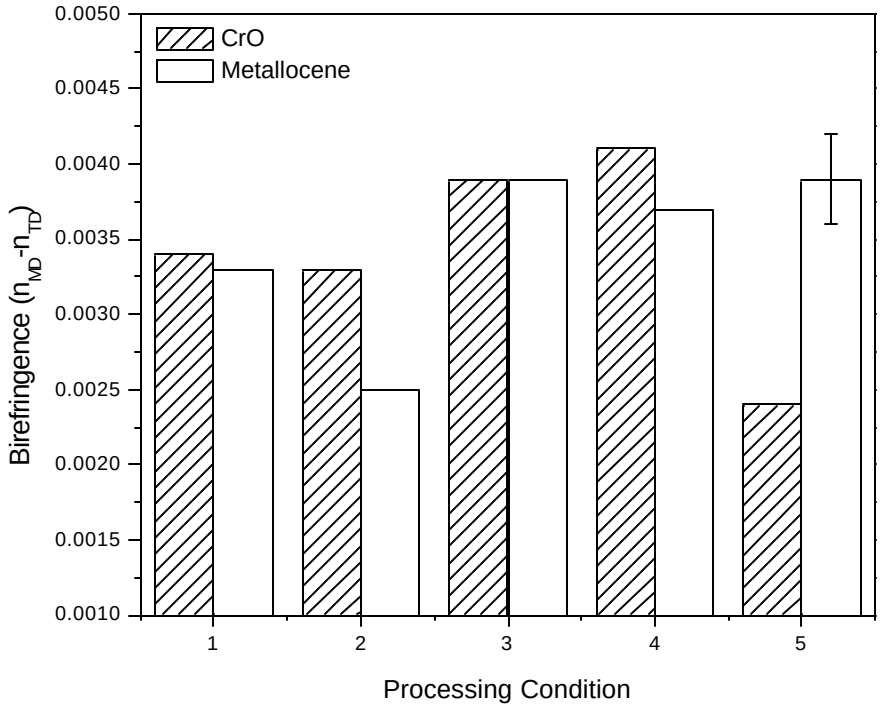

Figure 4.18. Comparison of birefringence in films produced from resins of nearly equal M_w but different polydispersity. Films presented are s7-s11 (metallocene M_w = 106 kg/mol) and s22-s26 (CrO M_w = 105 kg/mol). Processing conditions are listed in no specific order. Error bar represents accuracy with which birefringence values could be obtained, not error associated with measurement of multiple samples.

The limited pole figure results of Fig.4.10 suggested that overall the crystalline c-axis tends to display only very modest orientation. Therefore, it appears that the relatively low level of overall c-axis orientation and the complexities associated with chain rearrangement during crystallization result in film birefringence data which cannot be easily correlated with resin or processing parameters.

4.5.6 Small Angle X-ray Scattering

In the opening discussion regarding the general model of permeation behavior, it was emphasized that permeant molecules must travel through the amorphous material located between the crystalline lamellae. Therefore, the spacing between lamellae may influence permeation behavior. To investigate this possibility, SAXS experiments were conducted to analyze the distribution of lamellar long spacings in the films. Combining these results with the crystalline content can give an indication of the average size of the amorphous regions located between the lamellae. Representative scattering curves, taken along the film MD are shown in Fig.4.19. The films presented, s7-s11, were produced from the same resin using different processing conditions, normalized on film thickness. Noting that the peak in the scattering curve is related to the lamellar long spacing, it can be seen that there is very little variation between samples. Indeed, this is the case for all of the samples studied. Thus, it would seem that any variation in permeation performance is not due to differences in lamellar spacing. Also note that the breadths of the scattering peaks are similar, implying that the films have similar distributions of lamellar thicknesses.

Using the reciprocal of the scattering vector associated with the intensity peak as a measure of the long spacing, one obtains a value of ca. 300 Å as typical for these films. This value will be somewhat larger than the actual spacing due to the beam geometry of the instrument. Making the assumption that the structure can be treated as a perfectly stacked lamellar morphology, with alternating crystalline and amorphous domains, combining the SAXS and crystallinity results allows one to calculate the lamellar thickness and the amorphous phase thickness.

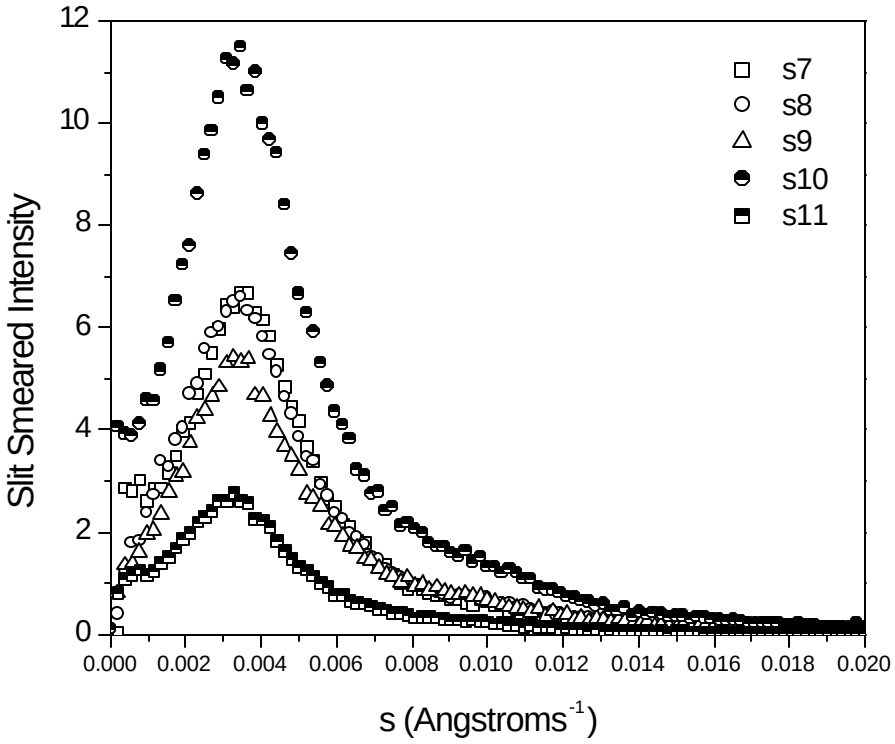

Figure 4.19. Slit smeared SAXS data of films s7-s11 (metallocene, M_w = 106 kg/mol). Data collected along film MD. Intensity is normalized on thickness, relative to a Lupolen standard.

This simple calculation returns thickness values of 190Å and 110Å, for the lamellar and amorphous phases respectively, as typical.

Because the intensity of scattering in these experiments is a function of several variables; relative volume fractions of the phases, scattering angle, and stacking coherence, it is difficult to assign a specific cause for the variation in peak intensity which is observed.

4.5.7 Small Angle Light Scattering

The typical arguments relating permeation behavior to morphology generally focus on structural features no larger in size than that of lamellar spacings. Thus, it is not immediately evident whether a study of structural features on a larger scale will be informative. The use of SALS in this study was not undertaken to investigate this point, as there were too many other variables for the possible effects of superstructure to be observed independently. Rather, as preferential orientation can be viewed on several scale lengths, SALS was used only to corroborate the orientation behavior observed using other techniques when superstructure was present. Typically, one would not expect to observe large, spherulitic like structures in oriented blown films. However, as the orientation levels are relatively low in these films, the conditions for the formation of superstructural elements were favorable in some films.

The dichroism results suggested, surprisingly, that when comparing films produced from resins of identical M_w but different polydispersities, the films produced from the narrower MWD resin will be more highly oriented. The films s2 and s26 represent broad MWD films while samples s11 and s34 were produced from narrow MWD resins. Their respective SALS patterns are compared in Fig.4.20. All four patterns display scattering indicative of sheaf-like structures oriented such that the lamellar growth direction is perpendicular to the MD[44]. However, the scattering produced by the narrow MWD, metallocene based films (s11, s34), is more highly anisotropic. As the sheaf structures resemble immature, growing sphereulites, this suggests that a greater degree of lamellar curvature and splaying (i.e. less orientation) can be found in the broad MWD films.

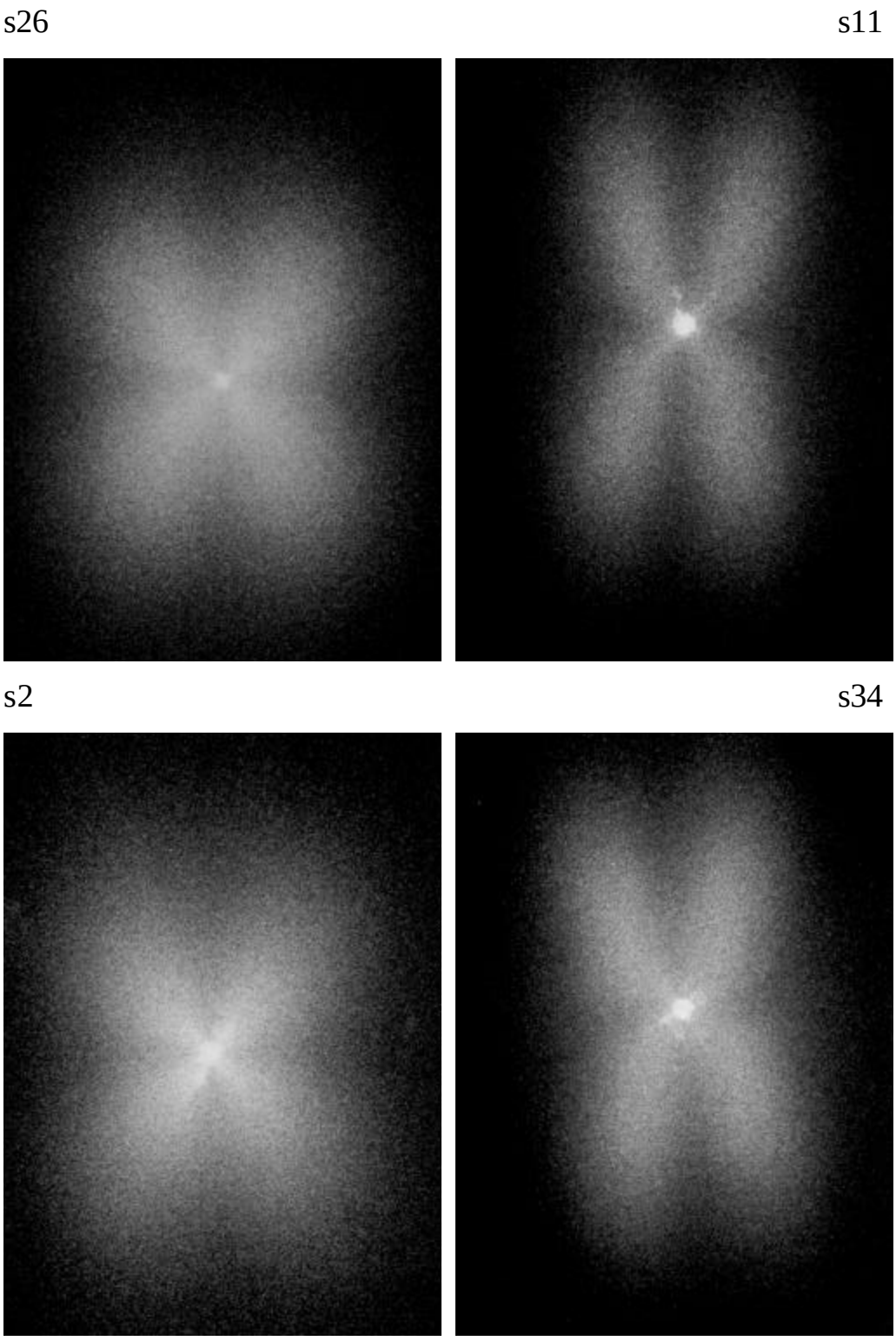

Figure 4.20. SALS patterns of films identical M_w, but different polydispersity. s2, s26 (CrO); s33, s34 (metallocene). Processing conditions: Upper patterns, base conditions; Lower patterns, reduced line speed. MD vertical, TD horizontal.

This result is in agreement with the dichroism results. Not all films yielded well defined SALS patterns. This is likely due to the lack of sheaf-like super structures in films with orientation levels greater than those presented in Fig.4.20. It was observed in this study that under identical processing conditions, the CrO resins, taken as a whole, were less prone to producing clear SALS patterns than the metallocene based resins. The presence of a high molecular weight tail in the MWD has been demonstrated to be effective at suppressing the formation of superstructure by Johnson et.al.[45], and may explain the behavior observed in this chapter.

4.5.8 Field Emission Scanning Electron Microscopy

FESEM was utilized to characterize the structures present at the surface of the films studied. While the information obtained by this method is strictly specific to the outer surfaces of the film, if no morphological gradients exist, it provides an indication of the overall orientation state of the film by allowing direct observation of lamellar features. Quantitative data cannot be obtained from these micrographs, but they do reveal some interesting structural differences in the films produced by the two catalyst technologies. In addition, general trends as a function of processing conditions and molecular weight can be observed.

The first pair of micrographs demonstrate the effect of M_w on film morphology for identical processing conditions. The films represented in Fig.4.21 are samples s12 (M_w = 150 kg/mol) and s3 (M_w = 123 kg/mol), both were produced from metallocene resins. The differences in morphology are subtle. Close inspection reveals a greater number of stacked lamellar structures in the higher M_w film. These structures appear "in the background" or beneath the more obvious curved lamellae. The fact that these structures are found more frequently in the higher M_w film suggest that its orientation level is greater. This observation is in agreement with previous x-ray and dicrhoism results. Furthermore, the lamellae in these stacked structures are oriented such that their surface normals are perpendicular to the film surface, an orientation which should facilitate permeation.

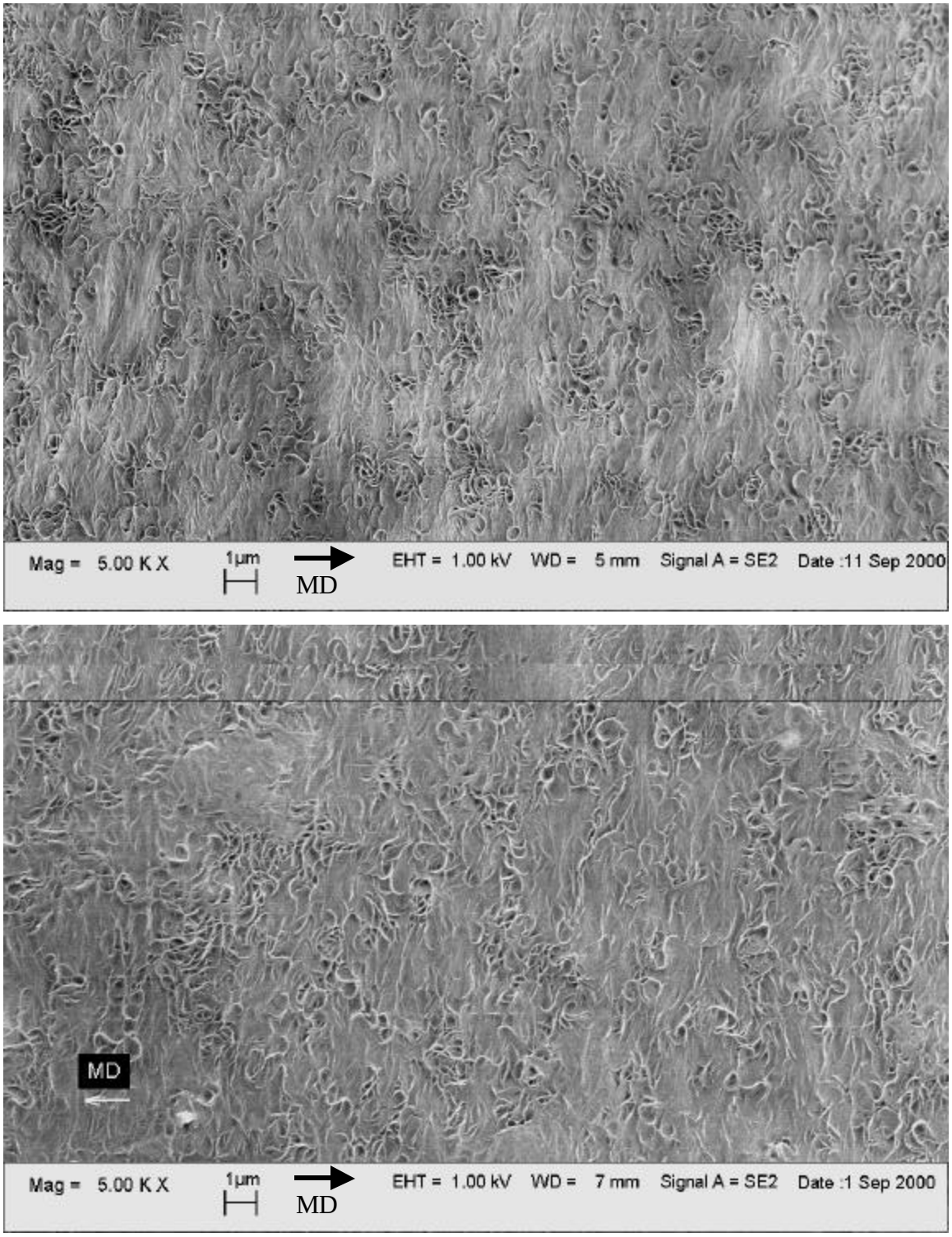

Figure 4.21. FESEM micrographs of metallocene based films. Upper; s12 M_w = 150 kg/mol, Lower s3 M_w = 123 kg/mol. MD horizontal in both micrographs. Note greater presence of underlying stacked structures in higher M_w film.

Likewise, the FESEM results demonstrate that, for a given resin, the processing conditions have an effect on morphology. A better example of this phenomenon is presented in Fig.4.22, where two films produced from resin A, under different conditions are compared. The films are s20 (reduced extruder output and die gap) and s21 (reduced FLH). Decreasing the line speed, with all other factors equal, leads to a lower processing stress and thicker film. Simultaneously decreasing the die gap and the extruder output leads to a thinner gauge film with greater MD drawing, relative to the decreased line speed conditions. Thus, it is expected that film s20 will have greater orientation than film s21. The micrographs of Fig.4.22 clearly show this to be the case. Also note, the presence of row nucleated structures which span tens of microns in length in sample s20. These row structures appear to be characteristic of the broader M_w resins.

A comparison of films produced from two resins of differing polydispersity, but of nearly equal M_w, is given in Fig.4.23. These films were both produced using the base set of processing conditions yet have resulted in very different surface morphologies. Note the large number of long, row nucleated structures in the broad, CrO resin which are absent in the metallocene film. Recall that the CrO resins possessed a substantial portion of high molecular weight material relative to the metallocene materials, as indicated by the higher moments of the MWD. This result is somewhat perplexing in that the pole figure, dichroism, and SALS results suggested that the narrower MWD resins produced greater orientation. The impression given by Fig.4.23 is that the orientation of the broader MWD film is much greater. Again, it should be emphasized that the FESEM results are only indicative of the structure at the surface and do not necessarily represent the bulk morphology.

In general, the FESEM micrographs confirm the expected orientation trends as a function of M_w and processing stress. Increases in these parameters leads to greater anisotropy. However, comparisons of morphology when polydispersity is included as a variable yield results which seem contradictory to those of the dichroism and light scattering studies. The high molecular weight tail present in the CrO based resins appears to be effective in producing long range, row nucleated structures.

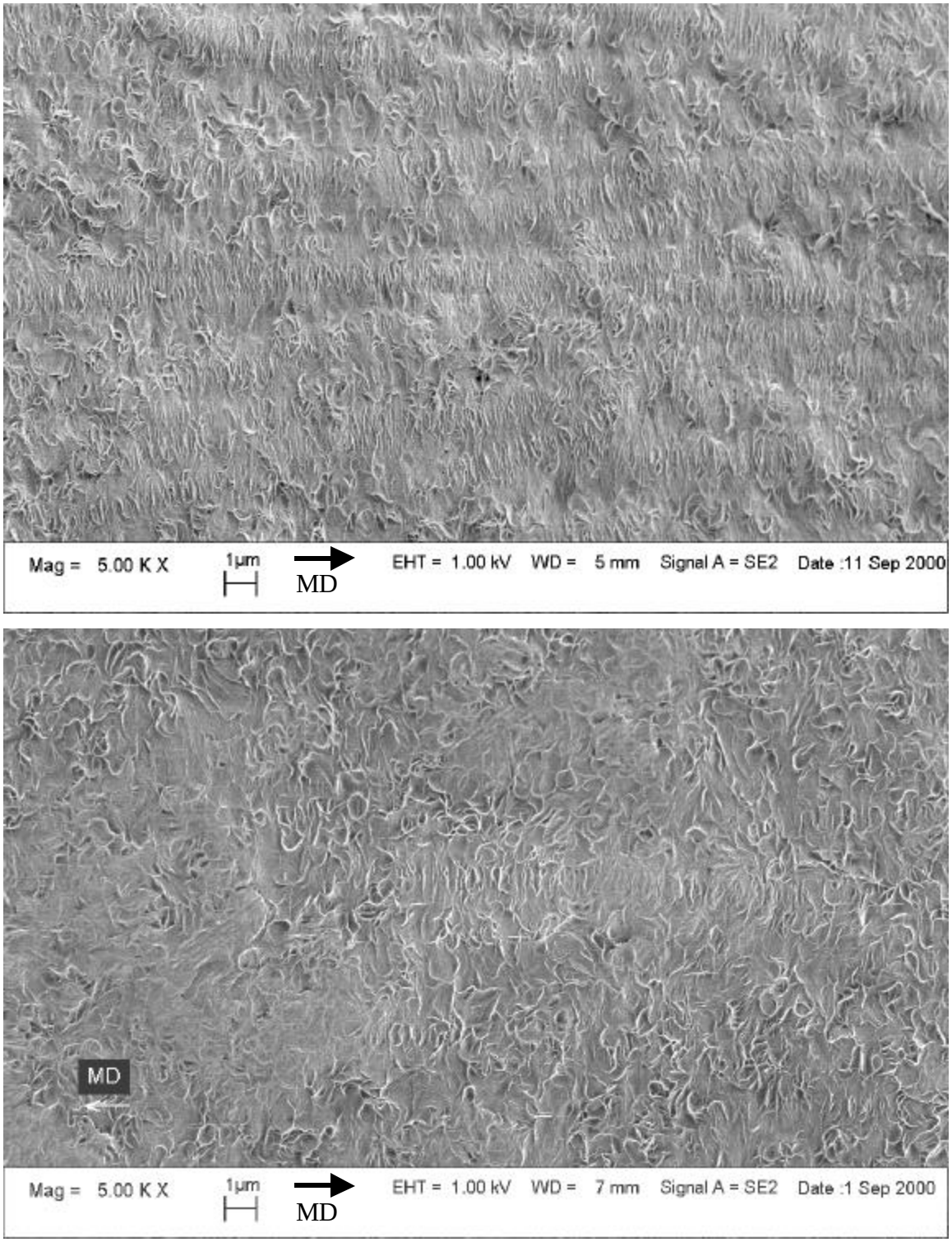

Figure 4.22. FESEM micrographs of films produced from resin A (CrO). Upper, s20 (reduced extruder output and die gap), Lower, s21 (reduced line speed). MD horizontal.

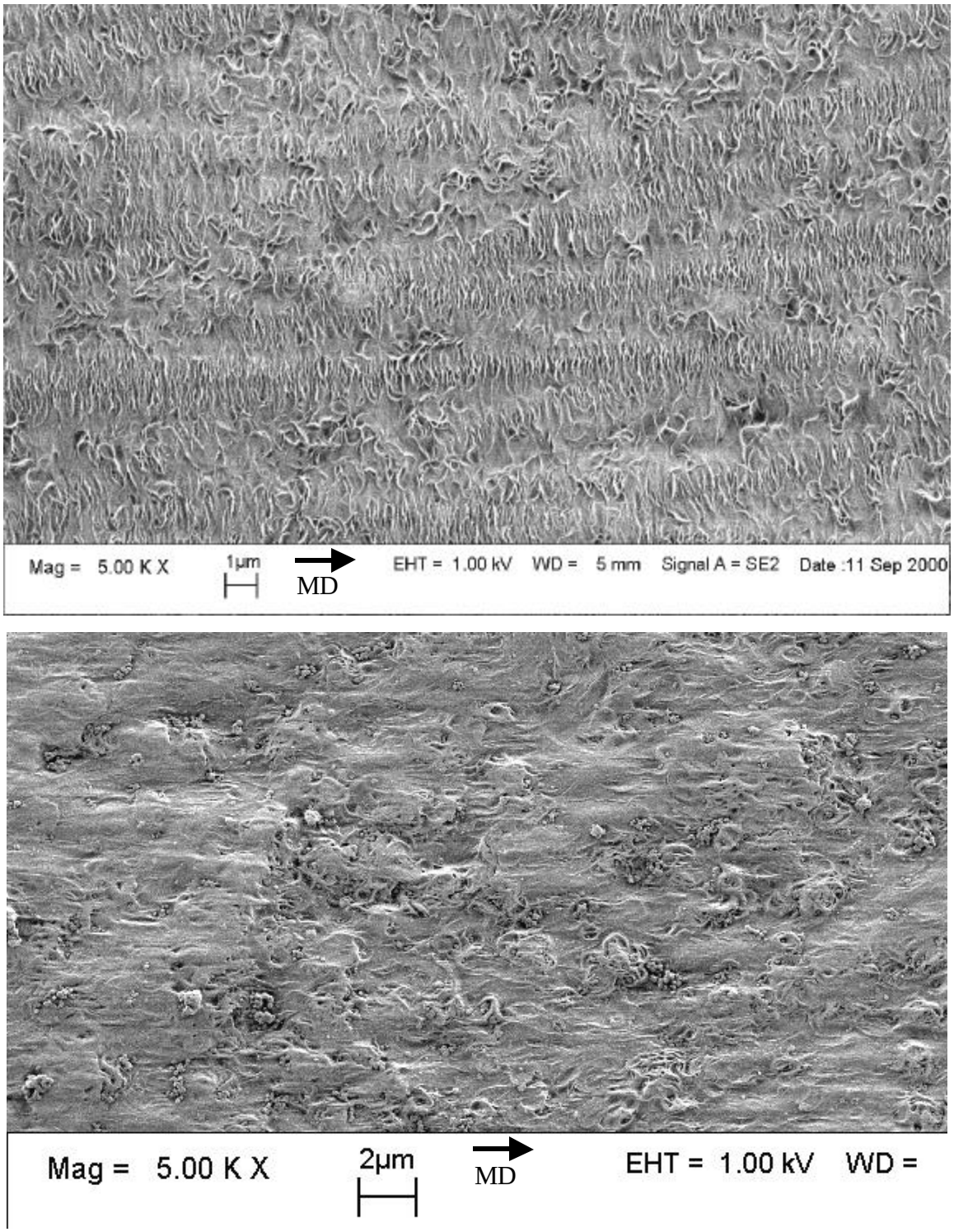

Figure 4.23. FESEM micrographs of films of similar M_w but different polydispersity. Upper, s22 (PDI = 8.2, M_w = 105 kg/mol), Lower, s7 (PDI = 5.1, M_w = 106 kg/mol). Base processing conditions. MD is horizontal. Note scales are slightly different.

4.5.9 Transmission Electron Microscopy

The primary goal of the limited number of TEM experiments performed was to identify the presence of any gradients in morphology from the film bulk to the surface. It has been speculated in the literature that a transcrystalline layer of surface nucleated material would lead to poor barrier performance[46]. Beginning with Fig.4.24, the effect of processing conditions on resin C are examined. Two micrographs representing cross-sectional views taken from the core of the film, looking down the TD are presented. Note the presence of bundles of lamellae, stacked together in small sheaves. The stacking is such that the lamellar normals are parallel to the MD. Comparing the two films, s5 and s6, it appears that the lamellae of film s5 are slightly less curved and row structures are slightly more evident. This is expected as sample s5 was manufactured with greater processing speeds and stresses. While differences in orientation behavior can be noted by TEM, this technique was not found to be the most effective or practical for discerning small variations.

Figure 4.25 contains a micrograph of film s5, taken near the surface of the film. The edge of the film is visible in the upper left corner. Row structures, much like those seen in Fig.4.24, in the central portion of the film, are evident in this region of the film as well. A lack of a discernable gradient in morphology was the general rule for the films studied in this manner.

Recalling the earlier FESEM results, it was noted that the CrO based films had a tendency to form well defined, long range row structures on the surface of the film. These row structures, with lamellae stacked perpendicular to the film surface, appear to provide likely routes for permeation. TEM micrographs taken near the surface of sample s21, a CrO based film which displayed row structures on its surface, are provided in Fig.4.26. These two micrographs reveal the difficulty in attempting to quantify structural features by observing thin cross-sections. In the upper micrograph, it appears that lamellae are well stacked perpendicular to the surface, as one would expect if the cross section cut through, and parallel to a row structure. However, in the lower micrograph no such features are preset. Thus, it can be seen that the observation of row structures,

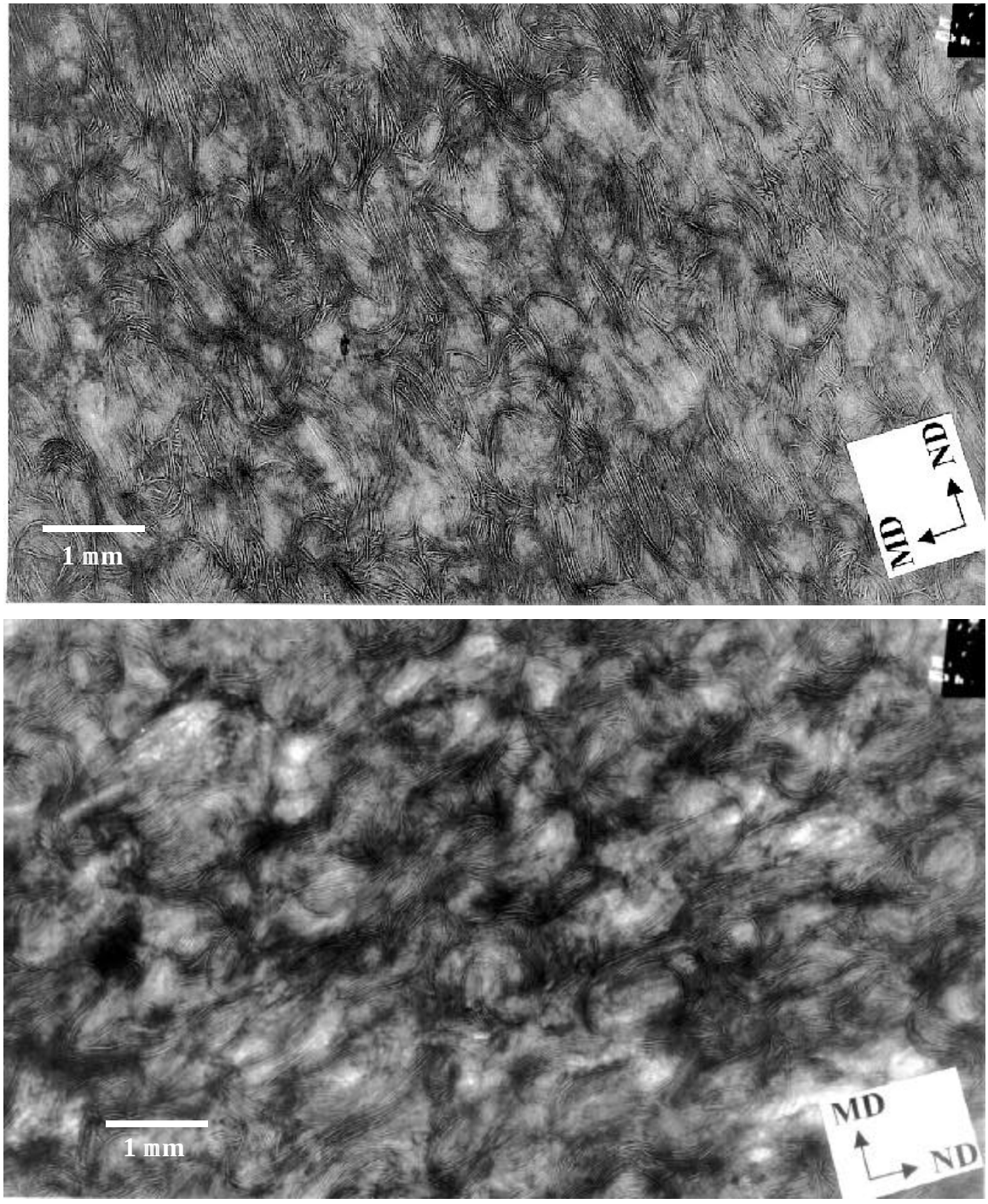

Figure 4.24. TEM micrographs of films s5 (upper) and s6 (lower) – metallocene resins using the base and reduced line speed processing conditions respectively. Images collected near the center of the films.

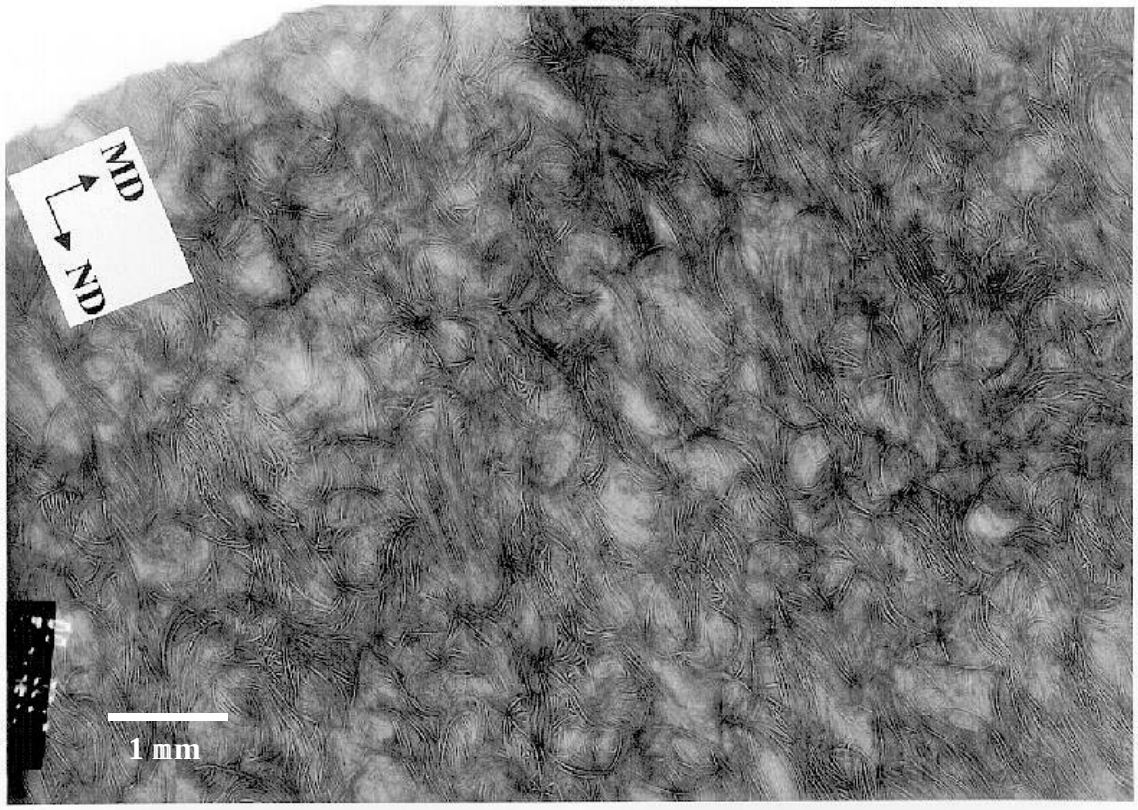

Figure 4.25. TEM micrograph of s5 taken near the surface of the film. Note that the surface is visible in the upper left corner.

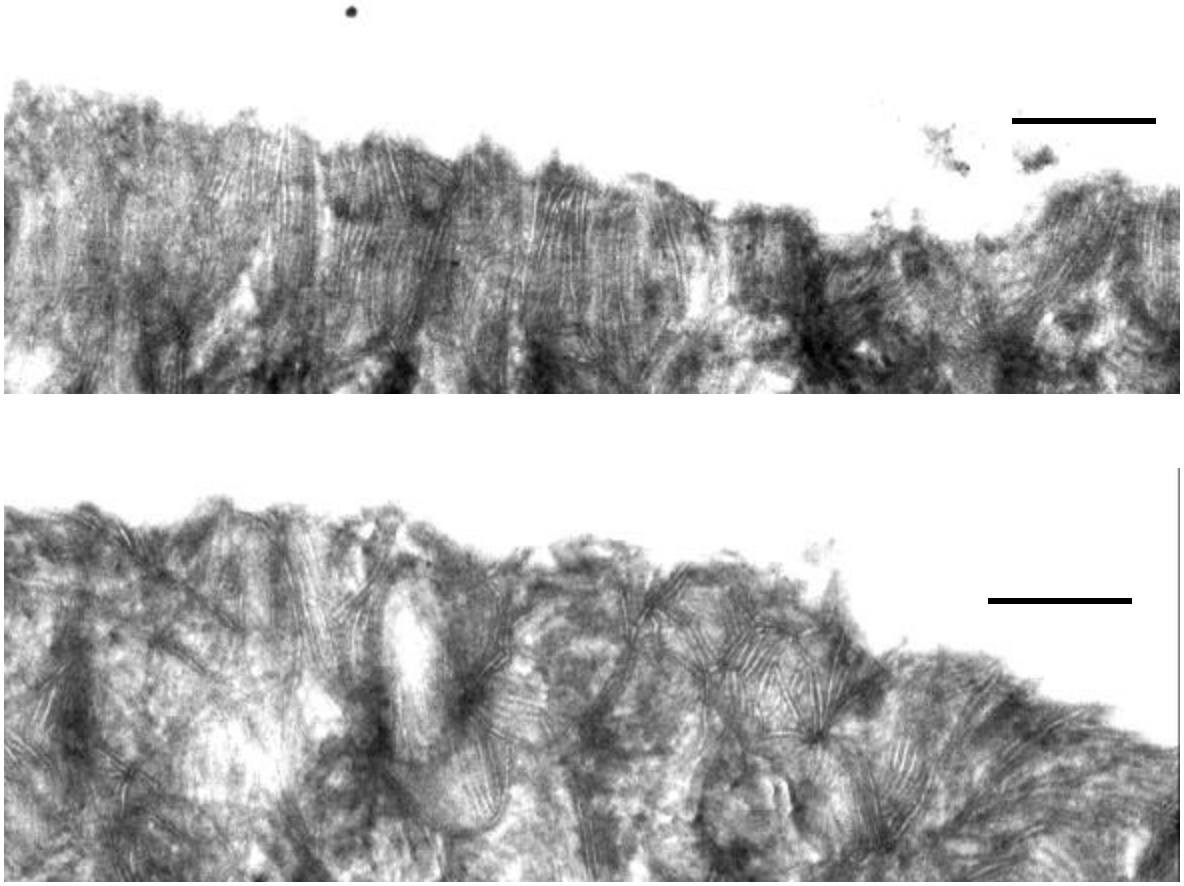

Figure 4.26. TEM micrographs of s21 taken near the surface of the film. Upper micrograph shows signs of row nucleated structures at the surface while the lower does not. Scale bars 500 nm. MD horizontal.

easily visualized by the FESEM, is problematic for the TEM. This is because, as stated above, the cross section must intersect and run completely parallel to the row structure in order for it to be viewed over its entire length.

The most important result provided by the TEM experiments is the conspicuous lack of surface nucleated lamellae growing perpendicular to the surface of the film. While instances of lamellae oriented perpendicular to the surface were noted, as in Fig.4.26, these structures appeared to be indicative of orientation induced row structures. *No evidence in the micrographs shown here, or others obtained in this study, suggest a surface nucleation phenomenon.*

4.6 Film Properties

The overall goal of this chapter is to relate processing and resin variables to structure formation, which can then be related to end film properties. To this point, the discussion has focused on general observations regarding the roles the process and resin play in determining final film structure. Now attempts will be made to relate this structure to end performance. Two properties will be of interest, modulus and permeation. The discussion will begin with the former.

4.6.1 Tensile Modulus of Films

Tensile stress-strain measurements were performed on a majority of the films, as an anisotropic mechanical response would be a clear indicator of preferential orientation. The discussion is limited to small strain properties (modulus) only as they are less sensitive to small flaws in the testing specimen. The acquisition of consistent, large strain data (elongation to break, toughness, etc.) proved difficult. The tensile modulus data acquired along both the MD and the TD are presented in Fig.4.27. With the exception of the anomalous result for s6, in all cases the tensile modulus is greater along the TD than the MD, a result which at first glance appears counterintuitive. The explanation of this phenomenon is described. Regardless of the details, the imbalance in

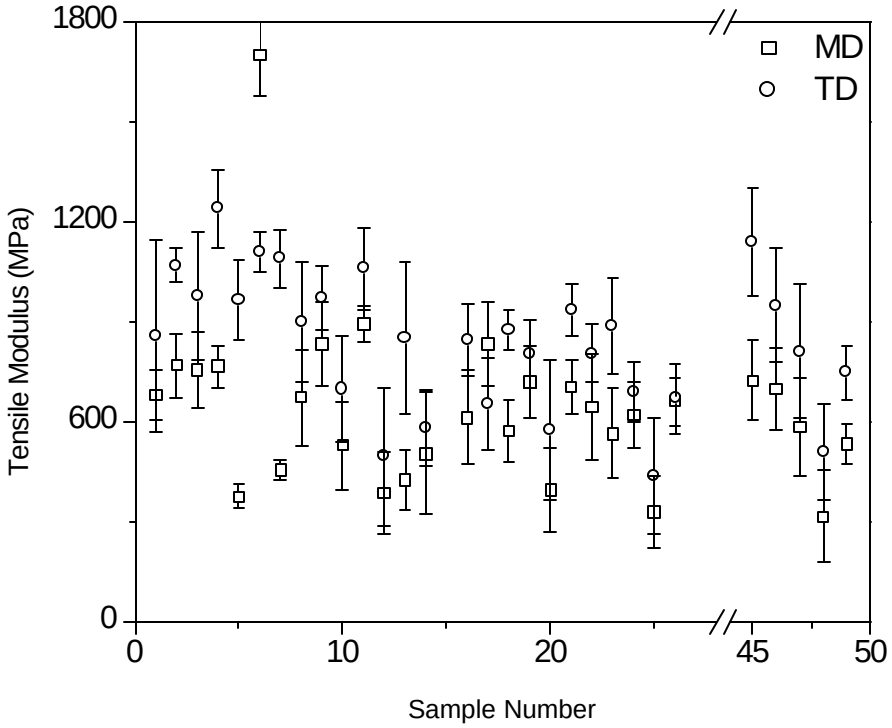

Figure 4.27. Tensile modulus data of selected films studied. With the exception of one anomalous case (s6) the TD modulus is larger.

mechanical response clearly indicates that all of the films examined posses orientation to some level.

The orientation produced in these films is in accordance with the K-M model of row nucleation, based on the anisotropy of the modulus. Because lamellar growth occurs perpendicular to the stretch direction (MD), there is, as noted in the morphological analysis, a tendency for the lamellae to stack with their normals parallel to the MD. In the extreme case where no lamellar curvature or twisting takes place, this would result in a laminated structure, with the amorphous and crystalline phases alternating along the MD, but forming nearly continuous domains along the TD. Thus, in this idealized case, the MD modulus is dominated by the amorphous phase because the "hard phase – soft phase" repetition occurs in series. In contrast, along the TD the "hard phase and soft phase" are arranged in parallel, thus the small strain response is dominated by the rigid, crystalline phase. While it is not suggested that a perfectly stacked structure is present in these films, the bias in mechanical response introduced by the low stress K-M morphology will certainly lead to this effect. Thus, the directional dependence of the modulus data supports the presence of row nucleated morphologies in these films. Similar results have been obtained by Yu[43] and Zhou[47] in studies involving tubular blown HDPE films (BUR = 1) with highly coherent stacking of MD lamellae.

Reviewing the data in Fig.4.27 a second time, it can seen that the variation in modulus, from highest to lowest, for a given direction is relatively modest in comparison to the error associated with the measurement. This comes as no surprise as the morphological data have indicated that the differences in orientation are real, but small. Recalling that the dichroism data was able to discern differences in orientation between films, it is instructive to determine if the differing levels of orientation can be correlated with the observed anisotropy in film modulus. In Fig.4.28 the crystalline b-axis orientation function is plotted against an indicator of mechanical anisotropy, the ratio of TD to MD modulus. As the negative orientation of the b-axis increases, it is expected that this ratio too will grow. The trend is noted, though weak. It should be reiterated that the changes in the TD/MD modulus ratio associated with the films studied is fairly modest, only spanning from about 1.3 to 1.6. This suggests that while the modulus

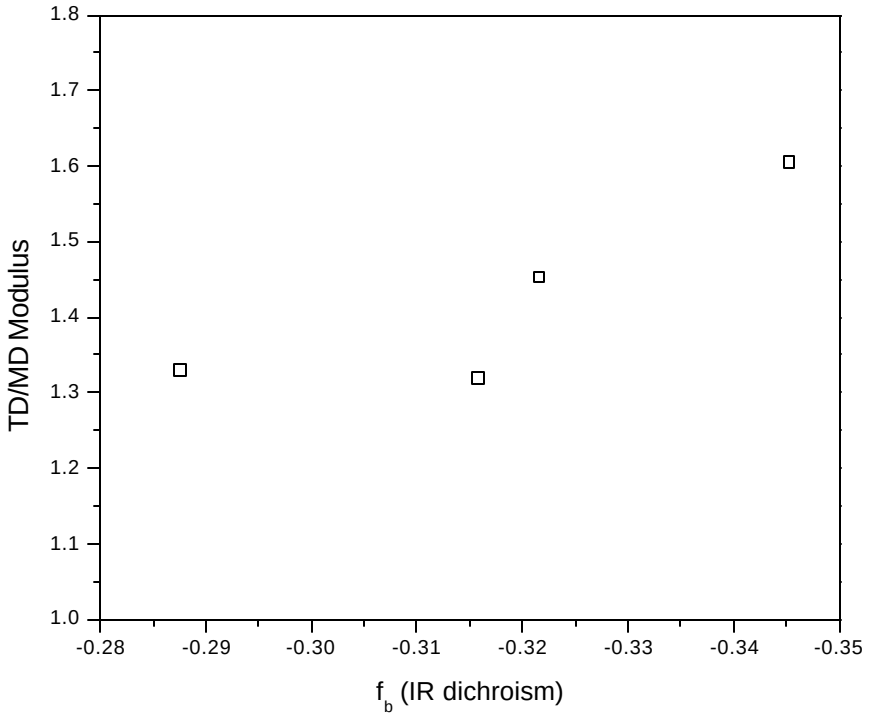

Figure 4.28. Ratio of TD/MD modulus used as a measure of anisotropy. Trend indicates increasing orientation leads to greater anisotropy of modulus. However, note that changes in modulus ratio are small.

values clearly indicate preferential orientation, they do not prove to be a highly sensitive measure of this anisotropy.

4.6.2 Moisture Vapor Transmission Rate (MVTR)

The property of initial interest to this study was the rate of water vapor permeation through the films. It has been noted that small differences in crystalline content and orientation exist in the films studied. Both are variables which are known to affect permeation. To gauge the level of variation found in MVTR performance over the set of conditions studied, Fig.4.29 is presented which plots the MVTR value, as provided by Chevron-Phillips staff, with error bars, for each of the films. The results are reminiscent of the modulus data, as the error bars suggest that the differences in MVTR are real, but not large over the range of conditions examined. Nevertheless, it may be possible to reach some general conclusions by examining the data more closely.

The first film property discussed was that of crystalline content. Based on the arguments made in the background section, it is expected that the permeation rate will scale with the square of the amorphous volume fraction. Of course, this relation should only hold strictly for a hypothetical morphology consisting of evenly dispersed, "spherical" crystalline domains. The MVTR data is plotted as a function of the amorphous volume fraction to the second power in Fig.4.30. The general relation seems to hold true. The plot clearly indicates that, on average, larger amorphous content films have greater permeation rates. And, as stated above, no correction has been made for differences in orientation among the films. The fact that the data points come far from falling on the same line or curve suggests that orientation effects may indeed be important.

The dichroism results should allow one to examine the effect of orientation on permeation performance. Recall, however, that only the thinnest gauge films in the study were suitable for this method of analysis. Figure 4.31 provides the comparison. Not surprisingly a weak trend is evident. Based upon the relatively small differences in MVTR and orientation in this study, it is unfortunately difficult to make strong associations which rise above the "noise" level set by measurement limitations.

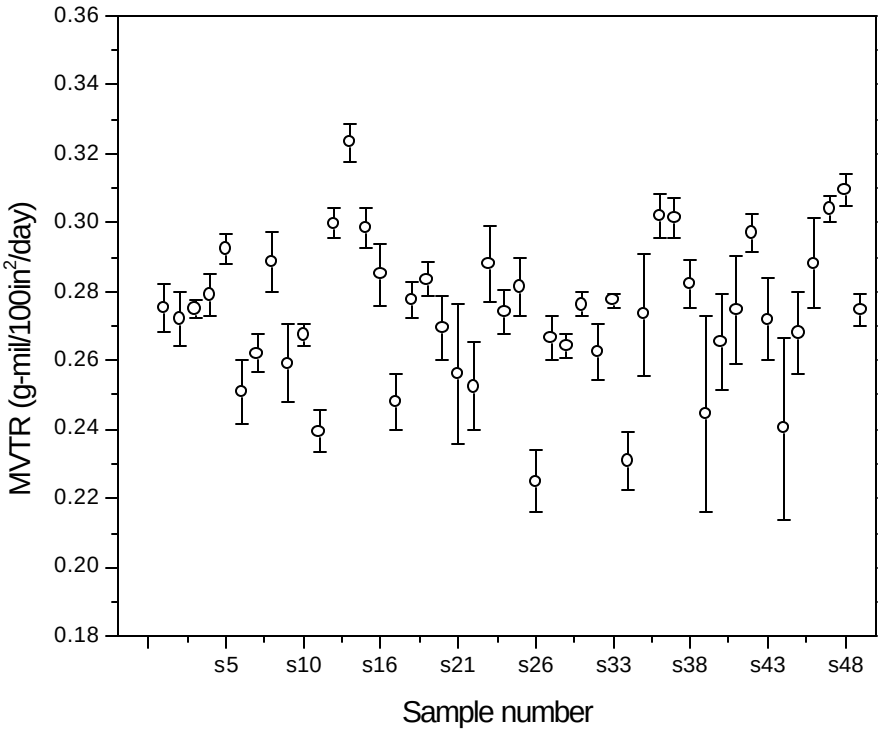

Figure 4.29. MVTR of all films examined in study.

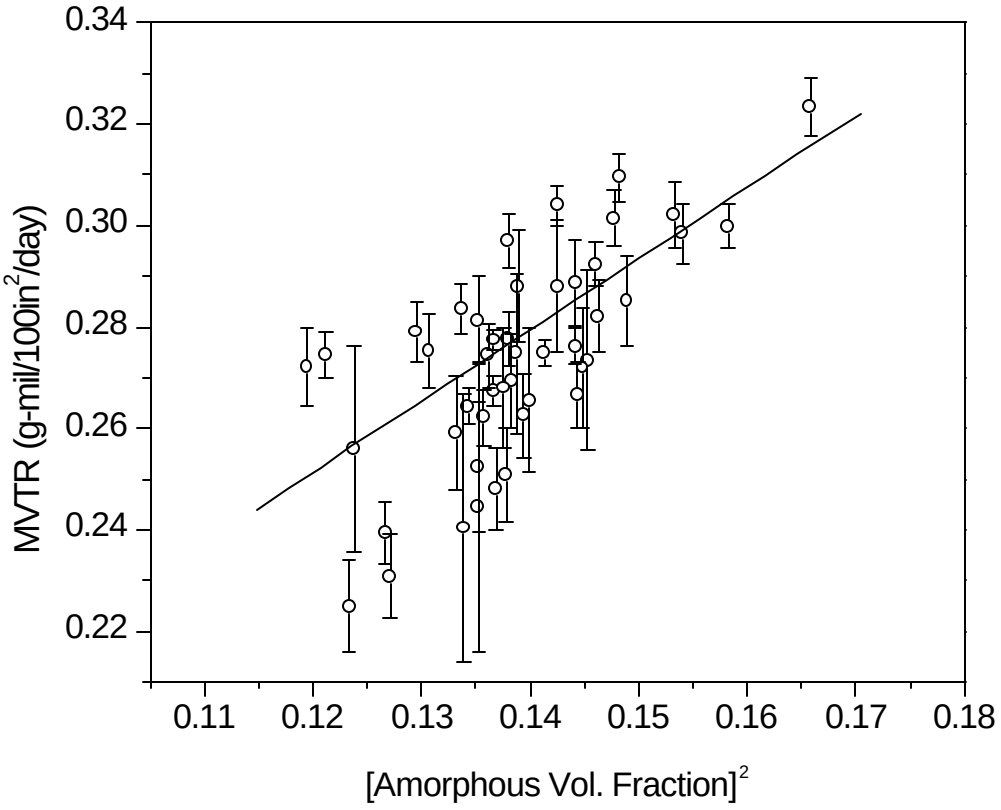

Figure 4.30. Correlation of MVTR with amorphous volume fraction raised to the second power. Line represents best fit trend line ($R^2 = 0.50$)

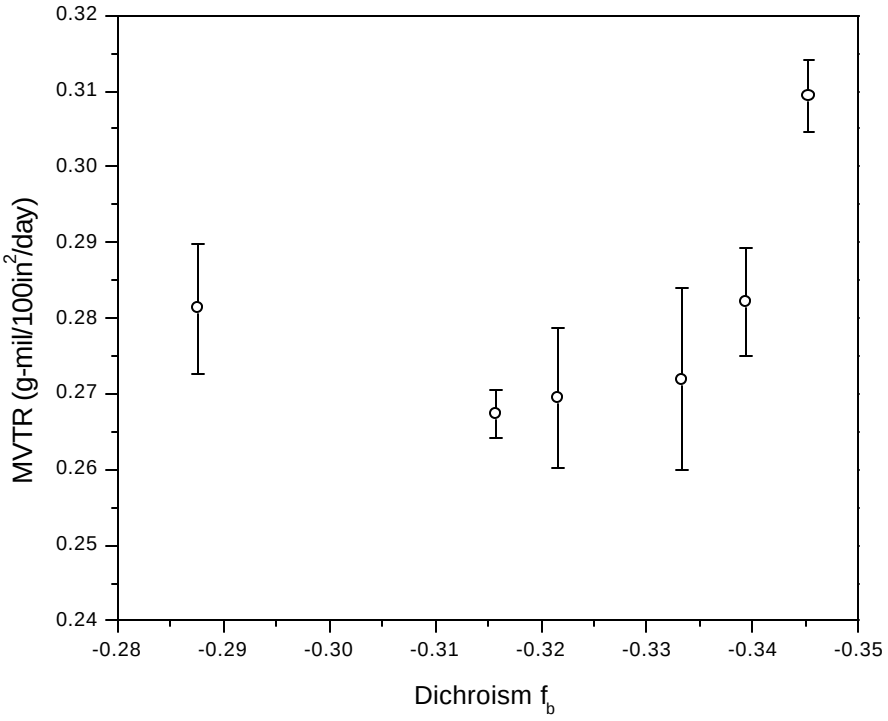

Figure 4.31. Correlation between orientation of the crystalline b-axis as determined by dichroism and MVTR.

Theoretically, a more correct analysis of the orientation effect would involve first normalizing out any differences in crystalline content. In Fig.4.32 the same data is plotted with MVTR results normalized on the square of amorphous content (nMVTR). It is expected that any variation in nMVTR in this plot should be solely due to orientation effects. However, the correlation here appears to be worse than in the previous figure. Of course, it is possible that the minimum in permeation performance suggested by the plot is real. One can imagine a scenario in which the level of amorphous phase orientation increases, along with crystalline phase orientation, up to a certain level. After this point, the orientation of the amorphous material, possibly well below the maximum attainable level, may cease to further increase, while the crystalline phase continues to preferentially align. If the reduction in amorphous phase chain mobility exerts a strong influence on the permeation behavior, at low levels of crystalline orientation, such a minimum might be observed.

One could potentially go on hypothesizing reasons for the observed correlations endlessly. But, due to the complexity of the morphologies involved, such an effort would be fruitless. The small variations in structure appear to be on a scale too fine to be definitively characterized. Furthermore, decoupling the small differences in crystalline content, from amorphous and crystalline phase orientation, with the required precision, appears not to be possible by the approaches taken. Therefore, in the subsequent discussion section, the focus will be on correlating known process and resin parameters with the films' MVTR performance. While it is likely that this approach will miss the structural factors which influence permeation behavior, it is hoped that a predictive tool, based upon observations of the general scaling behavior, can be developed.

4.7 Resin and Processing Time Scaling

Throughout this chapter, two factors have been considered controlling of the permeation behavior, crystalline content and its orientation. Therefore, a simple relation designed to predict MVTR performance should be based upon these factors. The quench time (QT), defined as the time required for the melt to travel from the die to the frost line,

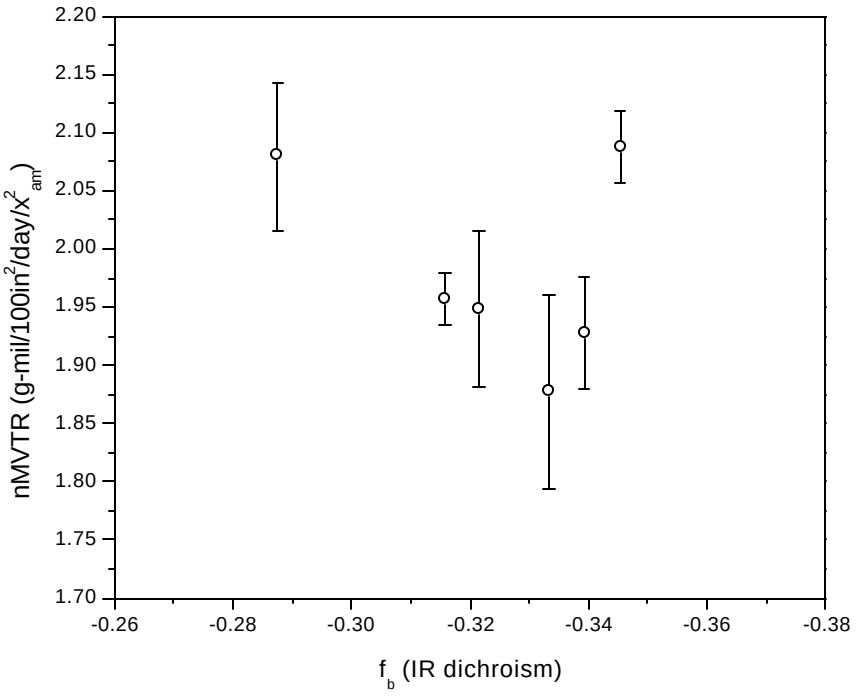

Figure 4.32. Crystalline content normalized MVTR (nMVTR) related to crystalline b-axis orientation as determined by dichroism.

should influence both the end crystalline content and the orientation. Longer quench times correspond to slower cooling and greater melt relaxation, thus potentially leading to greater crystallinity and less orientation, all other resin and processing factors being equal. By itself, the QT cannot account for differences in MVTR for films produced from the different resins, as it depends only on processing parameters. Thus, the QT can be thought of as defining a characteristic processing time. A general rule of thumb in polymer science states that when the characteristic processing time is shorter than the characteristic relaxation time of the polymer, orientation will occur. This scaling relationship, described earlier, is known as the Deborah number (De). In this study the De number will be defined as the ratio of the polymer relaxation time to the processing time. More specifically, as the ratio of the characteristic melt relaxation time, τ_η, as determined by the C-Y model, and the QT of the process. Thus, as the De number increases, signaling greater orientation and likely less crystallinity, it is anticipated that the MVTR will also increase. The relationship between the De number and MVTR is given in Fig.4.33. While the end points appear to give the correct behavior, the majority of the films do not follow this scaling. The lack of agreement is not entirely surprising as it represents a gross simplification of the process. If the De number does provided a measure of the induced molecular orientation due to process-resin interactions, then plotting the MVTR normalized on crystalline content against the De number should reveal any effects of orientation on permeation. This normalized plot is shown in Fig.4.34. Clearly no trend exists, thus either the De is not correctly predicting the orientation behavior of the system, or the orientation is not affecting permeation in a simple manner.

To determine reasons why the De may not accurately predict the MVTR behavior, an analysis of the input parameters must be made. First, consider the characteristic polymer time scale, given by the melt relaxation parameter. It is unlikely that one number can completely represent the viscous response of the material. Recall for the limited number of films amenable to these methods of examination, that the dichroism and light scattering data suggested that the narrower MWD resins tended to orient more than their equivalent M_w, broad MWD counterparts. However, because of their broader MWD, the CrO resins shear thin earlier, leading to larger values of τ_η. Based on the De

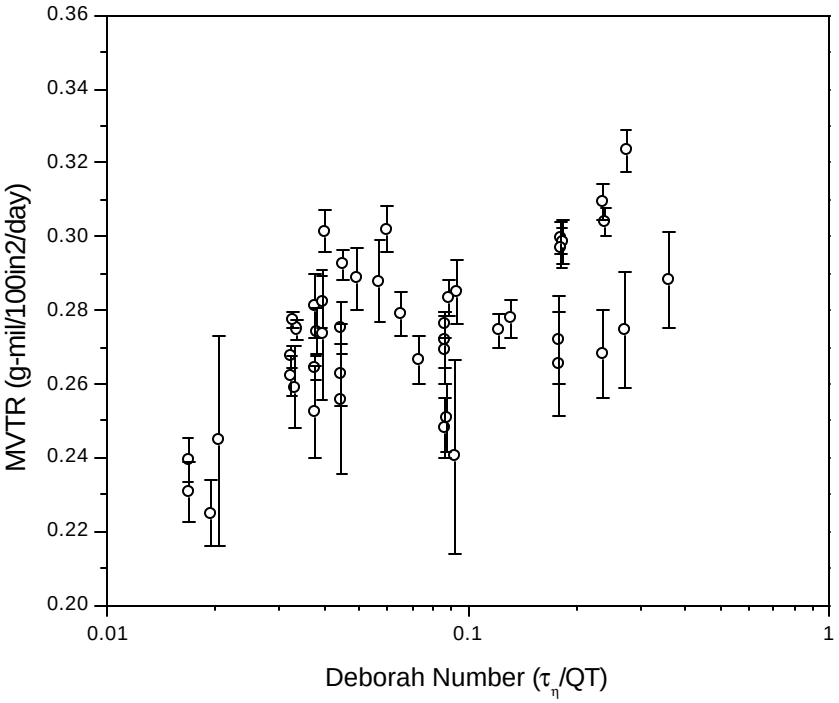

Figure 4.33. Correlation between dimensionless Deborah number and MVTR.

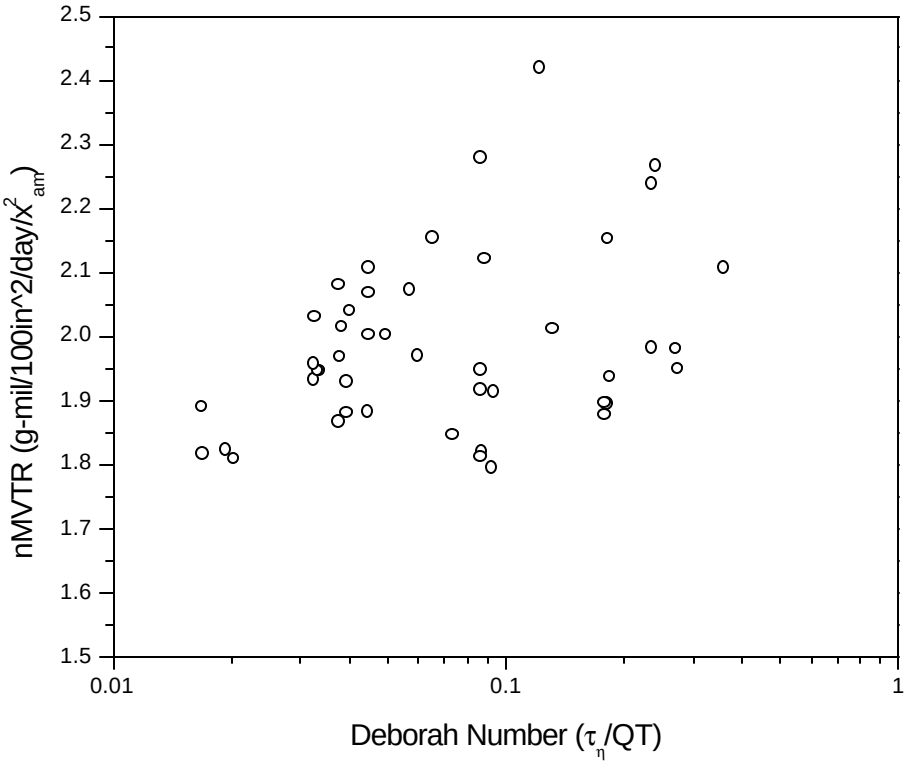

Figure 4.34. Permeation rate normalized on amorphous content as a function of De to predict orientation influence.

number approach, these larger values predict greater orientation for the broad MWD resins, even though the opposite trend is noted. This apparent discrepancy can be explained by returning to the viscosity data in Fig.4.2, in which the behavior of resins A and I were compared (M_w = 113 kg/mol, PDI's of 8.1 and 5.5 respectively). Note that at low shear rates the viscosity of resin A is greater. But, at the highest shear rate, due to the earlier onset of shear thinning in resin A, the narrower MWD material, resin I, begins to display a greater shear viscosity. Greater viscosities in the melt require greater stresses to achieve the same flow rate. Thus, the greater stresses experienced in the melt by the narrow MWD resins may explain why they tend to orient more than the broader MWD resins. These arguments suggest that a scaling parameter which accounts for the differences in stress encountered in the melt, as a function of the resin and processing characteristics, may be more appropriate than the use of an average relaxation time.

A rough estimate of the MD elongation rate was made by considering the change in velocity experienced by the melt using the relation show below[48],

$$\dot{e} \approx 2\frac{v_{FL} - v_{die}}{FLH} \qquad \text{Eq.4.9}$$

where the extension rate is approximately twice the difference in film velocity at the frost line and the die, divided by the FLH. This value provides an approximation of the deformation rates experienced in the process. Because extensional viscosity data is not available, the only recourse is to use the shear viscosity data as an indicator of the relative behavior for each resin. Thus, a simple "relative processing stress" term is suggested by multiplying the extension rate by the resin viscosity, calculated at this specified rate, from the C-Y model and multiplying by a factor of three in accordance with Trouton's rule. Obviously this will not represent the actual stresses present in the process as it completely neglects temperature dependencies and variations in the strain rate profile file of the bubble, for the different resins. Assuming that the permeation behavior of a film can be modeled as a function of the crystalline content and a correction factor for differences in tortousity, the introduction of the relative processing stress term is applied only as means to predict the relative levels of orientation induced in the films, and hence relative tortousity.

An admittedly crude indicator, here termed the "relative processing stress factor", is obtained as follows. Based upon the processing conditions used, Eq.4.9 was used to determine the extension rate encountered for each film. This extension rate was input into the C-Y model, using the appropriate parameters for each resin such that a shear viscosity at this rate could be determined, and then multiplied by a factor of three in accordance with Trouton's rule. It should be noted that Trouton's rule is only rigorously correct for Newtonian fluids, and the application to non-Newtonian fluids well above the low frequency limit is problematic. However, in the absence of extensional data, such a simplification was deemed necessary. Next, the materials were assumed to be generalized Newtonian fluids, such that the stress in the melt during processing could be calculated as the product of the extension rate and the viscosity at this rate. Thus, a stress for each film based on its particular processing conditions and resin were obtained. Finally, the stress value obtained for each film was divided by the greatest numerical stress value calculated for the set of films, in order to normalize the results such that the largest "relative processing stress factor" is equal to one. In Fig.4.35 the product of the square of the amorphous fraction and the "relative processing stress factor" is plotted against MVTR. While the correlation is improved over the De approach, only a very modest gain in agreement has been obtained. The improvement (R^2=0.55 first order exponential curve) is also small relative to the scaling based strictly on the amorphous content presented in Fig.4.30.

An alternative explanation for the variation in MVTR performance observed among the films could be based upon differences in amorphous phase orientation. Because none of the methods employed in this study allowed for the independent quantification of amorphous orientation, this topic has received little attention to this point. However, because permeation takes place in the amorphous phase, this study would not be complete without some discussion of its role. To a first approximation, one would expect that as the level of processing stress rises, the level of amorphous orientation in the final film will also increase. A relative indicator of amorphous orientation can be obtained through shrinkage measurements. In Fig.4.36 the results of a shrinkage test conducted along the MD in air at 110°C for 24 hrs are plotted as a function of the relative processing stress factor.

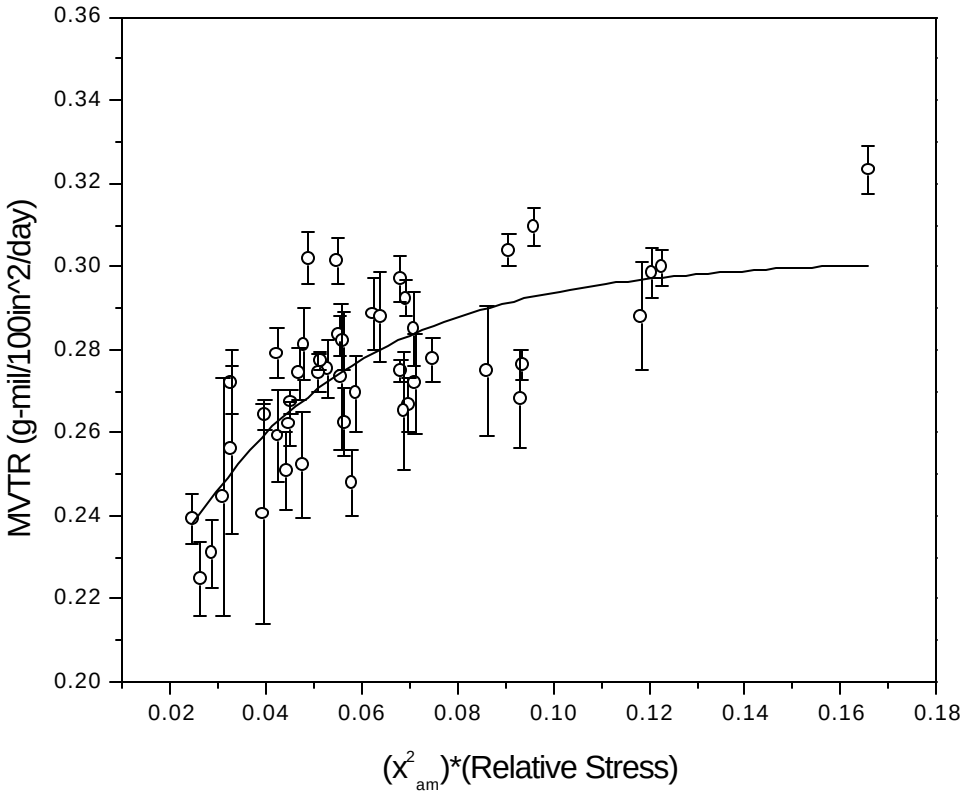

Figure 4.35. Correlation of MVTR with processing stress and amorphous fraction. Trend line represents first order exponential function ($R^2 = 0.55$)

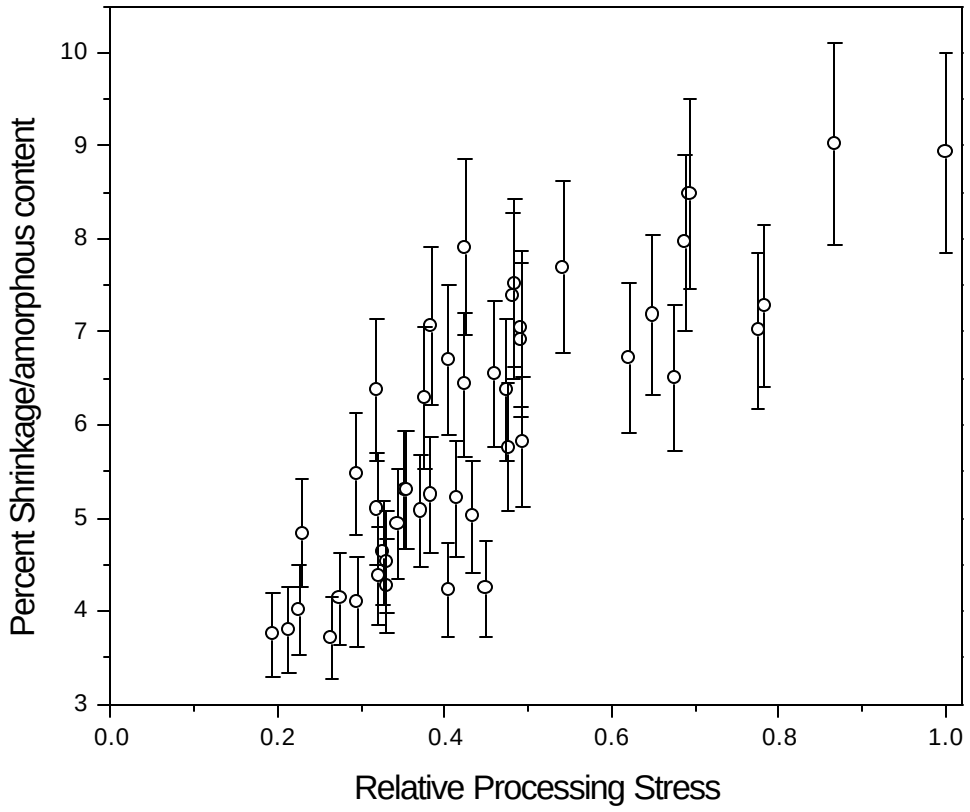

Figure 4.36. Correlation of normalized MD shrinkage with processing stress.

Similar results for tests along the TD are not included because of the small BUR employed (2.9), which resulted in no change in dimension or a small (~0.5%) expansion in this direction. In these MD results, as well as subsequent shrinkage plots, the shrinkage data has been normalized on amorphous phase content. Thus, the percent shrinkage data plotted indicates the films' measured shrinkage divided by its amorphous volume fraction. As expected, greater processing stresses induce higher levels of amorphous orientation. This observation is important because it suggests a competing effect between crystalline and amorphous orientation is present. Increasing processing stresses can lead to higher levels of amorphous phase orientation, which can act to hinder permeation, while at the same time promoting greater levels of crystalline orientation which decreases the length of the tortous path, thus aiding permeation. Indeed, as demonstrated in Fig.4.37, the magnitude of negative b-axis orientation, as determined for the thinnest films by infrared dichroism, correlates with greater amorphous orientation (shrinkage).

To gauge the importance of amorphous phase orientation in determining the barrier performance of these films, a plot of the nMVTR performance versus normalized shrinkage would be of interest. These results are plotted in Fig.4.38. No correlation is obtained. If no role was played by amorphous orientation in determining the barrier properties of these films, it would be anticipated that Fig.4.38 would show an *inverse* correlation between shrinkage and nMVTR. This is because those films with greater amorphous orientation also contain greater levels of crystalline orientation. *The effects of crystalline orientation are not normalized out of Fig.4.38.* Thus, the films with greater amorphous phase orientation would "appear" to provide the poorest barrier. Therefore, the orientation of the amorphous phase must have some influence on the MVTR performance. Furthermore, because the amorphous phase orientation is not normalized out of the crystalline orientation versus MVTR plots, and because the two types of orientation have the opposite effect on barrier properties, it suggests that if the effects of crystalline orientation on MVTR performance could be observed independent of the amorphous orientation, a stronger dependence of barrier on crystalline orientation would be noted.

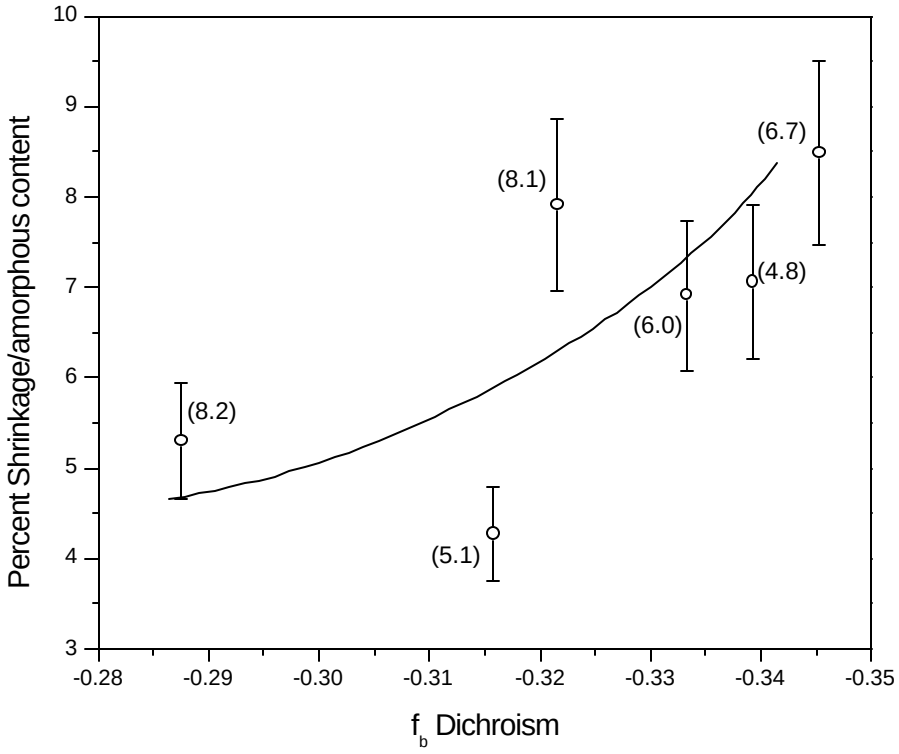

Figure 4.37. Correlation of normalized MD shrinkage with b-axis orientation as determined by infrared dichroism. Trend line included only to guide eye.

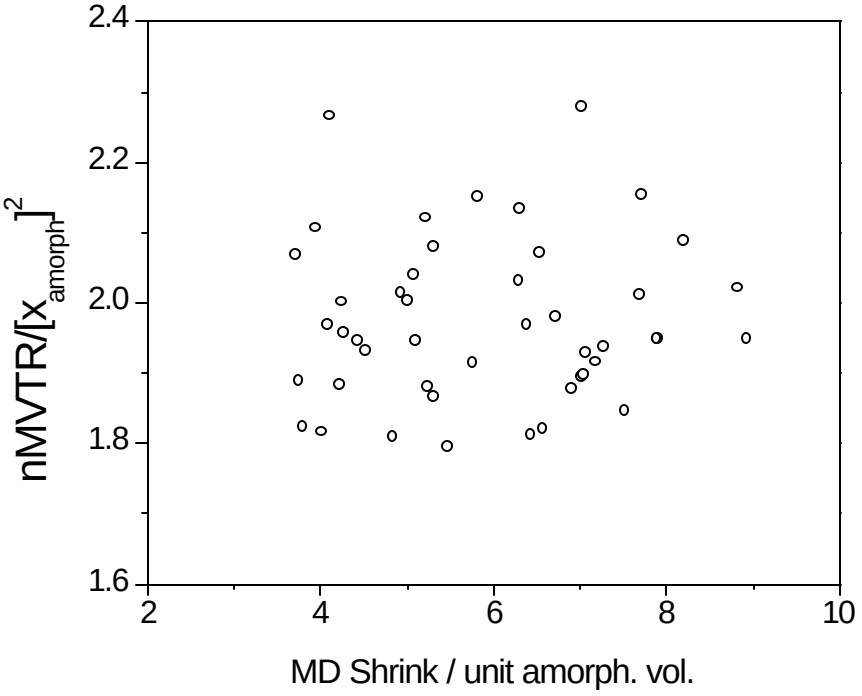

Figure 4.38. Correlation of normalized MD shrinkage and normalized MVTR performance.

Unfortunately, it is evident that simplified estimates of the processing and resin interactions do not provide the precision necessary to predict the small variations in permeation observed in this study. Because it is not readily evident how one balances the relative contributions of stress oriented crystallization and fibril nucleated crystallization, scaling with only a relative stress indicator, or relaxation time, may not be possible, as attempted above. *The results clearly suggest that increased stress in the melt, whether it be due to large viscosities or rapid processing, lead to poorer MVTR performance.* Thus, a general trend has been noted which can account for large differences. However, the data also suggest that the performance over a relatively narrow set of conditions, as encountered in this study, cannot be predicted a priori without further knowledge of additional factors.

4.8 Conclusions

A series of blown films produced from a number of HDPE resins was studied. The effects of M_w and MWD on the orientation of the films for equivalent processing conditions were examined. WAXS results demonstrated that, taken as whole, the set of films contained varying levels of crystalline orientation, though the differences were small. Furthermore, the WAXS data showed that all of the films studied contained morphologies which are consistent with the K-M model of low stress row crystallization. This conclusion was supported by the microscopy and mechanical properties data. The small BUR (2.9) employed in this study did not appear to induce substantial biaxial orientation. The application of IR dichroism to a limited number of films proved quite successful in quantifying the relative levels of crystalline orientation as a function of M_w and MWD. The dichroism data indicated that greater levels of orientation were obtained in films of narrower MWD, all other factors equal. The light scattering and pole figure data were supportive of this finding. However, because not all films contained superstructures amendable for light scattering study, and pole figures were not for all films studied, these results cannot be applied universally with certainty to all of the films.

It was reasoned that the narrow MWD, metallocene resins produced more highly oriented films because greater stresses were developed in the melt, relative to the broader MWD resins, due to their lesser propensity to shear thin. While the measurement of refractive indices provided a very accurate method for determining the crystalline content of the films, these same results applied to birefringence calculations showed no consistent agreement with the orientation behavior determined by the other techniques.

Microscopy indicated that the lamellae become increasingly oriented with their surface normals parallel to the MD as the processing stress increased. Furthermore, long range row nucleated structures were observed in the CrO based resins, but not in the metallocene resins, as a rule. This finding was attributed to the small, very high molecular weight fraction present in the broad resins, demonstrated by the higher moments of the MWD. These structures may also be a consequence of the slightly greater LCB content in the CrO based systems relative to the metallocenes. SAXS results revealed only slight variations in lamellar long spacing, and hence amorphous layer thickness, among films.

The permeation data suggested that, to a first approximation, the MVTR performance could be related to the square of the amorphous phase content, such that greater crystallinity led to improved barrier properties. Thus, longer quench times, which necessarily require slower cooling rate, are beneficial to MVTR performance as they lead to greater levels of crystallinity with less orientation, all other factors constant. Attempts to further correlate MVTR performance with processing stresses and orientation, using processing and resin parameters, proved problematic. While a general trend was noted that greater processing stresses lead to poorer barrier properties, the correlation could not be used as a predictor of a specific film's MVTR.

4.9 References

[1] Schlotter, N.E., Furlan, P.Y., *Polymer*, **33** (16) 3325 (1992).
[2] Peterlin, A., *Journal of Macromolecular Science – Physics*, **B11** (1) 57 (1975).
[3] Polymer Handbook 2nd edition, Ed. Brandup, J., Immergut, E.H., Wiley-Interscience, New York (1975).
[4] Peacock, A.J., Handbook of Polyethylene – Structure, Properties, and Applications,Marcel Dekker Inc., New York, (2000).
[5] Aggarwal, S.L., Tilley, G.P., Sweeting, O.J., *Journal of Applied Polymer Science*, **1** (1) 91 (1959).
[6] Lindenmeyer, P.H., Lustig, S., *Journal of Applied Polymer Science*, **9** 227 (1965).
[7] Desper, R.C., *Journal of Applied Polymer Science*, **13** 169 (1969).
[8] Maddams, W.F., Preedy, J.E., *Journal of Applied Polymer Science*, **22** 2721 (1978).
[9] Maddams, W.F., Preedy, J.E., *Journal of Applied Polymer Science*, **22** 2739 (1978).
[10] Maddams, W.F., Preedy, J.E., *Journal of Applied Polymer Science*, **22** 2751 (1978).
[11] Hofmann, D.Geiss, D., Janke, A., Michler, G.H., Fielder, P., Journal of Applied Polymer Science, 39 1595 (1990).
[12] Choi, K.J., White, J.L., Spruiell, J.E., *Journal of Applied Polymer Science*, **25** 2777 (1980).
[13] Choi, K.J., White, J.L., Spruiell, J.E., *Journal of Polymer Science; Polymer Physics*, **20** 27 (1982).
[14] Keller, A., Machin, M.J., *Journal of Macromolecular Science Physics*, **B1**, (1) 41 (1997).
[15] Ng, H.C., Leung, W.P., Choy, C.L., *Journal of Polymer Science: Polymer Physics*, **23** 973 (1985).
[16] Araimo, L., Candia, F., Vittoria, V., Peterlin, A., *Journal of Polymer Science: Polymer Physics*, **16** 2087 (1978).
[17] Eby, R.K., *Journal of Applied Physics*, **35** (9) 2720 (1964).
[18] Krohn, J., Tate, R., Jordy, D., *Proceedings of the SPE 55th ANTEC*, 1654 (1997).
[19] Todd, W., Podborny, W., Krohn, J.,*Proceedings of the SPE 57th ANTEC*, 95 (1999).
[20] Cowell, T.J., Johnson, J., *Polyolefins 2001 – International Conference on Polyolefins*, 275 (2001).
[21] Krohn, J., Jory, D., *TAPPI Journal*, **80** (3) 151 (1997).
[22] Culter, J.D., *Journal of Plastic Film and Sheeting*, **1** 215 (1985).
[23] Subramanian, P., *Polymer Engineering and Science*, **25** (8) 483 (1985).
[24] Vittoria, V., *Journal of Materials Science*, **30** 3954 (1995).
[25] Holden, P.S., Orchard, A.J., Ward, I.M., *Journal of Polymer Science, Polymer Physics*, **23** 2295 (1985).
[26] Hedenqvist, M., Angelstok, A., Edsberg, L., Larsson, P.T., Gedde, U.W., *Polymer*, **37** (14) 2887 (1996).
[27] Holden, P.S., Orchard, A.J., Ward, I.M., *Journal of Polymer Science, Polymer Physics*, **23** 709 (1985).
[28] Paulos, J.P., Thomas, E.L., *Journal of Applied Polymer Science*, **25** 15 (1980).
[29] Krohn, J.V., Podborny, W.R., Todd, W.G., *Journal of Applied Medical Polymers*, **4** (2) 75.
[30] Krohn, J., Tate, R., Jordy, D., *Journal of Plastic Film and Sheeting*, **13** 327.
[31] Pepper, R.E., Samuels, R.J., Encyclopedia of Polymer Science and Engineering, John Wiley and Sons, New York, **14** 261 (1988).
[32] Krishnaswamy, R., Janzen, J., *ANTEC 2001 - San Francisco*, SPE 297 (2001).
[33] Arnett, R.L., Thomas, C.P., *Journal of Physical Chemistry*, **84** 649 (1980).
[34] Raju, V.R., Smith , G.G., Marin, G., Knox, J., Graessley, W.W., *Journal of Polymer Science – Polymer Physics*, **17** 1183 (1979).
[35] Larson, R.G., *Macromolecules*, **34** 4556 (2001).
[36] Bird, R.B., Armstrong, R.C., Hassager, O., Dynamics of Polymeric Liquids - Vol.1, Wiley-Interscience, New York, (1987).
[37] Bin Wadud, S.E., Baird,D.G., *Journal of Rheology*, **44** (5) 1151 (2000).
[38] Janzen, J., Colby, *Journal of Molecular Structure*, **485-486** 569 (1999).
[39] Janzen, J., *Journal of Polymer Engineering and Science*, **32** 1242 (1992)
[40] Stacy, C.J., Arnett, R.L., *Journal of Polymer Science, Part A*, **2** 167 (1964)
[41] Wunderlich, B., Macromolecular Physics,Vol.1, New York, Academic Press (1973).
[42] Stein R.S., Newer Methods in Polymer Characterization, Wiley-Interscience, New York (1964).
[43] Yu, Ta-Hua, Ph.D. Thesis, Virginia Polytechnic Institute and State University, Chem. Eng. Dept. (1996).
[44] Wilkes,G.L., Stein, R.S., Structure and Properties of Oriented Polymers, Ed. I.M. Ward, Chapman and Hill, New York (1997).
[45] Johnson, M.B., Wilkes, G.L., Sukhadia, A., Rohlfing, D.C., *Journal of Applied Polymer Science*, **77** 2845 (2000).

[46] Muccigrosso, J., Phillips, P.J., *IEEE Trans. Electr. Insul*., **EI-13** (3) 172 (1978).
[47] Zhou, H., Wilkes, G.L., *Journal of Material Science*, **33** (2) 287 (1998).
[48] Krishnaswamy, R.K., Sukhadia, A.M., *Polymer*, **41** 9205 (2000).

Chapter 5

Thermal and structural characterization of Poly(acrylonitrile-co-methyl acrylate) copolymers. Effects of comonomer content on melting behavior.

5.1 Introduction

Polyacrylonitrile (PAN) is used predominately in the textile industry in dyeable acrylic fabrics. It is also widely used as a precursor material in the production of carbon fibers. The production of carbon fibers based on PAN is accomplished by first wet or dry spinning a PAN copolymer of suitable composition into a precursor fiber. The precursor fiber is then subjected to a regimen of increasing temperature in the presence of air or nitrogen under tension. Temperatures in the range of 250 – 400 °C are applied to

produce a fused material which will not flow and is insoluble. The initial product of the degradation reaction, shown in Fig.5.1, is often referred to as the "ladder polymer" structure[1-5]. While not fully understood at this time, studies suggest that the cyclization of the nitrile groups, which leads to the ladder structure, is the result of both intra and inter-molecular reactions[1]. It is well established that this reaction is highly exothermic. Increasing the temperature further leads to the elimination of hydrogen and nitrogen from the structure. This processing step is referred to as carbonization. At temperatures greater than 1200 °C, carbon represents 92% or more of the fibers elemental composition[6], existing in layers whose planes are preferentially oriented parallel to the length of the fiber[7-9].

While control of the degradation reactions is critical to the formation of a stable material for later carbonization, degradation reactions during the spinning process would make fiber formation impossible. Inter-molecular reactions involved in the formation of the ladder polymer act to crosslink the material. The premature formation of the ladder structure leads to a gelled system incapable of flow. Noting that; a) the melting temperature of PAN is 319 °C[10], b) the formation of the ladder structure proceeds rapidly at 300 °C, and c) that the reaction is highly exothermic (coupled with poor heat transfer properties) leading to an auto-catalytic response, it can be seen that the melt processing of a neat, homopolymer of PAN is not possible. At this time solvent based spinning is required to produce the precursor fiber and represents a significant portion of the end carbon fiber's price. Economic and environmental concerns dictate the need of costly solvent recovery systems to recycle the toxic solvents utilized. If developed, a melt processable system would thus substantially reduce the cost of carbon fiber production.

The global goal of the project was to develop a PAN based material which is both melt processable and suitable for conversion into low cost carbon fibers for use in the automotive industry. Within this larger framework, the focus of the research presented here is as follows. The thermal and structural characteristics of a series of copolymers composed of varying levels of methyl acrylate (MA) and acrylonitrile PAN were studied to gauge their suitability for use in the production of carbon fiber precursors.

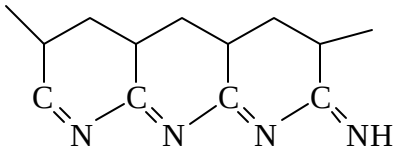

Figure 5.1. Structure of repeating sequence in "ladder polymer" formed during the initial stages of thermal degradation of PAN. This material is insoluble and does not flow.

Methyl acrylate was selected as the comonomer of choice because; it has traditionally been used as a comonomer industrially to impart dyeability to PAN fibers, MA has been shown to increase the temperature at which the initial degradation reactions begin[11], thus widening the processing window, and the ability of MA monomer to be copolymerized randomly with acrylonitrile[12].

This study shows that via the incorporation of the MA comonomer it is possible to lower the melting temperature of PAN to a temperature below the point degradation becomes rapid (ca. 300 °C+). Information regarding the presence or absence of a crystalline state of the acrylonitrile component was also obtained

5.2 Experimental Methods

The copolymers used in this study were kindly synthesized and analyzed for comonomer content and molecular weight by project collaborators in the laboratory of Dr. McGrath of Virginia Tech. The solution polymerization was graciously conducted by Dr. V. Bahnu as follows[12]. A 500 ml three necked flask with condenser, stirrer and nitrogen purge was used. The flask was charged with 50 ml of N,N-Dimethyl formamide (DMF) and purged with nitrogen for fifteen minutes. Next, the mixture of monomers, acrylonitrile (AN) and methyl acrylate (MA), along with the initiator, 2,2'-azo-bis-isobutyronitrile (AIBN), and chain transfer agent, dodecyl mercaptan, were added to the reaction flask. Total monomer content for each polymerization was held at 375 mmol. The reactions were conducted at 70 °C for six hours. The obtained polymer was washed with a 50 fold excess of deionized water and subsequently dried for 24 hours at 70 °C under vacuum. The final comonomer contents of the end materials were verified using ^{1}H and ^{13}C NMR.[12] Intrinsic viscosity measurements were performed in NMP at 25 °C. Absolute molecular weight data was also obtained for the materials using a Waters 260 GPC with differential refractometer detector and an online viscometric detector coupled in parallel. The solvent used was NMP with 0.02 M P_2O_5. A summary of the molecular weights and compositions of the materials studied is given in Table 5.1.

Table 5.1. Summary of intrinsic viscosity and molecular weight for materials studied. Note that the molecular weight of 95/5 is substantially lower than the other samples.

Material	IV	Mn (g/mol)
100/0	0.6	24,400
95/5	0.27	8,500
93/7	0.55	21,700
90/10	0.52	20,200
85/15	0.49	18,700

Samples will be referenced throughout according to composition using the following simple designation, (mols AN / mols MA). Thus the five materials used in this study are designated 100/0, 95/5, 93/7, 90/10, and 85/15 in order from lowest to highest comonomer content.

Thermal analysis was conducted using a Seiko instruments thermogravimetric and differential temperature analyzer (TG/DTA) with nitrogen purge to determine melting behavior prior to degradation using rapid heating rates (60 and 250 ºC/min). Aluminum pans with pierced lids were used to hold the 3-5 mg samples. The use of pierced lids allowed for the escape of residual water content. Additionally a Perkin-Elmer series 7 differential scanning calorimeter (DSC) with nitrogen purge was used to study the glass transition behavior for all materials and the melting behavior of selected samples. As with the TG/DTA experiments, aluminum pans with pierced lids were used to hold the 3-5 mg samples. A series of experiments were also conducted using a TA Instruments model 2920 modulated DSC (MDSC). An underlying heating rate of 2 ºC/min with a temperature modulation frequency and amplitude of 100 seconds and 0.5 ºC respectively. Again, sample masses were kept in the 3-5 mg range. For each of these three instruments, an initial thermal conditioning was conducted whereby each sample was brought to 200 ºC for two minutes from room temperature using a heating rate of 20 ºC/min. This step was conducted to erase any physical ageing effects and, as stated above, was found to be of use for removing residual water content in the materials. Water contents for all samples were approximately 2-3 wt% prior to conditioning. The plots included in this chapter do not include data from the conditioning step. For samples which were intentionally aged, the conditioning step was conducted prior to ageing.

Dynamic mechanical analysis (DMA) was conducted using a Seiko instruments DMS 210 at a frequency of 1 Hz with a temperature ramp of 2 ºC/min under nitrogen. Film specimens for testing were prepared as follows. The copolymer in powder form was placed in a mold formed by stacking multiple layers of aluminum foil with a hole punched through the center. The polymer in the powder filled mold was formed into a brittle, opaque film at room temperature under a pressure of approximately 20,000 PSI using a laboratory press. The mold with film was then transferred to a second press heated to a temperature of 150 ºC (above Tg but below Tm). One minute was allowed

for temperature equilibration before a pressure of 20,000 psi was applied for an additional two minutes. The mold with film was then removed from the press and allowed to quickly cool under exposure to room temperature. The resulting specimen thickness was approximately 0.3 mm. It is recognized that this procedure may not be ideal for producing an orientation free specimen. However, it was deemed necessary to keep the temperature and time of exposure to a minimum to prevent the onset of degradation. It should be noted that the temperature and pressure were sufficient to transform the opaque films into transparent films for the three highest comonomer content materials (85/15, 90/10, and 93/7) while the lowest content films (95/5 and 100/0) remained opaque. Of further note, samples prepared using this procedure showed identical heat flow behavior in the DSC to their powder form counterparts after the standard 200 °C conditioning step mentioned above, thus suggesting that the film preparation process did not result in degradation of the polymer.

Wide angle x-ray scattering (WAXS) experiments were conducted on films which were produced in the same manner as described above for the DMA. Certain films were further conditioned (described later where appropriate) using a specified heating schedule in the DSC prior to testing. A Philips 1720 tabletop generator was used to produce Ni filtered CuKα radiation of wavelength 1.54 Å. A Warhaus camera under vacuum was used to obtain flat plate photographs of the scattering patterns for exposure times of 2-4 hours.

5.3 Crystalline state of pressed films

As stated earlier, the goal of the global research project was to produce a melt spinnable PAN based material. The reader is also asked to recall that the melting point of PAN is 319 °C, which is above the temperature at which exothermic degradation reactions proceed at a rapid rate. Also stated earlier, it is this highly exothermic reaction that prevents PAN from being melt processed. There are two primary methods used to observe the melting of PAN without the use of solvents or diluents. The first method involves the incorporation of a comonomer into the chain which acts to depress the material's melting temperature. It is the effect of this melting point depression

phenomenon which forms the basis of this work. In theory, the addition of a sufficient level of comonomer should lower the melting point of the copolymer to a temperature at which complete melting is achieved prior to the onset of thermal degradation. However, depending on the chemistry of the comonomer, the degradation reaction may be moved to lower (catalyzed) or higher temperatures (inhibited). It should also be recognized that above a certain threshold of randomly added comonomer content the symmetry of the chain is so disrupted that no crystallization can take place. The second method used to study the melting of PAN based materials is to conduct experiments under conditions of such rapid heating that melting is fully achieved before the kinetics of the degradation reaction are allowed to accelerate. Attempts to study the copolymers materials using this method will also be discussed.

Before examination of the experimental findings it is important to address an additional issue that is a common source of confusion regarding PAN. This concerns the exact nature of the crystalline state found in PAN. The synthetic methods used in this study, as well as the procedures employed in industrial practice, produce an atactic chain. Thus, there is no reason *a priori* to assume that PAN should crystallize at all. Despite this fact, PAN is widely regarded as a semicrystalline material based on its thermal-mechanical response and because it produces a strong, sharp diffraction peak at $2\theta = 17°$ ($d = 5.30$ Å) and a weaker peak at $2\theta = 29°$ ($d = 3.04$ Å) by x-ray analysis. An examination of the diffraction behavior of PAN shows that upon orientation, there is an absence of meridional scattering reflections. To many researchers this has led to the conclusion that PAN consists of laterally ordered, rod like domains, or a two dimensional crystal similar to a nematic liquid crystalline texture[1,9,13-15]. The chains are considered to pack with a preferred spacing of 5.30 Å perpendicular to the chain direction, while there is no regular periodicity along the chain axis due to the atactic nature of the chains. Essentially the chains exist in an irregular helix of constant radius. These helices pack together in a parallel fashion to form the ordered structure. Various unit cells have been proposed for PAN based on these findings. This work will consider PAN to have hexagonal packing with no long range order along the chain axis. Furthermore, regardless of the exact nature of PAN in the solid state, *this study will consider PAN to be a system which can be described in the context of a traditional semicrystalline polymer*

through the observation of sharp scattering maxima as observed by WAXS and first and second order thermodynamic transitions as observed by thermal analysis.

As stated above, the primary goal of this investigation was to determine the effect of comonomer incorporation on the copolymer's crystalline state. The synthesized materials received in powder form were pressed into films as outlined in the experimental section for easier analysis by x-ray diffraction. The absence of sharp rings in the obtained scattering patterns would be a clear indicator of a lack of regular packing. The results for each copolymer composition are presented in Fig.5.2. From the homopolymer pattern, the two sharp reflections generally observed in PAN can be noted at $2\theta=17°$ (inner) and 29° (outer) respectively. Note also that the pattern appears typical of a semicrystalline polymer with the sharp rings corresponding to crystalline regions superimposed upon a background of diffuse scattering due to amorphous regions. Following the increase in comonomer content from one pattern to the next in Fig.5.2 it can be seen that the sharpness of the inner reflection decreases while the outer reflection eventually disappears at the highest comonomer level.

The increased diffuseness of the inner reflection suggests that the inter-chain distance of 5.30 Å, attributed to PAN's hexagonal packing in the crystalline state, is being partially disrupted by the incorporation of comonomer. Quantitative intensity data is provided in Fig.5.3 obtained from WAXS measurements obtained in reflection from melt pressed films. Two primary features are present in each curve, a sharp peak located at $2\theta = 17°$, and a broad peak, ending approximately at $2\theta = 29°$. Because the capabilities for transmission mode measurement were unavailable, the results could not be normalized on sample thickness. An alternate normalization scheme, obtained by dividing the measured intensity by the peak intensity obtained at $2\theta = 17°$ for each sample, allows changes in the relative intensities between the sharp and broad peaks to be compared from one sample to the next. Thus, it can be observed in Fig.5.3 that the intensity of the broad peak increases relative to the sharp peak with increasing MA content. Assuming a two phase morphological model, and attributing the sharp peak to crystalline material while assigning the broad peak to amorphous material, demonstrates that the crystalline content of the materials decreases with increasing MA content.

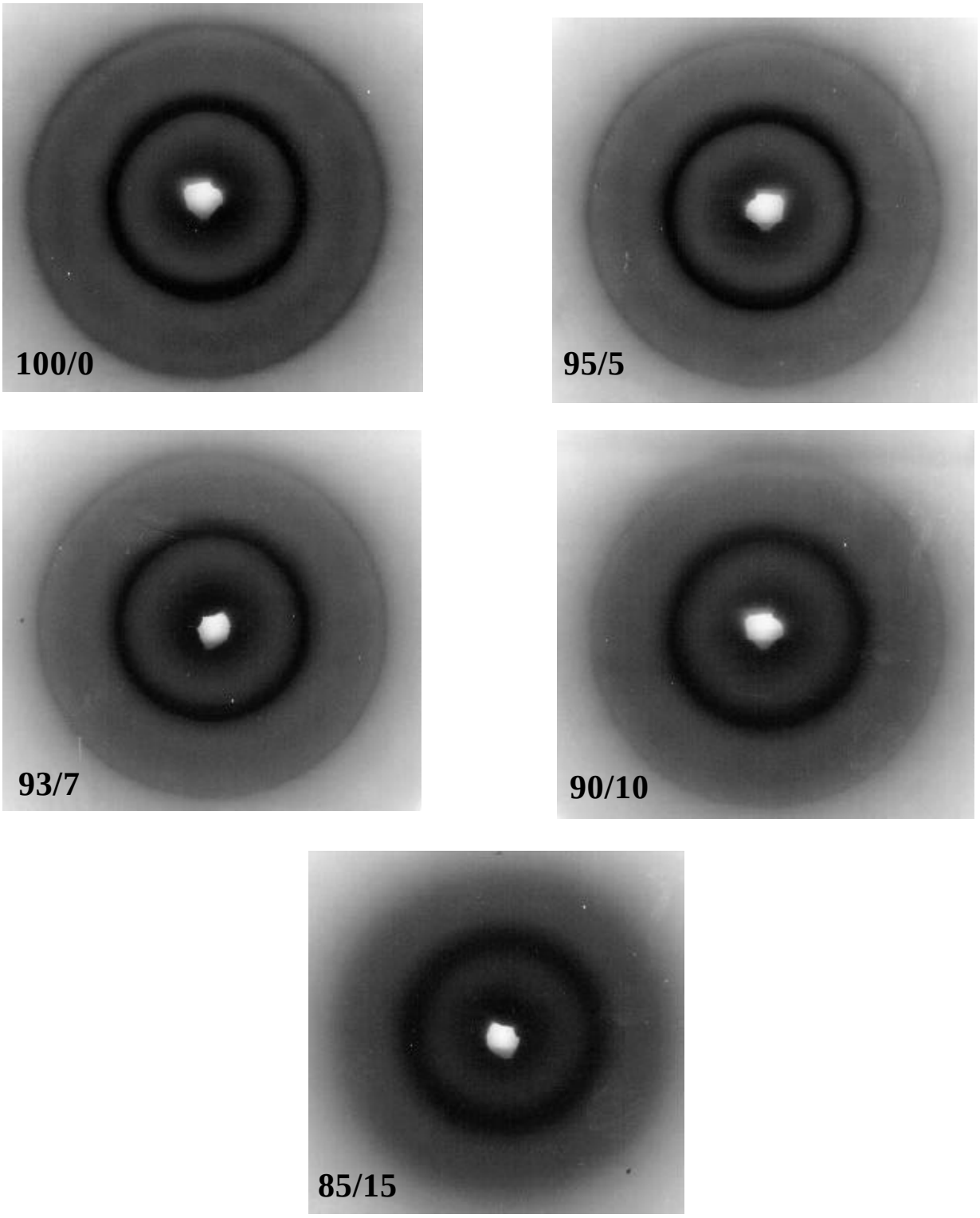

Figure 5.2. WAXS scattering patterns of PAN copolymers, copolymer content indicated in upper right corner of patterns as (AN-MA) mole percentages Sharp inner reflection corresponds to $2\theta = 17^{o}$ with 5.30 Å inter-chain packing distance. Outer ring corresponds to $2\theta = 29^{\circ}$ with approximately 3.04 Å spacing. Note disappearance of outer reflection and reduction in sharpness of inner reflection as comonomer content increases.

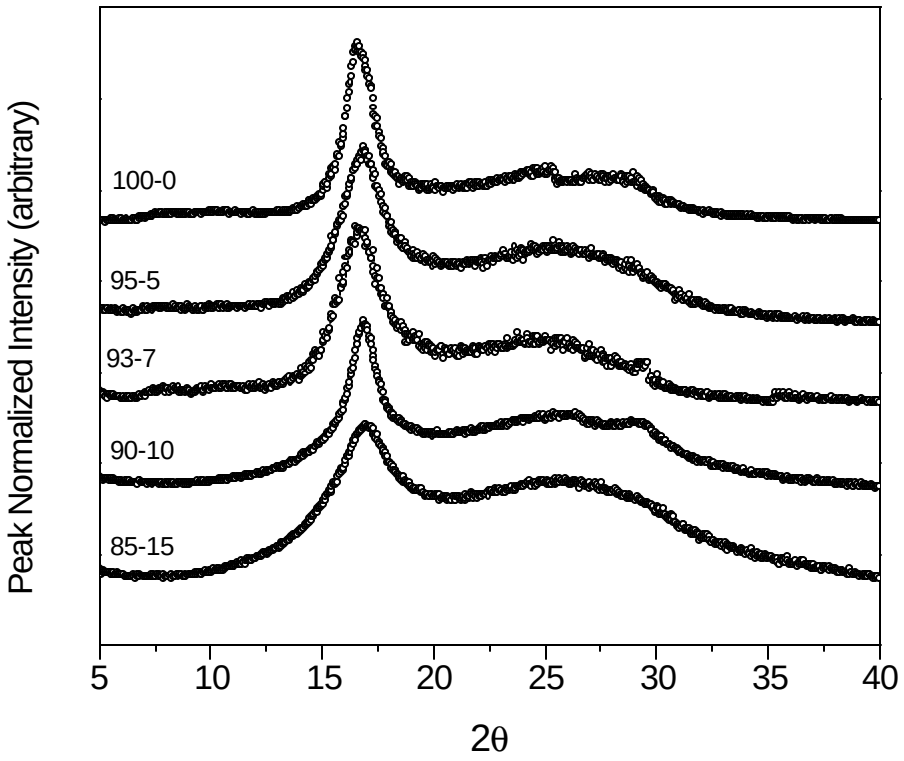

Figure 5.3. Powder diffractometer results normalized with respect to maximum peak intensity ($I_{norm}=I_{\theta}/I_{2\theta=17°}$). Note that relative heights of the sharp peak ($2\theta = 17°$) and the broad, underlying scattering becomes smaller with increasing MA content, suggesting a loss of crystalline material. Also note broadening of left shoulder on $2\theta = 17°$ peak with increasing MA content suggesting smaller and/or less perfect crystallites.

Furthermore, the data of Fig.5.3 also reveals that the sharpness of the $2\theta = 17°$ peak decreases with increasing MA content, showing that size and/or perfection of the crystallites is decreasing as greater levels of comonomer are incorporated.

The mechanism by which the spacing is disrupted may be reasoned as follows. Figure 5.4 shows the chemical repeat units of the PAN-co-MA copolymers studied. It is readily evident that the size of the methyl acrylate group of the comonomer is much larger than that of the cyano group of the homopolymer. It might be speculated that in a crystal with less than "perfect" structure, such as that found in PAN, cocrystalliation of the comonomer units with acrylonitrile units is possible. However, due to the size differential of the repeat units involved, such a situation seems very unlikely here. Thus, it is reasonable to assume that the MA comonomer will be rejected from the crystalline lattice. Because the methylacrylate cannot be incorporated into the crystalline phase, a disruption of the dimensions of the 5.30 Å spacing by the incorporation of MA units into the crystalline phase seems unlikely. However, as the comonomer content is increased, the size of the hexagonally packed domains should be decreased as the MA units will limit the length of continuous AN sequences along the chain. Smaller crystallites can be considered less perfect crystals than larger ones and should thus produce more diffuse reflections and also melt at a lower temperature.

Based on Figs.5.2,3 it can be seen that PAN-co-MA does indeed appear to be a semicrystalline material producing both sharp (crystalline) and diffuse (amorphous) scattering. The perfection of the crystalline phase is seen to decrease as the amount of comonomer content is increased. Hence, this result is qualitatively interpreted to arise from a decrease in the size of crystalline domains since the MA units should act to restrict the dimensions of such domains along the chain axis. Finally, a notable decrease in diffracted intensity at $2\theta = 17°$ relative to the broad scattering ending approximately at $2\theta = 29°$, demonstrates that the overall crystalline content of these materials is decreasing with increasing comonomer content.

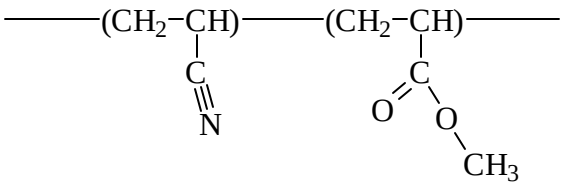

Figure 5.4. Repeat units of AN-MA copolymer. Left repeat unit of acrylonitrile. Right repeat unit of methyl acrylate. Note differences in size and chemical structure of side groups between the two repeat units, suggesting against possible co-crystallization.

5.4 Microstructure of PAN-co-MA materials based on reactivity ratios

The previous assertion that the MA units act to disrupt crystallinity is based on the assumption that their incorporation into the copolymer occurs in a random manner during synthesis. Recently as part of the overall project Wiles et. al[16] determined the reactivity ratios for AN and MA in DMF at 62 °C. The values are 1.29 and 0.96 for AN and MA respectively (note that the actual temperature of polymerization was 70 °C). A reactivity ratio is defined as the tendency for a radical of a given monomer to react with another monomer of its own kind relative to its tendency to react with the other monomer present. The values above show that the AN monomer has a small preference to react with itself relative to the MA, while MA radicals show almost no preference at all. In accordance with the calculations originally derived by Flory[17] the instantaneous composition of copolymer being produced as a function of monomer composition and reactivity ratios can be determined by Eq.5.1.

$$F_1 = \left(r_1 f_1^2 + f_1 f_2\right) \Big/ \left(r_1 f_1^2 + 2 f_1 f_2 + r_2 f_2^2\right) \qquad \text{Eq.5.1}$$

where

F_i = instantaneous copolymer mole fraction of unit i

f_i = instantaneous monomer fraction of unit i

r_i = reactivity ratio of i relative to other component

Taking unit one to be AN and using the above reactivity ratios, a plot of instantaneous copolymer composition as a function of AN monomer fraction is presented in Fig.5.5. This plot shows the reaction of AN with MA under these conditions follows closely the conditions commonly referred to as an ideal copolymerization. Because the composition of the copolymer at any instant nearly matches the composition of the monomer phase present, its composition will remain nearly constant as the

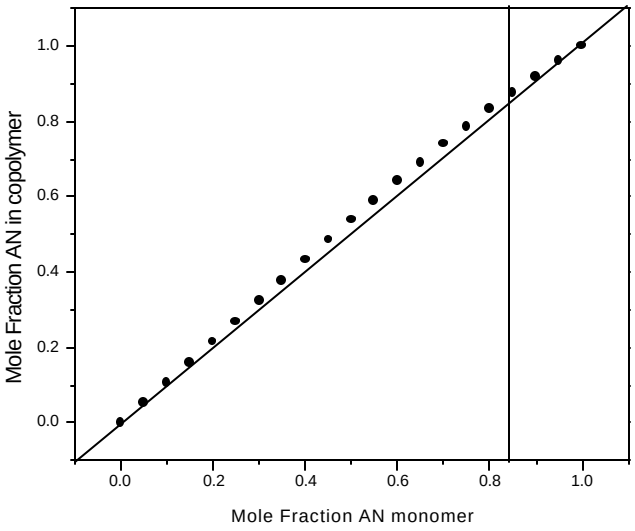

Figure 5.5. Relationship between instantaneous copolymer composition and current reaction mixture composition. Area to the right of the vertical line indicates the range of initial reactor compositions used in this study. Diagonal line indicates behavior for which the composition of copolymer produced is equal to the composition of the reaction mixture.

reaction proceeds with time in a batch process. Furthermore, because each of the reactivity ratios is close to a value of unity (no great preference for addition of AN relative to MA for either monomer radical) it can be expected that the addition of each monomer unit along the chain will be nearly purely statistical. Therefore the distribution of comonomers along the length a chain will be determined randomly, weighted only by the relative numbers of each monomer type present at that time. Based on the compositions studied, MA contents of 0 – 15 mol%, each chain should consist of MA units randomly distributed along its length, the number of which should, on average, be equivalent to the feed compositions. As stated in the experimental section, NMR and FTIR measurements verified this prediction[12].

5.5 Melting of the crystalline phase in PAN-co-MA by rapid heating

If indeed the level of crystallinity of these materials is changing as a function of comonomer content, then it should be possible to observe a change in the heat of fusion (or melting) per gram of copolymer as a function of comonomer content. However, as stated earlier, the nature of the crystalline state in PAN is such that its melting point is above the temperature at which degradation reactions occur for conventional heating rates. The magnitude of the exotherm of these reactions is also so substantial that they can completely mask the presence of any melting in a conventional DSC or DTA experiment. Furthermore, the heat liberated by degradation is sufficient to rapidly raise the temperature, accelerating the reaction and leading to a rapid transformation of the polymer. It has been shown that it is possible to observe the melting of PAN via DSC or DTA if a sufficiently rapid heating rate is used[18]. Because the phenomenon of melting is a first order thermodynamic transition, its occurrence should not be a function of the heating rate used. Neglecting the realities of heat transfer, the entire crystal should melt instantaneously once the melting temperature is attained. The same is not true of degradation. The rate of degradation should follow an Arrhenius temperature dependence. The extent of reaction should be a function of both the reaction temperature and the reaction time. During a typical DTA experiment in which the temperature is ramped at a constant rate, the reaction rate should initiate at a finite temperature and then

accelerate as the temperature is increased. If the heating rate is sufficiently rapid, it may be possible to reach the melting point before the degradation reaction has had sufficient time to initiate and progress.

Figure 5.6 shows the results of DTA experiments conducted at a heating rate of 60 °C/min for each of the materials. The most striking feature of this plot is the large exothermic event generated at elevated temperatures due to the degradation of the polymer. It can be seen that the temperature at which the reaction reaches its maximum rate, as determined by the peak of the reaction exotherm, increases as the amount of MA increases. This suggests that the MA inhibits the reaction. Secondly it can be seen that the magnitude of the reaction (integrated area of the exothermic event) decreases with increasing MA content. This latter result is expected as it is the lack of stability of the AN content at elevated temperatures which is responsible for the reaction. A close examination of the curves at temperatures below the exothermic events reveals small endothermic events that may be associated with melting. It is this portion of the curves that is of primary interest to this study.

The endothermic peaks seen in Fig.5.6 are re-plotted in Fig.5.7 using an expanded scale. With the scale changed, the endothermic melting events become readily apparent. The behavior is quite systematic for the comonomer containing samples. The crystalline content of the polymer should scale linearly with the area under the endothermic peak. Thus, as suggested by the WAXS patterns of Fig.5.2, the incorporation of MA units into the chain leads to a reduction of the crystalline content of the copolymer. Additionally, it can be seen that the melting temperature, as determined by the peak of the melting transition, increases with AN content. This result shows that the addition of MA acts to reduce the melting point of PAN. Extrapolating the melting trend from the copolymers, it appears that the lack of melting observed for the homopolymer in this series of experiments was due because the heating rate was not sufficiently rapid for melting to be observed prior to degradation.

The next logical step was to run the series again using a higher heating rate. A second round of experiments was conducted with a heating rate of 250 °C/min, after recalibrating for the rapid heating. The results of these runs are shown in Fig.5.8.

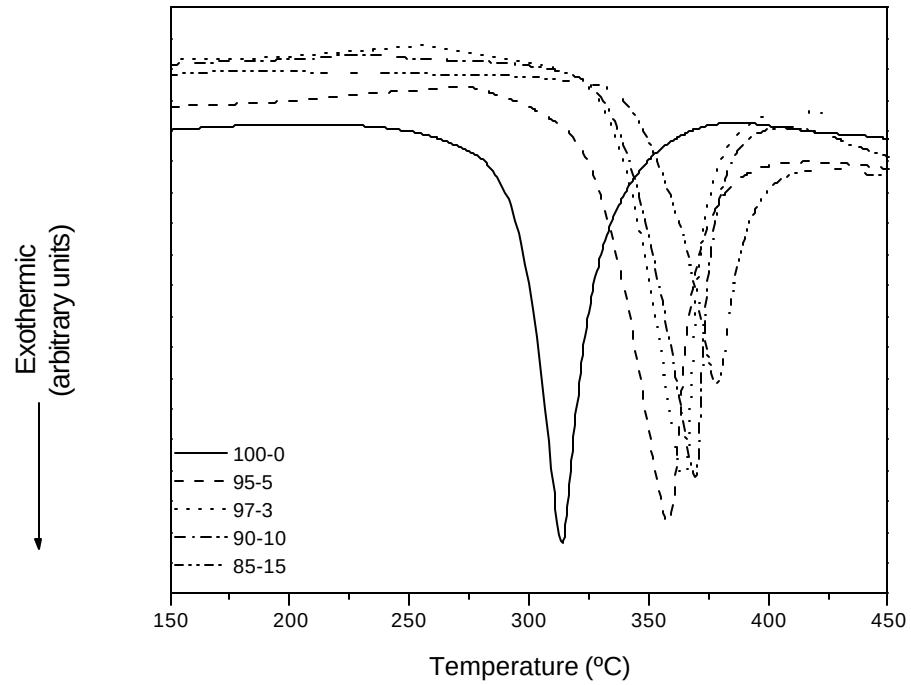

Figure 5.6. Exothermic degradation reaction of copolymers as shown by DTA using a heating rate of 60 ºC/min under nitrogen. Note amount of reaction increases and temperature of maximum reaction rate decreases with decreasing MA content. Prior to degradation small endothermic events representative of melting are observed.

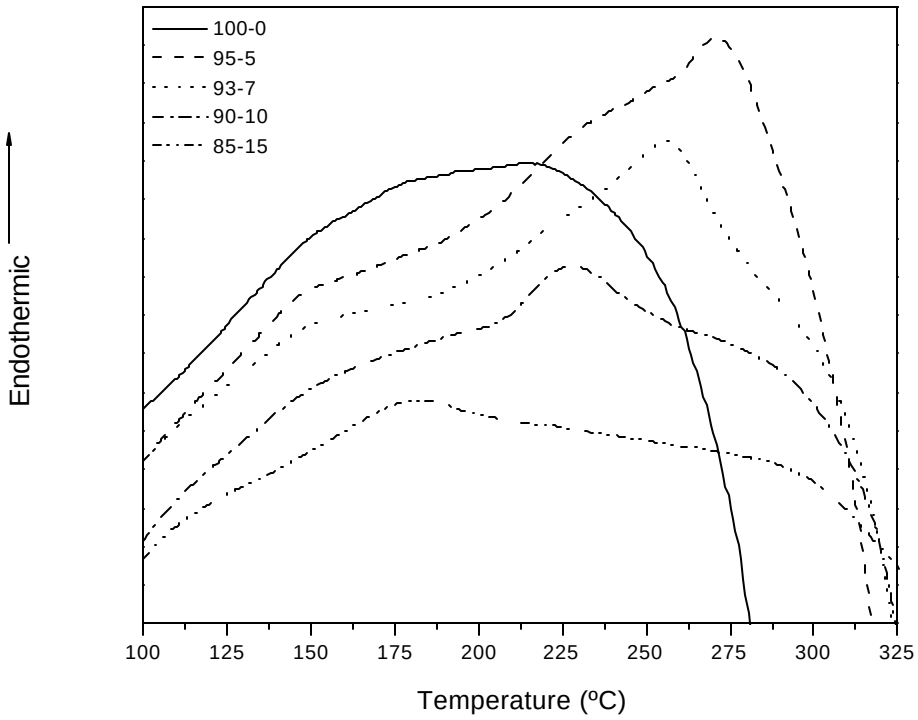

Figure 5.7. Melting behavior as determined using DTA at a heating rate of 60 ºC/min under nitrogen. Exothermic drop off at high temperatures represents beginning of degradation. Magnitude of melting increases, as does melting temperature, with increasing AN content except for the homopolymer (100-0) for which melting cannot be observed.

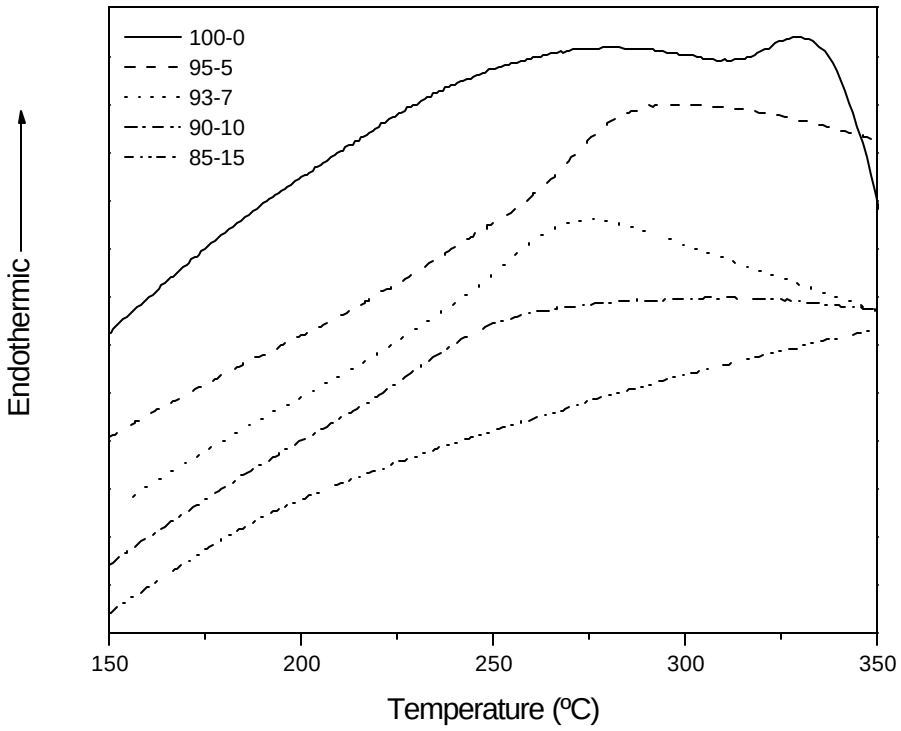

Figure 5.8. Melting behavior of materials as determined using DTA. Heating rate 250 ºC/min under nitrogen. Note endothermic melting event of homopolymer (100/0) superimposed over the beginning of the exothermic degradation reaction.

In this plot there is a clear endothermic event in the homopolymer superimposed over the beginning of the exothermic degradation. The quantification of the peak areas in this plot for determination of the relative levels of crystallinity is complicated by the overlapping of the endothermic and exothermic events. Relative to the data presented in Fig.5.7, the melting points appear at slightly higher temperatures and the peaks have been broadened. The broadening is expected as the rapid heating rate will result in a loss of resolution along the temperature axis. The increase in melting temperature with increased heating rate can be attributed to an unavoidable lag in the sample temperature relative to that which is measured at the base of the sample pans as the heating rate is increased. Taking the literature value of 319 ºC as the melting point of PAN homopolymer shows that the temperature lag is on the order of 10 ºC as the homopolymer melting point measured here is 330 ºC. Of course attaching an exact number to the melting peak of PAN in Fig.5.8 would require the deconvolution of the exothermic and endothermic events as well as accounting for instrumental limitations. *The primary focus here is the relative positions of the melting peaks as a function of comonomer content, not their absolute values.*

The result of greatest importance from these experiments is the observation that PAN copolymerized with between 5 to 15% MA produces a material which retains some of the semicrystalline texture of pure PAN but can be melted at a temperature before significant degradation begins. This suggests these PAN-co-MA materials behave as typical semicrystalline thermoplastics. The obvious implication of this result is the possibility of a melt processable PAN based material for use as a carbon fiber precursor. The next section presents DSC and DMA data to ascertain to what degree this latter statement is true for practical use.

5.6 PAN-co-MA as a Semicrystalline Thermoplastic

The two most basic quantities which can be used to characterize the thermal-mechanical behavior of a thermoplastic material are the glass transition and melting temperatures. By DSC reversible glass transition and melting transitions should be observable while DMA should demonstrate subsequent decreases in modulus as the material is brought through the rubbery and melting transitions.

The results of DMA experiments conducted at a heating rate of 2 ºC/min and frequency of 1 Hz for each of the materials is presented in Fig.5.9. The impact of increasing MA content on the dynamic mechanical properties of the copolymer are quite substantial. Recall that the DTA and WAXS results suggested that crystalline content scaled directly with AN content. The same trend can be noted here in that the 85/15 copolymer shows a much greater level of softening upon passing through the Tg in comparison to the lower MA content materials. Specifically, note a decrease in modulus of three orders of magnitude for 85/15 while a drop of less than one decade for the homopolymer occurs. The same conclusion can also be drawn from the increase in the magnitude of the damping peak at Tg with MA content. Also note how dramatically the lowering of the melting temperature with increasing MA content shortens the rubbery plateau of the copolymers. Based on the earlier DTA results it is surprising to see that the DMA results suggest the 95/5 copolymer is capable of considerable melting prior to substantial degradation at the extremely modest heating rate of 2 ºC/min employed. A small upturn in storage modulus is noted for the homopolymer at the highest temperatures, indicative of the formation of the stiff, ladder structure, as promoted by the degradation reactions. Finally, it can also be seen that incorporation of comonomer leads to a small but consistent lowering of the glass transition temperature as expected.

Based on the data presented thus far, the PAN-co-MA materials are clearly thermoplastic. However a "textbook" thermoplastic should be capable of being reprocessed time and again through melting and resolidification. The effect of multiple melting and cooling runs on the thermal properties of the materials were investigated by DSC. Figure 5.10 contains DSC scans for the PAN-co-MA with composition 85/15. Each heating step in this experiment was ended with a two minute hold at 200 ºC to eliminate residual nuclei. Despite the application of elevated temperatures for short periods of time, the 85/15 material shows no major degradation as evidenced by the reproducibility of the melting, crystallization, and glass transition temperatures.

With a melting temperature of roughly 150 ºC, the 85/15 PAN-co-MA can achieve complete melting and need not approach 300 ºC, the approximate onset of major thermal degradation noted in the DTA experiments.

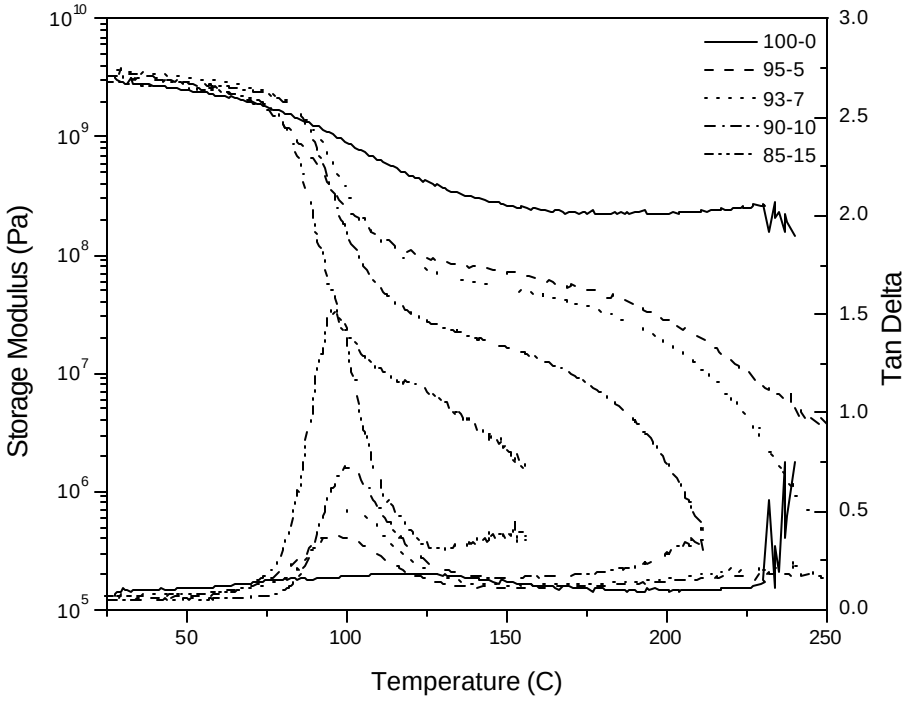

Figure 5.9. DMA results as determined at 1 Hz. Increasing MA content greatly increases amorphous content and lowers the glass transition and melting temperatures.

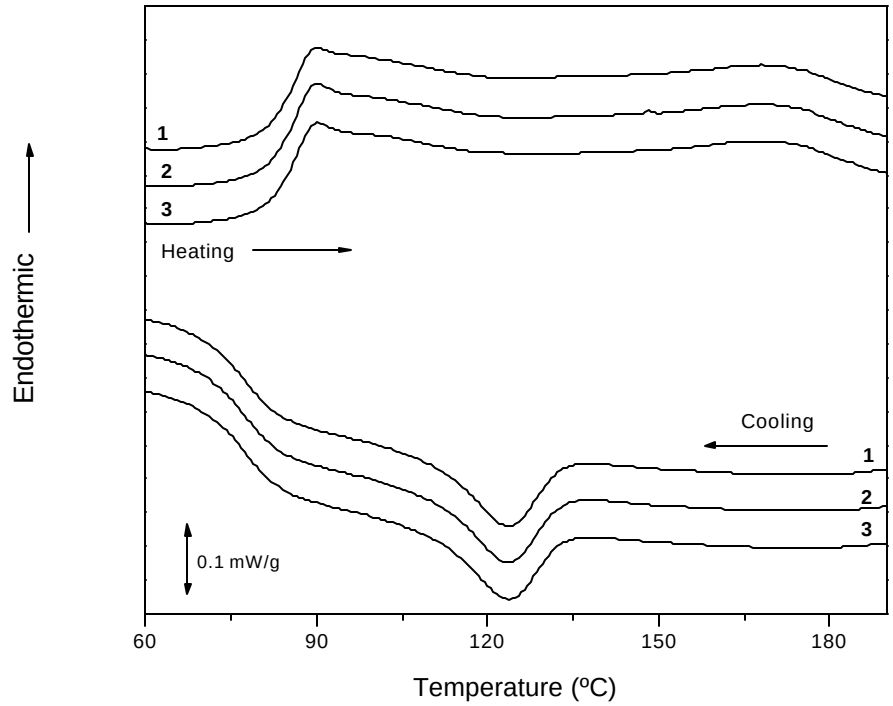

Figure 5.10. DSC trace of PAN-co-MA 85/15 for multiple heating and cooling cycles. Heating rate 20 ºC/min. Numbers represent 1st, 2nd, and 3rd cycles after initial heating (not shown) to 200 ºC to erase thermal history. Copolymer shows no signs of thermal degradation after multiple melting episodes. Also note that supercooled crystallization occurs over a relatively narrow temperature range relative to the broad melting span.

To further analyze the consequences of holding these materials at elevated temperatures, a second experiment was conducted in which the maximum temperature achieved at the end of each heating cycle was 250 °C. Again, each heating cycle ended with a two minute hold at the maximum temperature in an attempt to ensure full melting and destruction of nucleation centers. The results of this experiment are plotted in Fig.5.11. It is clearly evident that the magnitude of the melting and crystallization events decreases with each cycle. The reactions which occur in this temperature regime are often referred to as "stabilization". The stabilization reaction is thought to lead to the formation of a structure often termed a ladder polymer which was depicted earlier schematically in Fig.5.1. The rigid nature of the ladder polymer and the likely fact that it involves reactions between adjacent chains (intermolecular rather than solely intramolecular) means that a small amount of the material should affect the properties of the bulk polymer in the same manner that crosslinking might. Thus, the reaction converts crystalline and amorphous material to the rigid, ladder structure which acts to raise the Tg of the remaining amorphous phase by restricting its movement. Indeed, the DSC glass transition of the 85/15 copolymer was raised by 4°C in the third heating cycle relative to the first. Close examination also reveals that the glass transition has been somewhat broadend as a result of the thermal cycling.

The likelihood of degradation with multiple melting cycles will become greater as the MA content is decreased for two reasons. Recalling the results of the DTA experiments in Fig.5.7,8 the incorporation of MA acted to lower the melting temperature and simultaneously raise the onset of thermal degradation to higher temperatures. Thus, the temperature window for stability between melting and degradation will decrease from both ends as the comonomer content is decreased. This point becomes particularly important when the next copolymer material, 90/10, is analyzed.

An identical experiment was conducted for this material as shown in Fig.5.12. Again, a maximum temperature of 250 °C was used with a two minute hold. Three points become of immediate interest upon examination of the results. First the changes in behavior with each heating cycle are much more dramatic then in the previous examples. There is a much more severe decrease in the amount of crystallizable material.

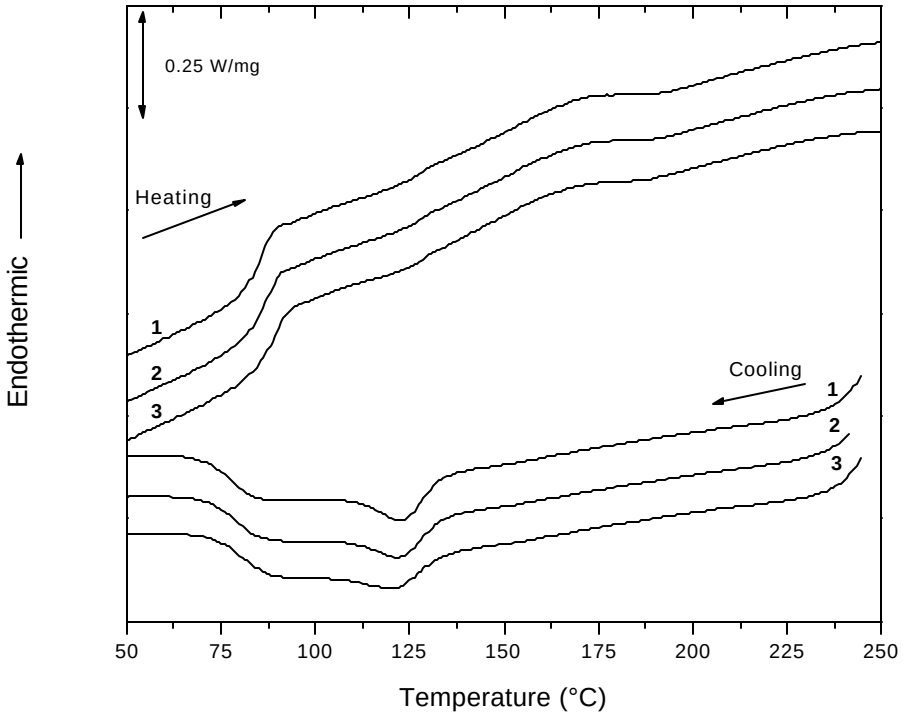

Figure 5.11. DSC trace of PAN-co-MA 85/15 for multiple heating and cooling cycles. Heating rate 20 °C/min. Numbers represent 1st, 2nd, and 3rd cycles after initial heating (not shown) to 250 °C to erase thermal history. Material was held for 2 minutes at 250 °C at the end of each heating run. Note decrease in magnitude of melting and crystallization events as well as small increase in the Tg.

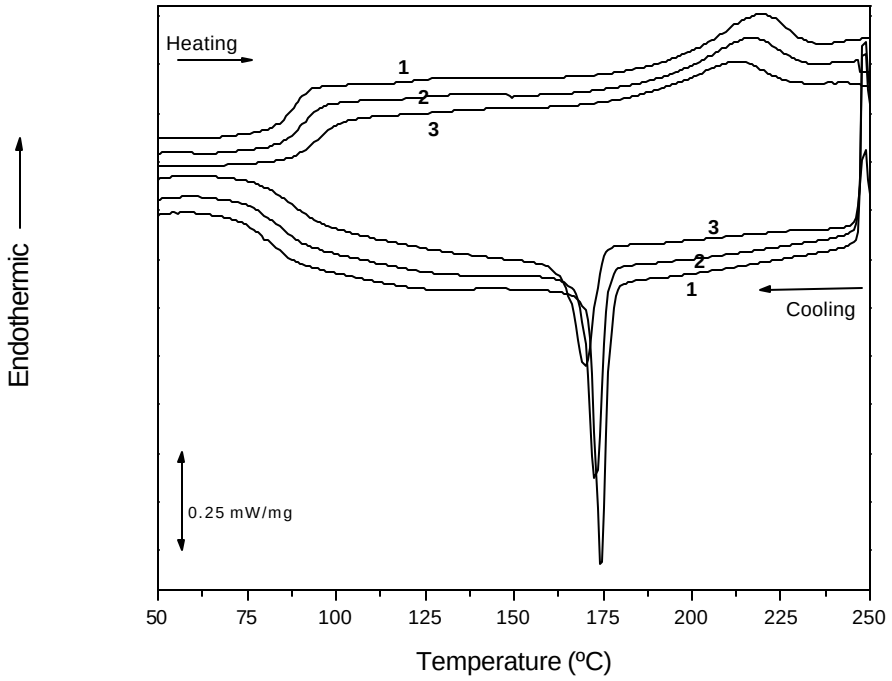

Figure 5.12. DSC trace of PAN-co-MA 90-10 for multiple heating and cooling cycles. Heating rate 20 ºC/min. Numbers represent 1st, 2nd, and 3rd cycles after initial heating (not shown) to 250 ºC to erase thermal history. Material was held for 2 minutes at 250 ºC at the end of each heating run. Note vertical shifts of the cooling portions are reversed to minimize curve overlap. Substantial degradation is suggested in the reduction of the magnitudes and shifting of the thermal transitions.

Secondly, it is apparent from this plot that the glass transition is not only being raised, but is also decreasing in magnitude as measured by the step change in heat capacity through the transition. Thirdly, in comparison with the 85/15 material, the first cycle (pristine) heats of melting and fusion are much greater. This result is in accordance with all of the earlier results which demonstrated that the amount of crystalline material was correlated with the AN content of the polymer.

It is also interesting to note from Fig.5.12 that both melting and crystallization temperatures are decreasing with further thermal cycling. It seems reasonable to associate the reduction of the melting temperature with the likelihood that the crystalline domains being formed on each successive heating are both smaller and less perfect due to the degradation process. Calculating the difference between the melting temperature and subsequent crystallization temperature shows a slight decrease in the level of supercooling for each successive cycle from 47 ºC to 44 ºC to 43 ºC respectively. However, as the melting of this material is fairly broad, making the definition of the melting point problematic, these values should not be regarded as absolute. They do suggest that while the degraded material may slightly increase the possibility of heterogeneous nucleation, the mechanism of crystallization which is occurring is consistent throughout the experiment. It also supports the hypothesis that the size and perfection of the crystallites formed decreases with each melting cycle as the changes are relatively small.

Figure 5.13 is included next to emphasize the fact that the melting process is wholly independent of the degradation reactions which are present in the same temperature range. Stated in an alternate manner, the act of melting the crystals does not lead to the degradation reaction. This plot is the result of an experiment using PAN-co-MA 90/10 employing a heating cycle that is identical to the method used in Fig.5.12 with one minor change. At the end of each heating cycle rather than waiting a full two minutes, the sample is held for only thirty seconds. Thus in Fig.5.13, the material has been subjected to the same maximum temperature for each cycle but for a shorter amount of time. The changes in the glass transition and the melting and crystallization events are much smaller in this plot relative to those of Fig.5.12, which involved the longer dwell times at elevated temperature.

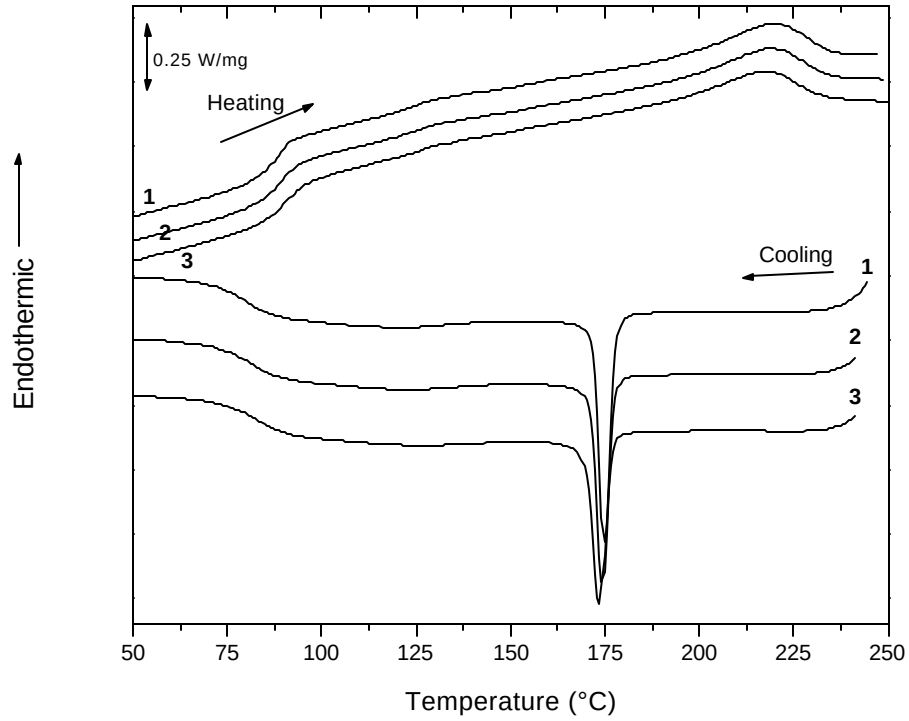

Figure 5.13. DSC trace of PAN-co-MA 90/10 for multiple heating and cooling cycles. Heating rate 20 °C/min. Numbers represent 1st, 2nd, and 3rd cycles after initial heating (not shown) to 250 °C to erase thermal history. Material was held for 30 seconds at 250 °C at the end of each heating run. Changes in thermal transitions with subsequent heating cycles is greatly reduced relative to Fig.5.12.

Thus it is quite evident that the degradation reaction is highly temperature dependent and involves a short induction time before rapid changes begin. While this makes the observation of melting possible, from a practical stand point, the delay in degradation at temperatures sufficient to melt PAN-co-MA materials is hardly long enough to consider these to have excellent melt stability. It should be noted, however, that *no stabilizers have been added to these samples*. For practical purposes, the addition of stabilizers to the material would be detrimental as the end goal is the production of a carbon fiber, a process which requires the eventual formation of the ladder polymer structure. In fact, a survey of the literature on PAN based materials for use as carbon fiber precursors finds no mention of the use of additives to promote thermal stability during spinning. However, there are numerous studies in which variables such as comonomer type, atmospheric composition, and additives to the spinning dope are investigated to ascertain their ability to *speed* the formation of the ladder structure during the initial heat treatment step.

Continuing in this series of experiments, the results for PAN-co-MA 93/7 are given in Fig.5.14. To achieve melting, a temperature of 260 °C was required for this copolymer. A dwell time of two minutes was used for consistency with the other tests. The additional ten degrees required to achieve melting for this higher AN content copolymer results in a substantial acceleration of the degradation process. By the third cooling and heating cycles, crystallization has been substantially reduced and the glass transition has been smeared to a point where it is barely recognizable. At first glance it appears that the 93/7 copolymer contains less crystallinity than does the 90/10 copolymer. However, it should be recalled that an initial thermal cycle to above the melt temperature, utilized for erasing the thermal history of the samples, is not shown in these plots. A great deal of degradation may have taken place in the 93/7 sample prior to observation of the first crystallization exotherm. No attempts were made to view the melting behavior of the 95/5 and 100/0 samples using DSC as the temperatures required for observation at moderate heating rates were too high to avoid large scale degradation on the first conditioning cycle.

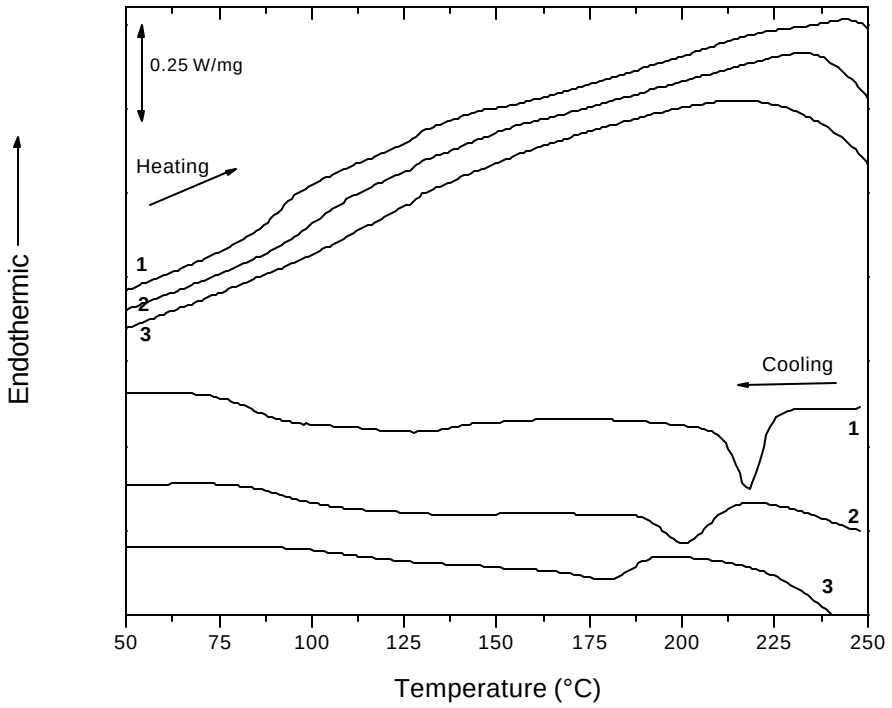

Figure 5.14. DSC trace of PAN-co-MA 93/7 for multiple heating and cooling cycles. Heating rate 20 °C/min. Numbers represent 1st, 2nd, and 3rd cycles after initial heating (not shown) to 260 °C to erase thermal history. Material was held for 2 minutes at 260 °C at the end of each heating run. Changes in thermal transitions with subsequent heating cycles are much pronounced relative to earlier examples.

5.7 Examination of the glass transition

A quantitative representation of the relative amounts of crystalline content can be obtained by examining the relative sizes of the step change in heat capacity for each sample. *Assuming that these copolymers can be represented by a simple two phase model*, the magnitude of the step change at Tg should be directly proportional to the amount of amorphous material present on a per unit mass basis. Thus, through observation of the glass transitions it should be possible to determine the relative crystalline contents among samples. A comparison of the relative step sizes at Tg as shown in Fig.5.15 is in accordance with all previous results. The magnitude of the glass transition event is observed to increase as the MA content of the copolymer is raised. These results show that MA acts to lower the crystalline content of the material as expected. A close examination of the Tg for each material shows a systematic increase in Tg with increasing AN content, with the exception of copolymer 95/5. The source of this discrepancy will be addressed shortly. An increase in Tg with AN content is to be expected using the simple Fox-Flory relation presented below in Eq.5.2 for random copolymers.

$$\frac{1}{T_g} = \frac{w_1}{T_{g1}} + \frac{w_2}{T_{g2}} \qquad \text{Eq.5.2}$$

where:

T_g = glass transition temperature of the copolymer
T_{gi} = glass transition temperature of homopolymer
w_i = weight fraction in copolymer of component I

Noting that the Tg of a MA homopolymer[19] is 10 °C, which is much lower than the Tg of PAN (~100 °C), the effect of its incorporation should be to lower the Tg of the copolymer relative to that of pure PAN. As evident from Fig.5.15, it is not trivial to determine the Tg of the homopolymer as its intensity appears to be very weak.

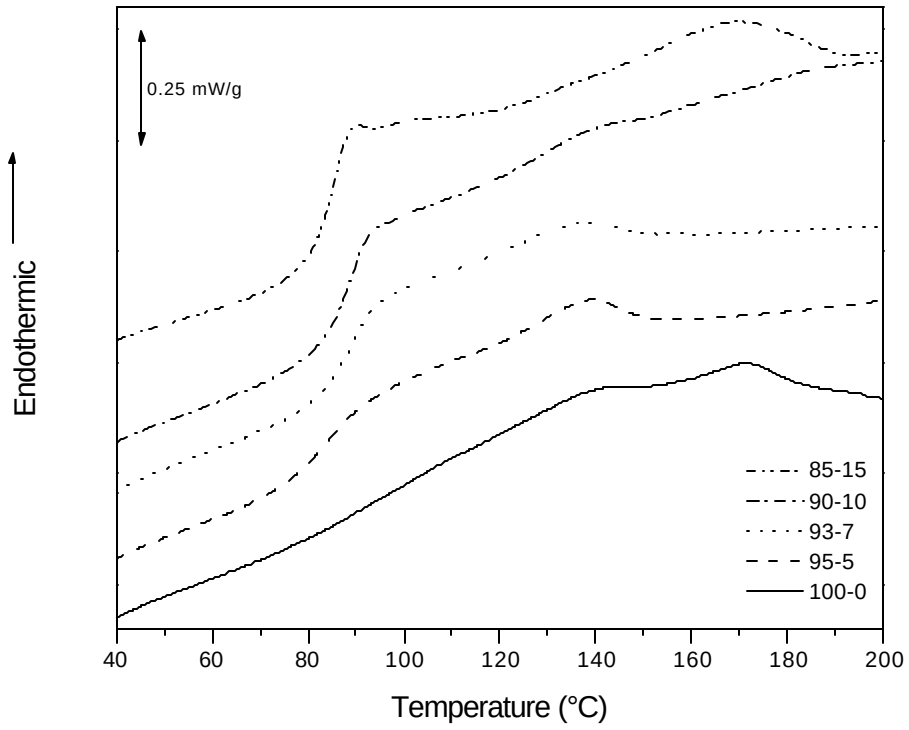

Figure 5.15. Glass transitions obtained with a heating rate of 20 °C/min after conditioning samples at 200 °C for 2 minutes. Step change at Tg decreases with increasing AN content suggesting that higher AN contents result in greater crystalline content. Tg increases with AN content with the exception of 95/5, see text for explanation of discrepancy.

In fact there is debate in the literature as to the exact Tg for PAN with values that extend from 78 °C to 150 °C given[20-22]. Using the values of the Tg's found for the copolymers in this study it should be possible to back calculate the Tg of PAN homopolymer if the Fox-Flory equation is valid for this system. Figure 5.16 compares the measured Tg values with the Fox-Flory equation assuming a value of 110 °C for the Tg of pure PAN. While the absolute values are fairly close to the model, it can be seen that if the data were to be extended over a greater range that the agreement appears to be less than satisfactory. Two basic hypotheses may be made to account for the discrepancy of the measured values with the model. Firstly, the Fox-Flory model does not take into account the fact that the level of crystallinity decreases as MA is incorporated into the copolymer. The lower level of crystalline content in the copolymer will make the model overestimate the Tg of the copolymer, as crystallites act to partially restrict motion of adjacent amorphous material. Secondly, the molecular weights of the samples may be a factor. Addressing this later point, it is well known that the glass transition temperature can be a strong function of chain length for linear polymers of low molecular weight. It is implicit in the model, by using the values of high molecular weight homopolymers, that the copolymer is also of high molecular weight. As one of the goals of this study was to produce a melt processable material, the molecular weights were purposely kept low so as obtain materials with reasonable viscosity. Four of the five materials in this study have approximately the same molecular weight (M_n) as exhibited earlier in Table 4-1, with one exception. The 95/5 content copolymer has a number average molecular weight of 8,500 g/mol that is substantially lower than the others (~ 20,000 g/mol). For this reason the Tg of the 95/5 copolymer does not follow the Tg trend as a function of comonomer content shown in Fig.5.16.

5.8 Insights into PAN structure through physical aging

Upon cooling from above Tg to temperatures below Tg, molecular mobility becomes drastically hindered. The reduction in mobility leads to a departure from thermodynamic equilibrium as the kinetics of contraction become so slow that they cannot keep pace with the finite cooling rate.

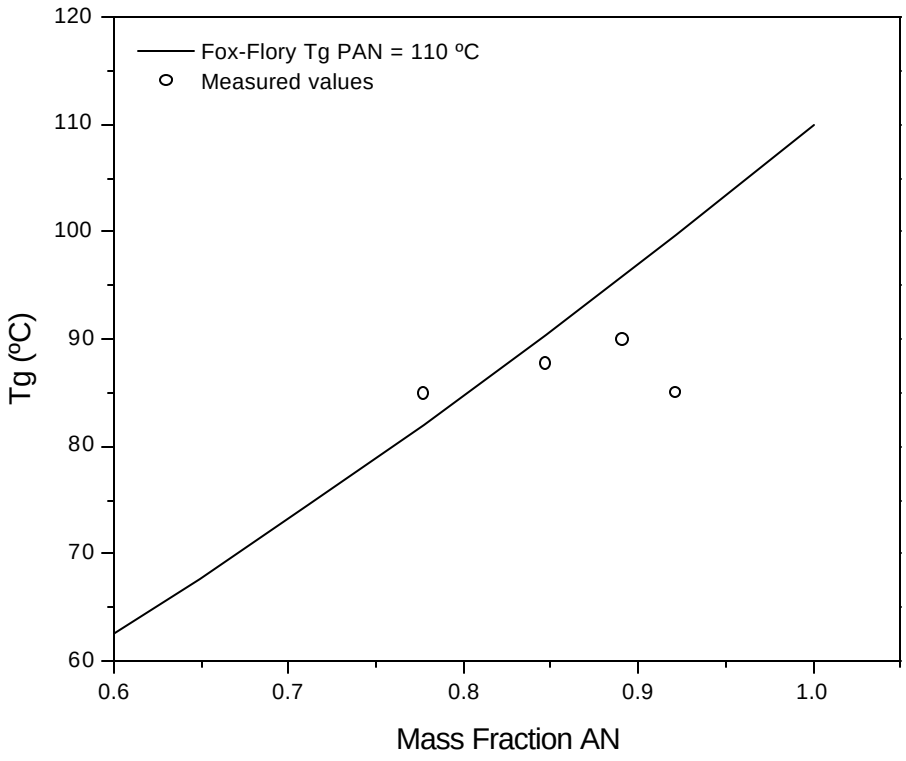

Figure 5.16. Fox-Flory predicted values for Tg versus measured values. Tg of PAN assumed to be 110 ºC for model calculations. Note general agreement though weighting factor appears incorrect (slopes differ).

Time spent below Tg is characterized by the polymer slowly attempting to restore equilibrium through further densification, if the chains have sufficient mobility. The approach of a non-equilibrium glassy material towards equilibrium below Tg is commonly referred to as physical aging. The rate at which the equilibrium state is approached is a function of the temperature of aging and the cooling history. The increase in density during aging results in a decrease in enthalpy as well. Upon heating above Tg, the enthalpy "lost" during this process can be noted through the re-absorption of heat as the density of the sample is returned to an equilibrium state. The heat signature of physical aging is the appearance of an endothermic event typically superimposed upon the glass transition. The exact position of this aging peak will depend on the temperature at which densification occurred. It was mentioned earlier that a debate still exists in the literature as to the true value of Tg for PAN. This portion of the study attempts to use the characteristic signature of physical aging to determine more precisely the location of the Tg of PAN homopolymer.

The debate over the glass transition of PAN largely stems from the unusual results which are often obtained using DMA. Routinely investigators have found two damping peaks, a lower peak at approximately 100 °C and an upper peak at roughly 130 °C. Depending on the study, the relative magnitude of one damping peak will be greater than the other. The results have not been consistent[20-22]. In all cases the magnitudes are substantially less than those typically observed for fully amorphous materials, as expected. This phenomena has been observed in this study as well as shown in Fig.5.17. Two damping peaks are observed for the homopolymer. *Interestingly the double peak is not noted in any of the samples containing comonomer*. A number of arguments have been put forth by others, reviewed in the literature by Bashir[20], for assigning Tg to either peak based on x-ray studies and comonomer studies, however all of the data has not been fully reconciled.

In theory, the detection of the upper limit of the glass transition in PAN should be a relatively simple procedure. A sequence of experiments conducted at different aging temperatures should yield aging peaks whose magnitudes will be proportional to the proximity of the aging temperature to Tg if this temperature was indeed below PAN's Tg. If the aging step is conducted above the Tg of PAN then no aging should be noted.

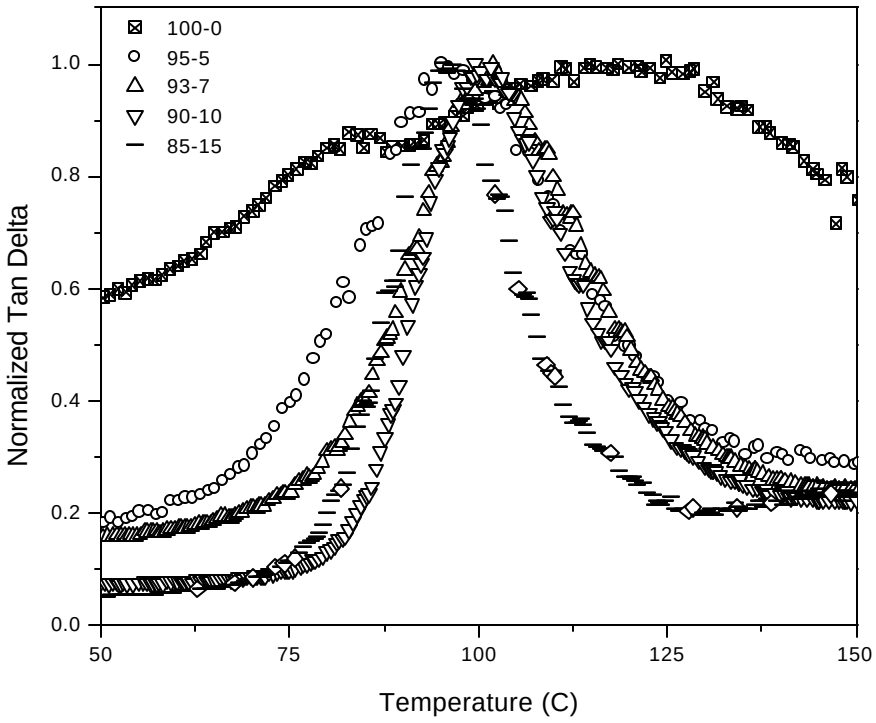

Figure 5.17. Normalized Tan delta (tan δ / tan δ_{max}) determined at 1 Hz. Note appearance of two maxima for 100/0 and possible shoulder on 95/5. Also note extreme breadth of the damping peaks for 100/0, possibly indicative of an extremely heterogeneous structure. See Fig.5.8 for relative magnitudes of damping peaks.

Recent research suggests that some low temperature melting peaks may closely resemble aging peaks, complicating the situation[23,24]. Figure 5.18 presents a set of three aging experiments conducted with a DSC using the 100/0 (homopolymer) sample. It can be seen that each of the three thermal treatments induces an endothermic event upon heating which is not present in the reheat step. The lowest temperature annealing schedule, 78 ºC, appears to produce an aging peak at 99 ºC. The asymmetric shape of the peak suggests that its appearance is superimposed upon an underlying step change in heat capacity. The middle annealing temperature, 120 ºC, produces an endothermic peak at 140 ºC. It is difficult to interpret whether this peak corresponds to an aging peak at the high end of the glass transition or is the result of the melting of small crystallites. The highest annealing temperature, 160 ºC, produces an endothermic peak at 180 ºC. The value of 180 ºC may be an underestimate as the onset of degradation appears to be superimposing itself upon the high side of this endothermic peak. Based on the position of this peak relative to the peak observed during the reheat step it appears that annealing at 160 ºC has resulted in the growth and perfection of a small population of highly imperfect crystals. The crystalline material which under modest heating and cooling rates melts at 170 ºC has been shifted to a higher melting temperature by the annealing at 160 ºC. These three results taken together suggest that the glass transition of PAN lies somewhere between the range of 80 and 160 ºC. This temperature window corresponds roughly to the broad, dual tan delta peaks observed by DMA in Fig.5.17. If an unambiguous determination of the endothermic event at 120 ºC could be made, this temperature window could be reduced further. The nature of this endotherm is further investigated in the next section.

5.9 Modulated Differential Scanning Calorimetry Results

The use of modulated differential scanning calorimetry (MDSC) should be capable of resolving the nature of the endothermic peak generated by the 120 ºC annealing step, by determining whether the process is reversible (melting) or irreversible (enthalpy relaxation). If the endothermic peak is the result of a reversible heat flow it is reasonable to interpret the heat treatment step to have occurred above Tg.

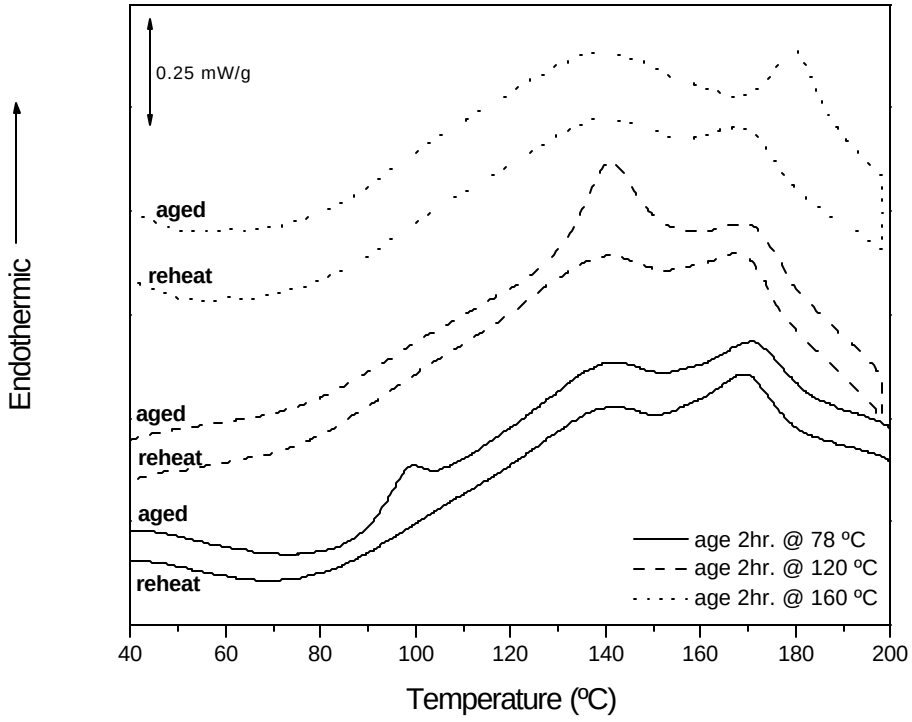

Figure 5.18. Physical aging study of PAN homopolymer. Each sample conditioned at 200 ºC for 2 minutes prior to rapid cooling to the aging temperature. After 2 hour aging period samples were cooled at 20 ºC/min to 20 ºC. Plot shows subsequent reheating at 20 C/min to 200 ºC (aged) and a second heating run (reheat) conducted after another 20 ºC/min cooling step.

If the endothermic peak is the result of a non-reversible heat flow, it implies that the heat treatment occurred below Tg. The total heat flow signal from four MDSC experiments involving annealing of the homopolymer at temperatures of 110, 120, 130 °C or no annealing are shown in Fig.5.19. A small endothermic event has been induced in each of the annealed samples. The vertical tick marks in this plot denote the temperature at which the annealing step was conducted. As in Fig.5.18, the temperature of the endothermic peak scales with the annealing temperature, occurring approximately over a temperature range 20 °C above the annealing temperature. The magnitudes of the observed events are not as great as those observed in Fig.5.18 because the MDSC experiments use a slower underlying heating rate relative to the conventional DSC experiments (2 °C/min vs. 20 °C/min). Unfortunately due to the relatively small heat signals generated by the annealing process in these semicrystalline systems, it is difficult to observe clean, sharp peaks from the data. To bring out the enthalpic events in the next three figures, the heat flow (total, reversible or non-revesible) from an unannealed 100/0 sample was subtracted from the data for the annealed sample. Thus, the data in Fig.5.20-22 can be thought of representing the excess enthalpy, induced by the annealing process, relative to an unannealed sample. In Fig.5.20 it can be seen that the endothermic peaks have now become clearer by using the subtraction procedure. However, it can also be seen that the subtraction also serves to add a small amount of noise to the data in the form of random ripples. To ensure that the noise is not mistaken for an endothermic event, vertical tick marks have been added to Fig.5.20-22. These marks can be used to the guide the eye to the temperature region in which the endothermic events were induced. Recall from Fig.5.19 that the endotherms were visible over a range of approximately 20 °C above the annealing temperature. Figure 5.21 contains the reversible heat flow component of the data presented in Fig.5.20. It is evident from Fig.5.21 that no endothermic event is detectable for the sample annealed at 110 °C. The endotherm appears to increase with annealing temperature. Because reversible heat flow should arise only from melting, it is apparent that at 110 °C the temperature is not great enough to induce the crystallization of a small fraction of the homopolymer. At temperatures of 120 and 130 °C a small amount of crystallinity was produced by the annealing step which subsequently melted during the heating scan.

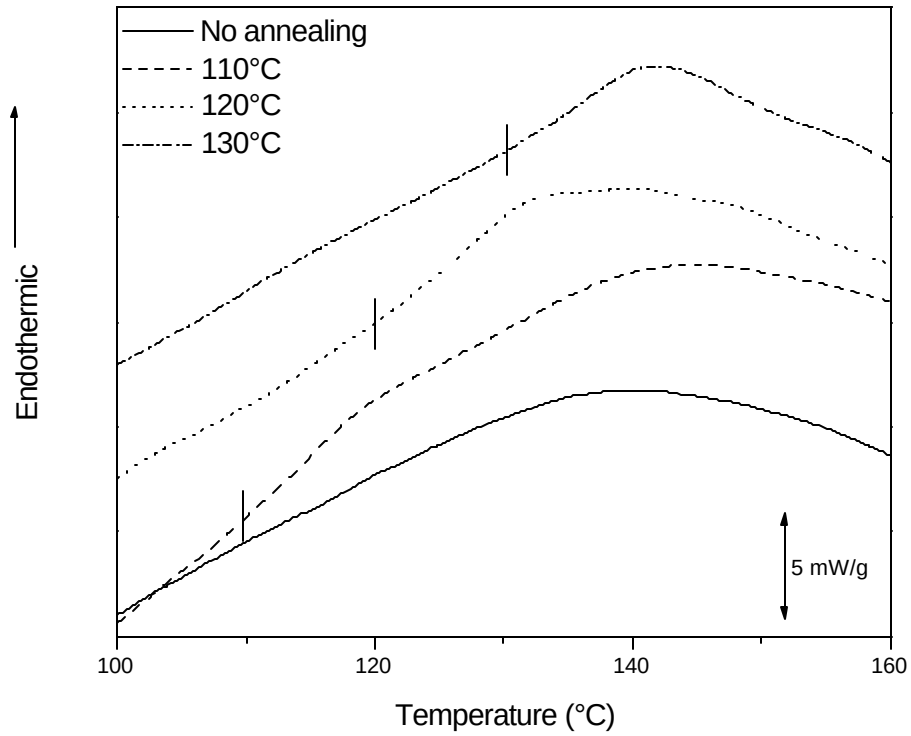

Figure 5.19. Total heat flow for 100/0 after various annealing conditions. Vertical lines demarcate temperature at which annealing occurred. Note apparent growth in the endothermic event upon reheating as a function of annealing temperature.

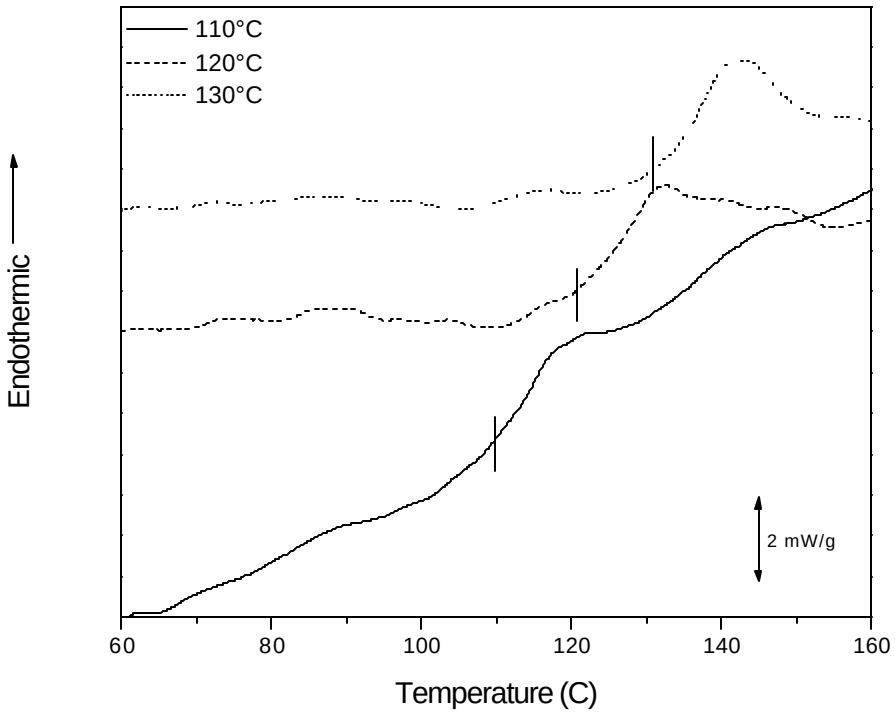

Figure 5.20. Total heat flow from MDSC of 100/0 annealed at different temperatures. A heating scan for an unannealed 100/0 has been subtracted from the annealed 100/0 data to provide what can be thought of as an excess enthalpy due to annealing relative to the unannealed materials. Annealing peak shifts with annealing temperature and appears to increase with annealing temperature. Vertical lines mark the temperature at which the annealing step was conducted.

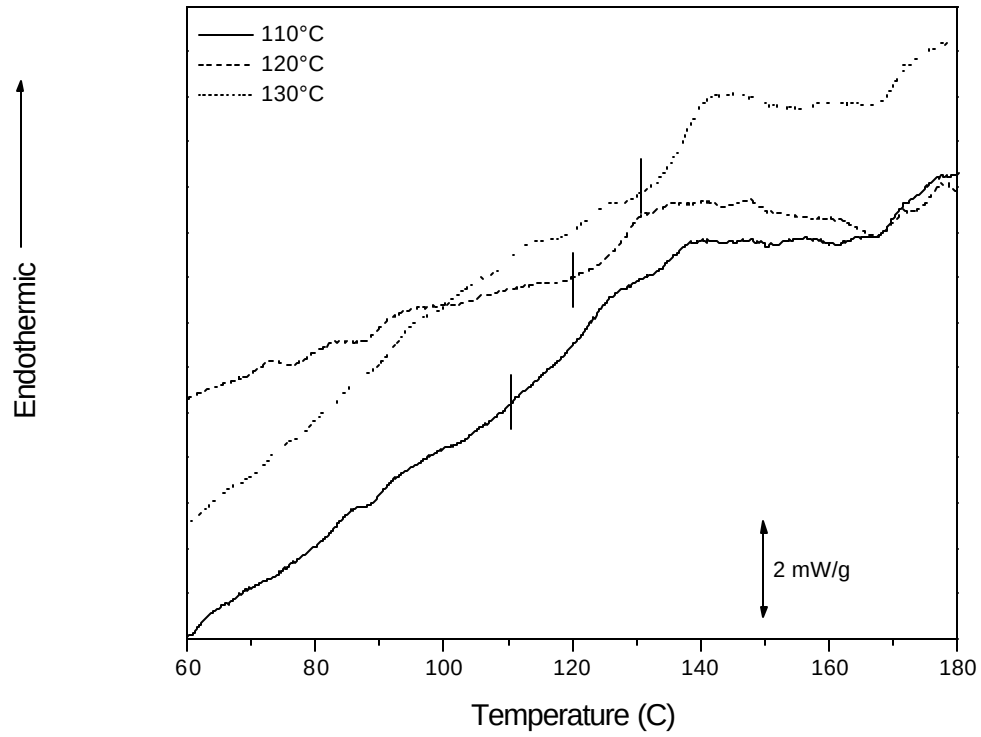

Figure 5.21. Reversible heat flow from MDSC of 100/0 annealed at different temperatures. A heating scan for an unannealed 100/0 has been subtracted from the annealed 100/0 data to provide what can be thought of as an excess enthalpy due to annealing relative to the unannealed materials. Annealing peak shifts with annealing temperature and appear to increase with annealing temperature. Vertical lines mark the temperature at which the annealing step was conducted.

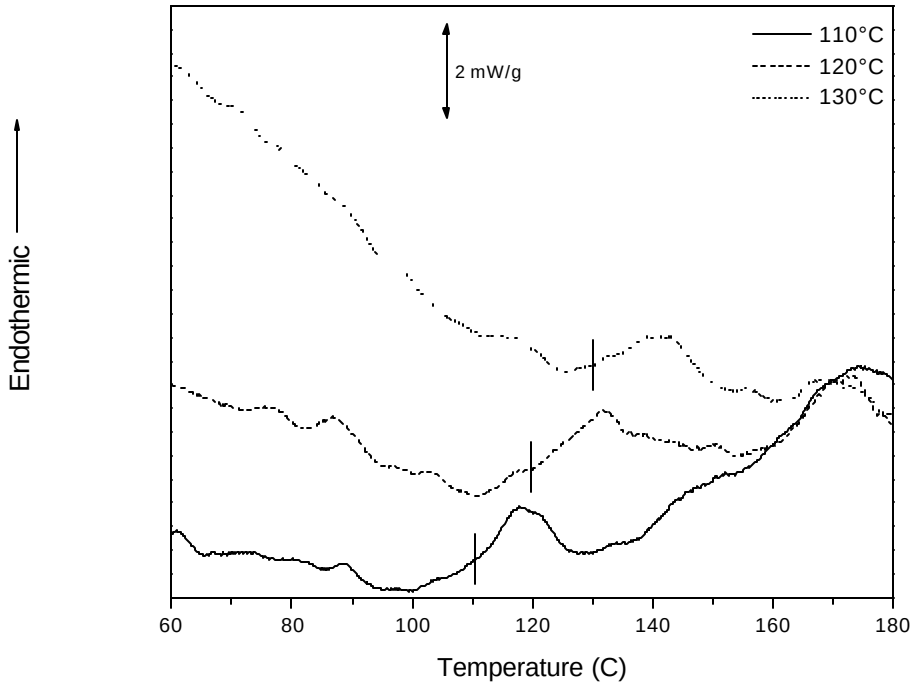

Figure 5.22. Non-reversible heat flow from MDSC of 100/0 annealed at different temperatures. A heating scan for an unannealed 100/0 has been subtracted from the annealed 100/0 data to provide what can be thought of as an excess enthalpy due to annealing relative to the unannealed materials. Annealing peak shifts with annealing temperature and appears to decrease with annealing temperature. Vertical lines mark the temperature at which the annealing step was conducted.

The rate of crystallization increased with annealing temperature. Thus, the analysis of the reversible heat flow suggests that the Tg of PAN must be above 110 ºC, but below 120 ºC. These values correspond roughly with the Tg value which can be inferred from the DMA tan delta results of Fig.5.17 if one takes the higher temperature tan delta peak as corresponding to Tg.

The non-reversible heat flow component of the data in Fig.5.20 is presented in Fig.5.22. Unfortunately these data are somewhat noisy. Of greatest importance is the clear presence of an endothermic peak for the sample annealed at 110 ºC, suggesting that physical aging has occurred. Thus, based on the data from Fig.5.20-22 it can be concluded that the endothermic peak noted in the homopolymer annealed at 110 ºC is due solely to physical aging. Curiously, the samples annealed at 120 and 130 ºC also show small endothermic peaks in Fig.5.22. It is difficult to quantify the relative areas of each peak due to the poor quality of the data. Recalling from Fig.5.21 that these two samples also show apparent melting behavior, it would appear that annealing at 120 and 130 ºC leads to *both* physical aging and crystallization. This finding suggests that the goal set forth at the beginning of this section, to define a narrow temperature range over which the glass transition in PAN occurs, may not be possible. Indeed, it appears that at temperatures of roughly 120 to 130 ºC portions of the material are above Tg while others are not. While it may be convenient to discuss the thermal properties of PAN in terms of a two phase semicrystalline model it appears that in reality PAN consists of a very heterogeneous mix of structural states. Apparently there are numerous "shades of gray" of mobility for PAN in the spectrum between material which can be considered amorphous and that which can be considered crystalline. The inadequacy of the two phase model to represent polymer behavior is not unprecedented. The material located at the boundaries between crystalline and amorphous phases at times has been defined as a third phase, referred to as the rigid amorphous phase (RAP)[25-27]. Accounting for the properties of the RAP, decreased mobility relative to the amorphous fraction, but lacking the packing order of the crystalline fraction, allows for discrepancies in crystallinity determination among various techniques to be explained. The quantification of the amount of RAP present requires the determination of the heat capacity as a function of temperature for the pure amorphous and crystalline phases respectively. Whether such

data could be collected is debatable. Based on some general observations regarding the rate at which PAN crystallizes to follow, obtaining a fully amorphous sample would be very difficult.

Of passing note, the use of MDSC also provides the opportunity to observe an additional interesting phenomenon. Because the MDSC can separate a reversible endothermic event, such as melting, from an irreversible exothermic event, such as degradation, it may be possible to observe melting behavior under conditions where it would be completely masked for conventional DSC. Figure 5-23 gives the results of a MDSC experiment for PAN with an underlying heating rate of 2 ºC/min after 2 minutes of conditioning at 200 ºC and subsequent cooling. A small melting event is evident in the reversible heat flow signal which is unobservable in the total heat flow signal due to the large magnitude of the non-reversible degradation reaction. Of additional note, Fig.5.23 shows that the initiation of degradation can occur at temperatures as low as 150 ºC.

5.10 Low melting fractions of PAN-co-MA

Close examination of the DSC curves presented to this point (e.g. Fig.5.15) shows what appear to be small melting endotherms fairly close to Tg, but far below the events that have been defined as the true melting points of the materials. Such a phenomenon is not unheard of in systems that do not crystallize "cleanly" due to defects or irregularities in chain architecture. For example both head-tail placement defects and changes in stereoregularity can lead to substantial portions of crystalline material which melt at temperatures below the expected melting point due to their highly imperfect structure. It is hardly surprising that such phenomena would be observed in PAN based materials since it is highly stereoirregular (atactic). To show that the small endotherms above Tg but below the upper melting temperature were indeed the result of the melting of imperfect crystals and not the result of residual moisture or some other source, Fig.5.24 is included. Samples were brought to 200 ºC to erase their thermal history and then annealed at 120 ºC for two hours. The DSC scans show the subsequent first and second heating cycles after the annealing procedure.

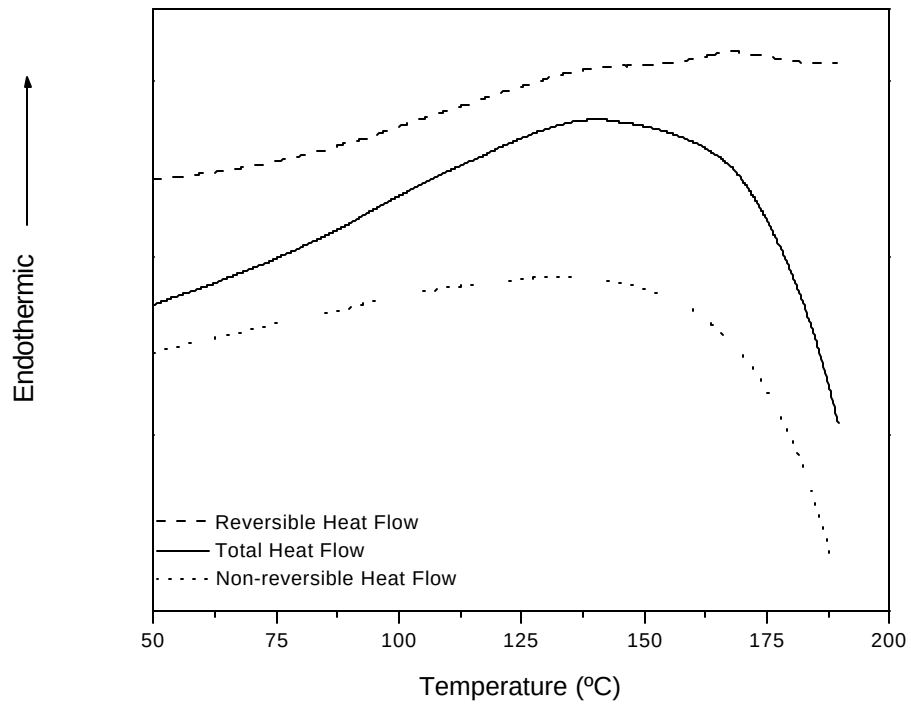

Figure 5.23. MDSC of PAN underlying heating rate of 2 ºC/min. Note small endothermic melting at approximately 170 ºC in the reversible heat flow signal which could not be observed in conventional DSC as represented by the total heat flow signal due to the magnitude of the exothermic degradation. Also note that degradation appears to be initiated at temperatures as low as 150 ºC when a slow heating rate is used.

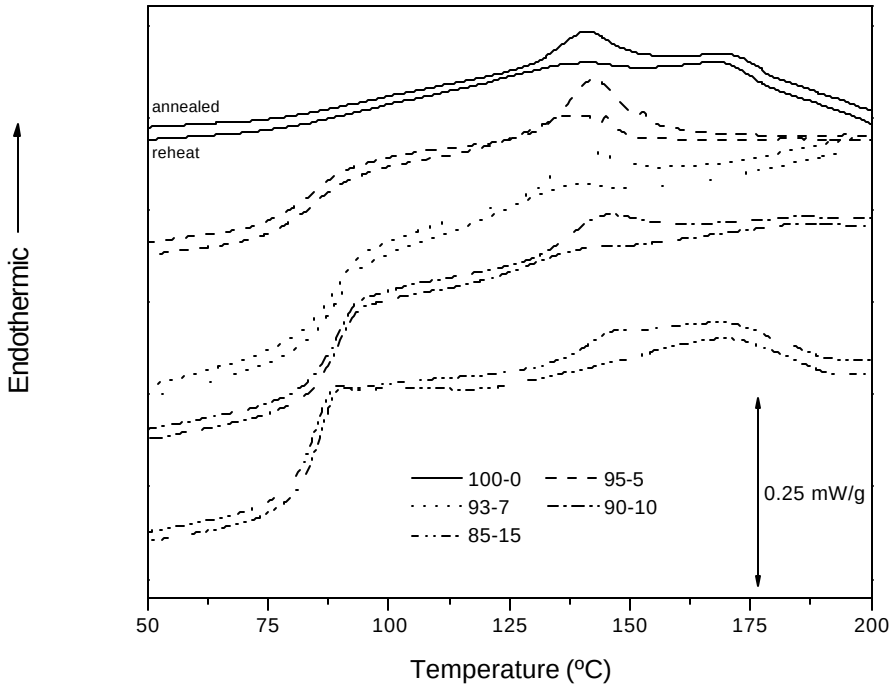

Figure 5.24. Results of annealing samples at 120 ºC for 2 hours. Upper curve of each pair represents first heat to 200 ºC after annealing, lower second heat after annealing. Annealing acts to increase the fraction of and raise the melting temperature of the low melting fraction.

In each case it can be seen that the endotherms centered at approximately 140 ºC after annealing are increased in size and shifted to slightly higher temperatures in comparison to their position relative to the reheat scan. This phenomena can be ascribed to small, imperfect crystals which were allowed to increase their perfection and/or lateral size during the annealing step and thus melt at a higher temperature.

5.11 Additional experiment to support melting hypothesis

As stated at the opening of the chapter, the global goal of this research project was to produce a melt spinnable PAN. Investigations into the viscosity of these materials, by project collaborators, showed that it was possible to measure the melt viscosity of the 85/15 and 90/10 PAN-co-MA materials used in this study[11]. To further support the contention that the critical factor in producing a melt processable PAN material is to first synthesize a material which melts well below the temperature degradation reactions begin, the following experiment was performed. The copolymer of composition 90/10 was taken to 250 ºC for two minutes to ensure melting. The sample was then quickly removed from the hot press and quenched in a dry ice – acetone mixture. The goal was to cool the melt rapidly enough to prevent crystallization. A WAXS pattern was then obtained and is shown in Fig.5.25. It is clear that the sharp reflections that were noted in this sample in Fig.5.2 have disappeared, suggesting that the sample was quenched rapidly enough to prevent any significant crystallization.

The need to use an extreme quenching procedure to prevent crystallization can be justified by studying similar quenching runs performed in the DSC. Figure 5.26 shows the results of experiments in which select samples were taken above their melting points and quenched at a rate of 200 ºC/min. *The apparent endothermic event present at the start of each cooling cycle is the due to the instrument and does not represent melting.* It can be seen that with the exception of the 85/15 copolymer, the others were able to undergo crystallization despite the rapid cooling conditions. While no quantitative crystallization rate studies were conducted, it appears that these materials can be considered to crystallize quite rapidly.

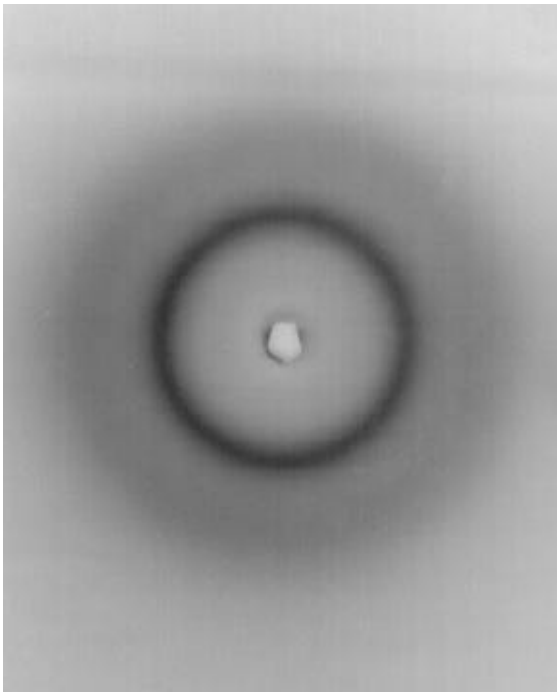

Figure 5.25. WAXS pattern of PAN-co-MA 90-10. Sample was melted by holding at 250 °C for two minutes and then quenched in a mixture of dry ice and acetone. Comparison to Fig.5.2 shows that the sample has lost its sharp reflections indicating a lack of ordered structures (crystallinity).

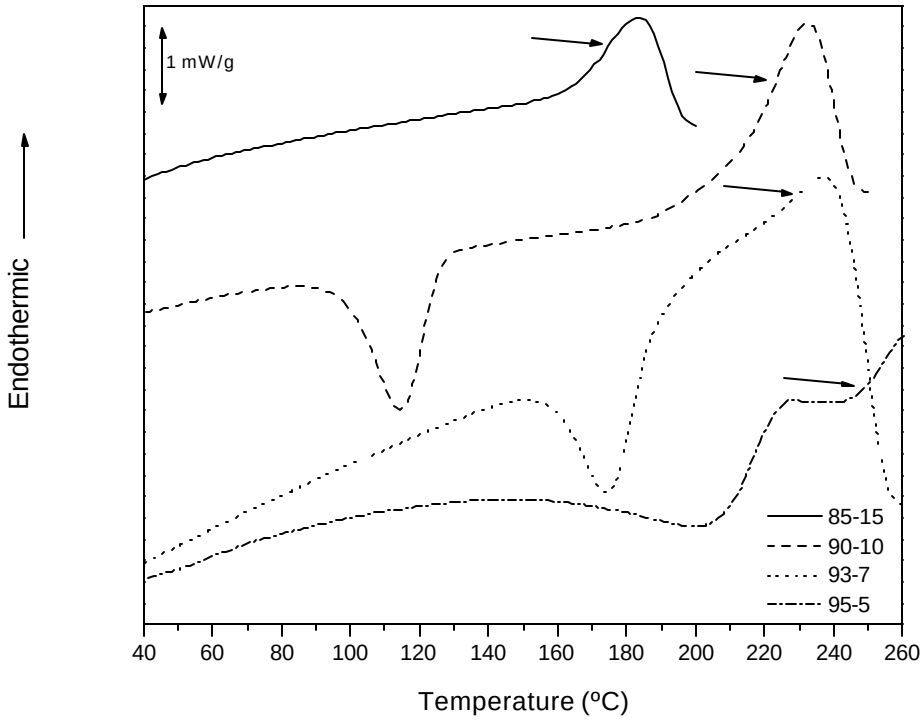

Figure 5.26. DSC traces of quenching experiments conducted at 200 ºC/min. Endothermic events at start of each cooling run are artifacts of the instrument, designated by arrows (start up "hooks"). Despite rapid cooling all samples with the exception of 85/15 crystallized.

To verify that the sample whose x-ray pattern was obtained in Fig.5.25 had been truly quenched, it was placed in the DSC to see if it would demonstrate typical melting behavior. The results are presented in Fig.5.27. It can be seen on the first heating after the quench, the sample readily crystallizes as soon as it is raised above Tg. While this result does not conclusively prove that there was zero crystallinity present after quenching, it does show that a substantial degree of crystallization was prevented by the quench. To verify that no serious degradation occurred during the melting step in the hot press, the subsequent cooling and heating curves are provided. Note that their behavior is typical of previous traces suggesting no major, irreversible structural changes were induced.

5.12 Melting – Viscosity Behavior

Additional insight into the processability of these materials can be gained by re-examining the DMA data in light of previously published rheological data[11]. In fig.5.28 dynamic parallel plate rheological data collected at 220°C are presented. Note the four orders of magnitude drop in viscosity at low shear rates (0.1 rad/sec) as the comonomer composition is increased from seven to ten mol%. This dramatic change in viscosity suggests a threshold comonomer content below which these materials will not be processable. The physical explanation for this change in viscous response with composition can be explained using the DMA results. Using the basic relationships between viscoelastic properties[28] the dynamic modulus data obtained in fig.5.9 are plotted as the corresponding complex tensile viscosity values in fig.5.29. Because the parallel plate results of fig.5.28 were obtained via shear it is expected that the values in fig.5.28 will be one third of those in fig.5.29. The values in fig.5.29 are somewhat larger, likely due to greater degradation/stabilization during the slow heating rate (2°C/min) employed in the DMA experiment in contrast to the single temperature measurements made in the rheological experiment. Of greatest interest is the viscosity of the materials at 220°C in fig.5.29, the same temperature data in fig.5.28 were collected. Figure 5.29 also demonstrates a dramatic change in viscous response as the comonomer content is increased from seven to ten mol%. However, the data in fig.5.29 make the nature of the

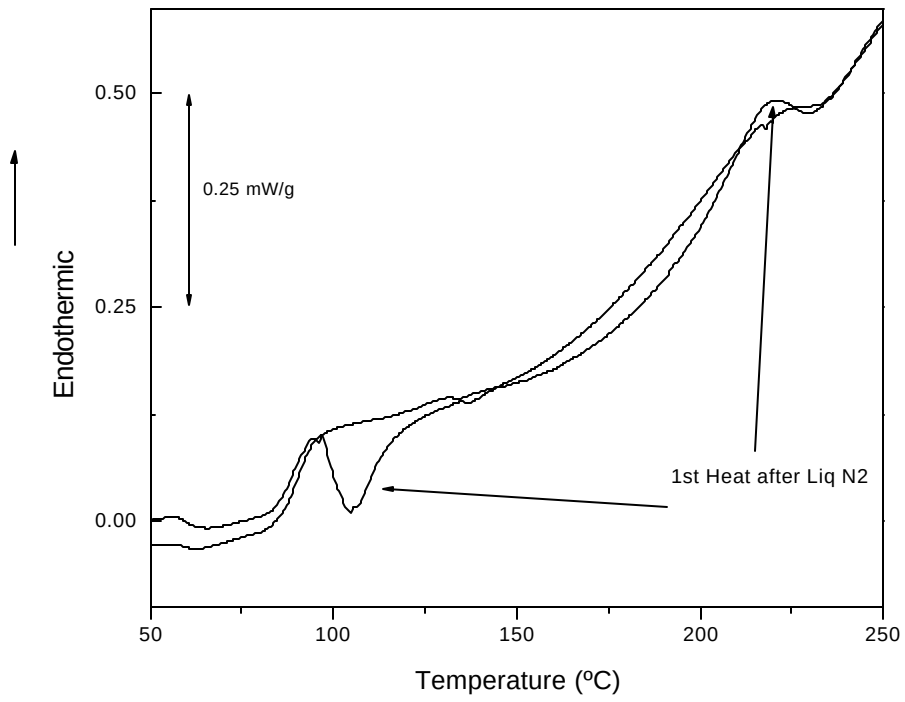

Figure 5.27. DSC trace of PAN-co-MA after quenching from the melt in a mixture of dry ice and acetone. Bottom two lines are first an second heats after quenching. Note immediate crystallization above Tg suggesting that quenching prevented crystallization.

abrupt change clear. At 220°C the 85-15 and 90-10 copolymers have fully melted (i.e. passed through the rubbery plateau) while the lower MA content copolymers have not. Thus, the dramatic change in viscosity observed in fig.5.28 is due to the differences in melting point among the copolymers. The 85-15 and 90-10 copolymers have melting points below the temperature at which the experiment was conducted, 220 °C, while the 93-7 and 95-5 materials have melting temperatures above 220°C.

5.13 Conclusions

This chapter has examined the thermal behavior of a series of solution polymerized PAN-MA copolymers without stabilizers. Qualitative trends in melting temperature, glass transition temperature, and crystal content were correlated with the level of comonomer. In addition, observations related to the structural heterogeneity of the system were made. Based on the data presented the following specific conclusions may be drawn from this research.

1) Increases in the content of comonomer clearly led to a reduction in the melting point of the copolymers as evidenced through DMA, DTA, and DSC results.
2) The melting point depression achieved in the two highest comonomer content materials (90/10, 85/15) was sufficient to achieve complete melting prior to the onset of thermal degradation using modest heating rates. This conclusion is supported by both DSC and DMA data.
3) The stability of these copolymers, with respect to reproducible melting and crystallization behavior over several melting/crystallization cycles, was found to be limited as shown by DSC. This is due to the proximity of the melting transitions to the onset of thermal degradation. Indeed, the MDSC data for sample 100/0 suggests that thermal degradation may initiate at temperatures as low as 150 °C.

4) Increases in comonomer content appear to lower the crystalline content of the copolymers. This trend is clear from the DTA, while the DSC and WAXS data are supportive.
5) Attempts to assign the glass transition of PAN to a narrow temperature may be futile. The thermal response of pure PAN suggests that a broad spectrum of structural motifs (levels of mobility) are present. The breadth of the upper DMA tan delta peak (~ 90 - 150°C) and the smeared nature of the glass transition as observed by DSC are indicators. Furthermore, experiments suggested that physical aging and crystallization process can occur concurrently when PAN is annealed at 110 °C. Thus, at a single temperature it appears that PAN contains amorphous regions with sufficient mobility to crystallize (characteristic of a material above Tg) while other regions remain in a relatively frozen state, which undergo physical aging (characteristic of a material below Tg).

The stated objective of this research was to determine if it is possible to lower the melting temperature of PAN based copolymers to a value substantially below the temperature at which rapid thermal degradation occurs. To this end, the research has been successful as melting transitions could be clearly and reversibly observed for the two materials of greatest comonomer content, 90/10 and 85/15. However, the melt stability of these materials appears to be somewhat limited. Choosing an arbitrary, but realistic, time of 30 minutes as the duration for which a small portion of the material is held up in the extruder during the spinning process, the results of this work suggest that substantial degradation would occur.

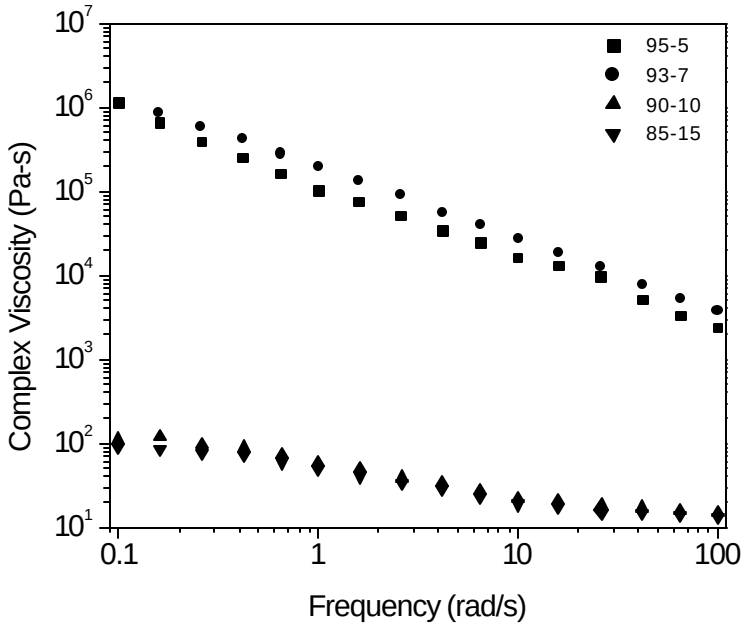

Figure 5.28. Complex viscosity of copolymers obtained at 220°C from previously published results[11]. Note four orders of magnitude drop in viscosity at low shear rates as the comonomer content is increased from seven to 10 mol%.

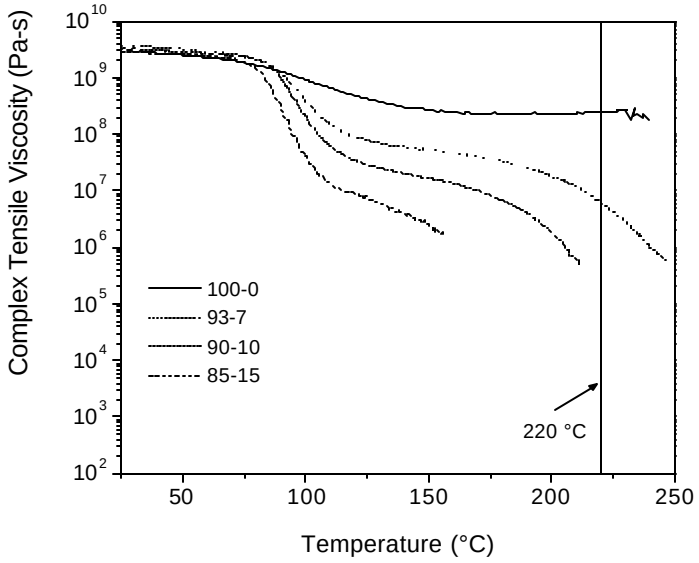

Figure 5.29. Complex tensile viscosity results derived from DMA data. Note that at 220°C the 85-15 and 90-10 copolymers have fully melted while the higher AN content materials have not, accounting for the large drop in viscosity noted in fig.5.28.

5.14 References

[1] Bashir, Z., *Carbon*, **29** (8) 1081 (1991).
[2] Bhat, G.S., Cook, F.L., Abhiraman, A.S., Peebles, L.H., *Carbon*, **28** (2/3) 377 (1990).
[3] Dalton, S., Heatley, F., Budd, P.M., *Polymer*, **40** 5531 (1999).
[4] Gupta, A.K., Paliwal, D.K., Bajaj, P., *JMS-Rev. Macromol. Chem. Phys*., **C31** (1) 1 (1991).
[5] Coleman, M.M., Sivy, G.T., *Carbon*, **19** 123 (1981).
[6] John P. Riggs, Encyclopedia of Polymer Engineering and Science, Vol.2, "Carbon Fibers", p.641,
[7] Johnson, D.J., *Journal of Physics Part D, Applied Physics*, **20** 286 (1987).
[8] Diefendorf, R.J., Tokarsky, E., *Polymer Engineering and Science*, **15** (3) 150 (1975).
[9] Jain, M.K., Abhiraman, A.S., *Journal of Materials Science*, **22** 278 (1987).
[10] Krigbaum, W.R., Tokita, N., *Journal of Polymer Science*, **43** 467 (1960).
[11] Rangarajan, P., Yang, J., Bhanu, V., Godshall, D., McGrath, J., Wilkes, G., Baird, D., *Journal of Applied Polymer Science*, **85** (1) 69 (2002).
[12] Rangarajan, P., Bhanu, V.A., Godshall, D., Wilkes, G.L., McGrath, J.E., Baird, D.G., *Polymer*, **43** 2699 (2002).
[13] Warner, S.B., Uhlmann, D.R., Peebles, L.H., *Journal of Materials Science*, **14** 1893 (1979).
[14] Tsai, A., Lin, C, *Journal of Applied Polymer Science*, **42** 3039 (1991).
[15] Bashir, Z., *Journal of Polymer Science Part B: Polymer Physics*, **32** 1115 (1994).
[16] Wiles, K., Bhanu, V., Pasquale, A., Long, T., McGrath J., *Polymer Preprints*, **41** 608 (2001).
[17] Flory, P.J., Principles of Polymer Chemistry, Cornell University Press, London (1953).
[18] Dunn, P., Ennis, B.C., *Journal of Applied Polymer Science*, **14** 1795 (1970).
[19] Polymer Handbook 2nd edition, Ed. Brandup, J., Immergut, E.H., Wiley-Interscience, New York (1975).
[20] Bashir, Z., *Journal of Macromolecular Science – Physics*, **B40** (1) 41 (2001).
[21] Yamane, A., Sawai, D., Kameda, T., Kanamoto, T., Ito, M., Porter, R., *Macromolecules*, **30** 4170 (1997).
[22] Kimmel, R.M., Andrews, R.D., *Journal of Applied Physics*, **36** (10) 3063 (1965).
[23] Velikov, V., Marand, H., *Journal of Thermal Analysis*, **49** (1) 375 (1997).
[24] Marand, H., Prasad, A., *Macromolecules*, **25** 1731 (1992).
[25] Lau, S.F., Wunderlich, B.J., *Journal of Polymer Science, Polymer Physics*, **22** 370 (1984).
[26] Lu, S.X., Cebe, P., *Polymer*, **37** (21) 4857 (1996).
[27] Alsleben, M., Schick, C., *Thermochimica Acta*., **238** 203 (1994).
[28] Aklonis J.J., MacKnight, W.J., Introduction to Polymer Viscoelasticity 2nd ed.. Wiley-Interscience, New York (1983).

Chapter 6

Summary and Recommendations for Future Work

The preceding chapters have presented three separate research projects. Because there is no direct connection between each area, they will be addressed separately. Here, the conclusions for each will be reviewed in turn, and recommendations for future work proposed.

6.1 Chapter 3: Unique Morphologies Consisting of Orthogonal Stacks of Lamellae in High Density Polyethylene Films – Formation in the Delayed Blow Out Process and Effect on Tear Properties.

6.1.1 Summary

This study investigated the effects of molecular and processing variables on the end structure of blown HMW-HDPE films using the delayed blow out, or high stalk, process. Under appropriate conditions it was found that two populations of lamellar stacks with their surface normals orthogonal to one another could be generated. At the lowest FLH studied, the resultant film morphology consisted of row nucleated structures oriented along the MD. Increasing the FLH was found to promote the formation of a second, orthogonal population of staked lamellar structures oriented along the TD. The delayed blow out process was conceptualized as consisting of two interrelated, but distinct processes. The first consists of MD stretching and relaxation in the neck region. The second is bubble expansion, resulting in TD expansion. The level of orientation induced in each step was reasoned to be a function of the resin's relaxation behavior, the time scale (strain rate and quench time) of the step, and the stresses generated. Conditions which led to greater stress levels resulted in larger effective BURs, thus favoring the formation of TD stacked material.

Measurements of tensile properties along the MD, TD, and 45° between these extremes, indicated that an anisotropic mechanical response could be linked to poor dart impact resistance. It was interesting to note that, under the conditions studied, it was possible to produce greater lamellar orientation balance in the plane of the film for the lower MW, narrow MWD resin by down gauging. The same was not true for the higher MW, broader MWD resin.

6.1.2 Future Work

The production of additional films, based upon these same resins, under alternative processing conditions would allow the general conclusions of the chapter to be tested. As it was found that the change in effective BUR has a substantial impact on the amount of TD stacked material formed, it would be interesting to determine if the two resins could be used to produce films of identical morphology by utilizing a slightly larger BUR for the narrower, lower MW resins, in comparison to that of the broader, higher MW resin, all other processing conditions equal. Along similar lines, the proper combination of decreased die gap and line speed would

allow films of the same gauge as studied in this chapter to be produced. However, these conditions would result in lower stresses in the bubble, and therefore would be expected to affect the relative amounts of MD and TD stacked material.

The microscopic observation of failure surfaces after tear and/or puncture tests may reveal additional information regarding the mode of failure. In this manner, it may be possible to observe differences in plastic deformation along the MD and TD directions which could explain observed differences in mechanical response.

Further insight into the nature of the MD and TD stacks might be gained by conducting creep experiments along the MD and TD directions, respectively, in the film which showed the most balanced lamellar orientation. It would be interesting to see if any anisotropy, possibly related to differences in tie chain connectivity between lamellae within a given stack, is observed. At present, techniques capable of quantifying such differences are not available.

Lastly, higher quality pole figure data would allow for the quantitative calculation of crystalline c-axis orientation. As tear anisotropy generally follows backbone orientation, it would be instructive to determine if the tear properties of these films could be correlated with the magnitude and nature (e.g. possibly planar-bimodal vs. planar-balanced) of c-axis orientation.

6.2 Chapter 4: Correlation of Moisture Vapor Transmission Performance with Structure-Property-Processing Relationships in Blown High Density Polyethylene Films

6.2.1 Summary

A series of blown films produced from a number of HDPE resins was studied. The effects of M_w and MWD on the orientation of the films for equivalent processing conditions were examined. WAXS results demonstrated that, taken as whole, the set of films contained varying levels of crystalline orientation, though the differences were small. Furthermore, all of the films studied contained morphologies which are consistent with the K-M model of low stress row crystallization, with uniaxial orientation. The

application of IR dichroism to a limited number of films proved quite successful in quantifying the relative levels of crystalline orientation as a function of M_w and MWD. The dichroism data indicated that greater levels of orientation were obtained in films of narrower MWD and greater MW, all other factors equal. The light scattering and pole figure data were supportive of this finding. It was reasoned that the narrow MWD, metallocene resins produced more highly oriented films because greater stresses were developed in the melt, relative to the broader MWD resins, due to their lesser propensity to shear thin. Microscopy indicated that the lamellae became increasingly oriented with their surface normals parallel to the MD as the processing stress increased. The permeation data suggested that, to a first approximation, the MVTR performance could be related to the square of the amorphous phase content, such that greater crystallinity led to improved barrier properties. Thus, longer quench times, which necessarily require slower cooling rates, are beneficial to MVTR performance as they lead to greater levels of crystallinity. Attempts to further correlate MVTR performance with processing stresses and orientation, using processing and resin parameters, proved problematic. While a general trend was noted that greater processing stresses led to poorer barrier properties, the correlation could not be used as a predictor of a specific film's MVTR.

6.2.2 Future work

The single most important follow up, which could be conducted with respect to this work, would involve the production of additional films such that a wider range of crystalline orientations would be observed. By magnifying the morphological differences it would be much easier to discern the impact of crystalline orientation on permeation. While the processing conditions used to produce such systems would not necessarily be of industrial significance, greater insight into the role of crystallization could be obtained.

Additional permeation experiments using more analytical and accurate methods would also be of benefit. The possible influence of amorphous orientation on permeation behavior has been neglected in this study. Sophisticated permeation measurements allow the equilibrium sorbed permeant concentration to be determined. This value is proportional to the amorphous phase free volume and represents the number of sites

available for permeation. Thus, if substantial constraints exist in the amorphous phase, the overall permeability will decrease. If one makes the entirely reasonable assumption that the conditions which lead to greater crystalline orientation in blown films also leads to greater amorphous orientation, it can be seen that there are two competing effects. Increases in crystalline orientation lead to greater permeation rates while concurrent increases in amorphous orientation lead to smaller permeation rates.

6.3 Chapter 5: Thermal and Structural Characterization of Poly(acrylonitrile-co-methyl acrylate) Copolymers. Effects of Comonomer Content on Melting Behavior

6.3.1 Summary

The thermal behavior of a series of PAN-MA copolymers was investigated. It was determined that the MA comonomer acted to lower both the glass transition temperature and the melting temperature of the copolymer relative to PAN homopolymer. WAXS patterns noted a qualitative decrease in scattered intensity and reduction in sharpness of the crystalline reflections, suggesting that the size and/or perfection of the crystallites was reduced with increasing MA content. The melting point depression was sufficient in the 90/10 and 85/15 MA content copolymers to allow for complete melting, prior to the onset of thermal degradation, using modest heating rates (20 °C/min). However, the melts of all the copolymers were relatively unstable, as the heats of melting and crystallization were observed to decrease after successive melting and crystallization treatments. Finally, some observations of the structurally heterogeneous nature of PAN homopolymer were made using DSC and MDSC. These studies suggested that PAN annealed at 110 °C contains regions undergoing crystallization while other, less mobile regions, undergo physical aging at the same time.

6.3.2 Future work

Based upon Flory's treatment of melting point depression in copolymers, the change in T_m is influenced by both the comonomer content (on a molar basis) and the

size of the comonomer unit. Thus, it would be interesting to note if similar reductions in T_m could be achieved by using lesser mole percents of a larger comonomer unit. From a practical standpoint, the success of such an experiment would suggest the use of comonomers which occupy the largest volume possible with the smallest mass possible. Thus, a substantial reduction in T_m could be achieved with less mass loss during subsequent carbonization.

The synthesis of copolymers incorporating a very small and flexible linkage may be an alternate route to T_m reduction in PAN based material. The atactic configuration of PAN limits the quality of packing that the crystalline phase can achieve in these systems. Thus, it may be possible for a small comonomer to become incorporated into the crystalline lattice. Mandelkern[1] has noted that the relatively high T_m of PAN is not the result of a large enthalpic gain upon crystallization, but rather reflects the small change in entropy, due to the somewhat stiff nature of the PAN chain. The incorporation of a flexible comonomer, capable of being incorporated into the crystalline phase, might substantially lower the T_m by decreasing backbone rigidity.

6.4 References

[1] Mandelkern L., Crystallization of Polymers, McGraw Hill, New York, 1964.

VITA

David Leonard Godshall was born August 28, 1973 in Antioch, Illinois though the majority of his primary education was received in Naperville, Illinois. Upon graduation from highschool in 1991, he attended Michigan State University and obtained his B.S. degree in Chemical Engineering in 1995. He then spent four months dropping bottles filled with carbonated water in the name of science for Crown Cork and Seal Inc. at their corporate research headquarters in Alsip, Illinois. David then returned to MSU for eight months of lab work with Dr. Alec Scranton before joining Virginia Polytechnic Institute and State University to obtain his M.S. under the guidance of Dr. Garth Wilkes in the Chemical Engineering department. Completion of his M.S. degree in 1999 was followed by three additional years of study under Dr. Wilkes to obtain a Ph.D. in the fall of 2002.